January 2019

Utilizing Immunopet To Measure Tumor Response To Treatment In Breast Cancer

Brooke Mcknight
Wayne State University, bnmcknight@gmail.com

UTILIZING IMMUNOPET TO MEASURE TUMOR RESPONSE TO TREATMENT IN BREAST CANCER

by

BROOKE N. MCKNIGHT

DISSERTATION

Submitted to the Graduate School

of Wayne State University,

Detroit, Michigan

in partial fulfillment of the requirements

for the degree of

DOCTOR OF PHILOSOPHY

2018

MAJOR: CANCER BIOLOGY

Approved By:

Advisor	Date

DEDICATION

I dedicate this to all of the little girls who dream of seeing, learning, and becoming "more", and to the people who support them every step of the way.

To those of you who did that for me - thank you for giving me "more".

ACKNOWLEDGEMENTS

Throughout my graduate career, I have received the support and guidance from many people who deserve my appreciation. This work would not have been possible without the support of my advisor, committee, colleagues, family, and friends.

Advisor

I would like to express my sincere gratitude to Dr. Nerissa Viola, who has been my advisor throughout my dissertation work. Thank you for providing me with an environment to learn, design projects, and cultivate the skills necessary to have a successful career. Without Dr. Viola, this project would not have been possible, and I am grateful for her wealth of knowledge and generosity that made it happen.

Committee

Throughout my dissertation research, I have received advice and encouragement from each of the members on my committee. Each mentor has provided me with valuable insight and expertise that has taken my project to another level. Dr. Anthony Shields has provided a clinical perspective to my project and has been an invaluable source of knowledge regarding imaging aspects of the experiments. Dr. Wei-Zen Wei has provided immunology expertise, without which the fourth chapter of this dissertation would cease to exist. She has also served as a co-mentor during my F-31 grant submission. Dr. Julie Boerner has been an advocate of mine since I was recruited into the program under her direction and has since provided vital insight into the biology of Src and the HER family signaling pathway. Dr. Matt Allen has challenged me with thoughtful questions regarding the chemistry of my projects, which has allowed me to gain this experience*. Each of my

committee members has provided me with mentorship for which I am especially grateful.

Viola Lab

Each member of the Viola lab has been a great source of support and friendship during my entire time in the lab. Jordan White has been a wonderful friend and peer. I am thankful for his help in keeping the lab organized and performing/troubleshooting experiments side-by-side on the days when I needed a little extra push to get going. I also am grateful for our similar taste in music, and the ability to rock out to 90s pop hits, 2000s hip hop, and Christmas music year-round. Dr. Akhila Kuda-Wedagedara has been a surrogate “big brother” in the lab, sharing with me his insights into the PhD process, helping me with the chemistry of my experiments, and acting as a sounding board when designing experiments.

Colleagues

I would also like to thank Dr. Heather Gibson, Claire McCarthy, and Joyce Reyes for their hands-on involvement in the project described in chapter 4. Agnes Malaysa, Dr. Lisa Polin, Kirk Douglas, Dr. Jessica Back, Xin Liu, Dr. Tom Mangner, Karri Stark, and the DLAR staff have all provided me with the support, knowledge, and hands-on assistance with various parts of my experiments, and I would have been much less organized without your attention to detail and expertise. Thank you all.

Cancer Biology Graduate Program

Of course, I must also thank the Cancer Biology Graduate Program for their continued support and guidance through this entire process. I would like to thank Dr. Larry Matherly for his management of the CB program and his interest in the success of the students. To Dr. George Brush, thank you for all of your input and advice over the years,

and for always making sure I have submitted my IDP correctly and on time. And to Nadia Daniel, thank you for always making sure the “trains run on time” – without your continued enthusiasm and dedication for the program and my personal success I would not be where I am today. Additionally, I would like to extend my sincere gratitude to the steering committee members from 2014-2018 for fostering a research-focused environment for the students to flourish.

Additional Significant Support

I must now thank the students, whom without there would be no program. I would like to specifically thank a few of the graduates who have provided me with invaluable insight, support, encouragement, and stories – Drs. Stephanie Blocker, Tom McFall, Rayna Rosatti, Chris McHugh, and Dan Feldmann. And to a few of the current students who are my confidants, friends, and consultants – Josh Heyza, Anthony Guastella, Laura Hurley, Nico Moses, Ethan Brock, Allison Mitchell, Kayla Connor, Adrianne Wallace-Povirk, and Josh Mandella – thank you for always being a text message, lab-themed snapchat, or Starbucks break away.

I would additionally like to thank Dr. David Ginsburg, Dr. Rami Khoriaty, Dr. Leslie Everett, and Suzann Labun for taking a chance on me back in 2013 when I was a junior at the University of Michigan. Without your support and training, countless letters of recommendation, abstract and CV editing, and continued advice, I would not be where I am today.

Family

I would like to acknowledge the people whose battles inspired me to apply for this PhD in particular. First, to my grandma-angel, Marilyn Gravila, who lost her 30-year battle

in 2000. Next, to my dad, and my cousins Brad Foster and Derek Adams, who have won or are still fighting their battles. Finally, to the countless family-friends who have allowed me to probe into their experiences for the purpose of expanding my cancer knowledge – your kindness in sharing your stories has made me a better scientist.

I would like to extend the largest thank you to my immediate family. None of my accomplishments would have been possible if not for your constant support, encouragement, and love. I want to give the most heartfelt thanks to everything they have done to keep me motivated throughout this process. To my dad, Mark McKnight, thank you for always being my confidence – even when I am not sure of myself. You have always pushed me to be better and do more, and I am forever grateful. I would like to thank my mom, Michelle McKnight, who has taught me everything I know about being a strong and intelligent woman. You have always been my rock and sounding board, and I thank you for your constant support. Together, you have provided me with a solid foundation to build a life upon, and I couldn't have done any of this without your financial support. Thank you from the bottom of my heart for the sacrifices you both made to provide me with a wonderful life.

I would like to thank my "bonus family" – John, Cheryl, Jared, and Jordan Dickow. You have all been here with me since sophomore year in college, so I feel as if you've been a part of this process every step of the way. Thank you for all of the phone calls, advice, and your constant curiosity in what I am doing, even if after a few minutes of explanation you wish you hadn't asked after all. I will forever cherish the holidays, weekends, and game nights spent together, that provided me with a little "escape" from

my constant studying.

Last but not least, I thank my husband, Justin Dickow. Who would've thought that back in 2011 when we met and began our relationship by spending countless hours studying at the BBB building and the Dude at the University of Michigan that we were setting up our lives for the next decade. Without your continued support, coaching, and "tough love" (when it comes to academics and my study habits), I would have never learned how to push myself academically or been able to complete a PhD. I owe this all to you and am so glad we can share in the fun times now that school is over! (for now…)

TABLE OF CONTENTS

LIST OF TABLES

LIST OF FIGURES

LIST OF ABBREVIATIONS

^{18}F-FDG	[^{18}F] – Fluorodeoxyglucose
ADCC	Antibody-dependent cell-mediated cytotoxicity
APC	Antigen presenting cell
BC	Breast cancer
CD3	Cluster of differentiation 3
CD8	Cluster of differentiation 8
CDx	Companion diagnostic
CISH	Chromogenic in situ hybridization
CT	Computed tomography
CTLA-4	Cytotoxic T-lymphocyte associated protein 4
DC	Dendritic Cell
DFO	Desferoxamine
DMSO	Dimethyl sulfoxide
EDTA	Ethylenediaminetetraacetic acid
EGFR	Epidermal growth factor receptor
ELISPOT	Enzyme-linked immunospot
ER	Estrogen receptor
FDA	Food and Drug Administration (USA)
FISH	Fluorescence in situ hybridization
GAPDH	Glyceraldehyde 3-phosphate dehydrogenase
HAMA	Human anti-mouse antibody

HER	Human epidermal growth factor receptor
HER2	Human epidermal growth factor receptor 2
HER3	Human epidermal growth factor receptor 3
HRP	Horseradish peroxidase
IACUC	Institutional animal care and use committee
IFNγ	Interferon gamma
IHC	Immunohistochemistry
imRECIST	Immune-modified Response Criteria in Solid Tumors
ITx	Immunotherapy
ImmunoPET	Immuno Positron Emission Tomography
i.p.	Intraperitoneal
i.v.	Intravenous
MIP	Maximum intensity projection
MRI	Magnetic resonance imaging
nEGFR	Nuclear epidermal growth factor receptor
NK cell	Natural killer cell
p-SCN-Bn-Deferoxamine	1-(4-isothiocyanatophenyl)-3-[6,17-dihydroxy-7,10,18,21-tetraoxo-27-(N-acetylhydroxylamino)-6,11,17, 22- tetraazaheptaeicosine] thiourea
p-SCN-Bn-NOTA	2-S-(4-Isothiocyanatobenzyl)-1,4,7-triazacyclononane-1,4,7-triacetic acid
PBS	Phosphate buffered saline
PD	Progressive disease
PD-1	Programmed death protein 1

PET	Positron emission tomography
PD-L1	Programmed death ligand 1
p.i.	Post-injection
p.o.	Per os (meaning: taken by mouth)
PR	Progesterone receptor
Radio-iTLC	Radio-instant thin layer chromatography
RECIST	Response Criteria in Solid Tumors
RTK	Receptor tyrosine kinase
SERD	Selective estrogen receptor degrader
SERM	Selective estrogen receptor modulator
s.c.	Subcutaneous
SUV	Standard uptake value
TAA	Tumor associate antigen
TBST	Tris-buffered saline tween20
TIL	Tumor infiltrating lymphocyte
Treg	Regulatory T cell
VOI	Volume of interest
TKI	Tyrosine kinase inhibitor
%ID/g	Percent injected dose per gram

CHAPTER 1: INTRODUCTION

Conventional imaging modalities, such as radiography, ultrasound, computed tomography (CT), and magnetic resonance imaging (MRI) have been used for years to identify and characterize many diseases, including cancer, based on anatomic differences in tissue density, their shape, size, and water content(1). Recently, with the advent of functional imaging modalities, clinicians have been able to characterize diseases based on changes at the molecular level(1). Positron emission tomography (PET) imaging is used clinically and for translational research to study these molecular mechanisms. In the clinic, PET has shown utility in diagnosing and staging cancer, assisting in radiotherapy treatment planning, and monitoring chemotherapy(2). Preclinically, PET has been used in small animal research where new molecular probes are employed to target, detect, and visualize processes associated with cancer.

1.1 Overview of Positron Emission Tomography (PET)

PET is a non-invasive imaging modality where a small mass of radioactive tracer is injected into the patient, and through a series of reconstruction algorithms, an image portraying specific tissue uptake of the tracer is displayed. First, a probe (a small molecule, antibody, or peptide) with an affinity for the molecular target is labeled with a positron emitting radioisotope. A table of common isotopes and their half-lives can be found in Table 1. Matching the physical and biological half-lives of the PET nuclide and the target probe, respectively, ensures that the probe accumulates in the tumor before the radioactivity decays and allows clearance from normal tissues. In this regard, enhanced signal-to-noise ratio – one of the primary considerations in diagnostic imaging

– is achieved.

Isotope	Half-Life
O-15	122.24 s
N-13	9.97 m
C-11	20.4 m
F-18	110 m
Cu-64	12.7 h
Y-86	14.72 h
Br-76	16.2 h
Ga-68	68.1 h
Zr-89	78.4 h
I-124	4.18 d

Table 1. Possible PET radioisotopes and their half-lives.

A patient is injected with the probe, and as the radionuclide decays it emits positrons that annihilate with electrons within the tissues producing two coincident photons that emit energy at 511 keV. Ring detectors made of scintillation crystals positioned around the subject pick up on the coincident photons and process their spatial location, energy, and arrival time, and through a series of reconstruction algorithms a final image is produced (Fig. 1)(3).

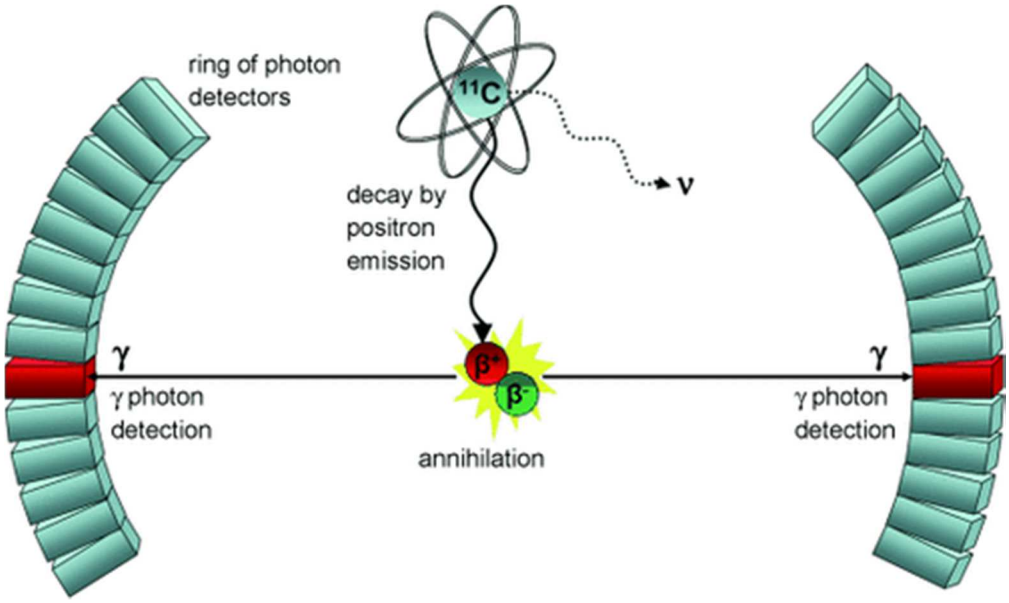

Figure 1. Principles of PET imaging. Upon decay, the radionuclide emits positrons that meet with electrons within the tissue that produces two gamma photons of 511 keV. This research was originally published in Angewandte Chemie Internaltional Edition. Philip W. Miller, Nicholas J. Long, Ramon Vilar, et al. Synthesis of 11C, 18F, 15O, and 13N Radiolabels for Positron Emission Tomography. 2008;47(47):36.

Several tracers are currently approved by the Food and Drug Administration (FDA) which target metabolism, proliferation, hypoxia, but the most common PET probe for cancer is ^{18}F-fludeoxyglucose (FDG). FDG is chemically known as 2-deoxy-2-(^{18}F)fluoro-D-glucose, which is an analog of glucose consumed by tissues in the body. Uptake of the tracer marks tissues scavenging for glucose, which is abundant in proliferating tumors. Since 2000, there has been a nine-fold increase in the number of FDG-PET scans performed in the U.S., possibly driven by the enhanced sensitivity and specificity of PET as compared to other imaging modalities(4). In 2011 it was estimated that 1.8 million FDG-PET scans were performed, with 94% of the scans for cancer patients(1). It is increasingly being used to assess therapeutic response and tumor biology, although a disadvantage is its background uptake in normal, high glucose-consuming tissues (brain, muscle), in situations where tumors lack metabolic activity, and lack of avidity for the

tracer. Additionally, FDG-PET is a non-specific tracer, and is unable to stratify patients who would benefit from a particular molecular treatment. Therefore, efforts have been made to develop tracers that target intracellular and cell-surface receptors that are uniquely expressed or overexpressed in cancer. In order to target these PET nuclides to receptors present on tumors, carriers in the form of small molecules, peptides, or antibodies must be linked to the nuclide and are employed to enhance the signal-to-noise ratio of the target to background uptake.

The research described throughout this dissertation solely focuses on the use of antibody-based tracers. The following section was adapted in full with permission from the Journal of Labelled Compounds and Radiopharmaceuticals "^{89}Zr-ImmunoPET companion diagnostics and their impact in clinical drug development" by Brooke N. McKnight and Nerissa T. Viola-Villegas, volume 61, issue 9(5).

1.1.1 ImmunoPET Tracer Development

Therapeutic monoclonal antibodies (mAbs) gained clinical utility in 1985 with the first FDA approval of the biologic, muromonab-CD3 (Orthoclone OKT3), specific for cluster of differentiation 3 (CD3), a co-receptor present on all T-cells(5). Since then, applications in cancer have been exploited with the approval of rituximab (Rituxin®) in 1997(6) followed by trastuzumab (Herceptin®) in 1998(7). By 2016, there were 24 monoclonal antibodies (mAbs) and antibody drug conjugates (ADC) approved by the FDA for cancer treatment. These mAbs are directed to a specific target ranging from tumor and cell-surface associated antigens to biomarker signatures within the tumor microenvironment. Despite their specificity and moderate safety profile, clinical efficacy of these mAbs remains limited due to perpetuating factors, including but not limited to i)

unpredictable tumor antigen density, ii) internalizing status of the mAb:antigen complex, iii) the success at which the antibody reaches the target, iv) vascular penetration, and, v) tissue distribution, which may impact adverse events (8–12). All of these factors underscore the need for precision medicine, borne out of the intent of tailoring the disease treatment and prevention by providing the right drug to the right patient at the appropriate time and dose.

A logical approach to precision medicine explores non-invasive imaging tools that can be repeatedly utilized to profile tumors at the molecular level, and to augment flaws present in biopsies from tumor heterogeneity or poor sample quality. With this perspective, antibody or immune-based positron emission tomography (immunoPET) was developed to provide a direct readout of antigen density present within each lesion; moreover, the pharmacokinetic and dosimetric properties of the mAb, in the case of radioimmunotherapy, can be considered cognate when compared to the imaging tool(13). Taken together, immunoPET has a high potential to influence and direct informed decisions in drug design and development.

The development of immunoPET tracers relies on the following principles: i) the biological and chemical properties of the mAb, ii) the radionuclide chosen iii) the chelate selected, and iv) the stability of the linker between mAb and chelate. MAbs for patient use are either humanized or made fully human to prevent human anti-mouse antibody response (HAMA)(14). The size of full-length biologics (~150 kDa) prolongs their half-life in the blood, which affects the time it takes to deliver to the tumor target and clearance from healthy tissues. Thus, pairing mAbs with long-lived radionuclides ^{64}Cu ($t_{1/2}$ ~ 12.7 h), ^{86}Y ($t_{1/2}$ ~ 14.7 h), ^{89}Zr ($t_{1/2}$ ~ 78.4 h), and ^{124}I ($t_{1/2}$ ~ 100.3 h) is the most common

strategy(15).

One limitation to using full mAbs specifically for imaging purposes is the long wait times between tracer administration and imaging acquisition, as well as higher radiation exposure of non-target organs. Tracer pharmacokinetics can be improved by decreasing its size, effectively reducing circulation time, and minimizing dose exposure to the patient(16). With this perspective, smaller fragment constructs are engineered offering shorter blood residencies and faster tumor target delivery. These fragments mostly retain the variable region where the antigen-binding site is primarily located. Suggested PET radionuclide tags to complement mAb fragments are provided in Table 2. Moderately-sized fragments (i.e. F(ab)'2 (~100-110 kDa), minibody (~75 kDa), and diabody (~50 kDa)) may be appropriately labeled with ^{18}F ($t_{1/2}$ ~ 109 min), ^{64}Cu ($t_{1/2}$ ~ 12.7 h) and ^{86}Y ($t_{1/2}$ ~ 14.7 h). Smaller-sized fragments like affibodies (~ 6 kDa), nanobodies or single domain antibodies (~12-15 kDa) can be radiolabeled with shorter-lived isotopes like ^{18}F and ^{68}Ga ($t_{1/2}$ ~ 68 min), which consequently decreases the radiation exposure of the patient(17). The caveat herein lies in the overall rate of clearance and nuclide site delivery of the mAb fragments.

Antibody Fragments	Recommended PET Nuclide	References
Affibody (~7 kDa), Nanobody (~12-15 kDa)	^{68}Ga ^{18}F ^{64}Cu	(18–23)
Diabody (~55 kDa)	^{18}F ^{64}Cu ^{89}Zr	(24–26)
Minibody (~80 kDa)	^{64}Cu ^{89}Zr	(27,28)
Fab'$_2$ (~100-110 kDa)	^{64}Cu ^{89}Zr ^{124}I	(29)

Table 2. Different antibody fragments and recommended PET radionuclide for companion diagnostic development

1.1.2 Zirconium-89 immunoPET tracers

Standardized production and commercial availability has made the development of Zr-89 radiolabeled mAbs relatively straightforward(17). As a radiometal, Zr-89 requires complexation to prevent random, non-specific binding to non-targeted tissue (usually the bone), which consequently lowers contrast. To date, only desferrioxamine (DFO), a known iron-sequestering siderophore with three hydroxamate groups is currently utilized as a chelate despite reports of metal:complex *in vivo* instability(30,31). DFO bioconjugation techniques were established either through non-specific attachment to terminal lysines(32,33) and cysteines(34) or through a more discriminate glycan selective labeling(35). A depiction of a mAb radiolabeled with ^{89}Zr through a DFO linker can be found in Figure 2.

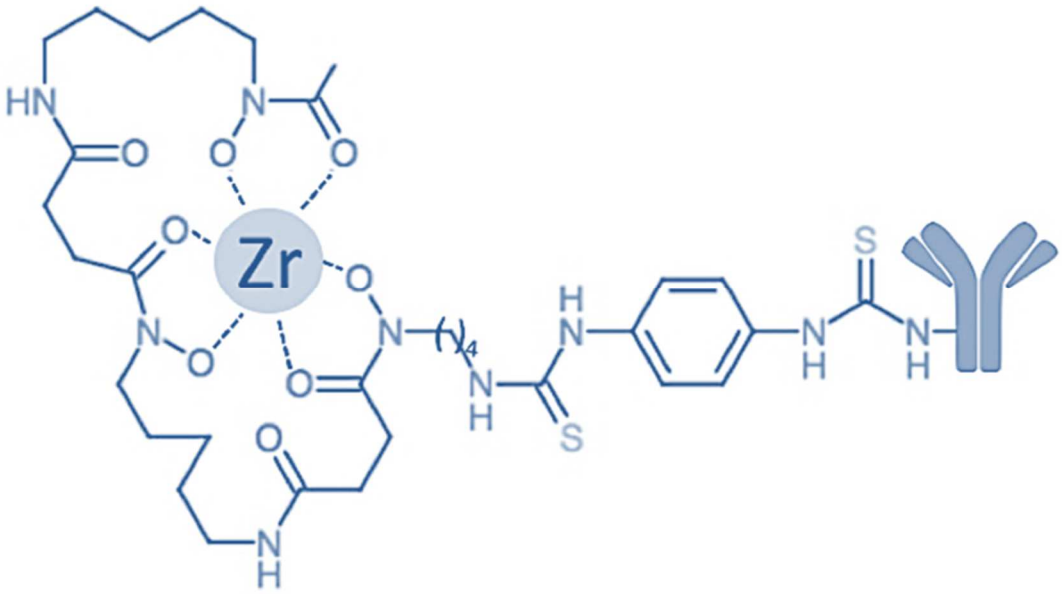

Figure 2. ^{89}Zr labeled monoclonal antibody. mAbs are conjugated to DFO at the terminal amine groups before undergoing radiolabeling with ^{89}Zr. The figure only shows one DFO conjugated to the antibody for clarity, but in reality there are often more DFO molecules bound depending on the method of conjugation.

Consequently, preclinical research flourished with many imaging probes developed to target different oncogenic molecular signatures. A significant number of these tracers were developed to target surface-bound biomarkers, such as i) members of the epidermal growth factor receptor family (e.g. EGFR(36), HER2(37) and HER3(38)), ii) prostate-specific membrane antigen (PSMA)(39), iii) prostate stem cell antigen (PSCA)(28), iv) CD20(40), v) CD44(41), vi) programmed death receptor (PD1)(42) and vii) programmed death ligand 1 (PD-L1)(43), to name a few. Imaging probes targeting secreted signaling proteins (e.g. VEGF, granzyme B, interferon-γ)(44–46), antigen/receptors bound to T cells (e.g. CD3(47), CD8(48)) and shed antigens (e.g. CA19.9(49), carcinoembryonic antigen or CEA(50)) were also investigated. With substantial preclinical data, a number of these tracers have progressed to clinical trials. The first study of a ^{89}Zr-mAb probe (^{89}Zr-cmAb U36) targeting CD44v6 in patients with head and neck cancer was reported in 2006(51). The number of ^{89}Zr-based immunoPET probes in the clinic tripled in 2013(30). As of this writing, to the best of our knowledge and after extensive search at clinicaltrials.gov, there are ~46 ^{89}Zr-mAbs that are currently undergoing or have completed patient trials, none of which are FDA approved. An overview of ^{89}Zr-based immunoPET probes can be found in Table 3.

ANTIBODY	TARGET	INDICATIONS	CLINICAL TRIALS IDENTIFIER	PHASE AND STATUS
Trastuzumab	HER2	Metastatic HER2+ Breast cancer	NCT01420146	Phase 1; Completed
		Metastatic HER2+ Breast cancer; to select patients for T-DM1 treatment	NCT01565200	Phase 2; Active, not recruiting
		Unsuspected HER2 Breast Metastases	NCT02286843	Recruiting
		Trastuzumab-resistant Breast Cancer; measure HER2 post-treatment with HSP90 inhibitor AUY922	NCT01081600	Phase ½; Completed
		Esophagogastric cancer	NCI-2016-00986, NCT02023996	Phase 1; Recruiting
		HER2+ primary malignancy	NCT03109977	Phase 1; Completed
		Breast Cancer	NCT02065609	Phase 1; Completed
Bevacizumab	VEGF	Inflammatory Breast Cancer	NCT01894451	Phase 1; not recruiting
		Pulmonary arterial hypertension	NCT03166306	Phase 1/2; recruiting
		Multiple Myeloma	NCT01859234	Unknown
		Breast Cancer	NCT01081613	Completed
		Neuroendocrine Tumors	NCT01338090	Completed
		Renal Cell Carcinoma	NCT01028638	Completed
		Breast Cancer	NCT00991978	Phase 1; Completed
huJ591	PSMA	Prostate cancer	NCT02693860	Phase 1; active not recruiting
		Metastatic prostate cancer	NCT01543659	Phase 1/2; active not recruiting
		Glioblastoma	NCT02410577	Completed
Girentuximab	Carbonic Anydrase IX	Renal cell carcinoma	NCT02883153	Phase 2/3, Completed
		Clear cell renal carcinoma	NCT03556046	Phase 1; Recruiting
Cetuximab	EGFR	Stage IV cancer	NCT00691548	Phase 1; Completed
		Colorectal cancer	NCT01691391	Completed
		Metastatic Colorectal Cancer	NCT02117466	Phase 1/2; Recruiting
Ipilimumab	CTLA-4	Melanoma	NCT03313323	Phase 2; Recruiting

Fresolimumab (GC1008)	TGF-β	Primary brain tumor	NCT01472731	Phase 2; Completed
Pertuzumab	HER2	HER2 positive malignancy	NCT03109977	Phase 1; Completed
IAb2M	PSMA	Metastatic prostate cancer	NCT01923727	Phase 1/2, Completed
		Prostate cancer, pre-prostatectomy	NCT02349022	Phase 2, Completed
		Prostate Cancer	NCT03675451	Phase 2; Recruiting
IAb22M2C	CD8	Non-Small Cell Lung Cancer, Small Cell Lung Cancer, Squamous Cell Carcinoma Head and Neck, Melanoma, Merkel Cell Tumor, Renal, Bladder, Hepatocellular, Triple Negative Breast, or Gastroesophageal Cancer, Hodgkin's Lymphoma	NCT03107663	Phase 1; Completed
Rituximab	CD20	Lung disease, interstitial pneumonitis	NCT02251964	Phase 2/3; Completed
GSK3128349 (Albumin domain binding antibody)	Albumin	Drug related side effects and adverse reactions	NCT02829307	Phase 1; completed
MPDL3280	PD-L1	Breast cancer, bladder cancer and non-small cell lung cancer	NCT02453984	Phase 1; recruiting
Pembrolizumab	PD-1	Non-small cell lung cancer	NCT03065764	Phase 2; active not recruiting
		Melanoma	NCT02760225	Recruiting
GSK2849330	HER3	Solid tumors	NCT02345174	Phase 1; Completed
AMG211	HER3	Advanced gastrointestinal cancer	NCT02760199	Phase 1; Completed
RO5479599	HER3	Metastatic and/or Locally Advanced Malignant HER3-Positive Solid Tumors of Epithelial Cell Origin	NCT01482377	Phase 1; Completed
MMOT0530A	Mesothelin	Unresectable pancreatic cancer, platinum-resistant ovarian cancer	NCT01832116	Phase 1; Completed
MSTP2109A	STEAP1	Prostate cancer	NCT01774071	Phase 1/2; On-going but not recruiting
HuMab-5B1 (MVT-2163)	CA19.9	Pancreatic Cancer; tumors that express CA19.9	NCT02687230	Phase 1; Recruiting

KN035	PD-L1	Advanced solid tumors	NCT03638804	Not yet recruiting
ABT806	EGFR VIII	Glioma	NCT03058198	Recruiting
Certolizumab	TNF-α	Rheumatoid Arthritis	NCT03546335	Phase 1; Recruiting
Avelumab	PD-L1	NSCLC	NCT03514719	Phase 1; Not yet recruiting
RO5429083	CD44	Neoplasms	NCT01358903	Phase 1; Completed
DS-8895a	EphA2	Solid Tumors	NCT02252211	Phase 1

Table 3. List of ^{89}Zr-immunoPET tracers that advanced to clinical trials

1.1.3 Clinical Impact of Companion Diagnostics

Understanding the molecular profile of a malignancy is necessary to determine treatment indications. A standard clinical strategy obtains tumor specimens through surgical or core needle biopsies in solid tumors for histopathological analyses. One can also analyze blood, urine, sputum, or cerebrospinal fluid, for circulating biomarkers(52). Biopsy-driven molecular profiling is often fraught with problems and limitations since access to the tumor sites may be difficult, often requiring complicated invasive procedures(53). Additionally, biopsies only sample a small portion of the global tumor, and analysis could miss important tumor characterizations. Tumor heterogeneity renders biopsies inconsistent, which can inadequately portray the presence and level of expression of the molecular signature; thus, requiring more tests to accurately characterize the tumor. Consequently, proper histopathological analysis of the receptor/antigen density may not be reflected, potentially eliminating a patient from benefiting from molecular-based treatments. Repeat biopsies are performed on patients to pathologically confirm malignancy to direct treatment decisions, but secondary biopsy results may not match the original pathology report(54). Moreover, multiple sequential biopsies are deemed impractical, unethical, and unsafe(55). In this regard, using a PET

probe to profile tumors could reduce cases of biopsy mismatch by looking at the entire tumor in an unperturbed, non-invasive setting.

ImmunoPET may potentially provide an image-guided molecular diagnostic tool where pathological results may not be able to confirm and identify true positive disease. It detects the target antigen and quantitatively measures its expression. The imaging agent ^{18}F-FDG has long been the standard PET tracer for detecting lesions, but it is limited to visualizing tumor metabolism. Moreover, weak tumor avidity or probe accumulation, non-specific tissue binding, and low metabolic lesions can pose problems, hindering detection(56). Pandit-Taskar *et al*. conducted identification of metastatic bony lesions using the anti-PSMA PET tracer, ^{89}Zr-J591 and analyzed against lesions detected by ^{18}F-FDG, bone scans (^{99m}Tc-medronic acid (MDP)) and computed tomography (CT). ^{89}Zr-J591 was able to detect four occult lesions, which were undetected by FDG and other imaging assays(57). Out of 21 lesions, 19 were PSMA-positive as identified by ^{89}Zr-J591. Of these select osseous lesions, two were biopsy-proven negative, but further assessment using magnetic resonance imaging confirmed one of the lesions as metastatic with a repeat biopsy confirming the malignancy.

Dose escalation studies using ^{89}Zr-IAB2M (anti-PSMA minibody) in patients were conducted with 10 mg, 20 mg, or 50 mg of IAB2M (Fig. 3)(58). Differences in biodistribution were minor across all doses. Decreased blood pool activity coupled with an increased liver and GI tract accumulation was observed over time. The highest lesion uptake was seen in the 10-mg cohort with optimal biodistribution for imaging, as well as improved delineation of bony metastatic sites. Of note, increased doses of the cold IAB2M

resulted in slower serum clearance due to mass effects, although a non-significant decrease in liver uptake was noted in the 50 mg cohort.

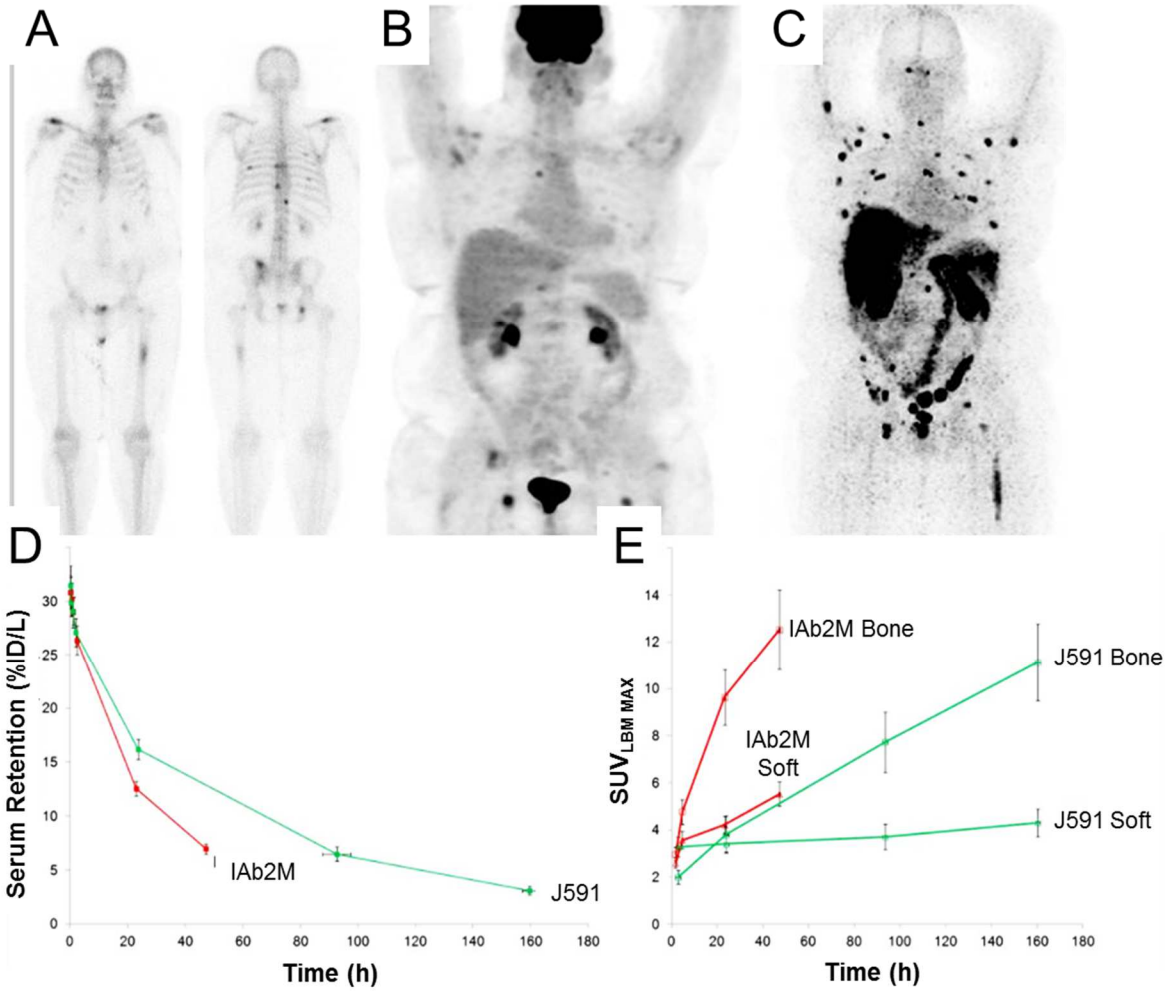

Figure 3. Confirmation of malignancy Differences in lesion detection in a metastatic prostate cancer patient using ^{99m}Tc - MDP (bone scan) showed lesions in the ribs and vertebrae (A), ^{18}F - FDG PET scan displayed uptake in the femur and in the vertebrae (B), and ^{89}Zr−IAB2M imaging identified more true - positive lesions than ^{99m}Tc - MDP and ^{18}F - FDG (C). A comparison of serum clearance (D) and lesion uptake (E) between ^{89}Zr - IAB2M (minibody) and ^{89}Z-J591 (full length mAb cognate) over time. This research was originally published at JNM Pandit-Taskar N,Donoghue JA, Ruan S, et al. First-in-Human Imaging with ^{89}Zr-Df- IAB2M Anti-PSMA Minibody in Patients with Metastatic Prostate Cancer: Pharmacokinetics, Biodistribution, Dosimetry, and Lesion Uptake. J Nucl Med.2016;57(12):1858-1864. © by the Society of Nuclear Medicine and Molecular Imaging, Inc.

Perhaps the most impact immunoPET has contributed can be gleaned from the pioneering study investigating the biodistribution of ^{89}Zr-trastuzumab in patients with metastatic BC (Fig. 4). Djikers *et al.* observed rapid hepatic excretion and low blood pool levels of the tracer in breast cancer (BC) patients who are naïve to trastuzumab with extensive HER2+ tumor mass in the liver; consequently, a false-negative readouts in distal metastatic sites was exhibited(59). The hepatic “sink” and poor uptake in metastatic lesions were attributed to slow extravasation of the drug through the vascular compartment compared to fast pharmacokinetic clearance of the mAb at low dose levels. In this study, a 10 mg and 50 mg loaded dose displayed terminal half-lives of 1.5 and 4.3 days respectively; in contrast, tumor penetration and accumulation of ^{89}Zr-trastuzumab occurred between 4-5 days. To gain perspective, administered therapeutic doses (4 mg/kg loading plus 2 mg/kg maintenance dose) reached an average terminal half-life of ~28.5 days when at steady state. Another important finding of this pivotal clinical trial was the importance of drug receptor occupancy. The fast pharmacokinetics of low trastuzumab doses led the authors to estimate drug/receptor occupancy by considering the amount of HER2 per tumor cell and the liver mass of the patient. The mass (1.2 kg) was obtained through image analysis of normalized PET/CT scans. The authors rationalized that a 50 mg dose of trastuzumab, equivalent to 2.0×10^{17} trastuzumab molecules (via conversion through Avogadro’s number) cannot fully saturate over a kg (1.2 kg) of tumor tissue based on the following approximations. A gram of tumor tissue is nearly comprised of ~1×10^9 cells. Each single cell, on average, possesses 2 million HER2 receptor sites. Thus, in the patient’s case, there are ~2.4×10^{18} HER2 receptor molecules present in the hepatic metastases, 10-fold higher than the 50 mg dose (1.2×10^3

g tumor tissue × 1×10^9 cells/g × 2×10^6 HER2 receptors/cell)(60,61). The majority of the dose (50 mg) accumulated in the extensive liver metastasis. This created the impetus to vary doses in patients who are naïve to trastuzumab versus those receiving this treatment with the former requiring more mAb administered (50 mg vs. 10 mg, respectively).

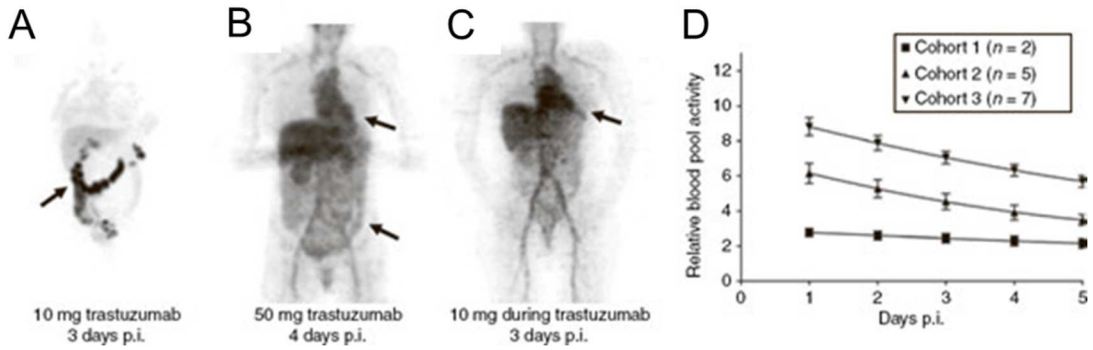

Figure 4. Receptor Occupancy. ^{89}Zr-trastuzumab PET biodistribution in patients given 10 mg of ^{89}Zr-trastuzumab (untreated) (A), 50-mg ^{89}Zr-trastuzumab during concurrent trastuzumab treatment (B), and 10-mg ^{89}Zr-trastuzumab during concurrent trastuzumab treatment (C) show different clearance rates in the blood pool (D), and should be considered when dosing patients in the clinic. This research was originally published at Clin Pharmacol Ther. Dijkers EC, Oude Munnink TH, Kosterink JG, et al. Biodistribution of ^{89}Zr-trastuzumab and PET imaging of HER2-positive lesions in patients with metastatic breast cancer. Clin Pharmacol Ther. 2010;87(5):586-592.

Taken together, these pivotal biodistribution studies underscore the substantial dependence of mAb-based therapies (e.g. ado-trastuzumab emtansine (T-DM1)(62), pertuzumab(63), rituximab(64)) on pharmacokinetics for personalized dosing strategies. Current clinical protocol relies on body weight to determine drug doses administered. ImmunoPET CDx can potentially transform this practice by facilitating the assessment of effective patient-tailored doses based on the extent of tumor burden and mAb pharmacokinetics.

A clinical study assessing ^{89}Zr-rituximab as an imaging biomarker of CD20 in patients with relapsed or refractory diffuse large B cell lymphoma was correlated against pathologic findings (Fig. 5)(65). Biopsy-proven lesions (5/6 patients) showed

concordance with the tumor uptake of ^{89}Zr-rituximab. A strong uniform staining of CD20 was correlated with a high SUV_{peak} of 12.8 while a moderate, heterogeneous CD20 expression corresponded to a tumor uptake of SUV_{peak} ~ 3.2-5.4. In certain cases, the pathology may lead to discordance with the immunoPET data. One patient demonstrated a biopsy-mismatch with CD20 PET displaying a positive tumor uptake (SUV_{peak} ~ 3.8) but negative pathology. The lesion was conclusively assessed as a true positive.

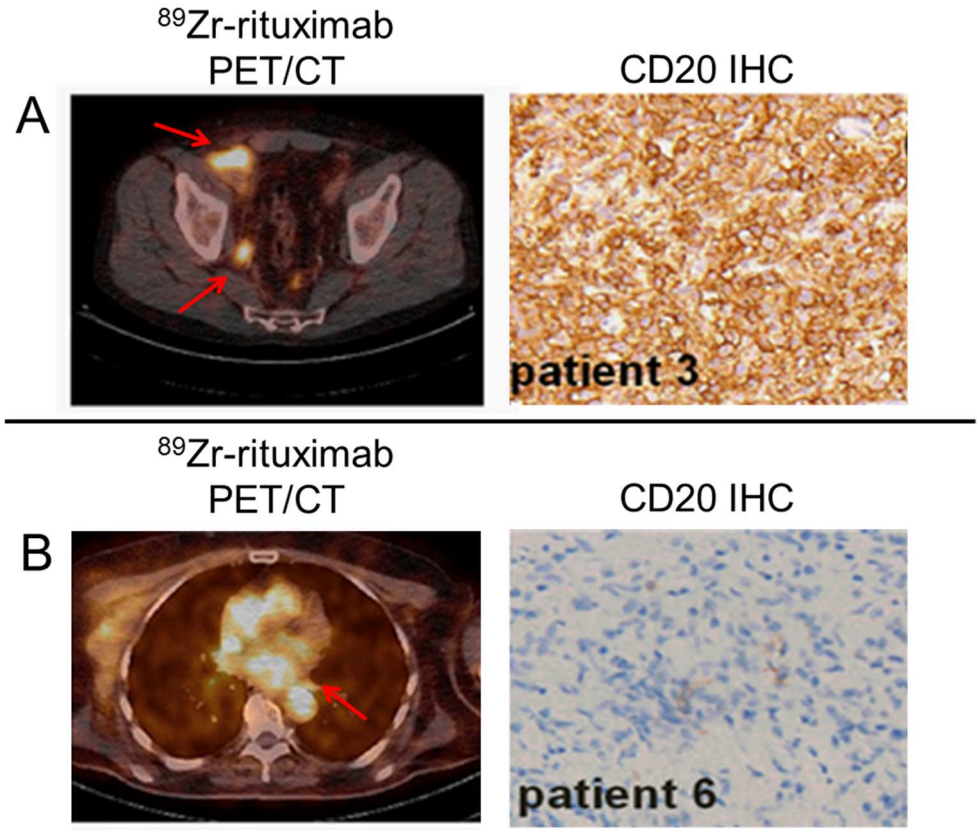

Figure 5. ImmunoPET findings in relation to pathology. Concordance (A) and (B) discordance of ^{89}Zr-rituximab-PET/CT (left) with CD20 pathology via IHC (right). Arrows point to lesions on the PET scan. This research was originally published at PLOS One Jauw YW, Zijlstra JM, de Jong D, et al. Performance of ^{89}Zr-Labeled-Rituximab-PET as an Imaging Biomarker to Assess CD20 Targeting: A Pilot Study in Patients with Relapsed/Refractory Diffuse Large B Cell Lymphoma. PLoS One. 2017;12(1):e0169828 and modified for use under the creative commons license https://creativecommons.org/licenses/by/4.0/).

Another concrete example was presented by Ulaner *et al*. investigating HER2-PET in patients with HER2-negative primary BC (Fig. 6) (54). Of the 20 patients, 15% (3/20) were identified by ^{89}Zr-trastuzumab as having unsuspected HER2-positive metastases with proven pathologies. In this study, a patient who was diagnosed with ER+/HER2- invasive ductal BC presented two years later with several bone lesions and was observed HER2-PET avid. Biopsy of the right ilium (SUV~ 5.9) confirmed metastases but with an ambiguous IHC score of 2+. Confirmation of the foci as true-positive was made using MSK-IMPACT assay. Of note, the authors emphasized that the intensity of the PET tracer on foci can indiscriminately assess true- from false-positive lesions. The study reported ~30% (6/20) of the patient population was conservatively categorized as false-negative due to negative pathology even with foci avidity for the probe. The relatively high incidence of false-positive lesions was attributed to non-specific uptake of free Zr-89, particularly in osseous sites, which marginalizes the use of this nuclide for detecting bone metastases.

Collectively, tumor heterogeneity can impact go/no-go treatment decisions with standard biopsy results rendering ambiguity to some extent. In these cases, immunoPET can reinforce and potentially resolve equivocal tumor pathology. However, confirmation of true-positive or -negative lesions as visualized by immunoPET needs to be meticulously validated.

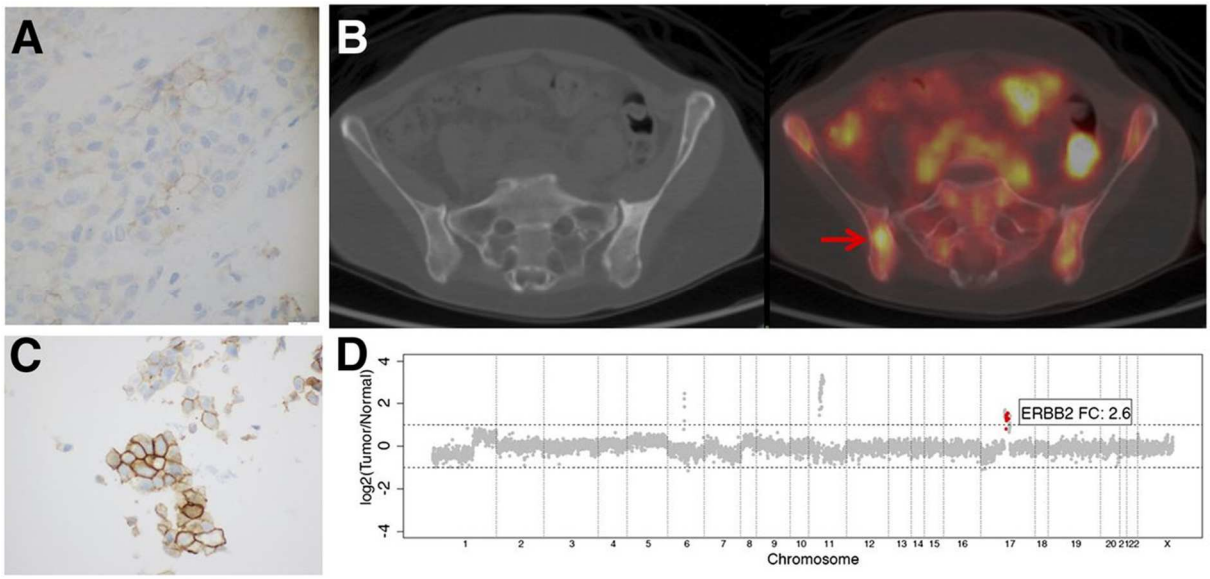

Figure 6. PET readout gave true-positive results despite discordance with biopsy findings. PET readout gave true-positive results despite discordance with biopsy findings. An ER+/HER2- invasive ductal BC patient with confirmed negative pathology in the primary lesion (A) but presented with HER2-PET positive disease 2 years after primary diagnosis (B). Biopsy of the same site resulted in an ambiguous IHC score (2+) (C) Red arrow points to the lesion. MSK-IMPACT assay confirmed the foci as true-positive (D). This research was originally published in JNM. Ulaner GA, Hyman DM, Ross DS, et al. Detection of HER2-Positive Metastases in Patients with HER2-Negative Primary Breast Cancer Using ^{89}Zr-Trastuzumab PET/CT. Journal of Nuclear Medicine : official publication, Society of Nuclear Medicine. 2016;57(10):1523-1528. ©by the Society of Nuclear Medicine and Molecular Imaging, Inc.

A first-in-human study investigated by Lamberts *et al.* evaluated ^{89}Zr-MMOT0530A in pancreatic tumors and metastases expressing mesothelin (MSLN)(66). Pre-treatment scans showed a mean SUVmax of 11.5 ± 5.6 lesions in the pancreas. Patients received the antibody-drug conjugate DMOT4039A (MMOT0530A bound to MMAE) followed by ^{89}Zr-MMOT0530A PET, 4 days post injection of the tracer. After treatment, 9 out of 11 patients presented with stable disease, and two patients had progressive disease. Those with progressive disease showed an uptake in liver metastasis with the PET tracer. This suggests that ^{89}Zr-MMOT0530A-PET can be used to visualize pancreatic cancer lesions,

as well as guide individualized antibody-based treatment with the ADC DMOT4039A.

The landmark ZEPHIR study evaluated the predictive value of HER2 PET/CT in combination with FDG PET prior to T-DM1 treatment in patients with metastatic breast cancer (Fig. 7)(67). From the 55 patients enrolled, 16 (29%) were negative for HER2-PET while 39 patients were categorically classified as positive for HER2-PET/CT, depending on lesion heterogeneity. From the HER2-positive pool, 28 patients displayed an objective response (OR) after 3 cycles of T-DM1. In combination with post-treatment (after 1 cycle of T-DM1), a 100% positive predictive value (PPV) was achieved for HER2-PET imaging (72% PPV) in combination with early treatment FDG-PET imaging based on RECIST 1.1. Moreover, a time-to-treatment failure of ~ 11.2 months in the HER2-positive group and ~3.5 months for the HER2-negative group were identified. A negative predictive value of 88% in patients with low HER2-PET was deemed clinically significant. To date, this is the first trial that used a three-prong strategy that employed imaging biomarkers for go/no go treatment decisions in the clinic. In conclusion, these clinical trials highlighted the potential of immunoPET to measure functional effects of targeted treatment, making this imaging technique a conceivable predictive and prognostic biomarker.

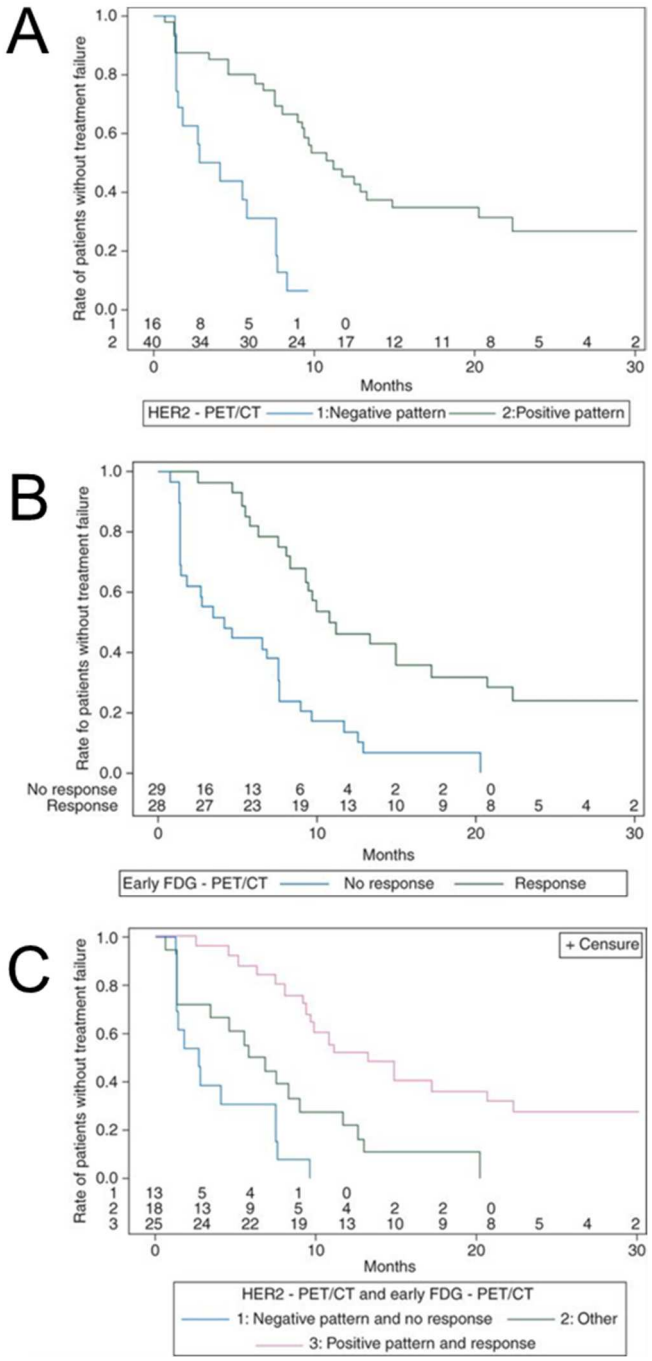

Figure 7. Predictive markers of treatment. Time-to-treatment failures were evaluated based on HER2-PET/CT (A), early FDGPET/CT (B) and combination of both HER2- and FDG-PET/CT (C). This research was originally published in Ann Oncol. Gebhart G, Lamberts LE, Wimana Z, et al. Molecular imaging as a tool to investigate heterogeneity of advanced HER2-positive breast cancer and to predict patient outcome under trastuzumab emtansine (T-DM1): the ZEPHIR trial. Ann Oncol. 2016;27(4):619-624.

1.1.4 Practical Considerations

While immunoPET CDx may seem straightforward, several aspects of using this imaging technique need to be deliberated. The amount of dose administered and the interval between tracer administration and imaging acquisition warrant investigation to obtain an optimized contrast between lesions and background. In the case of ^{89}Zr-trastuzumab, the optimal imaging time for a ~37 MBq (50 mg) intravenous injection was observed between 4-5 days after injection(59). At this period, low blood pool activity and high tumor avidity was established. Imaging at longer periods >6 days can compromise the spatial resolution and image quality(59). At higher activities (~185 MBq/50 mg) administered, ^{89}Zr-trastuzumab still generated high quality spatial resolution in images acquired between 5-6 days post-injection(68). The scan periods of 4-6 days depending on the dose are typical for other full-length mAb tracers in clinical trials(54,65,68,69). For smaller biologics-based tracers, ^{89}Zr-IAB2M, for example, demonstrated shorter interval wait times with the best lesion to background ratio identified at 48 h p.i.(58) Safety profiles of ^{89}Zr-labeled mAbs require careful assessment to limit radiation-related toxicities. Whole body effective doses reported in a number of early phase studies ranged from 0.41 mSv/MBq for ^{89}Zr-IAB2M(58), 0.87 ± 0.14 mSv/MBq for ^{89}Zr-ibritumomab tiuxetan(70), 0.47 mSv/MBq for ^{89}Zr-trastuzumab(71) and 0.264 mSv/MBq for ^{89}Zr-panitumumab(18) whereas FDG-PET(72) had a reported mean effective dose of 0.0199 ± 0.0032 mSv/MBq.

Engagement of immunoPET CDx as predictive imaging biomarkers in the clinic should continue to be explored in the clinical translational efforts toward precision medicine. It has already shown success in accurately profiling lesions at the molecular level when pathology is incorrect, discovering the density of targets available, and

determining the biodistribution of therapy before treating the patient. Sequential imaging in test-retest studies can provide a viable tool to appropriately dose patients, but should be used with caution during treatment regimens. In a nutshell, immunoPET is still at its early stages of clinical development and will most likely require further standardization (i.e. streamlined SUV readout analysis, chemistry optimization) and validation through other molecular profiling tools. Once harnessed, its benefits can provide a powerful impact in patient management.

1.2 Overview of Breast Cancer and Selected Subtypes

Breast cancer (BC) is the most commonly diagnosed cancer in women, as well as the leading cause of cancer-related deaths(73). BC is typically referred to as a single disease, but it is clinically and molecularly heterogeneous, with many ways to categorize tumors. Still, clinical decisions rely on the assessment of three markers: the expression of the estrogen receptor (ER), progesterone receptor (PR) and the overexpression of the human epidermal growth factor receptor 2 (HER2)(73). The accurate assessment of these biomarkers assists in tumor classification and aids in appropriate treatment decisions. This section will mainly discuss HER2 and EGFR, molecular therapeutic strategies, and current diagnostic techniques.

1.2.1 HER family

The HER family is a group of transmembrane receptor tyrosine kinases (RTK) with four members: EGFR, HER2, HER3, and HER4 (Fig. 8). They are deregulated in many cancer subtypes, but are most commonly recognized in BC, lung cancers, and glioblastoma. In breast cancer, the EGFR gene is amplified in up to 5% of cancer cases, and the HER2 gene is amplified by up to 30%. They all share a common structure

comprising of an extracellular domain, a single transmembrane domain, and an intracellular domain with a conserved carboxyl terminal tail and catalytic kinase domain(74). A key function of their activity is within the dimerization portion of the extracellular domain(74). When a ligand binds the dimerization domain, it changes the conformation of the receptor allowing for dimerization and inter-receptor interactions, although HER2 is the exception, since it has no known ligand(74). Table 4 describes the HER receptor binding combinations.

After dimerization, the receptors will phosphorylate their tails and activate downstream signaling cascades, such as the phosphatidylinositol-3-kinase (PI3K)/Akt pathway, the Janus kinase, and phospholipase C pathway; all which affect and promote cell proliferation, survival, and adhesion(75). Additionally, the Src pathway responds to upstream HER family signaling(75). The signaling potency of receptors is governed by the particular dimer pair. For example, heterodimers are more active than homodimers, with the heterodimer HER2-HER3 possessing the most signaling activity(76).

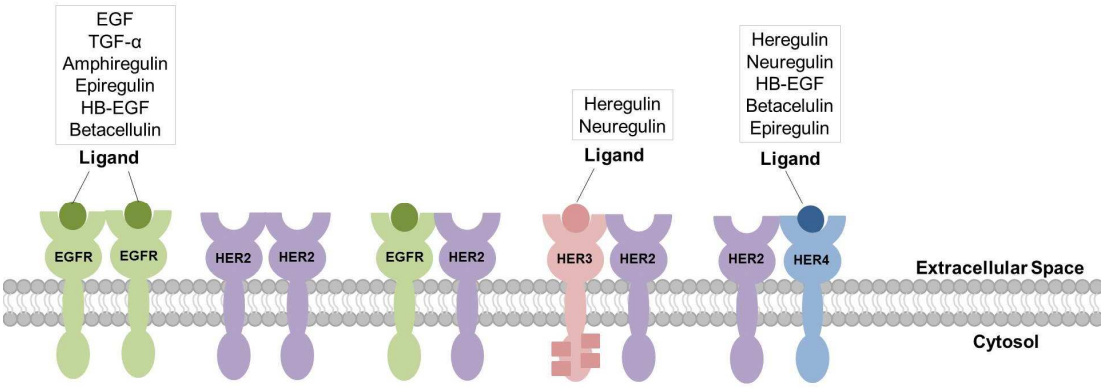

Figure 8. HER family members and ligands. EGFR, HER2, HER3, and HER4 are all capable of dimerizing upon ligand binding and activation, except for HER2 which does not have a known ligand.

Dimers	Ligands
EGFR-EGFR	EGF, EPG, TGFα, AR, BTC, HB-EGF, EPR
EGFR-HER2	EGF, EPG, TGFα, AR, BTC, HB-EGF, EPR
EGFR-HER3	EGF, EPG, TGFα, AR, BTC, HB-EGF, EPR, Nrg-1, Nrg-2
EGFR-HER4	EGF, EPG, TGFα, AR, BTC, HB-EGF, EPR, Nrg-1, Nrg-2, Nrg-3, Nrg-4
HER2-HER2	None
HER2-HER3	Nrg-1, Nrg-2
HER3-HER3	Nrg-1, Nrg-2
HER3–HER4	BTC, HB-EGF, EPR, Nrg-1, Nrg-2, Nrg-3, Nrg-4
HER4-HER4	BTC, HB-EGF, EPR, Nrg-1, Nrg-2, Nrg-3, Nrg-4

Table 4. HER family member dimer pairs and activating ligands.

1.2.2 EGFR

The human epidermal growth factor receptor 1 (EGFR) or HER1 is a transmembrane protein comprised of an extracellular ligand binding domain, a transmembrane domain, and a cytoplasmic domain with kinase activity (Figure 9). When its ligands, such as EGF, transforming growth factor α (TGFα), or amphiregulin (AR) binds to the extracellular region, a conformational change on the EGF receptor is triggered that allows dimerization with another EGFR molecule, or a heterodimer with another RTK(77). Upon dimerization, EGFR kinase is activated, allowing for autophosphorylation and transphosphorylation of the intercellular tails that serve as docking sites for downstream proteins containing the Src Homology 2 (SH2) domain(77). The primary activated pathways include the RAS/RAF/MEK/ERK, PI3K/AKT, and PLCγ/PKC pathways, but

activation of Src tyrosine kinases have been documented(77). Additionally, EGFR can signal from different compartments of the cell including the nucleus.

The nuclear EGFR (nEGFR) signaling network has recently been implicated in cancer progression and response to EGFR-targeted therapies. nEGFR has been detected in cancer cells of primary tumor specimens, as well as other highly proliferating tissues(78–81). Additionally, high expression of nEGFR has been correlated with poor clinical outcome in patients with breast cancer, in particular(82), as well as in many other cancers(82,83). Due to the many pathways that EGFR functions within, EGFR as a treatment target has been strongly pursued over the last 30 years(77).

1.2.3 EGFR expression in TNBC

Approximately 10-20% of global BC patients will be diagnosed with a tumor lacking the three targetable biomarkers, ER, HER2, and PR, and are considered “triple negative” (84). TNBC is a more aggressive BC subtype, disproportionately affecting premenopausal African or Hispanic women, and accounts for 25% of BC deaths(85). TNBC patients have a poorer outcome compared to other BC subtypes presenting with known molecular targets, and many of these tumors must be treated with chemotherapy as the mainstay in the neoadjuvant, adjuvant, and metastatic setting(85). Yet despite promising results, there have been cases of increased toxicity without improvements to survival(86). This may be in part due to the fact that BC is a heterogeneous disease with complex variances in genes, epigenetics, and protein expression within each individual’s tumor(87). Due to this complexity, efforts have been made to classify tumors into subgroups based on homogeneous patterns of sensitivity to other therapies(88).

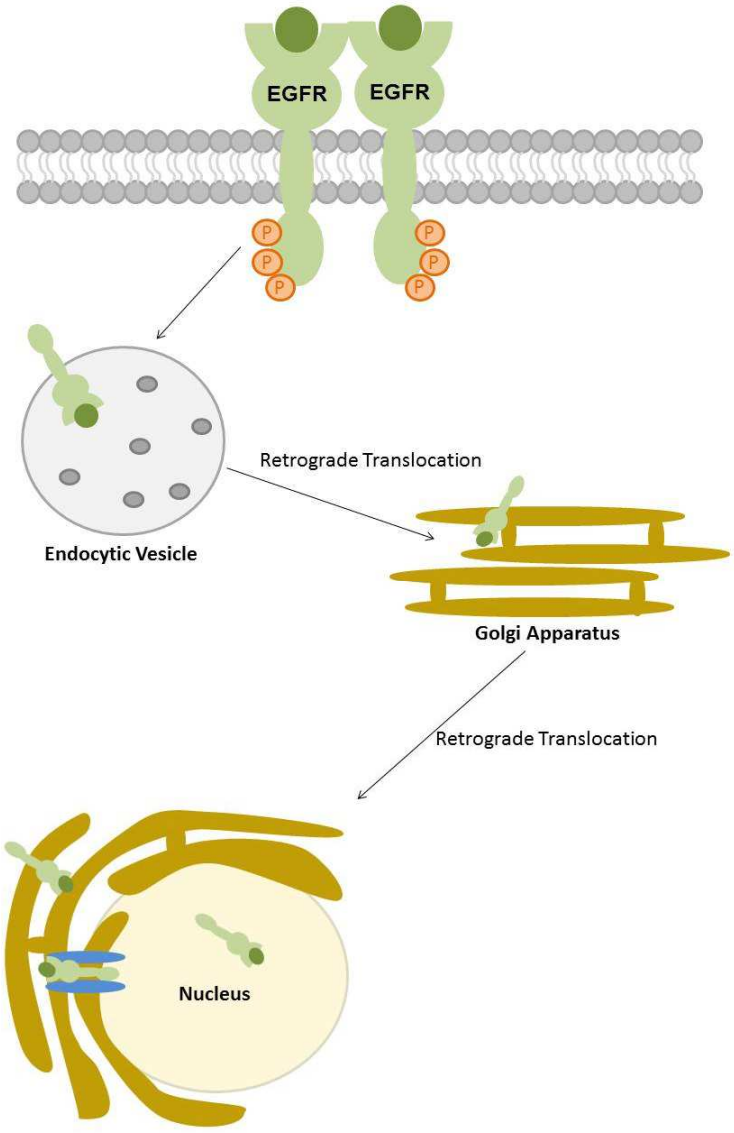

Figure 9. EGFR trafficking to the nucleus. Upon ligand binding and activation, EGFR homodimerizes and induces transautophosphoylation. This causes internalization to endocytic vesicles. EGFR then undergoes translocation through the Golgi apparatus and into the endoplasmic reticulum outside of the nucleus. EGFR then moves through the outer and inner nuclear membranes through the nuclear pore complex. Finally, EGFR interacts with Sec61 and is released from the ER into the nucleus.

Lehmann and colleagues have defined six new TNBC subtypes based on gene expression profiles: basal-like 1, basal-like 2, mesenchymal, mesenchymal stem-like, immunomodulatory, and luminal androgen receptor(89). Within these subtypes, there is further stratification based on gene mutations, which lead to possible actionable

pathways, such as PARP inhibitors, anti-angiogenic antibodies and inhibitors, PI3K and mTOR inhibitors, AKT inhibitors, and immunotherapy, to name a few(90). One of these actionable pathways has been shown to be EGFR. In one study, EGFR was overexpressed in 89.47% of cases of invasive BC(91). Similar results were also observed in a study among 151 TNBCs where 27% of cases were scored as 3+ for EGFR and 37% were scored as 2+ by IHC, confirming high EGFR expression(92). Therefore, targeting EGFR in TNBC is a critical need.

1.2.4 EGFR targeted therapies in BC

To date, two successful approaches towards targeting EGFR in cancer therapies have been explored. The first approach involves targeting the kinase activity of the receptor through the use of tyrosine kinase inhibitors (TKIs) that bind to the ATP-binding sites of the receptor. There are currently three FDA approved TKIs – erlotinib (Tarceva®), gefitinib (Iressa®), and lapatinib(Tykerb®)(93). A second approach uses mAbs to target the extracellular domain of EGFR and block natural ligand signaling and dimerization, which are outlined in Table 5.

Drug	Treatment Type	Clinical Trial	Phase/ clinicaltrials.gov identifier	Notes (M/ = approved)
Panitumumab (Vectibix®)	Human mAb	Breast	II/NCT02593175 II/NCT01036087 II/NCT01009983	M/2006 – colorectal
		Malignant neoplasm of Breast	II/NCT02876107	
		Metastatic Breast	II/NCT00894504	
Cetuximab (Erbitux®)	Chimeric mAb	Breast	II/NCT00232505 II/NCT00275041 II/NCT00463788 II/NCT00633464 II/NCT00600249 I/NCT03319459 I/NCT02627274 I/NCT02124148	M/2004 - colorectal
Laprituximab emtansine (IMGN-289)	Chimeric mAb	Solid Tumors	I/NCT01963715 (terminated)	Conjugated to drug DM1
Necitumumab (Portrazza®)	Humanized mAb	Solid Tumors	II/NCT01606748	M/2015 - NSCLC
SCT-200	Humanized mAb	Breast	II/NCT03692689	
Anti-EGFR-immunoliposome-dox	EGFR-targeted liopsome	Breast	II/NCT02833766	
Gefitinib (Iressa®)	Small molecule inhibitor	Breast	II/NCT01732276 II/NCT00739063	M/2015 - NSCLC
Poziotinib	Small molecule inhibitor	Metastatic Breast	II/NCT02544997	
Lapatinib (Tykerb®)	Small molecule inhibitor	Breast	II/NCT00820924	M/2007 – HER2+ Breast
Erlotinib (Tarceva®)	Small molecule inhibitor	Breast	II/NCT00503841	M/2004 - NSCLC

Table 5. EGFR targeted treatments for BC.

Cetuximab was FDA approved in 2006 for the treatment of colorectal cancers in the metastatic setting(94). It is a chimeric monoclonal antibody that targets domain II of EGFR with a higher binding affinity than natural ligands transforming growth factor (TGF) and EGF, effectively blocking the ligand-binding domain and preventing dimerization(77). Similarly to trastuzumab, cetuximab is capable of antibody-dependent cell-mediated cytotoxicity (ADCC) and complement-dependent cytotoxicity(95,96). Cetuximab can also block EGFR phosphorylation and promotes internalization of the receptor which reduces proliferation(97). Upon cetuximab binding to EGFR, phosphorylation will be induced which can trigger downstream responses such as aberrant growth signals or apoptosis(98,99). Due to its efficacy, it has been combined with many other treatments such as chemotherapy and radiotherapy, resulting in tumor depletion in mice, and improved chemotherapy efficacy in humans(100). It has limited dose toxicities, with only about 10% of patients reporting a severe toxicity(101).

Surprisingly, clinical trials focusing on EGFR-TKIs and mAbs in TNBC have been disappointing, potentially due to resistance mechanisms(77). These pathways of resistance include the angiogenesis pathway, increased EGFR degradation, dysregulation of EGFR internalization, oncogenic shift (increased expression of other HER family members), constitutive activation, and increased expression of ligand growth factors(77).

Cetuximab as a monotherapy has shown dismal response rates in TNBC(102). In a phase II clinical trial, patients who received one or fewer chemotherapy regimens were randomly assigned to cisplatin plus cetuximab, or cisplatin alone. While cetuximab alone did not result in an increased overall response rate, its combination with cisplatin doubled

objective response rate, suggesting there is hope for cetuximab in TNBC(102).

In another phase II clinical trial on metastatic TNBC patients, Carey et al. had patients receive cetuximab alone or with carboplatin after progression. Overall response rates were 6% with cetuximab alone, or 17% with combination therapy, and EGFR expression as a single marker did not provide a significant correlation with clinical response(103). Due to its failure to yield improved response rates using EGFR-targeting mAbs without prior EGFR profiling, it has been suggested to stratify patients first by their expression of target biomarkers before they undergo treatment, and has been explored in colorectal cancer with some success.

Due to its success in other cancers, investigations have been made to find biomarkers to better stratify patients and predict responses. Most obvious, EGFR expression levels were hypothesized to correlate with cetuximab response. Unfortunately, early clinical trials failed to find a correlation between EGFR expression and clinical response to EGFR therapy in BC(104). This finding led to the belief that IHC-based EGFR measurements are not robust predictors for cetuximab therapy, and they moved onto other methods, such as EGFR copy number and mutation status. So far, only KRAS mutations(105), BRAF mutations(106), and IGF1R expression(107) status have correlated with response to cetuximab therapy, which none of these biomarkers have been implemented in TNBC, highlighting a need for an approved method to monitor EGFR-therapy response rates. One notable resistance pathway to cetuximab treatment in TNBC was highlighted as the subcellular localization of EGFR (108).

1.2.5 HER2-positive BC

The HER2 receptor is amplified or overexpressed in about 20% of all diagnosed

BCs(109). Albeit significant efforts to develop anti-HER2 agents, there is still a significant number of patients with HER2+ BC that progress within 5-10 years of treatment(109). The value of HER2 as a prognostic factor is controversial. In 88% of early studies looking at over 40,000 cancer patients, harboring the HER2 amplified gene or HER2 protein overexpression was a negative prognostic factor for traditional chemotherapy, independent of other prognostic variables(109). However, the advent of HER2 specific treatments, such as the monoclonal antibody trastuzumab (Herceptin®), has improved treatment outcomes for patients in the adjuvant and metastatic setting(102). Trastuzumab has been tested in many major clinical trials for patients with HER2+ breast cancer, with the median overall response rates ranging from 15.6-25.1 months(109).

1.2.6 Current companion diagnostics for HER2-positive BC

Due to the prognostic value of HER2-receptor presence and response to HER2-targeted treatment, it is now recommended that all primary, metastatic, and recurrent BC be tested for HER2(110,111). Currently, there are many FDA-approved *in vitro* companion diagnostics for HER2 overexpression, including five immunohistochemistry assays (IHC), three tests to quantify HER2 gene copy numbers through fluorescence in situ hybridization (FISH), one chromogenic in situ hybridization (CISH), and a dual in situ hybridization (ISH) assay(109). These *in vitro* diagnostic techniques require an invasive procedure of collecting sample tissue from a patient. Due to tumor heterogeneity, the sample collected may not fully represent the entire tumor microenvironment, potentially yielding inconclusive results. Additionally, tissue can only be collected from a patient with accessible tumors, limiting the utility for hard to access cancers.

IHC staining is a semi-quantitative, but subjective, method for determining HER2 status, since HER2 is expressed in all breast epithelial cells. Results are scored from 0 to 3+, which measures the amount of HER2 protein present in the cell, with a score of 3+ called “HER2 positive”(112). Although IHC is an available, low cost, and easy method to determine HER2 status, its interpretation is subject to reader bias(112). For example, comparing HER2 overexpression measured by IHC on-site and HER2 amplification measured by FISH at a reference lab revealed low concordance rates (66-87%)(112). FISH, on the other hand, is more reliable and sensitive, but it requires special equipment and training to appropriately perform the test(113). Additionally, HER2 expression can vary between primary and metastatic sites, making it difficult to characterize each individual lesion(114,115).

On the other hand, fluorescence in situ hybridization (FISH) testing is an automated slide-based DNA-hybridization using fluorescent probes. It is a more objective scoring system, although it is an expensive test and requires specialized microscopes. Chromogenic in situ hybridization (CISH) is a similar test where instead of a fluorescent probe, a chromogenic probe is used. These tests are binary, providing a “positive” or “negative” HER2 score, and not a numeric value.

Since the advent of immunoPET, efforts have been made to use imaging as a means to characterize breast lesions with trastuzumab as a tracer. In a study by Dehdashti *et al.,* women with HER2+ and HER2- BC underwent a PET/CT scan after administration of a ^{89}Zr-labeled HER2-specific antibody (trastuzumab)(116). The PET/CT uptake was correlated to HER2 status determined by IHC or FISH of a primary or metastatic lesion. They found that 88.2% of HER2+ patients had a positive PET/CT scan,

and 93.7% of HER2- patients had a negative PET/CT scan. This translated to a positive-predictive value of 83.3% and a negative predictive value of 50% in differentiating HER2 positive from negative tumors. They conclude that ^{89}Zr-trastuzumab has the potential to characterize the complete tumor burden in BC patients for HER2 status, obviating the need for multiple invasive tissue samples. Additionally, it addresses the issue of interpatient heterogeneity of HER2, and can further aide in treatment decisions.

1.2.7 HER2-targeted treatment strategies

At time of writing, there are five FDA-approved targeted therapies for HER2+ disease, including monoclonal antibodies (mAb), antibody-drug conjugates (ADC), and small molecule inhibitors (Table 6).

Drug	Type	Target	Mechanism
trastuzumab (Herceptin®)(117)	mAb	Juxtamembrane domain IV	Cell intrinsic effects Antibody dependent cell-mediated cytotoxicity
pertuzumab (Perjeta®)(118)	mAb	Dimerization domain II	
ado-trastuzumab emtansine (Kadcyla®)(119)	Antibody-Drug conjugate	Juxtamembrane domain IV	Binds to HER2 like trastuzumab and delivers emtansine
lapatinib (Tykerb®)(120)	Small molecule inhibitor	EGFR/HER2	Bind to the ATP binding cleft in tyrosine kinase domain to block catalytic activity
neratinib (Nerlynx®)(121)	Small molecule inhibitor	EGFR, HER2, HER4	

Table 6. FDA approved HER2-targeted treatments for HER2+ BC

Trastuzumab (Herceptin®) is a humanized monoclonal antibody targeted against HER2. It was approved in 1998 for the treatment of metastatic HER2+ disease, and was the first anti-HER2 agent on the market. In 1998, the “pivot trial”, a randomized phase III trial testing chemotherapy alone versus chemotherapy and trastuzumab, showed a median overall survival of 25.1 months in patients who received trastuzumab, and impacted the FDA approval of trastuzumab for metastatic breast cancer that same

year(109). It has radically improved outcomes in HER2+ breast cancer patients, with a study in 2014 of 4,000 patients showed that adding trastuzumab to chemotherapy improved overall survival from 75.2% to 84%, and is listed as an essential medicine by the world health organization(122,123). Its mechanism of action is not fully understood, but it is thought to evoke antibody-dependent cellular cytotoxicity (ADCC), disrupt downstream signaling pathways, inhibit cell cycle progression, and act as an antiangiogenic agent upon binding to HER2(124). Early clinical response rates ranged from 12-68% response, with the best responders observed in patients with an IHC or FISH score of 3+. The addition of trastuzumab to other therapies increased progression free survival by 2-3 months(124). The success from these trials and the many others has resulted in a 1 year-long cycle of adjuvant trastuzumab as standard of care for HER2+ tumors, as well as provided proof-of-concept that targeting HER2 would improve patient outcomes.

The phase III study comparing lapatinib (Tykerb®), an oral TKI of HER2 and EGFR, to capecitabine in patients with HER2+ metastatic breast cancer improved progression free survival(125), and, therefore led to its FDA approval in 2007. Recently, two antibody-based therapies and a small molecule TKI were FDA approved: pertuzumab, TDM-1 and neratinib. Pertuzumab (Perjeta®) prevents the pairing of HER2 and HER3; the results from the phase III CLEOPATRA study demonstrated a synergistic effect achieved when pertuzumab was combined with trastuzumab and docetaxel with patients showing improved progression free survival(126). TDM-1 (Kadcyla®), approved in 2013, links a cytotoxic agent to trastuzumab, specifically delivering emtansine to HER2+ tumors. A randomized phase III EMILIA study demonstrated improved overall and

progression free survival of TDM-1 compared to capecitabine plus lapatinib(127). Finally, neratinib (Nerlynx®) is an oral TKI that inhibits EGFR, HER2, and HER4, approved in HER2+ patients based on the exteNET phase III clinical trial(128). A phase III trial of women with stage 1-3 HER2+ BC who previously completed trastuzumab therapy, patients were randomized to neratinib (Nerlynx®) or placebo. Those who received neratinib had significantly improved 2-year disease free survival.

More new HER2 agents or potential combination therapies either under preclinical development or FDA-approved for other HER2+ cancers can be potential treatments in BC in the future(129). HER2 antibodies MGAH22, MCLA-123, and ZW-25, and ADCs SYD 985 and DS-8201 are all past phase I clinical trials. New TKIs tucatinib, poziotinib, and pyrotinib (Nerlyxn®), are all through phase II trials.

Even with the diverse availability of treatments, because of HER2 mutations (intrinsic and acquired) causing drug resistance, there are differences in sensitivity between patients and therapies. Changes in downstream pathways or activation of parallel oncogenic pathways can potentially contribute to resistance. Particular attention should be given to identifying acquired resistance mechanisms to help optimize HER2 directed therapies(130).

1.3 Mechanisms of resistance to treatment in BC

In hormone receptor positive BC (ER+ and PR+), endocrine therapy is the mainstay(131). Endocrine therapy includes the use of selective ER modulators (SERMS) which act as tissue specific estrogen receptor agonists and antagonists. Selective ER down regulators (SERDs) competitively bind ER with a greater affinity than SERMs, and reduce transcription of ER regulated genes. Aromatase inhibitors block estrogen

synthesis and prevent their growth-stimulating effects. Development of resistance is thought to be due to genetic factors (ESR1, CCDC170 mutations, for example), loss of ER expression, crosstalk between compensatory receptors (HER2, EGFR) and epigenetic factors(132). For TNBC, first line neoadjuvant platinum-based or taxane chemotherapy is the mainstay, and comes with its own set of challenges. Most often, resistance stems from an increase in the cell's ability to efflux the drug, which results in decrease net intracellular accumulation(133). In HER2+ BCs, resistance pathways can develop after trastuzumab (Herceptin®) therapy from upregulation and compensation from other HER family members, epitope masking, and enzymatic cleavage of the trastuzumab binding site(134). Additionally, cells can develop adaptive responses by down-regulating tumor suppressors PTEN and PI3K/Akt(135,136), or through alteration of downstream pathway signaling, through the PTEN/PI3K/AKT/mTOR pathway, and even the Src pathway(137).

1.3.1 Overview of Src

Src is expressed in all normal, mammalian cells and is classified as a proto-oncogene(138). The Src gene produces a protein produced called Src that is a member of the Src family kinase (SFK) group, which is a group of non-receptor tyrosine kinases(138). SFKs are involved in many cellular processes and their aberrant signaling has been associated with tumor promoting events, such as cell proliferation and survival(138). The most studied mechanism of Src function is its interaction with RTKs, such as EGFR and HER2 through its SH2 and SH3 domains(139). Src also plays a role in tumor metastasis, with roles in regulating the cytoskeleton, cell migration, cell-cell

adhesions, and invasion (Fig. 10)(140).

Pre-clinically, Src appeared as a promising therapeutic for cancer, although efficacy of single agent Src inhibitors in solid tumors has not shown promise in Phase II clinical trials(139). This is in part due to its activation in many resistance pathways. In particular, SFKs are an important component in chronic myelogenous leukemia (CML) due to their direct interaction with BCR-ABL(141). Src is shown to be involved in steroid receptor signaling and endocrine resistance(142). Src activation is observed in 40% of ER-positive (143) and in up to 70% of primary human BC with concomitant HER2 or EGFR expression(144). The synergism between EGFR, ER, and Src facilitates hormone signaling and confers resistance to targeted therapies(145). The mechanism of resistance most important to this body of work is the interaction between Src and the RTKs EGFR and HER2. It has been previously reported that in many cancers, targeting SFK dramatically enhances the efficacy of anti-RTK therapies(146).

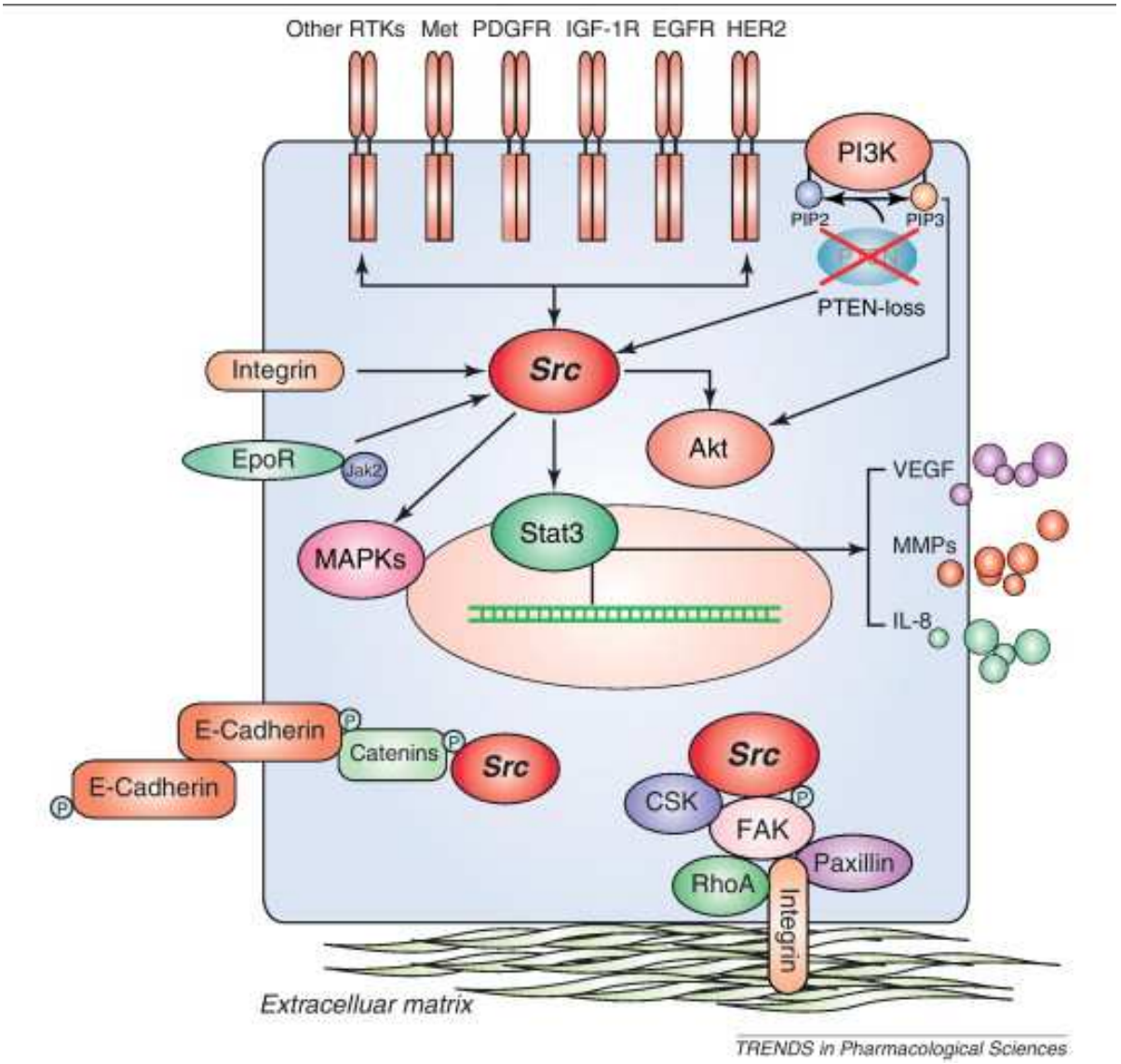

Figure 10. Src signaling and downstream pathways. Src interacts with many RTKs and facilitates their downstream signaling to promote cell survival. Major Src downstream activation includes: (i) AKT activation and cell proliferation, (ii) stat3 activation and transcription upregulation, (iii) disruption of cell-cell junctions through p120-catenin, and (iv) stabilization of adhesion through FAK phosphorylation. This figure was reprinted with permission from Trends in Pharmacological Sciences. Targeting Src family kinases in anti-cancer therapies: turning promise into triumph, Siyuan Zhang and Dihua Yu. 2012;33(3):7.

1.3.2 Src inhibitors

Due to its role in promoting tumorigenesis, there has been extensive developments of small molecule inhibitors targeting Src dysregulation(138). Dasatinib (Sprycel™, Bristol-Meyers Squibb) was the first FDA-approved Src/ABL inhibitor for the treatment of CML(147). Other inhibitors include saracatinib (AZD0530, AstraZeneca) and bosutinib (SKI-606, Wyeth)(148). Src inhibitors typically have low toxicity, but as a monotherapy they have dismal response rates in solid tumors(139). Dasatinib in particular has shown < 25% clinical benefit in phase II trials in BC, prostate cancer, and melanoma(149). Additionally, targeting Src though dasatinib failed to show a significant clinical benefit in metastatic colorectal(147) and small cell lung cancer(150). Saracatinib additionally failed to show benefit in prostate(151), pancreatic, and metastatic head and neck cancer(95), gastric adenocarcinoma(152), and ER/PR negative metastatic BC(153). Not surprisingly, no Src inhibitors have been FDA-approved for treating solid tumors as a monotherapy(139).

For the past 30 years, Src monotherapy has lacked efficacy, but recently, new studies have provided a foundation for future clinical trials(139). One of the challenges in developing Src inhibitors is the lack of biomarkers available for Src-targeted therapy, making patient selection and stratification difficult. Previous clinical trials were performed on patients unselected for Src activation. This led to poor treatment outcomes, warranting re-examination of the Src activation pathway in the hopes of a target for subsequent clinical trials. In a recent study of 23 colorectal cancer cell lines, Src pathways activation was observed and correlated with enhanced sensitivity to Src inhibitor saracatinib, supporting the hypothesis that looking into Src pathway activation is beneficial for

improved treatment outcomes(154). In a trial of pancreatic cancer patients, Src activation was observed and noted. They found that patients with Src activation were more sensitive to dasatinib, as compared to their non-activated counterparts, and furthermore, those patients with Src localized to the cytoplasm had increased survival(155). These results highlight Src activation as a molecular target and are looked into more thoroughly in the next sections.

1.3.3 Src hyperactivation and its role in trastuzumab-resistance in HER2+ BC

Despite its success in HER2+ BC, some patients who receive trastuzumab will relapse. Some proposed mechanisms of resistance have included HER2 forming heterodimers with other family members and effectively blocking trastuzumab binding, an increase in expression of HER2, and shedding of the extracellular domain leaving the form of the receptor (p95) which does not bind to trastuzumab but retains kinase activity(156).

HER2 directly associates with Src as it activates its downstream signaling and stability(157). It has been shown that Src signaling is up-regulated in trastuzumab resistant tumors(157), as well as *de novo* trastuzumab-resistant cells(158). A particular oncogenic variant, HER2Delta16, induces Src function and activates Src to confer trastuzumab resistance(159). Src inhibition has been shown to sensitize trastuzumab-resistant BC to trastuzumab(158). One study has shown that combination treatment with saracatinib and an anti-HER2 antibody (clone H2-18) produces a greater antitumor effect on trastuzumab-resistant (PTEN wt) breast cancer(160). An additional study has shown that cells overexpressing wild-type Src were resistant to trastuzumab(158). Clinically, there is a correlation between phosphorylation of Src at tyrosine reside 416 (Y416) and

total Src abundance ($p = 0.025$), and patients with higher levels of phospho-Src in tumors had a lower clinical response rate and progressive disease after trastuzumab(158).

1.3.4 Src and its role in EGFR-overexpressing cancers

Src activation has been shown to promote resistance in anti-EGFR therapies. Particularly, Src is responsible for the full activation of EGFR(161), and it physically associates with activated EGFR(162). Once Src binds to EGFR, EGFR undergoes a conformational change. This leads to autophosphorylation at the tyrosine residue 416 (Y416) and subsequent transient activity, which leads to phosphorylation of downstream targets, such as EGFR on tyrosine 845 (Y845)(144). Y845 is situated in a conserved position within the activation loop of EGFR, and is necessary for full activity of the receptor(163). It has been discovered that Src can directly phosphorylate EGFR on Y845, strengthening the communication between the two proteins(164). This residue also acts in concert with the redistribution of EGFR from the membrane to intracellular vesicles, and has been suggested as a marker of drug response in NSCLC, breast, and colorectal cancers(164).

EGFR and Src are shown to be upregulated in a majority of lung, colorectal, and pancreatic cancers(165). Additionally, Src is commonly activated in EGFR-overexpressing cells and its activation enhances EGFR signaling of downstream PI3K-Akt pathway(158). In one study, it was reported that cells with acquired cetuximab resistance have increased Src activity, potentially due to its cooperation with EGFR and resultant signaling to HER3 and PI3K/Akt. A decrease in HER3 phosphorylation and PI3K/Akt signaling is observed when cetuximab-resistant cells are treated with dasatinib, which was coupled with a decrease in proliferation and survival(166). In a different study

of breast cancers expressing EGFR, HER2, and HER3, dasatinib treatment resulted in apoptosis and growth inhibition in a dose dependent manner(167). This was accompanied by decreased EGFR and Src phosphorylation, suggesting that these two RTKs are prime targets for BC therapy. In non-small cell lung cancer (NSCLC) in particular, Src is highly active and associated with cetuximab resistance(166). Most notably, it has been shown in a non-small cell lung cancer cell line H226, that cetuximab-resistance leads to overexpression of EGF, and concomitant nuclear translocation of EGFR mediated by Src. Treatment of these resistant cells with dasatinib resulted in loss of nuclear EGFR, increased membrane EGFR expression and cetuximab re-sensitization, further supporting the hypothesis that EGFR nuclear compartmentalization impacts cetuximab efficacy(168). Additionally in colorectal cancer, dasatinib re-sensitized cetuximab-resistant tumors to cetuximab(169).

EGFR localization, in particular, has been investigated as a potential resistance mechanism in breast cancer. Extensive reports have shown EGFR family members being shuttled from the plasma membrane to the nucleus, with nEGFR expression demonstrating poor clinical outcomes in breast cancer(80,81,137,170). nEGFR acts as a transcription factor, interacting with STAT3 and E2F1. When in the nucleus, EGFR is associated with gene transcription, DNA repair, and radioresistance.

1.4 Immune oncology

Despite significant advances in BC chemo- and molecular therapies, a proportion of patients with localized disease still remain refractory to treatment, or suffer relapse. Furthermore, those with metastatic disease are rarely cured. In BC, it is believed that immunosuppression and inflammation become induced and contribute to

progression(171). Particularly in TNBC, BC gene profiling has demonstrated patterns of immune gene activation(172). In approximately 50% of HER2+ BCs inflammatory signatures are observed which correlate with improved outcomes(173). Additionally, high levels of tumor infiltrating lymphocytes (TILs) have been associated with improved response to neoadjuvant chemotherapy(174). Due to these observations, recent advances in immunotherapy highlight the potential to harness the immune system for improved tumor responses in the adjuvant and monotherapeutic space (175).

The immune system can impact tumor growth and prevention through the immunoediting process. This is comprised of three stages called elimination, equilibrium, and escape. In the elimination phase, the tumor is destroyed by inflammation, infiltration of effector cells, and production of tumor-inhibiting cytokines(176). The escape phase is characterized by sustained inflammation comprised of immunosuppressive cells and soluble molecules(177). In equilibrium, the tumor is neither proliferating nor dying off, and can turn into the other two stages based on the immune response.

1.4.1 The immune pathway

The primary cells responsible for killing breast tumor cells are CD8+ CTLs and natural killer (NK) cells. Induced CTLs target specific antigens expressed on BC cells, and their infiltration into the tumor microenvironment has been associated with improved outcomes, particularly in the TNBC or basal subtype(178). Combining immunotherapy and chemotherapy has also been shown to enhance the activity of CTLs and is coupled with enhanced antitumor effects(179), and the positive effect of vaccines has been shown to be achieved through CTL-mediated recognition and destruction of breast cancer(180). NK cells, on the other hand, are cells of the innate immune system that kill tumors cells

unrestricted by major histocompatibility complex (MHC) class(69). Decreased NK activity has been observed in patients with familial breast cancer, stage IV breast cancer, and during breast cancer progression. When profiling gene expression in breast cancer-associated stroma, it has been found that CTL and NK associated genes were enriched and predictive of better outcomes. Overall, it has been suggested that CD8+ T cells and NK have strong antitumor activity against BC(181).

It is now accepted that BCs have an infiltration of leukocytes, and this can either promote tumorigenesis or elimination(182) (Fig. 11), and in BC these TILs have been established as a putative biomarker of treatment prognosis(183). There have been many retrospective studies published that suggest an association between pathologic complete response to neoadjuvant treatment and the presence of TILs in solid tumors, potentially representing a robust and reproducible predictive factor(184). Particularly, a decrease in regulatory T cells confers response to treatment, and restores anticancer responses in non-responders(184). This hypothesis has been supported by studies reporting that some patients treated with high-dose interleukin-2 (IL-2) show durable responses and an increase in response to TIL therapy, where others do not(185). More recently, the inhibition of PD-1 alone results in response rates of 20-30% of patients, but upon combination with CTLA-4 blockade, this response rate increases to 57%(186). The varying response rates between patients has been hypothesized to be due to TILs presence, with higher PD-1 responding patients having more CD8+ T cells in their tumor bed(187). Therefore, ways to monitor presence of TILs before selecting a treatment type is of upmost importance.

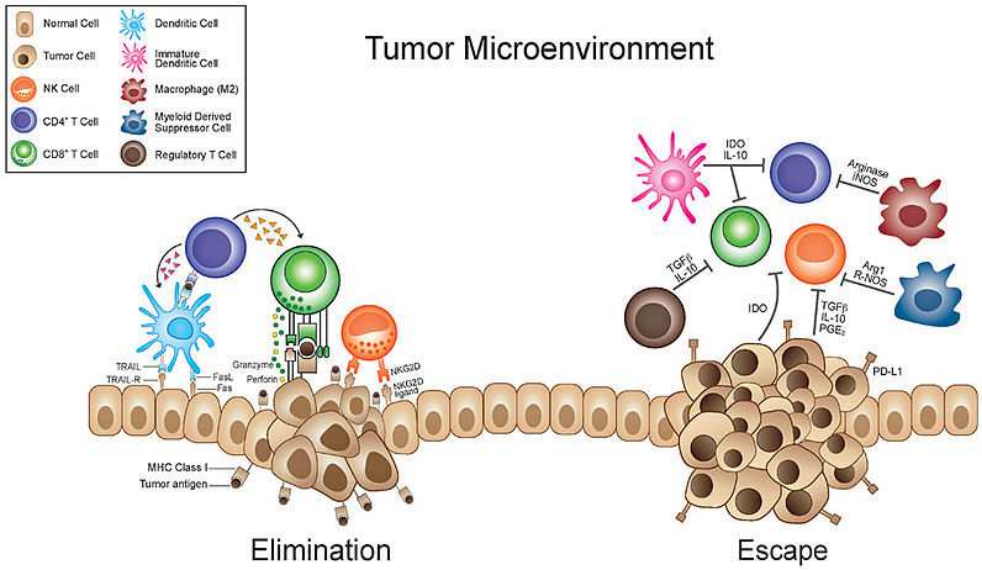

Figure 11. TIL infiltration and its mechanism for eliminating tumors. Tumors in the elimination phase (left) have an influx of active dendritic cells, NK cells, and T cells which produce cytokines and signals to stop tumor proliferation. In the escape phase, these infiltrates are now engaged with the tumor environment, and the tumor is able to proliferate. This figure was reproduced with permission under the creative commons license from: http://www.frontiersin.org/files/Articles/51138/fonc-03-00197-HTML/image_m/fonc-03-00197-g001.jpg

1.4.2 FDA-approved and emerging immunotherapies

Cancer immunotherapy is defined as the utilization of naturally derived or synthetically generated compounds to enhance or stimulate the immune system. The main types of immunotherapy include adoptive T-cell transfer, viruses, monoclonal antibodies, and cancer vaccines(175). During adoptive T-cell transfer, a patient's own T-cells are genetically engineered to recognize cancer cells. Oncolytic viruses are specifically modified viruses that avoid normal tissue and recognize a tumor associated antigen. Once inside the cancer cell, the virus will replicate and then rupture the tumor cell. As of writing, talimogene laherparepvec (T-VEC) is the only approved treatment of this kind, for melanoma(188). Monoclonal antibodies are immune cell manufactured

proteins that specifically recognize an antigen on a target cell. These antibodies will suppress the activity of a cancer-associated protein, or kill the cancer cell entirely(189). Finally, vaccines will expose the immune system to a specific antigen for prevention (prophylactic) or treatment(190). Once the immune system recognizes the vaccinated antigen on the cancer cell, they will facilitate its elimination. In this work, monoclonal antibodies and vaccines with respect to BC treatment will be discussed in further depth.

Targeted monoclonal antibodies are a mainstay in BC immunotherapy since the late 1990s with the advent of trastuzumab for HER2+ BC; there are a total of 32 FDA approved antibodies as of 2017(191). The goal of monoclonal antibodies is to target tumors and (a) directly kill the tumor, (b) switch the immune system to attack the tumor, (c), attract immune cells to the tumor microenvironment, (d) decrease tumor vascularization, and (e) inhibit migration(191). Currently, antibodies used in treatment are either used alone or in combination with cytotoxic chemotherapy, radiotherapy, inhibitor molecules, other antibodies, or vaccines.

The most common use of mAbs is in the context of immune checkpoint inhibitor blockade, targeting CTLA-4, PD-1, or PD-L1(192). When the antibody binds to each of these molecules, it inhibits receptor binding; thus, blocking the immune checkpoint pathways from getting activated. In the case of CTLA-4 blockade, it prevents activation of T cells, whereas the PD-1 and PD-L1 blockade affects tumor and T-cell interactions. The FDA-approved immune checkpoint inhibitors are: ipilimumab (Yervoy®, anti-CTLA-4), pembrolizumab (Keytruda®, anti-PD-1), nivolumab (Opdivo®, anti-PD-1), atezolizumab (Tecentriq®, anti-PD-1), avelumab (Bavencio®, anti-PD-L1), durvalumab (Imfinzi®, anti-PD-L1). These immunotherapies are approved for many disease types,

including melanoma, NSCLC, and metastatic RCC(192). In 2017, the FDA approved pembrolizumab (Keytruda®) for adult and pediatric patients with unresectable or metastatic, microsatellite instability high or mismatch repair deficient solid tumors that have progressed following prior treatment, making it the first FDA-approved tissue agnostic drug, meaning that the drug is prescribed based on the presence of target biomarker, and not due to tumor type(193). Due to the success achieved in other tumors targeting checkpoint inhibitors with monoclonal antibodies, it is being tested in breast cancer as well through many clinical trials (Table 7).

Target	Tumor Type	Clinical Trials Identifier
CTLA-4	HER2-	NCT02536794
	TNBC	NCT02381314
PD-1	Advanced TNBC	NCT02661100
	HER2-	NCT02661100
	HER2+	NCT02129556
	BC	NCT02309177
	TNBC	NCT02404441
	TNBC	NCT02555657
PD-L1	BC	NCT02643303
	TNBC	NCT02628132
	TNBC	NCT02685059
	TNBC	NCT02725489
	Metastatic BC	NCT02425891
	TNBC	NCT02478099
	HER2+ Metastatic	NCT02649686
	Advanced TNBC	NCT02708680

Table 7. List of checkpoint inhibitor antibodies currently in clinical trials and their BC subtype.

Historically, vaccines have been developed for disease prevention, and have focused on targeting B cell immunity and producing a lasting innate immune response(175). Cancer vaccines, in contrast, have been developed to stimulate T cell

responses for the treatment of a pre-existing cancer. These vaccines target antigens specifically expressed or altered in the tumor, either due to mutations, splice variations, or overexpression(175). Early cancer vaccines targeted CD8+ T cells with short peptides that bound to MHC class I molecules (EMENS), but these responses were short-lived and ineffective. This inspired a new wave of delivery methods which would target both CD8+ effector T cells and CD4+ helper T cells(194). These antigens are delivered as peptides, proteins, named DNA, vectors, or dendritic cells(175). To enhance the response, antigen delivery is typically combined with adjuvants such as granulocyte-macrophage colony-stimulating factor (GM-CSF) or water in oil emulsions(175). A list of current cancer vaccines can be found in table 8.

	Study	**NCI Identifier**
DNA/ Viral	AVX901	NCT01526473
	Plasma mammaglobin-A	NCT00807781
	adHER2-/neu dendritic cell	NCT01730118
	HER2/neu peptide	NCT01376505
	Human MUC1 in adenovirus	NCT02140996
	CEA/TRICOM	NCT00048893
Peptide/Protein	Folate receptor binding peptide	NCT02019524
	Sialyl Lewis-KLH	NCT00470574
	Multiple Peptide	NCT01259505
	DEC-205/NY-ESO-1 Fusion Protein CDX-1401	NCT00304096
	GP2	NCT00524277
	NY-ESO-1	NCT01522820
	MUC-1 peptide	NCT00986609
	Multi-peptide	NCT01660529
	E75 peptide	NCT01570036
	Globo H-KLH	NCT01516307
	NeuVax	NCT01479244
	HER2 intraceullular protein	NCT01922921
Cellular	HER-2 peptide/adoptive HER2-specific T cells	NCT00791037
	Allogeneic whole-cell vaccine	NCT00722228
	GSK2302024A	NCT01220128
	PANVAC	NCT00179309
	Allo-stim breast cancer vaccine	NCT01741038

Table 8. Current cancer vaccine clinical trials.

The most advanced vaccines have targeted BC patients overexpressing HER2.

These patients have been shown to have low levels of antibodies and T cell immunity for HER2, and these vaccines were therefore designed to amplify this low-level response(191). The NeuVax (nelipepimut-S) with adjuvant GM-CSF has demonstrated an improved 5-year disease-free survival of 89.7% compared to control (80.2%)(195). There is currently a phase III study looking into the prevention of recurrence (NCT01479244) and a phase II study evaluating efficacy in combination with trastuzumab (NCT01570036). A list of ongoing vaccine clinical trials in BC can be found in table 9.

Clinical Trial Identifier	BC Subtype	Vaccine Type
I - NCT02427581 (Suspended)	TNBC	Poly ICLC
I - NCT01730118	HER2+	HER2 dendritic cell vaccine
I/II - NCT02018458	TNBC ER+/HER2-	Dendritic Cell Vaccine
II - NCT01570036	HER2+	E75
I/II - NCT02061332	BC, DCIS	HER2 pulsed dendritic cell vaccine
I - NCT01376505	BC	HER2 vaccine
I - NCT02140996	BC	Ad-sig-hMUC-1/ecdCD40L vector vaccine

Table 9. Current BC vaccine clinical trials.

Since vaccines created by short peptides can be costly, a variety of viral vectors have been developed to deliver antigens. Common vectors include the poxvirus family, measles, and adenovirus(175). Viral vectors generate more robust immunity than naked DNA or peptide delivery, but after repeated load delivery they can induce antibodies against the viral antigens that limit immunogenicity(175). To circumvent this, viral vaccines use a series of vectors for immune priming. For example, the PROSTVAC vaccine is a recombinant viral vaccine that contains genes encoding PSA and three co-stimulatory molecules for T cells(196). Its cousin, the PANVAC vaccine, is a recombinant poxviral vaccine encoding the MUC1 and CEA genes, with one T cell co-stimulatory

molecule.

Dendritic cells have also been used as vaccines, since they can be generated from the peripheral blood of patients and are loaded with antigen peptides. These vaccines are typically potent, but they are technically challenging and require expertise and specialized laboratories for processing(175).

Cellular vaccines are derived from patient whole tumor cells or dendritic cells fused with tumor cells and injected back into the patient. Monitoring these immunotherapies, though, can be complex, especially since determining which of the tumor antigens are immunogenic, and production of this treatment is labor-intensive. The first FDA approved cellular vaccine was sipuleucel-T (Provenge^{TM}) and approved in 2010 for the treatment of advanced prostate cancer(197). It works by re-infusing patients with their own APCs that have been pulsed with prostatic acid phosphatase and GM-CSF. In the phase III IMPACT trial, it demonstrated improved median overall survival by 4.1 months prostate cancer(196). An investigational agent named lapuleucel-T (APC8024, Neuvenge) is the HER2 cognate of sipuleucel-T and contains peripheral blood mononuclear cells cultured with recombinant HER2 linked to GM-CSF, and has been studied in BC. In a phase I clinical trial with 18 patients, it was well tolerated, with 5.5% patients achieving a partial response, and 16.6% of patients achieving stable disease for up to 1 year(198).

1.4.3 Evading immunotherapy in BC

Regulating T cell response is necessary to minimize autoimmunity, and therefore the immune system has developed a series of checkpoint blockades to aid in this process. Cytotoxic T-lymphocyte associated protein 4 (CTLA-4) is a homologue of cluster of differentiation 28 (CD28), a T cell co-stimulatory molecule, that binds to B7 on APCs. B7

has a higher affinity for CTLA-4 than it does for CD28, allowing for CTLA-4 to outcompete this activation and pause immune activation. CTLA-4 is constitutively expressed on regulatory T cells (Treg), and will become upregulated in T cells after their activation. In response, CTLA-4 expression will inhibit T cell activation and the efficacy of an anti-tumor response.

Programmed death protein-1 (PD-1), on the other hand, is a CD28 and CTLA-4 homologue that is induced on normal, activated T cells. PD-1 promotes apoptosis in activated T cells within the periphery, and it reduces apoptosis of Treg cells(194). When these checkpoints fail, an armory of specialized cells will eliminate tumor-promoting cells(199).

Along with dysfunctional antigen presenting cells, the tumor itself actively modifies the tumor microenvironment to suppress effector T cells and induce inflammation. As a result, the tumor microenvironment contains a robust population of regulatory T cells and myeloid-derived suppressor cells (MDSC), which suppress innate and adaptive responses(200).

With the overexpression of a number of checkpoint molecules, the tumor evades T cell recognition. Chronic exposure of the cancer cells to antigen leads to PD-1 upregulation and lead to T cell exhaustion(194). Additionally, programmed death ligand-1 (PD-L1) is the ligand of PD-1 and is found upregulated in tumors. When PD-L1 is expressed, T cells are prevented from recognizing tumor-specific antigens. In cancer, high levels of PD-L1 in the tumor have been correlated with poor prognosis and progression(201). Dysregulation of immune checkpoint blockade pathways can lead to tumorigenesis, and efforts to target these pathways have been made. Recently, many

immunotherapies have been developed to target checkpoint signaling axes.

1.4.4 Current challenges in monitoring vaccine immunotherapy

Immunotherapy has dramatically increased cancer survival and response rates for the past few decades. This is possibly due to its potential to achieve long-term disease control in a significant population of patients as compared to targeted therapies. Additionally, tumor progression while on immunotherapy peaks later combined with a median duration of response spanning up to years. Unfortunately, the mechanism behind this long-term response is unclear, and a strict definition of clinical endpoints is lacking.

The most commonly used clinical guidelines defining tumor response to immunotherapy come from the immune-modified response evaluation criteria in solid tumors (imRECIST). This criteria was adapted from response criteria in solid tumors (RECIST), since immunotherapy can produce unconventional responses and overall survival benefits that were not captured by RECIST(202). Criteria for imRECIST define tumor burden as unidimensional with up to five target lesions and two per organ. New lesions do not categorically represent progressive disease (PD), and measurable new lesions are then incorporated into the total tumor burden. Non-target lesions do not define PD, and contribute to definition complete response. PD can be negated by subsequent non-PD after 4 weeks from the first documented tumor. Additionally, best response may occur after any number of PD assessments(202).

For vaccines response monitoring, in particular, a few immunodynamic endpoints have been defined, depending on the vaccine type(203). For dendritic cell vaccines, T cell response post vaccination in the tumor via IHC is a standard measurement. Additionally, multicolor immunofluorescence of Treg cells, CD1a, CD8, CD94, CD207,

and HLA-DR calculated as a ratio of pre/post scores are also encouraged. For non-cell based vaccines, peripheral blood mononuclear cells (PMBCs) are characterized. T cell receptor repertoire analysis Flow cytometry is used to quantify and phenotype the T cell response, and is a highly quantitative, reproducible, and standardized test(204). T cell functions are calculated through flow cytometry of perforin, granzyme, and intracellular cytokine expression. Additionally, ELISPOT can be used to assess functionality after antigen-specific stimulation, but is limited by lack of reproducibility and requires a knowledge of antigens to be tested(205). Whole T cell repertoire through CDR3 spectratyping and next generation sequencing is now being used to assess T cell diversity(206). This method does not require an a priori knowledge of antigens and can be performed with less than 1 mL of whole blood. While these methods all provide insight into the immune system after vaccination, they require tissue or blood samples from the patient, and do not recapitulate events within the entire tumor microenvironment in situ in the analysis. Furthermore, site monitoring of the immune response still remains of critical consideration in the field of immunotherapy, and molecular imaging techniques have been employed.

ImmunoPET imaging has been targeting immune biomarkers CTLA-4, PD-1, CD47, CD11b, T cell receptor, CXCR4, B7-H3, granzyme B, CD3+ T cells and IFN-γ in various preclinical studies(207,208). ^{89}Zr- and ^{64}Cu- labelled PD-L1(209) and ^{89}Zr-MPDL3280A (NCT02453984) PET tracers are in clinical development for imaging PD-L1. First-in-human PD-L1 imaging studies demonstrated heterogeneous tumor uptake among tumors with minimal PD-L1 expression through IHC, coupled with high background uptake in secondary lymphoid tissues(210). This study proved clinical

feasibility, although improvements are necessary to improve background uptake and expression correlating to imaging results. ^{18}F-Clofarabine (CFA) is in development for monitoring immune cell proliferation through deoxycytidine kinase imaging(211). T cell activation through the deoxyguanosine pathway is in trials using ^{18}F-D-arabinofuranosylguanine (AraG) PET imaging(212). CD8+ T cells are imaged through ^{89}Zr/^{64}Cu-anti-CD8(213,214) and ^{89}Zr-IAB22M2C PET imaging(58).

The potential for imaging provides a unique opportunity to directly monitor immune responses within the tumor microenvironment before tumor shrinkage and response can be verified through other means. Immunotherapy regimens are still being optimized, and significant efforts have been made to identify and validate predictive biomarkers to aid in treatment decisions. These biomarkers could be used alone or in combination imaging, and additionally with ex vivo analysis and validation throughout treatment.

1.5 Specific aims and summary of research

The studies outlined in this dissertation have been partitioned into three specific aims. In the first aim found in Chapter 2, titled “Monitoring Src Status after Dasatinib Treatment in HER2+ Breast Cancer with ^{89}Zr-trastuzumab PET imaging”, I explored the relationship between Src and HER2 is explored as is the ability of ^{89}Zr-trastuzumab to monitor changes in HER2 after Src treatment. In this study, upon abrogation of Src signaling with dasatinib, an increase in ^{89}Zr-trastuzumab binding and uptake was observed in *in vitro* cell studies and *in vivo* animal studies of trastuzumab-sensitive (BT-474) and trastuzumab-resistant (JIMT-1) lines. The uptake to standard ^{18}F-FDG imaging was compared to find that this metabolic tracer failed to distinguish differences in tumor uptake after dasatinib treatment. *Ex vivo* tumor analysis showed a correlation between

pSrc (Y416) abrogation and pHER2 (Y1221/1222) expression, and ^{89}Zr-trastuzumab uptake.

In the second aim, described in Chapter 3, entitled “Using ^{89}Zr-cetuximab PET imaging to visualize membrane EGFR expression following dasatinib treatment in TNBC”, the ability of ^{89}Zr-cetuximab was explored to measure changes in EGFR localization after dasatinib treatment, and if any correlation can be made with an improved response to combination dasatinib and cetuximab treatment. Using TNBC cell lines MDA-MB-231 (KRAS mutant), MDA-MB-468 (KRAS wild-type-wt), an increase in ^{89}Zr-cetuximab binding and internalization was demonstrated after dasatinib treatment, coupled with a decrease in both pSrc (Y416) expression, and in nuclear EGFR expression as shown by western blots. *In vivo* studies of using the tumors established from these two cell lines including a TNBC patient-derived xenograft (JAX TM00089, KRAS wt), an increase in ^{89}Zr-cetuximab uptake was demonstrated after dasatinib treatment, with a concomitant improvement in treatment responses with combination dasatinib and cetuximab therapy in kras wild-type cell lines. *Ex vivo* validation studies showed a correlation between EGFR expression and ^{89}Zr-cetuximab uptake.

In the final aim found in Chapter 4, titled “Using immunoPET to monitor tumor response to immunotherapy”, the ability for ^{89}Zr-labeled anti-IFNγ (^{89}Zr-anti-IFNγ) was evaluated to visualize changes in tumor uptake after a HER2/neu DNA vaccine that induces an active T-cell response against rat neu antigen. In transgenic mice and mice bearing syngeneic tumors, a significant increase was observed in ^{89}Zr-anti-IFNγ uptake within the tumor after vaccination, with a low uptake in secondary lymphoid organs (spleen, lymph nodes). Further validation indicated that this was due to an increase in

IFN-γ production and CD8 T-cell infiltrates within the tumor.

As is pertains to this thesis, ways to monitor response to targeted therapy and immunotherapies are warranted. These results will provide fundamental insights into the biology of the tumor microenvironment for further refinement of treatment strategies and combinations.

CHAPTER 2: MONITORING SRC STATUS AFTER DASATINIB TREATMENT IN HER2+ BREAST CANCER WITH ^{89}ZR-TRASTUZUMAB PET IMAGING

This chapter was adapted in full from “Monitoring Src status after dasatinib treatment in HER2+ BC with ^{89}Zr-trastuzumab PET imaging” by Brooke McKnight and Nerissa T. Viola-Villegas, originally published in Breast Cancer Research and used with their permission.

2.1 INTRODUCTION

The human epidermal growth factor receptor 2 (HER2) has become a critical therapeutic target with trastuzumab (Herceptin®) as the mainstream, first-in-line standard of care in HER2-positive BC patients(215,216). Unfortunately, response rates to HER2-targeted therapy remain dismal due to acquired and *de novo* resistance, which in part, can be attributed to alterations in receptor tyrosine kinases (RTKs)(189), and downstream signaling transduction pathways, such as Src(217,218).

Src is a non-receptor tyrosine kinase expressed ubiquitously that interacts with several RTKs(158). Its activation enhances cellular migration and survival(149). It has been shown that the hyperactivation of Src leads to HER2 stabilization and vice versa(157), establishing a functional relationship between the two oncogenes(157). This was reported in a study by Tan et al. wherein Src abrogation concomitantly led to decreased HER2 levels within 7-14 days of treatment with a Src inhibitor, PP2 *in vitro*(157). Thus, Src is implicated as a key molecule in resistance to trastuzumab therapy, making this signaling axis an attractive target for inhibition.

Dasatinib (Sprycel®) is a Src and BCR/ABL tyrosine kinase inhibitor and was FDA-approved for leukemia in 2006(219). Preclinical data reported by Seoane et al. demonstrated the synergistic effects of dasatinib with trastuzumab as evidenced by

attenuated phosphorylated levels of Src, ERK and AKT in HER2+ BC(220). These preclinical findings were validated in a prospective phase I-II trial exploring combinatorial efficacy and safety of dasatinib, trastuzumab and paclitaxel in patients with BC(221). Monitoring of tumor response to this drug cocktail was conducted through immunohistochemistry (IHC) analysis of patients' skin samples. However, better ways to non-invasively monitor tumor response can be achieved by exploring the direct causal relationship between HER2 and Src.

In this study, the potential of ^{89}Zr ($t_{1/2}$ ~ 3.27 d) labeled trastuzumab was investigated as a surrogate tool to monitor biologic effects of dasatinib (Sprycel) treatment in HER2+ BC. First evaluation the specificity of ^{89}Zr- trastuzumab in BT-474 (HER2+/ER+/PR-), JIMT-1 (HER2+, trastuzumab resistant), and MDA-MB-468 (triple negative) cell lines was evaluated with its ability to resolve changes in HER2 expression during dasatinib treatment. Next, the utility of ^{18}F-FDG and ^{89}Zr-trastuzumab as a predictive imaging tool was examined using the same group of mice-bearing BT-474 and JIMT-1 tumors treated with dasatinib. After imaging, HER2 PET uptake was correlated to changes in tumor volume, immunoblots, and immunohistochemistry.

2.2 RESULTS

2.2.1 Characterization of ^{89}Zr-trastuzumab

Radiolabeling yields of >95% were obtained with >97 % purity after purification via spin column. A specific activity of 2.98 ± 0.2 mCi/mg (20.9 ± 5.6 Bq/μmol) was established. The labeled antibody retained immunoreactivity towards HER2 with 85% retention (Figure 12**,** n = 3).

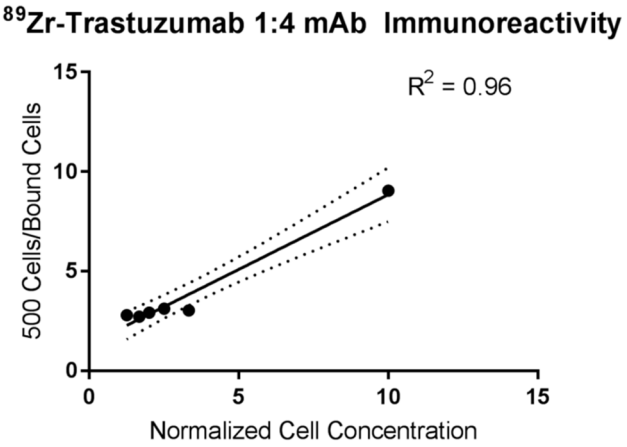

Figure 12. ^{89}Zr-trastuzumab retains immunoreactivity in BT-474. Immunoreactivity of ^{89}Zr-trastuzumab showed retained reactivity with r^2 = 0.96.

2.2.2 *In vitro* treatment studies with dasatinib

BT-474 (Fig. 13A) and JIMT-1 (Fig. 13B) cells were treated with increasing concentrations of dasatinib to achieve an IC_{50} value for 72 h post-treatment. IC_{50} value of 1.3 ± 0.12 μM and 0.22 ± 0.09 μM were achieved for BT-474 and JIMT-1 respectively. BT-474 and JIMT-1 cells were treated with dasatinib for 6-48 h and western blots were performed on treated and untreated cell lysates to observe protein expression. In BT-474 cells (Fig. 13C), there was no change in total HER2 or total Src protein expression upon treatment with dasatinib. After 6 h of exposure to dasatinib, total abrogation of pSrc (Y416, directly associated with dasatinib Src tyrosine kinase activity(222)) and pHER2 (Y1221/1222, autophosphorylation site) were observed. In JIMT-1 cells (Fig. 13D), attenuation of pHER2 (Y1221/1222) after 24 h and pSrc (Y416) activity after 6 h was displayed post-dasatinib treatment. There was no change in total HER2 or Src protein levels upon treatment as shown by densitometry.

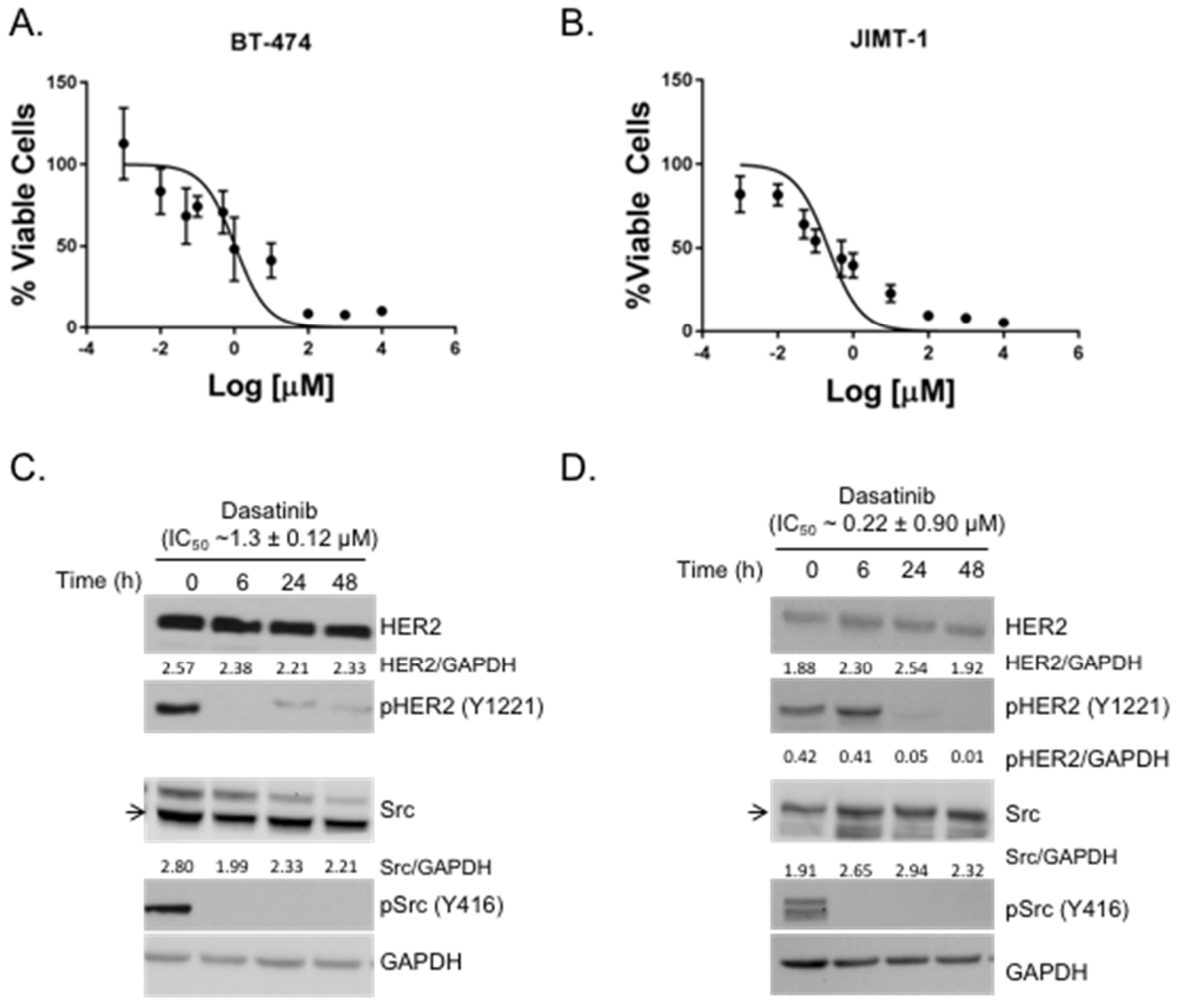

Figure 13. Dasatinib treatment decreases pSrc (Y416) and pHER2(Y-1221) protein levels in vitro. BT-474 (A) or JIMT-1 (B) cells were treated with increasing concentrations of dasatinib for 72 h to achieve IC_{50} values of 1.3 ± 0.12 μM and 0.8 ± 0.02 μM, respectively. BT-474 cells (C) and JIMT-1 (D) were treated with IC_{50} dasatinib up to 48 h and western blots were performed for HER2, Src, pSrc (Y416), and pHER2 (Y1221/1222). Densitometry results are shown as the ratio of target protein/GAPDH.

Next, the ability of HER2 to internalize trastuzumab after dasatinib timecourse treatment was investigated using ^{89}Zr-trastuzumab (Fig. 14). A steady decrease in ^{89}Zr-trastuzumab internalization was exhibited by both BT-474 and JIMT-1. Internalization of ^{89}Zr-trastuzumab in untreated BT-474 was measured at 10.37 ± 1.62% without dasatinib treatment, however, internalized fractions decreased after 6 h and 24 h of dasatinib

treatment with ~7.68 ± 0.53% ($p = 0.02$), and 7.42 ± 0.74% ($p = 0.03$) respectively. At 48 h, only ~4.78 ± 0.42% ($p = 0.006$) of the radiotracer was found intracellularly. JIMT-1 cells also showed a decrease in internalization upon treatment. From 2.6 ± 0.25% internalized in untreated cells, bound activity was reduced to 1.22 ± 0.10% ($p = 0.009$) after 24 h, and 0.17 ± 0.5% ($p < 0.0001$) after 48 h of treatment. No significant reduction in internalized radiotracer was observed after 6 h of dasatinib exposure (1.96 ± 0.46%, $p = 0.10$).

These results are similar to the amount of total membrane-bound HER2 present extracellularly (and thus, available for tracer targeting) during dasatinib treatment as represented by the total amount of ^{89}Zr-trastuzumab bound (Fig. 14). Compared to untreated BT-474 cells with 14.10 ± 1.22% bound radiotracer, a decrease was observed in treated groups after dasatinib exposure for 6 h (11.79 ± 1.00%, $p = 0.0854$) and 24 h (11.42 ± 2.04%, $p = 0.038$). Further reduction was observed after 48 h with 8.88 ± 1.44% ($p = 0.0002$). In JIMT-1 cells, a similar trend was observed with lower ^{89}Zr-trastuzumab binding in groups treated for 6 h (2.46 ± 1.02%, $p = 0.9578$), 24 h (1.26 ± 1.00%, $p = 0.2075$) and 48 h (0.34 ± 0.21%, 0.0277) relative to untreated cells at 3.16 ± 0.50%.

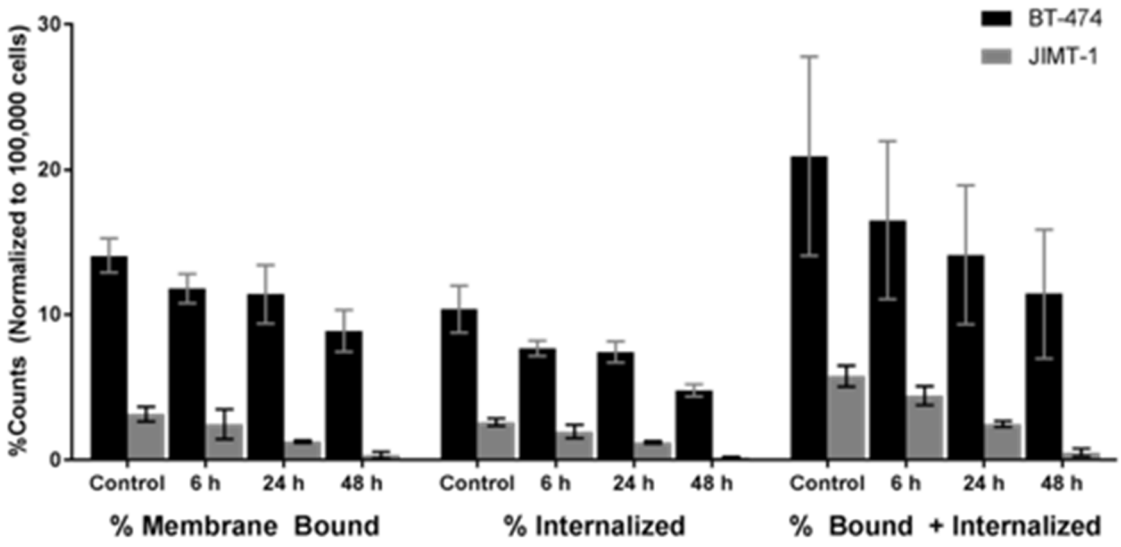

Figure 14. ^{89}Zr-trastuzumab binding and uptake decreases upon dasatinib treatment. Internalization and binding assays of ^{89}Zr-trastuzumab on BT-474 and JIMT-1 cells treated with dasatinib IC_{50} from 0-48 h showed a decrease in probe internalization and binding over time

These results are in good agreement with the western blot findings. In BT-474, an abrogation of pHER2(Y1221/1222) was observed after 6 h dasatinib treatment. Coupled with the internalization assays, the same decrease in tracer internalization was observed after 6 h. Similarly, in JIMT-1, a decrease in pHER2 after 24 h dasatinib treatment was observed, which is where drop off in internalization of the tracer occurs. These results suggest that there is an association between dasatinib treatment and a decrease in internalization, which results in a reduction in total cellular accumulation (^{89}Zr-trastuzumab %bound + internalized).

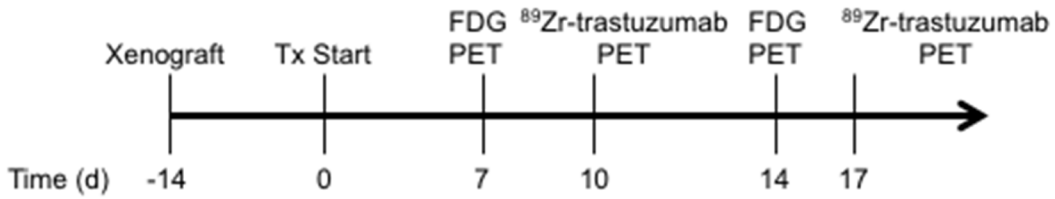

Figure 15. ^{89}Zr-trastuzumab binding and uptake decreases upon dasatinib treatment. Treatment and imaging scheme illustrate treatment of tumors for 7 d and/or 14 d with dasatinib followed by PET imaging with ^{18}F-FDG. ^{89}Zr-trastuzumab was administered a day after with imaging acquired 48 h p.i. Tx = Treatment.

2.2.3 Validation of ^{89}Zr-trastuzumab specificity to HER2

From *in vitro* studies using BT-474 (HER2+/ER+), JIMT-1 (HER2+/ER-), and MDA-MB-468 (HER2-/ER+) cells, co-administration of 25-fold unlabeled trastuzumab exhibited lower binding of ^{89}Zr-trastuzumab in HER2+ cell lines and did not change binding in MDA-MB-468 HER2- cell line (Fig. 16A). In BT-474, there was a 6-fold decrease of ^{89}Zr-trastuzumab binding in trastuzumab blocked cells compared to control (1.07 ± 0.24% vs. 6.64 ± 1.14%, $p < 0.0001$). JIMT-1 cells exhibited a 2-fold decrease in ^{89}Zr-trastuzumab binding in 25-fold trastuzumab blocked cells compared to control (0.65 ± 0.18 vs. 1.46 ± 0.24, $p = 0.0007$). MDA-MB-468 cells did not exhibit a difference in ^{89}Zr-trastuzumab binding between 25-fold blocked cells and control (0.71 ± 0.40 vs. 1.11 ± 0.56, $p = 0.34$).

Mice bearing BT-474, JIMT-1, or MDA-MB-468 xenografts were imaged with ^{89}Zr-trastuzumab at 48 h p.i. (Fig. 16B-C). MDA-MB-468 tumors exhibited the lowest uptake of 3.9 ± 0.6 %ID/g, compared to BT-474 (17.9 ± 2.2 %ID/g, $p < 0.001$) and JIMT-1 (7.7 ± 0.6 %ID/g, $p < 0.001$) tumors. Interestingly, there was significantly less ^{89}Zr-trastuzumab uptake in JIMT-1 tumors compared to BT-474 ($p < 0.0001$).

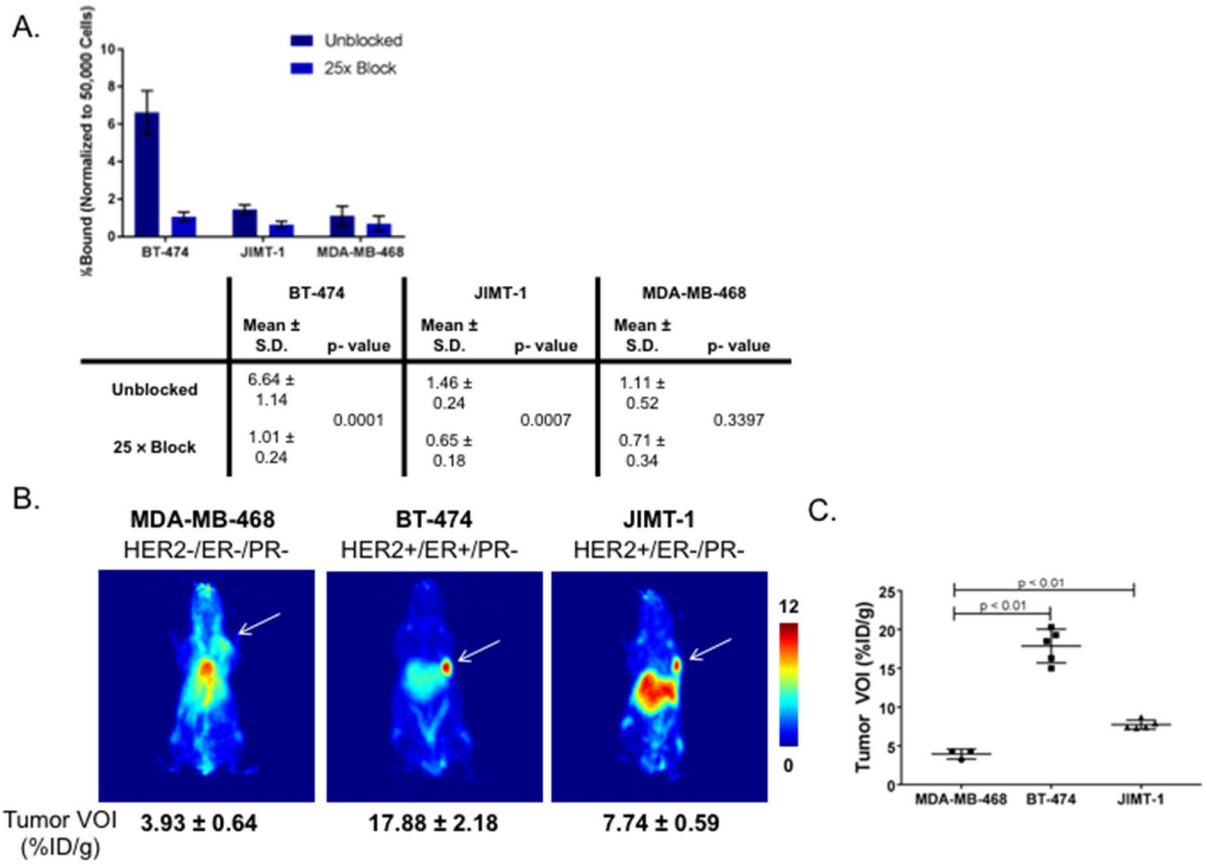

	BT-474		JIMT-1		MDA-MB-468	
	Mean ± S.D.	p- value	Mean ± S.D.	p- value	Mean ± S.D.	p- value
Unblocked	6.64 ± 1.14	0.0001	1.46 ± 0.24	0.0007	1.11 ± 0.52	0.3397
25 × Block	1.01 ± 0.24		0.65 ± 0.18		0.71 ± 0.34	

Figure 16. ^{89}Zr-trastuzumab is specific for HER2. BT-474, JIMT-1, and MDA-MB-468 cells were incubated with 100 ng ^{89}Zr-trastuzumab alone or co-incubated with 25-fold unlabeled Trastuzumab before being lysed and radioactivity measured using a gamma counter (A); nude mice bearing MDA-MB-468, BT-474, or JIMT-1 tumors were imaged with ^{89}Zr-trastuzumab 48 h p.i. (B); tumor ROIs showing significant uptake in HER2+ tumors, but no uptake in MDA-MB-468 HER2- tumors (C).

Tissue distribution addressed concerns against enhanced permeation retention (EPR) effect. In BT-474 tumor, ^{89}Zr-trastuzumab uptake in the tumor was 16.01 ± 3.78 %ID/g, which is significantly higher than an isotype-matched IgG control (1.02 ± 0.87 %ID/g, p = 0.0002) (Fig. 17, Table 10). ^{89}Zr-trastuzumab had an average tumor uptake of 4.13 ± 2.36 %ID/g (Fig. 17, Table 11) in JIMT-1 tumors, whereas the non-specific IgG control probe exhibited a significantly lower tumor accumulation of 0.79 ± 0.24 %ID/g (p = 0.0338).

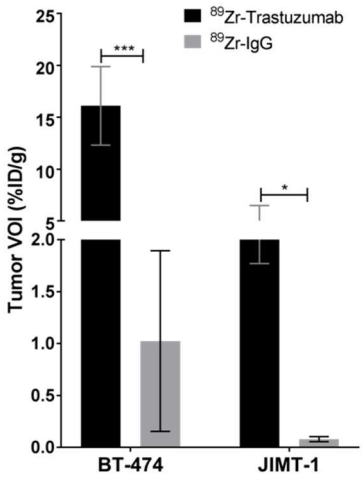

Figure 17. ^{89}Zr-trastuzumab tumor uptake compared to isotype matched control. Mice bearing BT-474 and JIMT-1 tumors were injected with ^{89}Zr-IgG or ^{89}Zr-trastuzumab and tumors were removed 48 h p.i. and measured using a gamma counter. In both cell lines, specific ^{89}Zr-trastuzumab uptake is significantly higher than isotype control IgG.

	^{89}Zr-trastuzumab			^{89}Zr-IgG		
	Mean		**S.D.**	**Mean**		**S.D.**
Blood	2.39	±	1.14	1.71	±	1.01
Tumor	16.10	±	3.79	1.02	±	0.87
Heart	3.17	±	1.43	0.50	±	0.21
Lungs	13.37	±	9.79	0.50	±	0.28
Liver	9.27	±	5.56	9.12	±	2.66
Kidneys	4.53	±	3.85	5.27	±	2.47
Stomach	1.86	±	1.23	0.59	±	0.30
Intestines	3.74	±	0.80	3.44	±	1.41
Spleen	8.15	±	3.75	0.54	±	0.35
Pancreas	1.76	±	1.20	0.21	±	0.20
Brain	0.25	±	0.29	0.15	±	0.04
Bone	10.34	±	3.26	0.03	±	0.01
Muscle	0.33	±	0.18	0.06	±	0.02

Table 10. ^{89}Zr-trastuzumab and ^{89}Zr-IgG biodistribution in BT-474 tumors.

	^{89}Zr-trastuzumab			^{89}Zr-IgG		
	Mean		**S.D.**	**Mean**		**S.D.**
Blood	6.69	±	2.53	1.23	±	0.65
Tumor	4.13	±	2.36	0.08	±	0.02
Heart	2.20	±	0.92	0.39	±	0.18
Lungs	3.01	±	2.25	0.65	±	0.44
Liver	4.70	±	1.46	9.43	±	6.96
Kidneys	4.49	±	1.28	5.10	±	1.59
Stomach	1.13	±	0.46	0.34	±	0.17
Intestines	3.79	±	1.07	3.08	±	0.35
Spleen	2.79	±	1.38	0.36	±	0.16
Pancreas	0.93	±	0.38	0.12	±	0.06
Brain	0.33	±	0.19	0.12	±	0.04
Bone	0.65	±	0.40	0.02	±	0.01
Muscle	0.33	±	0.17	0.04	±	0.04

Table 11. ^{89}Zr-trastuzumab ^{89}Zr-IgG biodistribution in JIMT-1 tumors.

2.2.4 *In vivo* monitoring of tumor response to dasatinib

Mice bearing palpable BT-474 tumors were dosed with dasatinib for 7 and 14 days and imaged with ^{18}F-FDG and ^{89}Zr-trastuzumab (Fig. 18). Tumor uptake of ^{18}F-FDG was not statistically different between untreated mice (3.60 ± 1.51% ID/g) and those treated with dasatinib for 7 d (3.86 ± 0.59 %ID/g, $p = 0.99$) and 14 d (4.63 ± 0.21 %ID/g, $p = 0.80$) (Fig. 19A). In comparison, ^{89}Zr-trastuzumab exhibited a significant decrease in tumor accumulation in both treated groups (7 d: 11.05 ± 2.10 %ID/g, $p < 0.0001$, and, 14 d: 9.2 ± 1.85 %ID/g, $p < 0.0001$) compared to untreated tumors (17.88 ± 2.18 %ID/g) (Fig. 19B).

No significant difference in probe uptake was observed between 7 and 14 d treated cohorts (p = 0.3925) (Fig. 19C). A correlation between changes in tumor volumes measured prior and after treatment vs. ^{89}Zr-trastuzumab VOI PET uptake displayed a significant positive correlation (r = 0.85, p = 0.001) (Fig. 19D) wherein a decrease in tumor volume matched a lower PET readout.

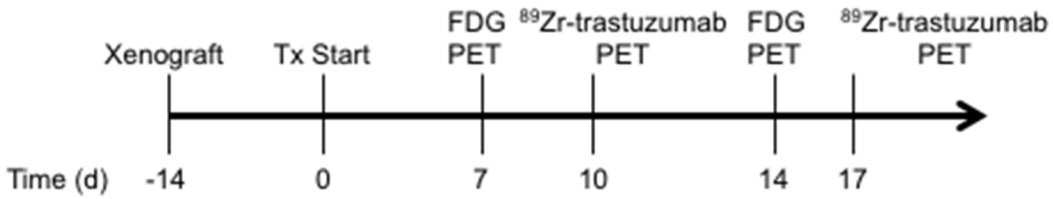

Figure 18. ^{89}Zr-trastuzumab binding and uptake decreases upon dasatinib treatment. Treatment and imaging scheme illustrates treatment of tumors for 7 d and/or 14 d with dasatinib followed by PET imaging with ^{18}F-FDG. ^{89}Zr-trastuzumab was administered a day after with imaging acquired 48 h p.i. (B). Tx = Treatment.

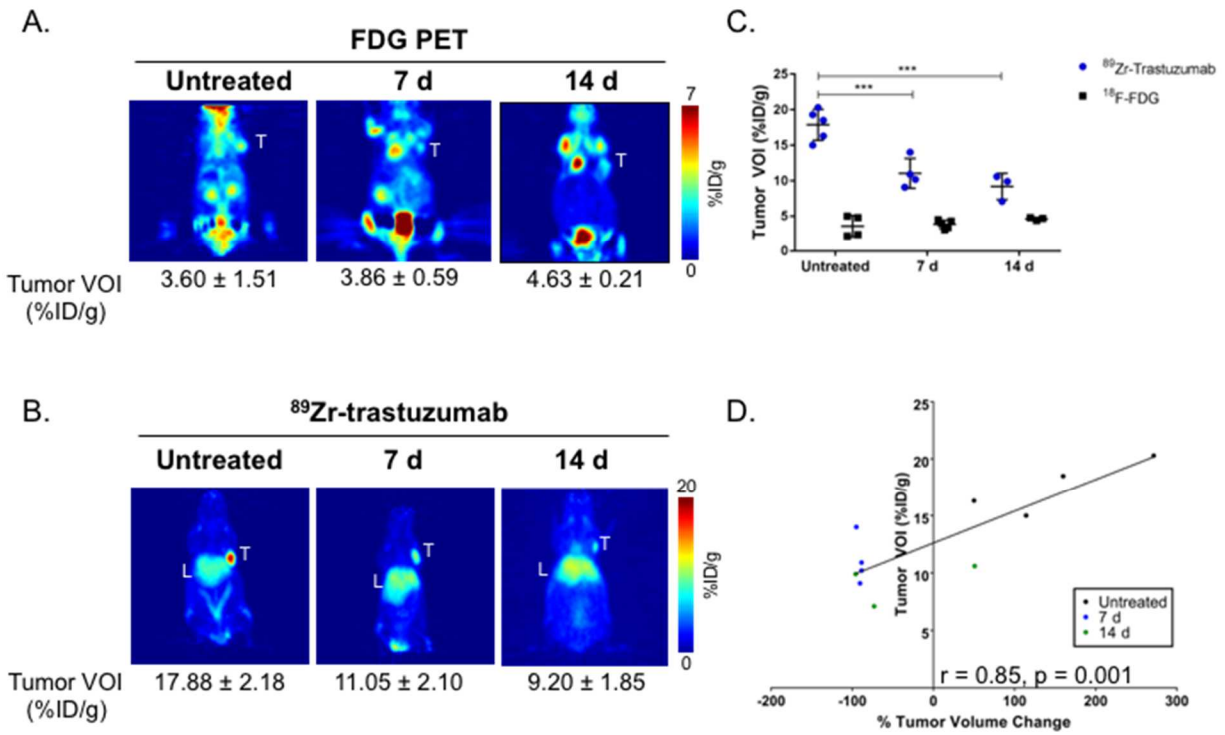

Figure 19. ^{89}Zr-trastuzumab PET imaging predicts tumor response to treatment in BT-474 xenografts. Untreated (left) and treated BT-474 tumors for 7 d (middle) or 14 d (right) with 75 mg/kg dasatinib were imaged with FDG-PET (A). In the same group of mice, PET imaging with ^{89}Zr-trastuzumab demonstrated attenuated tracer accumulation in treated groups compared to control (B). Tumor VOIs demonstrated lower tumor uptake of ^{89}Zr-trastuzumab in treated groups compared to control; no observed changes were detected by FDG in both control and treated groups (C). % change in tumor volume during treatment correlated with ^{89}Zr-trastuzumab uptake (D). T = tumor, L = liver. *** denotes $p < 0.001$.

In JIMT-1 tumor bearing mice, FDG-PET did not distinguish untreated tumors (3.81 ± 0.78 %ID/g) vs. dasatinib-treated groups (7d: 3.36 ± 0.89 %ID/g, $p = 0.7338$; 14 d: 3.20 ± 1.37 %ID/g, $p = 0.6126$) (Fig. 20A). Using the same mice, tumor uptake of ^{89}Zr-trastuzumab displayed VOIs of 8.04 ± 0.71 %ID/g for control; a two-fold decrease in uptake after 7 d (3.88 ± 1.47 %ID/g, $p < 0.0001$) and 14 d (4.45 ± 1.23 %ID/g, $p < 0.0001$) was observed during dasatinib treatment (Fig. 20B). Similar to BT-474 xenografts, there

was no observed difference in tracer accumulation observed between treated cohorts (p = 0.7120) (Fig. 20C). Changes in tumor volumes displayed a direct, positive correlation with ^{89}Zr-trastuzumab PET uptake (r = 0.82, p = 0.0002) (Fig. 20D).

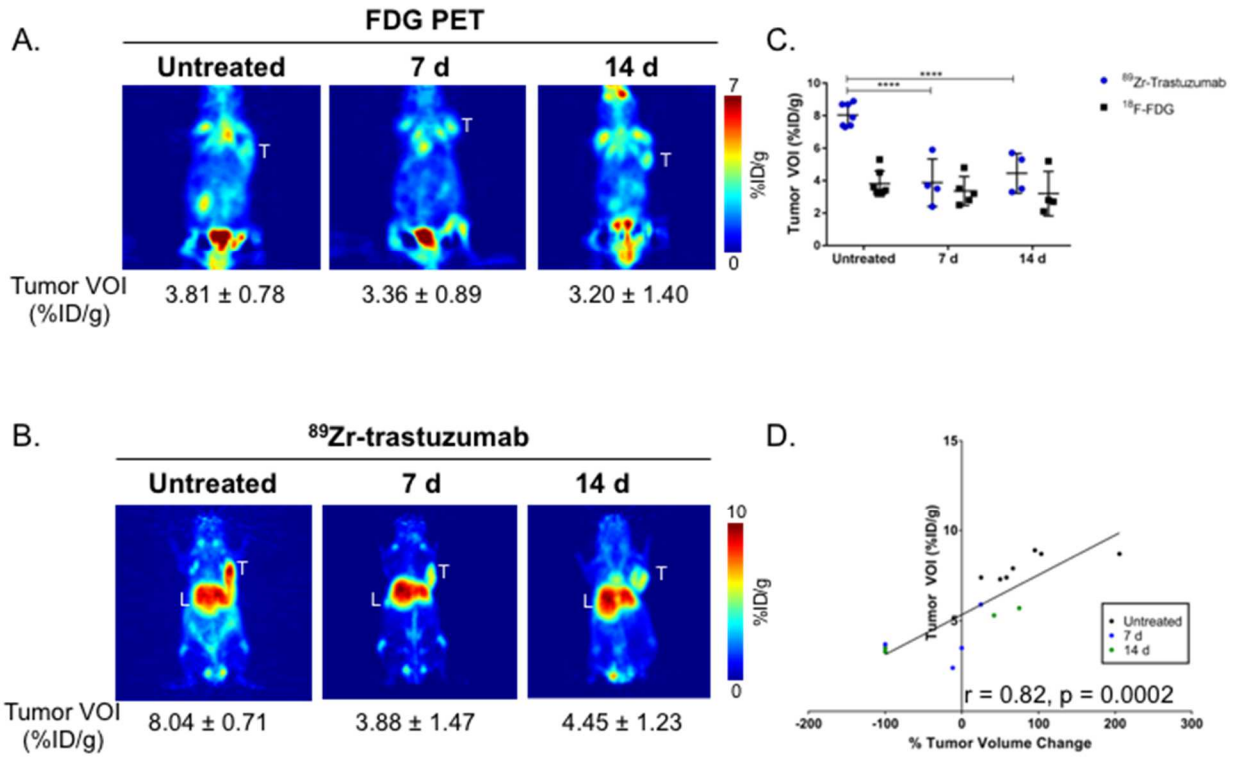

Figure 20. ^{89}Zr-trastuzumab PET imaging predicts tumor response to treatment in JIMT-1 xenografts. Untreated (left) and 7 d (middle) or 14 d (right) treated JIMT-1 tumors imaged with FDG (A). The same group of mice imaged with ^{89}Zr-trastuzumab after 48 h p.i. (B). VOIs drawn on the tumors displayed lower accumulation of ^{89}Zr-trastuzumab in treated groups compared to control but no change in FDG-PET tumor uptake was observed across all cohorts (C). % Change in tumor volume correlated with ^{89}Zr-trastuzumab uptake (D) T = tumor, L = liver. *** denotes p < 0.001.

2.2.5 *Ex Vivo* analysis of BT-474 and JIMT-1 Tumors

After imaging, tumors were removed for *ex vivo* validation of the PET readout. From the immunoblot analysis, BT474 tumors showed a moderate decrease in total Src levels upon treatment with dasatinib, whereas its activity was mitigated by 2.6-fold as displayed by pSrc (Y416) levels in both 7 and 14 d treated cohorts (Fig. 21A). Additionally,

there is a decrease in total HER2 via densitometry after 7 d and 14 d treatments (Fig. 21A). A positive correlation between pSrc (Y416) (r = 0.70, p = 0.025) (Fig. 21B) and pHER2 (r = 0.64, p = 0.046) (Fig. 21C) (measured by densitometry) against tumor VOI

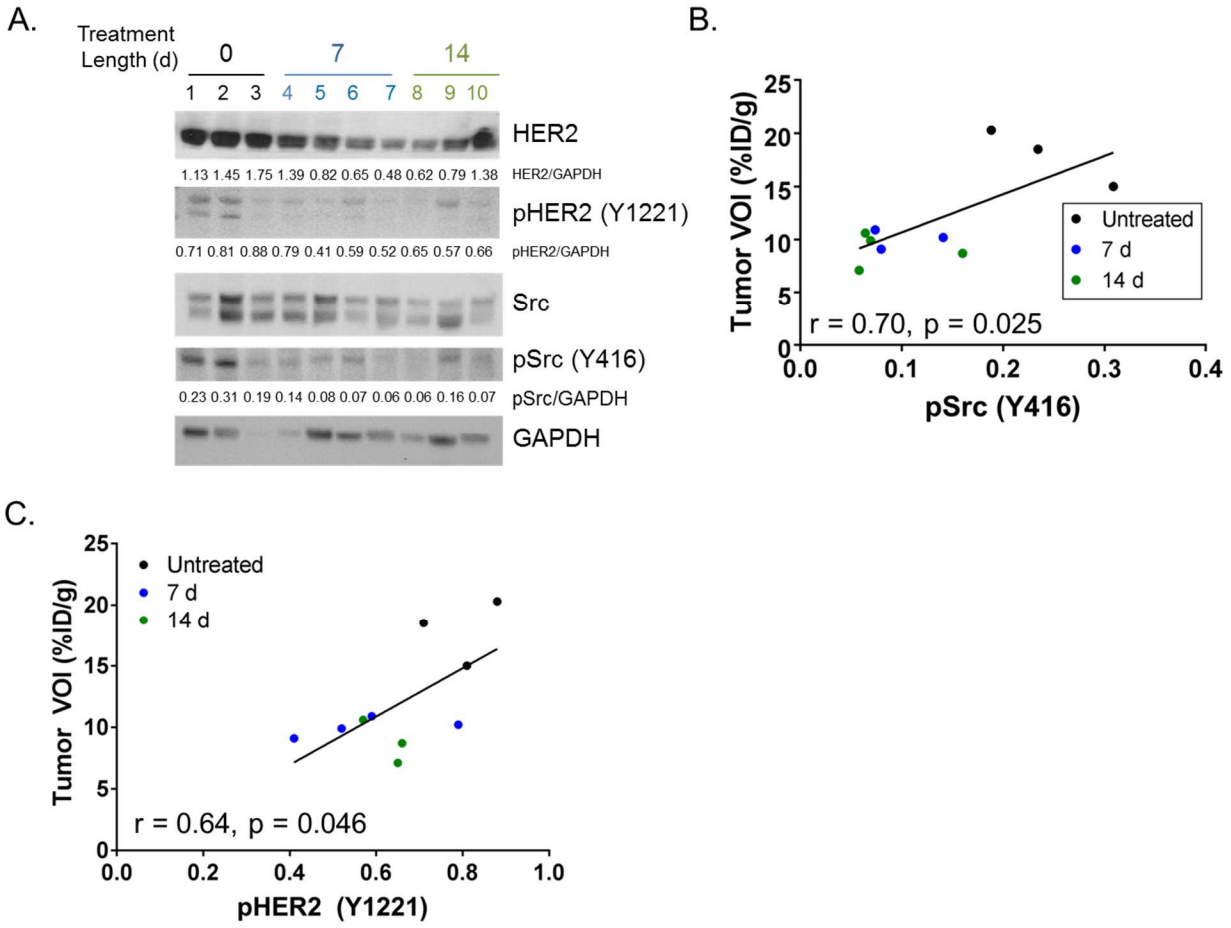

values for BT-474 was observed.

Figure 21. Ex vivo validation on excised BT-474 tumors confirm PET uptake. Western blots were performed for HER2, Src, and pSrc (Y416) expression using BT-474 tumor lysates (A); a plot of the pSrc (Y416) densitometry shows a linear relationship with ^{89}Zr-trastuzumab PET uptake (B); a plot of the pHER2 (Y1221) densitometry vs. tumor VOI shows a positive linear relationship with ^{89}Zr-trastuzumab PET uptake (C).

Treated and control JIMT-1 tumors did not show a difference in total HER2 or Src expression, however, a noticeable decrease in both pSrc and pHER2 after 7 and 14 d treatments was displayed (Fig. 22A). Moreover, a significant, positive association

between pSrc (Y416) (r = 0.68, p = 0.022) and ^{89}Zr-trastuzumab tumor VOI was achieved (Fig. 22B). A direct relationship between dephosphorylated HER2 and tracer uptake in the tumor was also demonstrated (r = 0.63, p = 0.037) (Fig. 22C).

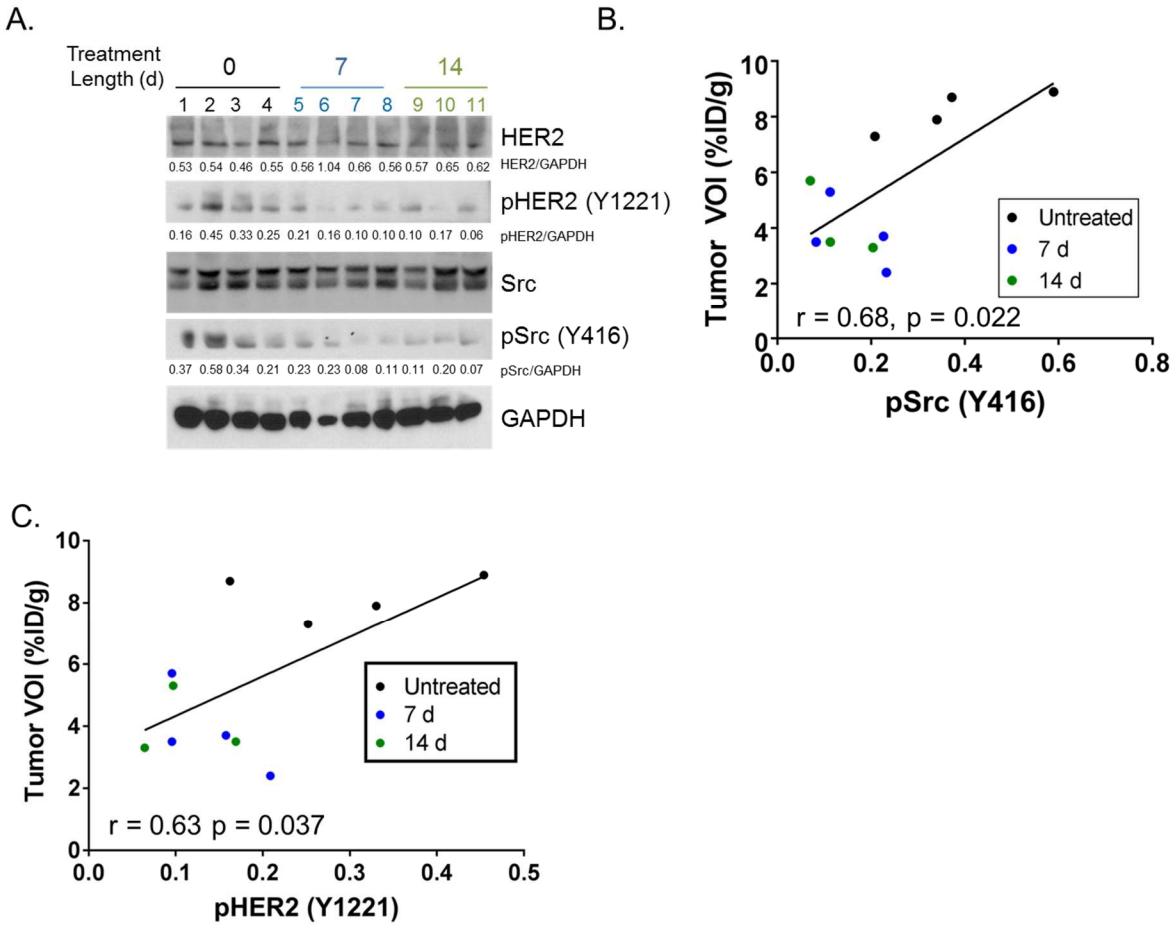

Figure 22. Ex vivo validation on excised JIMT-1 tumors confirm PET uptake. Western blots were performed for HER2, Src, and pSrc (Y416) expression using JIMT-1 tumor lysates (A); a plot of the pSrc (Y416) densitometry shows a linear relationship with ^{89}Zr-trastuzumab PET uptake (B); a plot of the pHER2 (Y1221) densitometry vs. tumor VOI shows a positive linear relationship with ^{89}Zr-trastuzumab PET uptake (C).

IHC was performed to visualize subcellular localization of HER2 and pSrc (Y416) in excised tumors. Unmodulated BT-474 tumors showed strong positive membranous HER2 staining (Fig. 23A, top left panel), whereas, predominant cytoplasmic HER2 localization was exhibited in tumors treated for 14 days with dasatinib. (Fig. 23A, top

right). Lower pSrc (Y416) staining was observed in treated tumors (Fig. 23A, bottom right) compared to control (Fig. 23A, bottom left). Control JIMT-1 tumors exhibited lower expression of membrane-localized HER2 (Fig. 23B, top left) compared to BT-474 but translocation to cytoplasmic regions was observed in treated sections (Fig. 23B, top right). Higher pSrc (Y416) staining is displayed in control (Fig. 23B, bottom right) versus dasatinib treated tumor sections (Fig. 23B, bottom left).

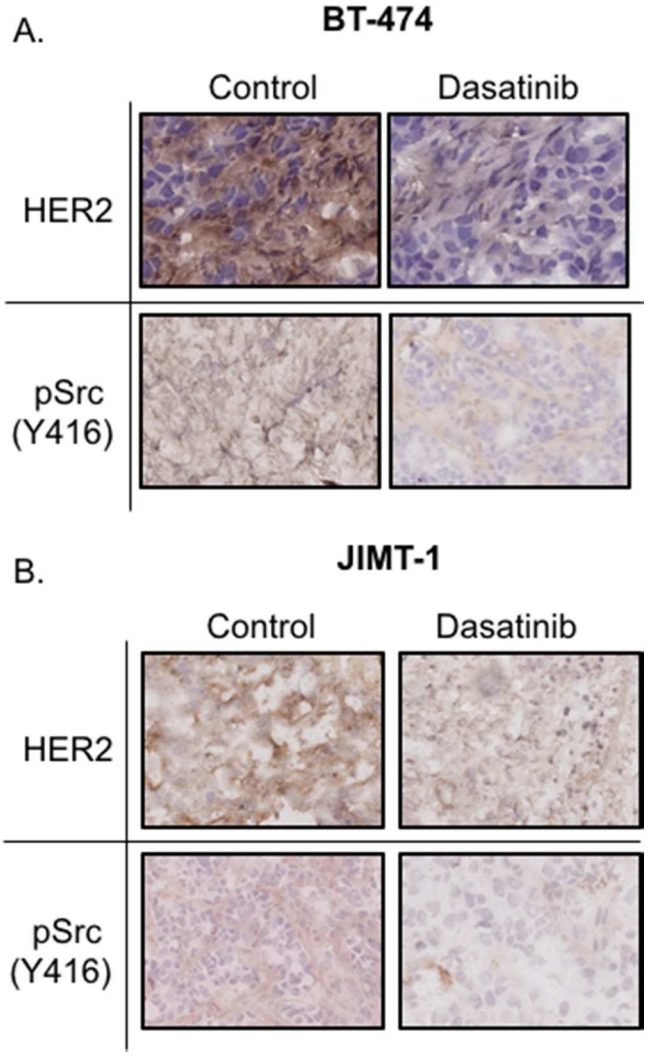

Figure 23. Immunohistochemistry on excised BT-474 and JIMT-1 tumors show HER2 and pSrc (Y416) changes. IHC (40× magnification) was performed on excised BT-474 tumors (A) and JIMT-1 (B) showing HER2 (top) and pSrc (Y416, bottom) expression with (right) and without (left) dasatinib treatment (A).

2.3 DISCUSSION

Trastuzumab has been the standard of care for two decades for HER2+ BC(134). Unfortunately, about half of patients with HER2-overxpressing BC do not respond to trastuzumab due to *de novo* and acquired resistance mechanisms(223). The non-receptor tyrosine kinase Src was shown to be a key modulator of trastuzumab response, and is an important downstream node of multiple trastuzumab resistance pathways(149,158,218,223,224). Targeting Src with dasatinib *in vitro* re-sensitized trastuzumab-resistant cell lines, suggesting this pathway as a strategy to overcome resistance(158). Additionally, patients with high levels of phosphorylation of Src at the Y416 residue have presented a lower clinical response rate and higher progressive disease after trastuzumab treatment, compared to those with lower pSrc (Y416) levels, suggesting that pSrc activation is correlated with trastuzumab resistance(225).

Clinical trials (NCT01306942, NCT00566618, and NCT00820170) are currently examining dasatinib as part of a multicombinatorial treatment in BC. Previous studies have focused on monitoring dasatinib response by radiolabeling dasatinib itself(226). This method has its limitations, since this can potentially miss functional effects upstream or downstream of the Src signaling pathway. Previous studies have demonstrated the relationship of Src and HER2 where it is shown that hyperactivated Src is stabilized by aberrant HER2 signaling, and one study in particular demonstrated that modulating c-Src with PP2 *in vitro* decreased HER2 levels after 7 days of treatment and abrogated it completely after 14 days of treatment(157,227). Thus, HER2 PET as a surrogate predictive marker of dasatinib treatment is worth investigating with ^{89}Zr-trastuzumab PET imaging currently in patient trials not only for HER2+ tumor detection(228) but as a marker

of response to other targeted treatment (NCT01081600 for AUY922 HSP90 inhibitor, NCT01565200 for T-DM1).

Previous studies have stated that using ^{89}Zr-trastuzumab PET imaging to monitor response to therapy would only be feasible if the drug is directly acting on HER2(59). Using ^{89}Zr-trastuzumab as a surrogate marker of targeted inhibition of effector molecules downstream of the HER2 signaling pathway has been conceptually proven, for example with Hsp90 inhibition(37). To the best of our knowledge, this is the first study that demonstrated the potential of ^{89}Zr-trastuzumab PET to monitor Src response to dasatinib treatment. Specifically, we have shown that ^{89}Zr-trastuzumab detects lower membrane HER2 expression with concomitant internalization of HER2 after 6 h (BT-474) or 48 h (JIMT-1) dasatinib treatment, as shown by our internalization assays. The lower internalization was coupled with a lower total HER2 present on the cell surface, confirmed by ^{89}Zr-trastuzumab binding experiments and western blots of pHER2(Y1221/1222), which activates HER2 receptor activation. From our *in vivo studies,* ^{89}Zr-trastuzumab detected changes in HER2 expression upon inhibition of functional Src, where standard-of-care FDG-PET imaging has failed to detect differences in tumor uptake after dasatinib treatment. Importantly, the PET uptake directly correlated with tumor regression. The PET results were histologically validated with a concomitant decrease in membranous HER2 staining in treated groups coupled with the abrogation of pSrc (Y416) staining. Furthermore, western blot analysis probing for functional Src activity exhibited a direct relationship with the HER2 PET readout. It is worth noting that our studies are limited to single agent Src inhibition; the utility of HER2 PET in combinatorial therapies including

Src in HER2+ BC still warrants further investigation.

In conclusion, ^{89}Zr-trastuzumab can potentially delineate changes in Src activity in HER2+ BC in both trastuzumab-sensitive and resistant phenotypes.

CHAPTER 3: USING ^{89}ZR-CETUXIMAB PET IMAGING TO VISUALIZE MEMBRANE EGFR EXPRESSION FOLLOWING DASATINIB TREATMENT IN TNBC

3.1 INTRODUCTION

TNBC accounts for 20% of all diagnosed BC and lack of therapeutic targets (ER/PR/HER2) makes it more difficult to treat, resulting in chemotherapies such as taxane or anthracycline as the mainstay standard of care(229). While many TNBC patients initially respond to chemotherapy, the high rate of recurrence and progression makes it a far more aggressive disease with worse prognosis compared to other subtypes.

Gene expression profiling studies identified EGFR as a potential biomarker indicating possible treatments due to its overexpression in TNBC(230,231). A number of EGFR-targeted therapies that were previously approved for other cancer types are currently explored for TNBC, including monoclonal antibodies (panitumumab and cetuximab) and small molecule inhibitors (gefitinib, erlotinib, and afatinib)(232). Unfortunately, achieving significant response rates in the clinic were dismal(233,234) possibly due to the lack of biomarkers to select appropriate patients who would be predited to respond. One explanation may be attributed to the receptor's nuclear translocation, diminishing drug targeted delivery to cell-surface receptors. nEGFR acts as a transcription factor regulator involved in tumorigenesis(235,236). Interestingly, the expression of nEGFR has been correlated with poorer outcomes in many cancers(82,237,238), and resistance to anti-EGFR therapies, including cetuximab(168,239). Previous studies have shown that Src Family Kinase (SFK) inhibition with dasatinib blocks nEGFR translocation, transporting EGFR to the plasma membrane; thus, enhancing cetuximab sensitivity in TNBC and non-small cell lung cancer

(168,239,240).

Studies developing ^{89}Zr($t_{1/2}$ ~ 3.27 d) labeled cetuximab (Erbitux®) as a positron emission tomography (PET) tracer have been reported. This EGFR-specific imaging probe is currently in clinical trials to select cancer patients who may benefit from cetuximab treatment in many cancer types(241–243). To date, ^{89}Zr-cetuximab has shown promise in visualizing tumors expressing EGFR, and could be used to monitor EGFR receptor expression and steer individualized treatments(244).

In this aim, it was hypothesized that ^{89}Zr-cetuximab could be used as a tool to monitor membrane EGFR expression after dasatinib treatment in TNBC. ^{89}Zr-cetuximab specificity was evaluated in EGFR-positive TNBC cell lines MDA-MB-231 (KRAS mutant) and MDA-MB-468 (KRAS wild type (wt)) and was compared against low EGFR-expressing TNBC MDA-MB-453 (KRAS mutant) cells. After establishing the tracer's specificity, its potential to assess changes in membranous EGFR density was investigated in both EGFR-positive TNBC xenografts post-treatment with dasatinib through *in vitro* internalization assays and western blots. An EGFR-positive, Kras wt TNBC patient derived xenograft (PDX, JAX TM-00089) was also investigated for *ex vivo* treatment studies. Validation of ^{89}Zr-cetuximab PET was conducted using western blots, immunohistochemistry (IHC) and autoradiography.

3.2 RESULTS

3.2.1 Radiolabeling and characterization of ^{89}Zr-cetuximab

^{89}Zr-cetuximab radiolabeling yields of >90% were obtained with >95% purity after purification via spin column. A specific activity of 4.7 ± 0.3 mCi/mg was established. The

labeled antibody retained immunoreactivity towards EGFR with 74.8 ± 3.4% (Fig. 24) n=3).

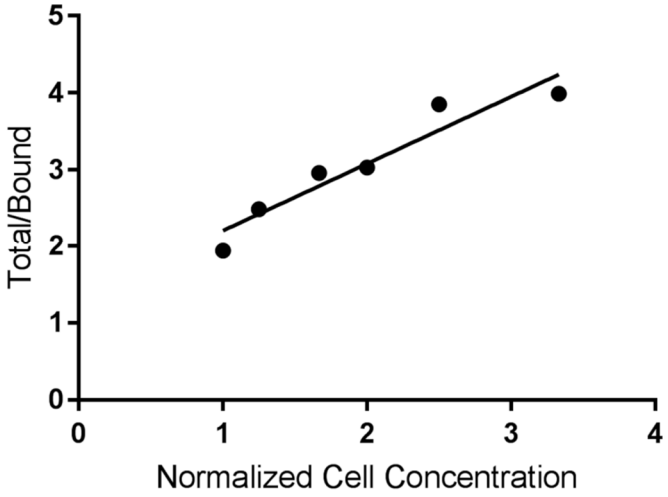

Figure 24. ^{89}Zr-cetuximab retains immunoreactivity in MDA-MB-468. A Lindmo assay was performed to measure immunoreactivity of ^{89}Zr-cetuximab after modifications and shows retained reactivity towards EGFR.

The potential of ^{89}Zr-cetuximab was investigated to assess changes in membranous EGFR levels was examined. Using the same treatment scheme, treated and untreated cells were incubated with ^{89}Zr-cetuximab at 4 °C to prevent internalization. Surface-bound activity increased for both MDA-MB-231 (17.9 ± 3.6% vs. 26.0 ± 3.0%, p = 0.042) and MDA-MB-468 (18.9 ± 0.6% vs. 47.3 ± 3.8 %, p = 0.0002) after dasatinib treatment (Fig. 25A).

Internalization rates of ^{89}Zr-cetuximab after dasatinib treatment were investigated over time and compared against membrane bound fractions (Fig. 25B). An increase in internalization of the tracer after 48 h of drug treatment compared to control was observed in MDA-MB-231 cells (16.6 ± 3.3% vs. 26.2 ± 3.7%, p = 0.0002). Similar but more pronounced effects were observed in treated MDA-MB-468 cells where internalized fractions were higher by 1.5-fold (27.7 ± 3.33%, p = 0.0098) and three-fold (42.6 ± 4.39%,

$p < 0.0001$) at 24 h and 48 h respectively, compared to control groups (17.9 ± 0.8%). Membrane-bound activity for both cell lines did not show a significant difference between control and treated groups likely due to internalization. The low-EGFR expressing MDA-MB-453 demonstrated minimal binding and internalization of the tracer. Collectively, this *in vitro* binding assay suggests that the radiotracer was able to measure higher membrane-localized EGFR levels after blockade of Src activity.

A.

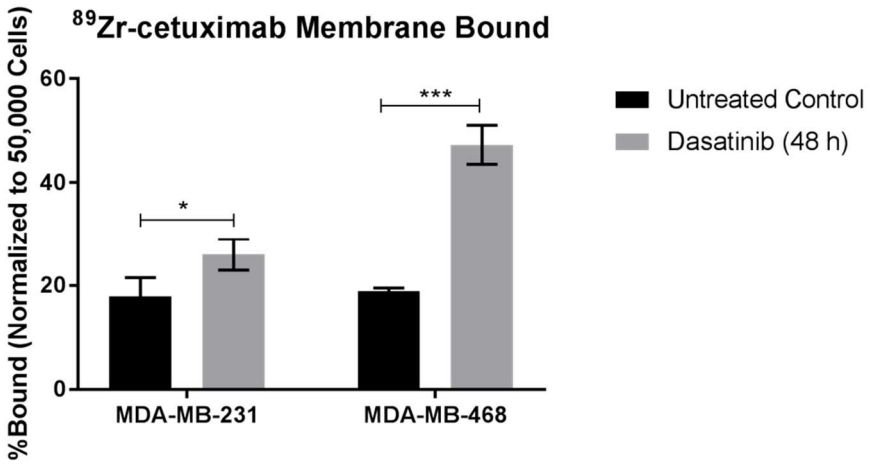

B.

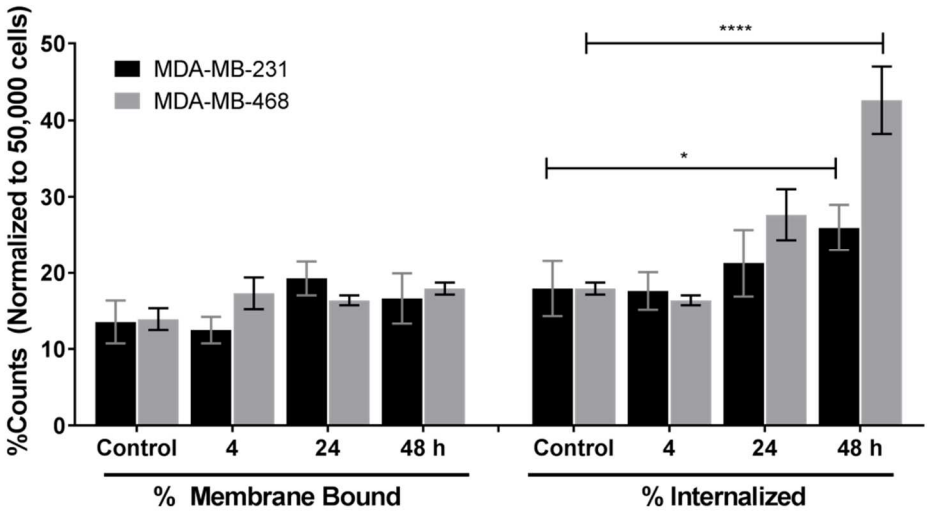

Figure 25. Internalization and uptake of ^{89}Zr-cetuximab. MDA-MB-231 and MDA-MB-468 cells exposed to dasatinib for 48 h showed higher surface-bound ^{89}Zr-cetuximab compared to untreated controls (A); incubation from 8-48 h with dasatinib showed higher internalized fractions of the tracer at later time points (B). * denotes $p < 0.05$, *** denotes $p < 0.001$.

The low-EGFR expressing MDA-MB-453 demonstrated minimal binding and internalization of the tracer (Fig. 26). This suggests that exposure to dasatinib resulted in higher membrane-bound EGFR levels available, which can be visualized and quantified by ^{89}Zr-cetuximab. Importantly, an increase in cell surface EGFR concomitantly leads to higher receptors available for drug delivery.

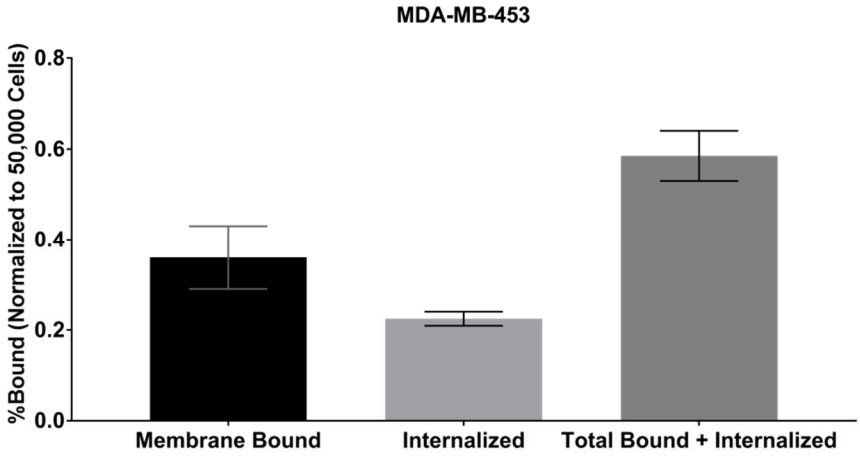

	%Membrane Bound (mean ± S.D.)	p-value	%Internalized (mean ± S.D.)	p-value	%Total + Bound (mean ± S.D.)	p-value
MDA-MB-231	17.92 ± 3.6	0.001	16.6 ± 3.3	0.001	36.8 ± 3.9	<0.001
MDA-MB-468	18.92 ± 0.6	<0.001	17.93 ± 0.8	<0.001	34.6 ± 3.6	<0.001
MDA-MB-453	0.36 ± 0.1		0.22 ± 0.02		0.59 ± 0.1	

Figure 26. Non-specific tracer uptake in MDA-MB-453. In vitro ^{89}Zr-cetuximab internalization in MDA-MB-453 cells (A). Comparison of ^{89}Zr-cetuximab tracer % bound, internalized, and total tracer bound and internalized between MDA-MB-231, MDA-MB-468, and MDA-MB453 cell lines (B).

3.2.2 ^{89}Zr-cetuximab is specific for tumors expressing EGFR *in vivo*

The specificity of ^{89}Zr-cetuximab for EGFR was investigated through *in vivo* imaging using mice bearing different EGFR-expressing TNBC tumors (MDA-MB-468 = MDA-MB-231 > MDA-MB-453). In MDA-MB-231, tumor uptake was 6.8 ± 1.0 %ID/g at 24 h p.i. and 7.0 ± 0.4 %ID/g at 48 h p.i. Tumor accumulation plateaued at 96 h with 8.7 ±

2.9 %ID/g (Fig. 27A,C). In MDA-MB-468 xenografts, tumor uptake was 7.8 ± 1.3 %ID/g at 24 h p.i., 7.6 ± 1.7 %ID/g at 48 h p.i. and 6.8 ± 1.2 %ID/g at 96 h p.i. (Fig. 27B-C). At 48 h p.i., the optimal time where tumor-to-background was identified, the accumulation of ^{89}Zr-cetuximab was significantly lower in this control tumor compared to MDA-MB-231 (6.7 ± 0.4 %ID/g, $p < 0.0001$) and MDA-MB-468 (7.6 ± 1.7 %ID/g, $p = 0.0012$) (Fig. 27D).

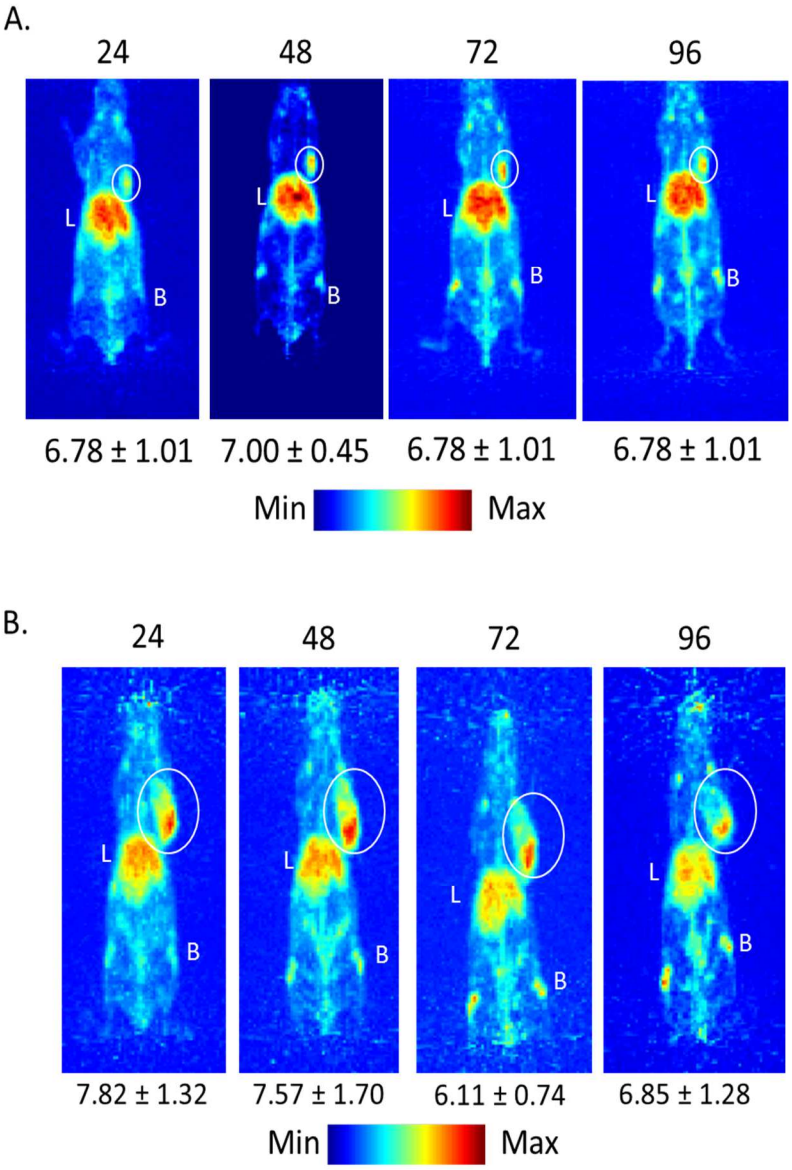

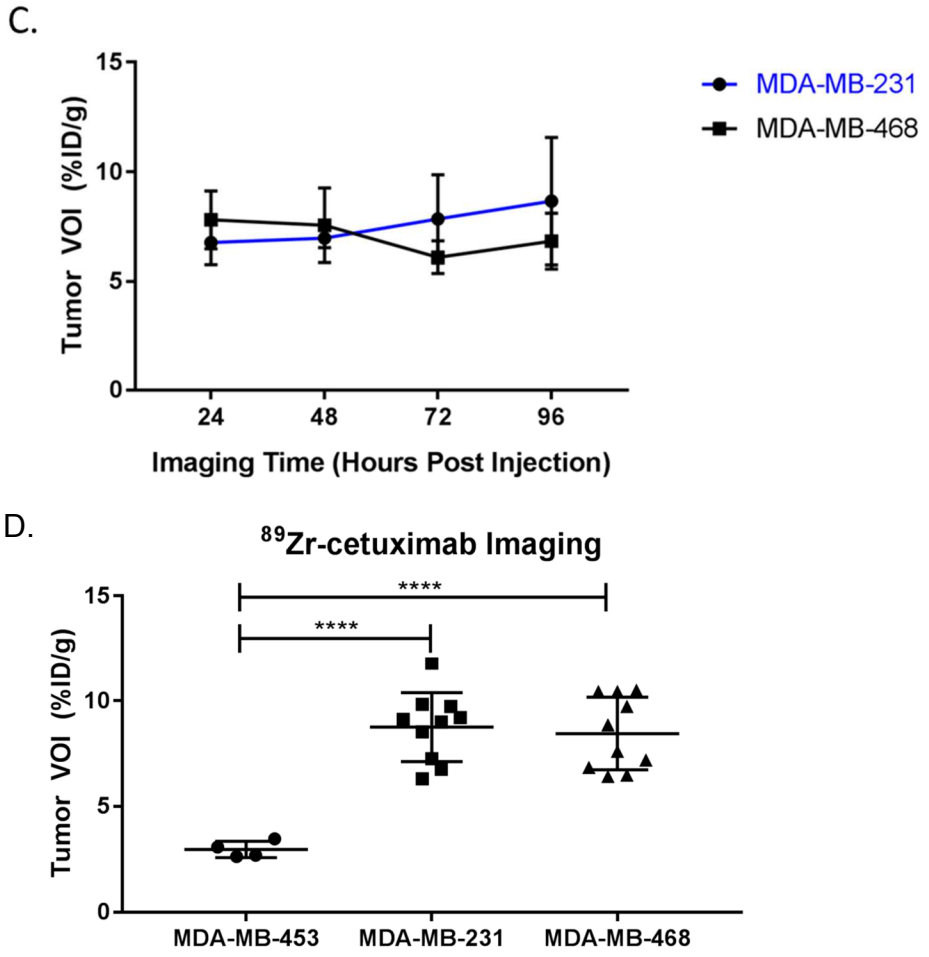

Figure 27. In vitro timecourse imaging of ^{89}Zr-cetuximab in MDA-MB-231 and MDA-MB-468 xenografts. Female nude mice bearing MDA-MB-231 tumors were injected with ^{89}Zr-cetuximab and imaged from 24-96 h p.i. and tumor VOIs were measured (A). Female nude mice bearing MDA-MB-468 tumors were injected with ^{89}Zr-cetuximab and imaged from 24-96 h p.i. and tumor VOIs were measured (B). Tumor time activity curve demonstrating tumor VOIs throughout imaging time in both cell lines (C). ^{89}Zr-cetuximab imaging tumor VOIs in MDA-MB-231 and MDA-MB-468 tumor bearing mice (D). *** denotes $p < 0.001$.

3.2.3 EGFR expression after dasatinib treatment *in vitro*

The half maximal inhibitory concentration (IC_{50}) values of 0.88 ± 0.10 μM (Fig. 28A) and 19.3 ± 0.06 μM (Fig. 28B) were achieved for MDA-MB-231 and MDA-MB-468 cells, respectively.

A.

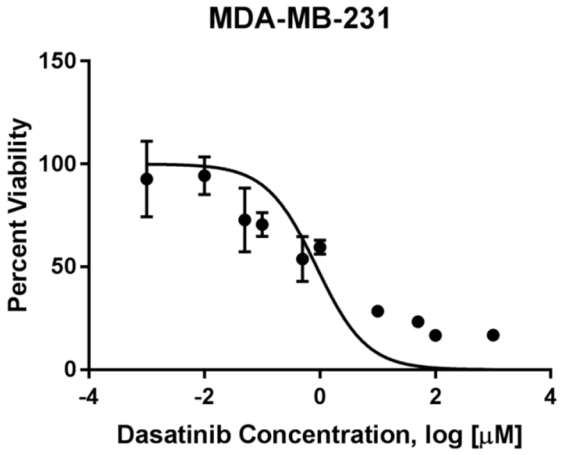

B.

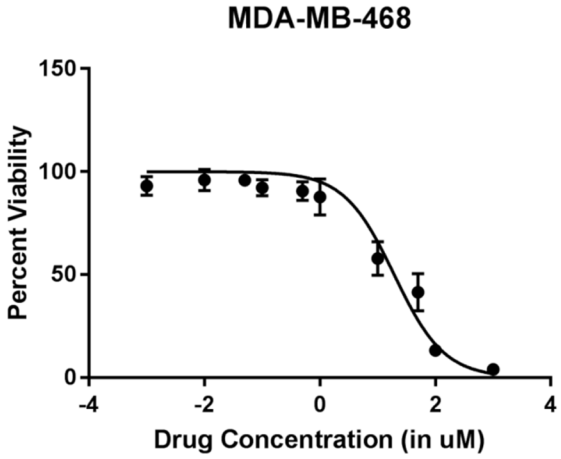

Figure 28. Achieved IC_{50} values for MDA-MB-231 and MDA-MB-468 cells.
MDA-MB-231 (A) or MDA-MB-468 (B) cells were treated with increasing concentrations of dasatinib for 72 hours to achieve IC_{50}.

In MDA-MB-231 cell lysates (Fig. 29A) incubated with dasatinib for 48 h, a decrease in phospho-EGFR (Y845) from 1.17 to 0.8 and phospho-Src (Y416) levels from 1.19 to 0.74 as measured by densitometry were observed. Total levels of EGFR remained the same. In MDA-MB-468 cells (Fig. 29A), a two-fold decrease in pEGFR (Y845, 1.17 to

0.69) and pSrc (Y416, 1.87 to 0.83) levels after 48 h exposure to dasatinib was also observed. Total EGFR levels changed between untreated and (0.88 to 0.95) treated cells. Total Src levels for both cell lines were slightly lower in the treated lysates.

Next, using the same cell lines, the nuclear (N) and membranous plus cytoplasmic (C) localization of EGFR after treatment was investigated(Fig. 29B). In MDA-MB-231, there is approximately 21.3% nEGFR present in the untreated samples, which dropped to as much as 10-fold upon treatment. Interestingly, total Src protein in the nuclear region increased in cells exposed to the drug (43% to 59%). In MDA-MB-468 cells (Fig. 29C), 64% of EGFR was found in the nucleus of the untreated samples, whereas treatment decreased localization to 45%. More nuclear Src i was observed (50%) in the treated cells compared to control (41%). Collectively, these results demonstrates concordance with previous reports wherein mitigated Src activity and expression decreased nuclear EGFR.

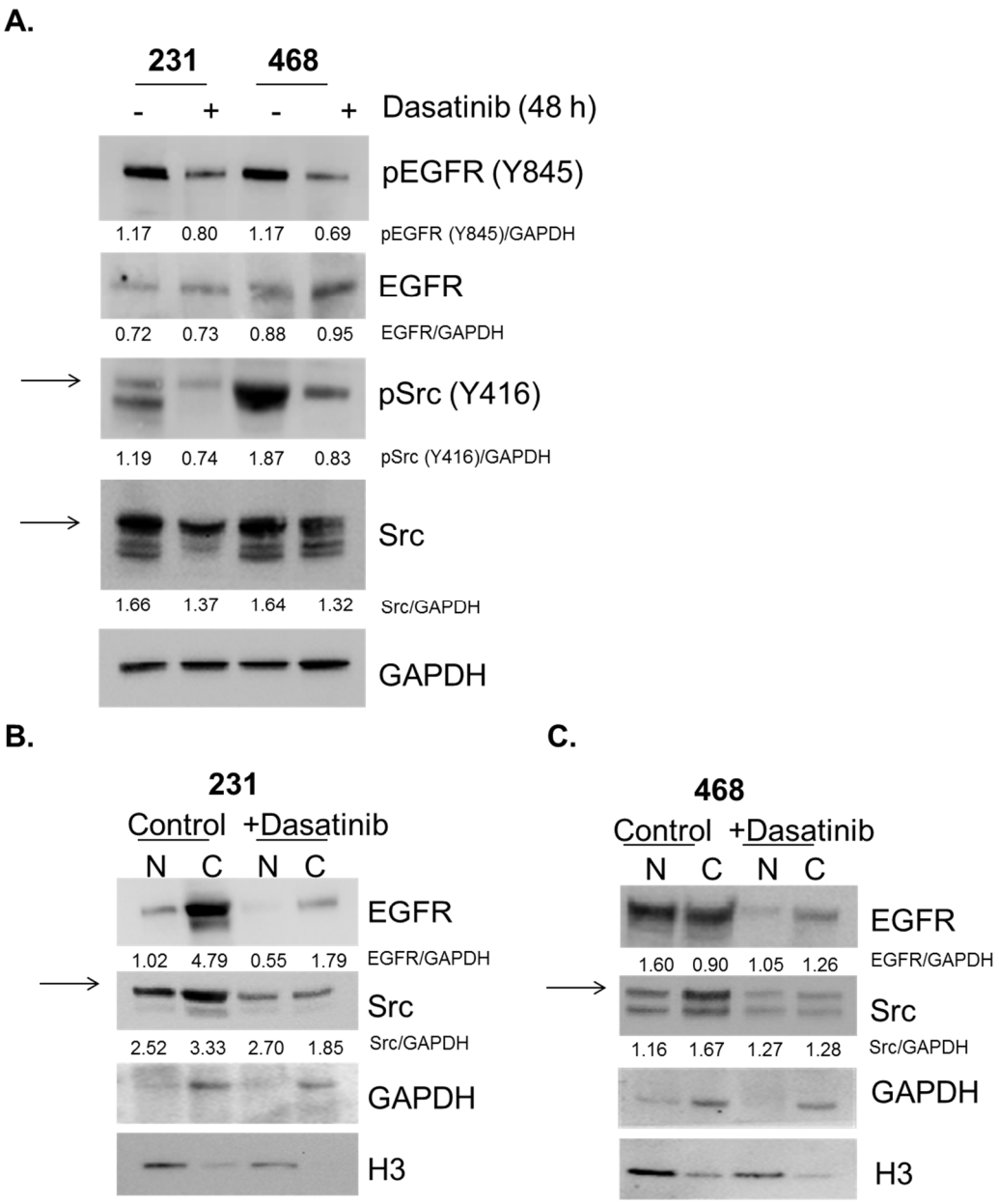

Figure 29. In vitro dasatinib treatment alters EGFR compartmentalization. MDA-MB-231 (left) and MDA-MB-468 (right) cells were treated with dasatinib IC_{50} (+) values for 48 h or left untreated (-). Lysates were evaluated for pEGFR (Y845), EGFR, pSrc (Tyr416), and Src (A); nuclear (N) and membrane plus cytoplasmic (C) extracts were collected from MDA-MB-231 (B) and MDA-MB-468 (C) cells after 48 h dasatinib treatment or from control cells and evaluated for EGFR and Src localization.

3.2.4 *In* vivo monitoring of membrane EGFR with ^{89}Zr-cetuximab

Tumor-bearing athymic nude mice treated with either dasatinib or vehicle (Fig. 29) were imaged with ^{89}Zr-cetuximab at 48 h p.i. In MDA-MB-231 xenografts, (Fig. 30A) ^{89}Zr-

cetuximab had higher tumor accumulation in treated vs. control groups (8.7 ± 1.6 %ID/g vs. 11.9 ± 3.7 %ID/g, p = 0.025)(Fig. 30B).

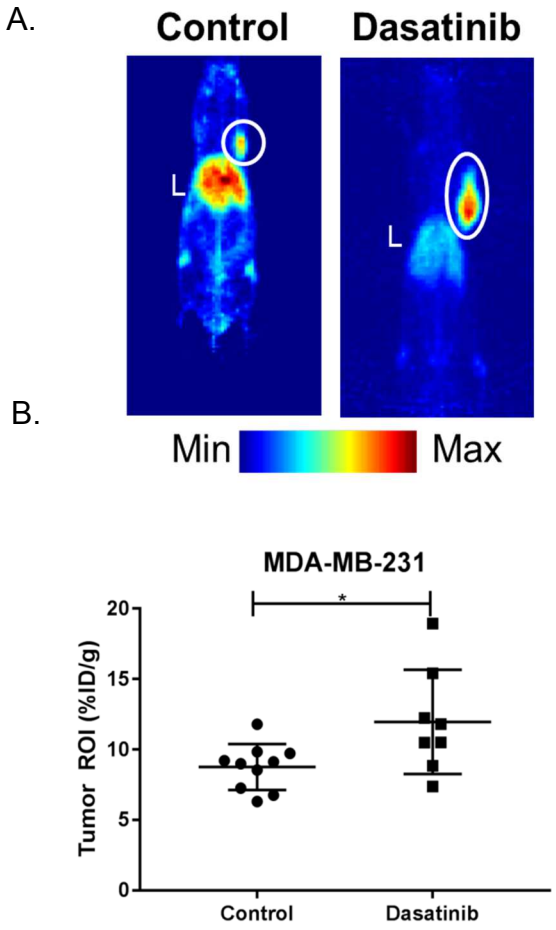

Figure 30. In vivo ^{89}Zr-cetuximab PET imaging in MDA-MB-231 xenografts. Mice bearing MDA-MB-231 tumors were left untreated (left) or treated with dasatinib (right) for 5 days before undergoing ^{89}Zr-cetuximab PET imaging at 48 h p.i. (A). ^{89}Zr-cetuximab tumor VOIs demonstrate higher uptake of the tracer in treated mice compared to control (B). * denotes $p < 0.05$.

Autoradiography of excised tumors demonstrated spatial distribution of the tracer with higher focal uptake observed in treated (Fig. 31A, right) vs. control (Fig. 31A, left) tumor sections. Immunohistochemistry on serial sections displayed compartmentalization of EGFR (Fig. 31B, top) and pSrc (Y416) (Fig. 31B, bottom) levels with (left) and without (right) treatment. In control tumors, elevated EGFR protein appeared localized to the

nucleus, whereas after dasatinib treatment an increase in membranous staining of EGFR was observed. Cytoplasmic phospho-Src (Y416) staining was observed control tumors but staining was abrogated upon treatment.

Western blot densitometry analysis demonstrated a significant increase in total EGFR in treated mice when compared to untreated mice (0.35 ± 0.05 vs. 0.23 ± 0.07, p = 0.043) (Fig. 31C, Table 12). Functional EGFR (pEGFR-Y845) was mitigated after dasatinib treatment. Based on densitometric ratios of EGFR/GAPDH, a ratio of 0.64 ± 0.31 was observed in control tumors vs. 0.08 ± 0.16 in treated groups (p = 0.0173)(Table 12). An almost three-fold decrease in pSrc (Y416) expression was displayed between tumors that were given vehicle and dasatinib (1.57 ± 0.554 vs. 0.638 ± 0.06, p = 0.0151). Total Src expression was not significantly different between control and dasatinib treated tumors (0.498 ± 0.13 vs. 0.583 ± 0.10, p = 0.3406). A positive correlation was achieved between total EGFR and tumor VOI (r = 0.83, p = 0.011) (Fig. 31D).

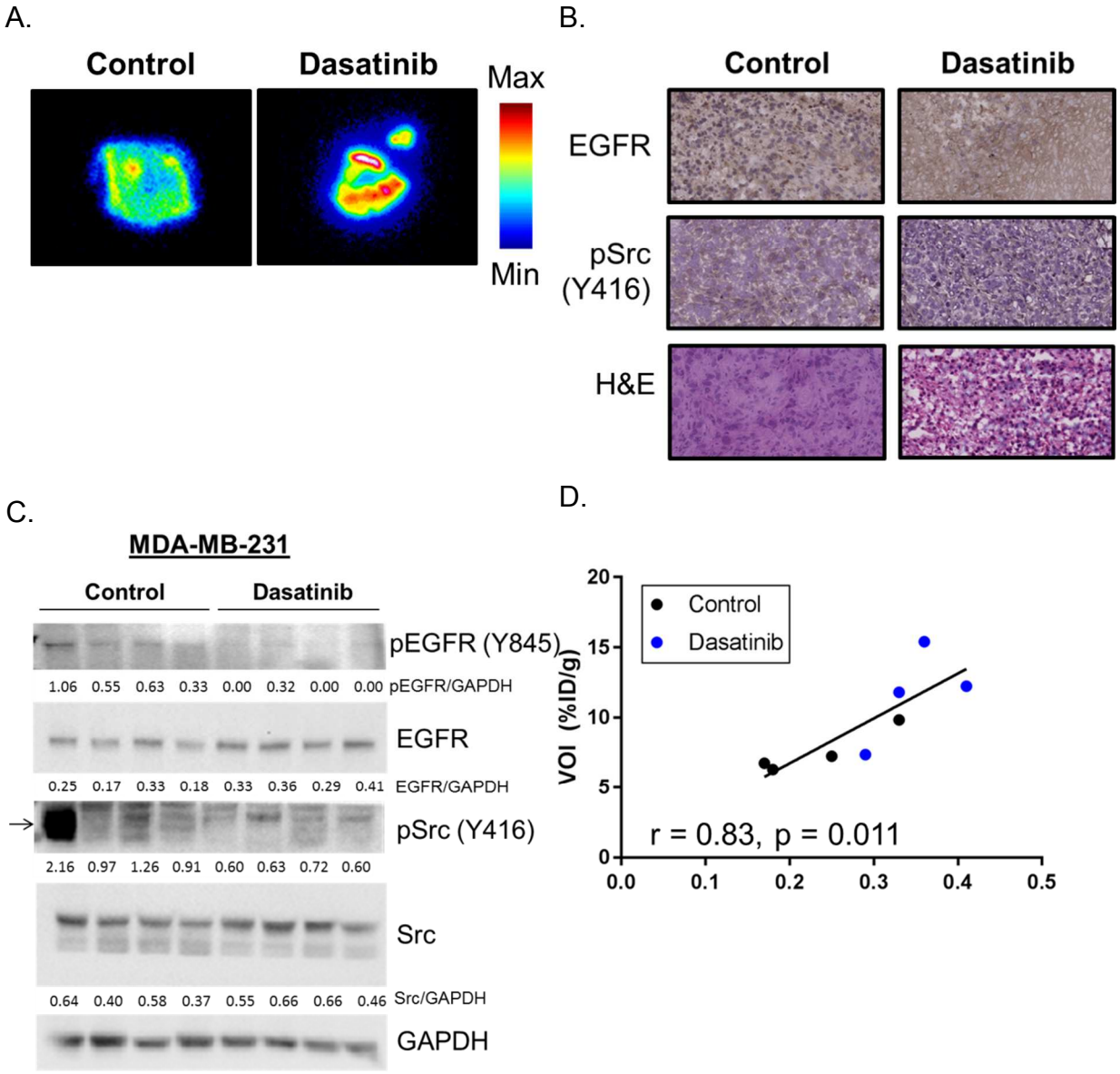

Figure 31. Ex vivo analysis on MDA-MB-231 tumors. *Ex vivo* autoradiography (A), H&E (B, bottom), and IHC of EGFR (B, top) and pSrc (Y416, B, middle) shows differences in tracer localization and expression after dasatinib treatment (right) compared to control (left). Western blots of control (left) and dasatinib treated (right) tumors were evaluated for pEGFR (Y845), EGFR, pSrc (Y416), and Src (C). Densitometry for EGFR was correlated to tumor VOI (D).

	Control Mean ± S.D.	Dasatinib Mean ± S.D.	P-value
pEGFR (Y845)	0.64 ± 0.31	0.08 ± 0.16	0.02
EGFR	0.23 ± 0.07	0.35 ± 0.05	0.04
pSrc (Y416)	1.6 ± 0.55	0.64 ± 0.06	0.02
Src	0.5 ± 0.13	0.58 ± 0.1	0.34

Table 12. Densitometry of MDA-MB-231 tumors.

Treated MDA-MB-468 tumors (Fig. 32A) exhibited an almost two-fold increase in ^{89}Zr-cetuximab uptake compared to control, untreated tumors (14.25 ± 3.92 %ID/g vs. 8.45 ± 1.72 %ID/g, p = 0.0013) (Fig. 32B).

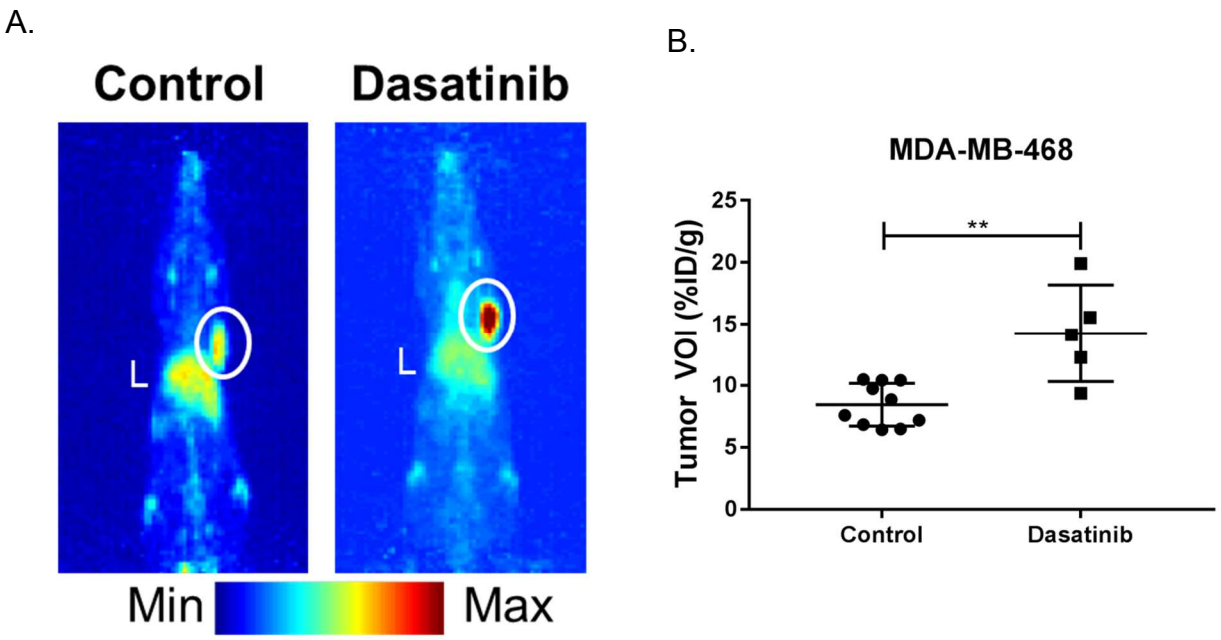

Figure 32. In vivo ^{89}Zr-cetuximab PET imaging in MDA-MB-468 xenografts. Mice bearing MDA-MB-468 tumors were left untreated (left) or treated with dasatinib (right) for 5 days before undergoing ^{89}Zr-cetuximab PET imaging at 48 h p.i. (A). ^{89}Zr-cetuximab tumor VOIs demonstrate higher uptake of the tracer in treated mice compared to control (B). ** denotes $p < 0.01$.

Autoradiographic images of excised tumors displayed an increase in tracer uptake in dasatinib treated (right) tumors compared to control untreated tumors (left) (Fig. 33A). IHC on serial sections for EGFR (top) showed dark positive EGFR staining in the nucleus

and cytoplasm in untreated tumors, which changed to strong membranous EGFR staining after treatment. A close examination of pSrc (Y416) expression (bottom) also showed a positive cytoplasmic stain in untreated tumors, which was attenuated in the treated tissue sections (Fig. 33B).

Immunoblots further reinforced the tracer readout. A significant increase in total EGFR (0.12 ± 0.03) compared to control tumors (0.05 ± 0.03, p = 0.024) was achieved (Fig. 33C, Table 13). Phosphorylation of EGFR at Y845 displayed a decreasing trend after dasatinib treatment compared to control (0.07 ± 0.03 vs. 0.11 ± 0.4). We observed a two-fold decrease in pSrc (Y416) protein after dasatinib treatment (0.30 ± 0.6 vs. 0.47 ± 0.02, p = 0.006). Similarly, to MDA-MB-231, there was no significant change in total Src protein level after dasatinib treatment (0.56 ± 0.08 vs. 0.58 ± 0.12, p = 0.842). Densitometry of total EGFR significantly correlated with tumor VOI (r = 0.89, p = 0.007)(Fig. 33D).

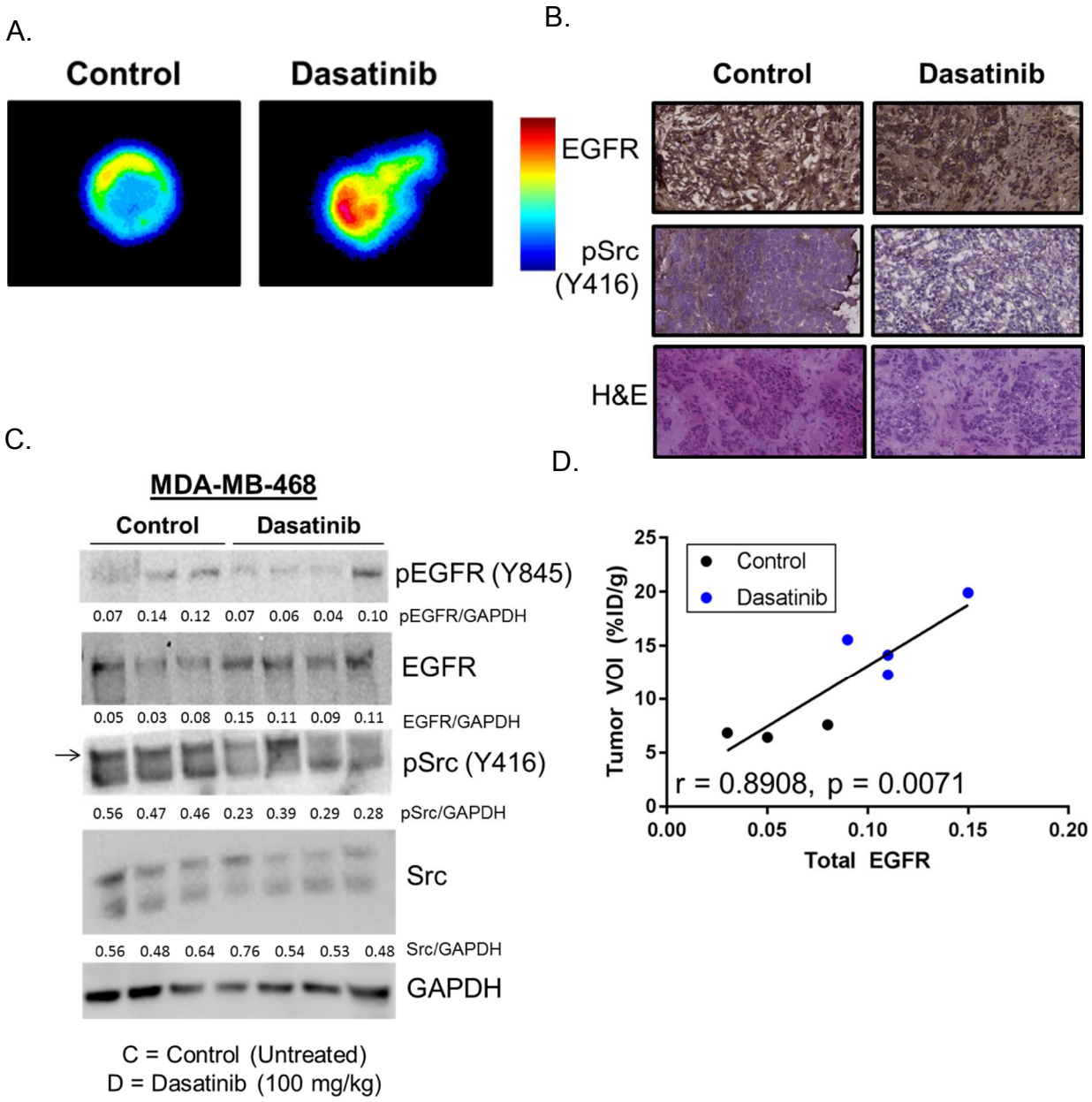

Figure 33. Ex vivo analysis on MDA-MB-468 tumors. *Ex vivo* autoradiography (A), H&E (B, bottom), and IHC of EGFR (B, top) and pSrc (Y416, B, middle) shows differences in tracer localization and expression after dasatinib treatment (right) compared to control (left). Western blots of control (left) and dasatinib treated (right) tumors were evaluated for pEGFR (Y845), EGFR, pSrc (Y416), and Src (C). Densitometry for EGFR was correlated to tumor VOI (D).

	Control Mean ± S.D.	Dasatinib Mean ± S.D.	P-value
pEGFR (Y845)	0.11 ± 0.04	0.07 ± 0.03	0.12
EGFR	0.05 ± 0.03	0.12 ± 0.03	0.02
pSrc (Y416)	0.47 ± 0.01	0.3 ± 0.06	0.01
Src	0.56 ± 0.08	0.58 ± 0.12	0.84

Table 13. Densitometry of MDA-MB-468 tumors.

3.2.5 Effects of combinatorial dasatinib and Cetuximab therapy

The addition of cetuximab in combination with dasatinib after neoadjuvant Src inhibition was next explored. In this longitudinal study, mice treated with dasatinib prior to PET imaging were further stratified into two arms after PET imaging. One group received continuous dasatinib treatment while a second group received dasatinib plus cetuximab (Fig. 34). The same control group of mice used in the imaging scan was monitored for tumor progression throughout the study.

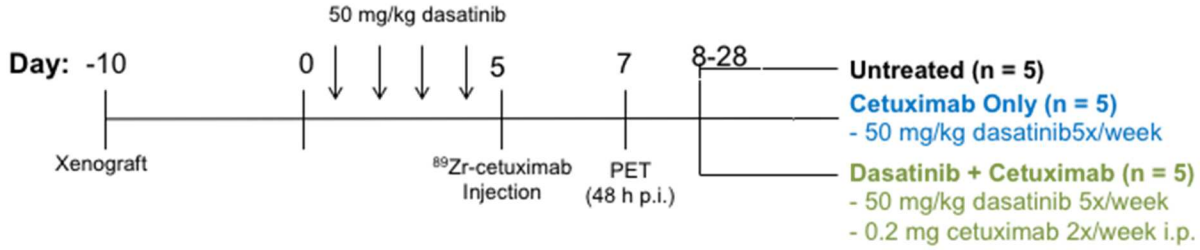

Figure 34. Treatment Scheme. Mice were implanted with MDA-MB-231 or MDA-MB-468 tumors and allowed to acclimate for 10 days before either receiving dasatinib (50 mg/kg for 5 d) or left untreated. Mice then underwent 89Zr-cetuximab PET imaging 48 h p.i. of the tracer. After imaging, dasatinib treated mice were stratified into treatment groups of dasatinib only (50 mg/kg for 5 d) or dasatinib (50 mg/kg for 5 d) plus cetuximab (0.2 mg i.p. 2x/week).

In MDA-MB-231 tumor bearing mice, no tumor response benefit was achieved in both treatment arms (Fig. 35A). No correlation was derived between ^{89}Zr-cetuximab VOI

and % change in tumor volume after treatment (Fig. 35B) (r = 0.095, p = 0.735).

On the other hand, a synergistic effect was observed in MDA-MB-468 tumors (p = 0.021) receiving the combinatorial therapy compared to dasatinib treatment alone (Fig. 35C). An examination of the correlation between tumor VOI and % change in tumor volumes revealed a negative correlation wherein higher accumulation of ^{89}Zr-cetuximab in the tumor resulted in slower growth. (r = -0.62, p = 0.013)(Fig. 35D).

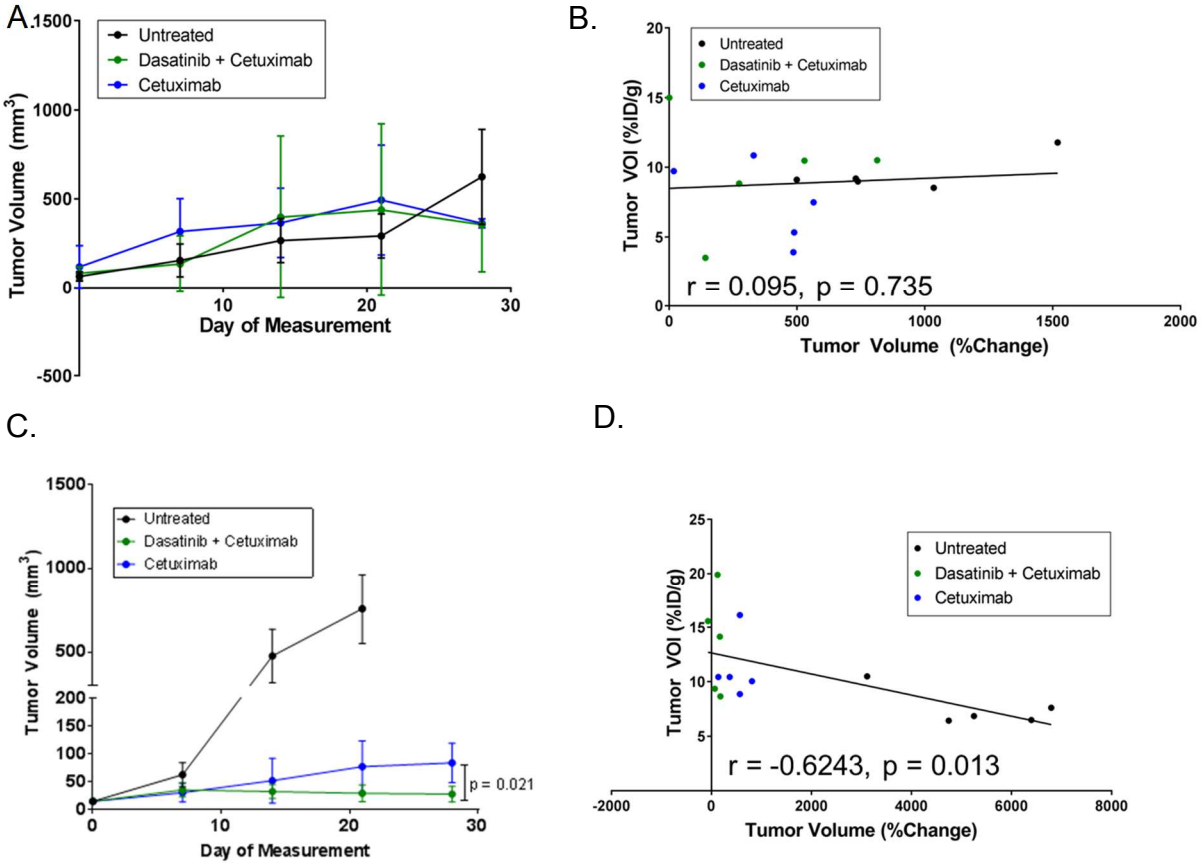

Figure 35. Tumor response to combination treatment or cetuximab alone. Tumor volume (mm^3) of MDA-MB-231 tumors undergoing treatment for 30 days (A). Correlation between ^{89}Zr-cetuximab tumor VOI (%ID/g) and percent change in tumor volume after treatment regimen in MDA-MB-231 (B). Tumor volume (mm^3) of MDA-MB-468 tumors undergoing treatment for 30 days (C). Correlation between ^{89}Zr-cetuximab tumor VOI (%ID/g) and percent change in tumor volume after treatment regimen in MDA-MB-468 (D).

3.2.6 Evaluating changes in EGFR localization after Dasatinib Treatment in TNBC PDX

The effects of dasatinib treatment and the potential of ^{89}Zr-cetuximab to monitor changes in membranous EGFR density in an EGFR-expressing TNBC PDX tumor model was investigated. Palpable tumors dosed with dasatinib for 5 days had a significantly higher tracer uptake compared to the control untreated arm (7.27 ± 2.3 %ID/g vs. 4.48 ± 1.14 %ID/g, p = 0.0273) (Fig. 36A-B).

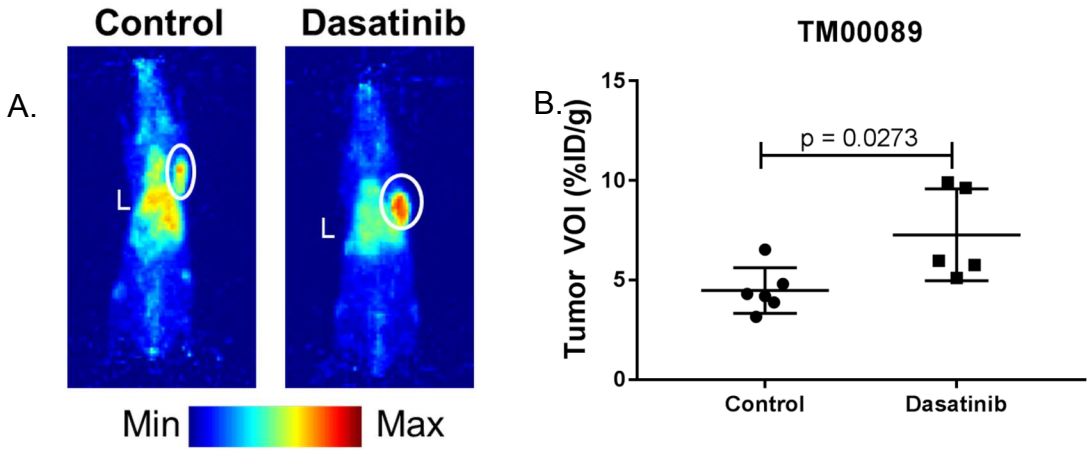

Figure 36. ^{89}Zr-cetuximab PET imaging in TM00089 PDX tumors. Mice bearing TM00089 PDX xenograft tumors were treated with dasatinib (50 mg/kg for 5 d) or left untreated before imaging with ^{89}Zr-cetuximab at 48 h p.i. (A). ^{89}Zr-cetuximab tumor VOIs demonstrate higher uptake of the tracer in treated mice compared to control (B).

Tumors were removed post-imaging for autoradiography and IHC. ^{89}Zr-cetuximab tracer distribution increased in the dasatinib treated tumor (Fig. 37A, right), compared to control tumor (Fig. 37A, left). Immunohistochemistry on serial sections for EGFR was evaluated (Fig. 37B). Positive nuclear and membranous EGFR staining in control tumors (left) were observed, whereas in dasatinib-treated tumors (right), an increase in diffused membranous EGFR staining was observed (Fig. 37B, top). Examination of pSrc (Y416) expression (Fig. 37B, bottom) showed a decrease in total staining between control,

untreated tumors (left) and dasatinib treated tumor sections (right).

To assess the treatment response to combination dasatinib and cetuximab therapy, the mice were treated with the combination for three additional weeks and tumor volumes were measured (Fig. 37C). There was a significant ($p = 0.0006$) improvement in response to treatment in the combination mice compared to untreated control. Untreated mice had an average tumor volume of 85.18 ± 26.71 mm^3, compared to combination treated mice with an average tumor volume of 3.53 ± 7.07 mm3, with 3 out of the 4 tumors completely regressing in volume. Change in tumor volume expressed as a percentage of starting tumor volume was correlated to 89Zr-cetuximab tumor uptake (%ID/g) (Fig. 37D). There was a significant, negative correlation between tumor regression and VOI ($r = -0.682$, $p = 0.043$).

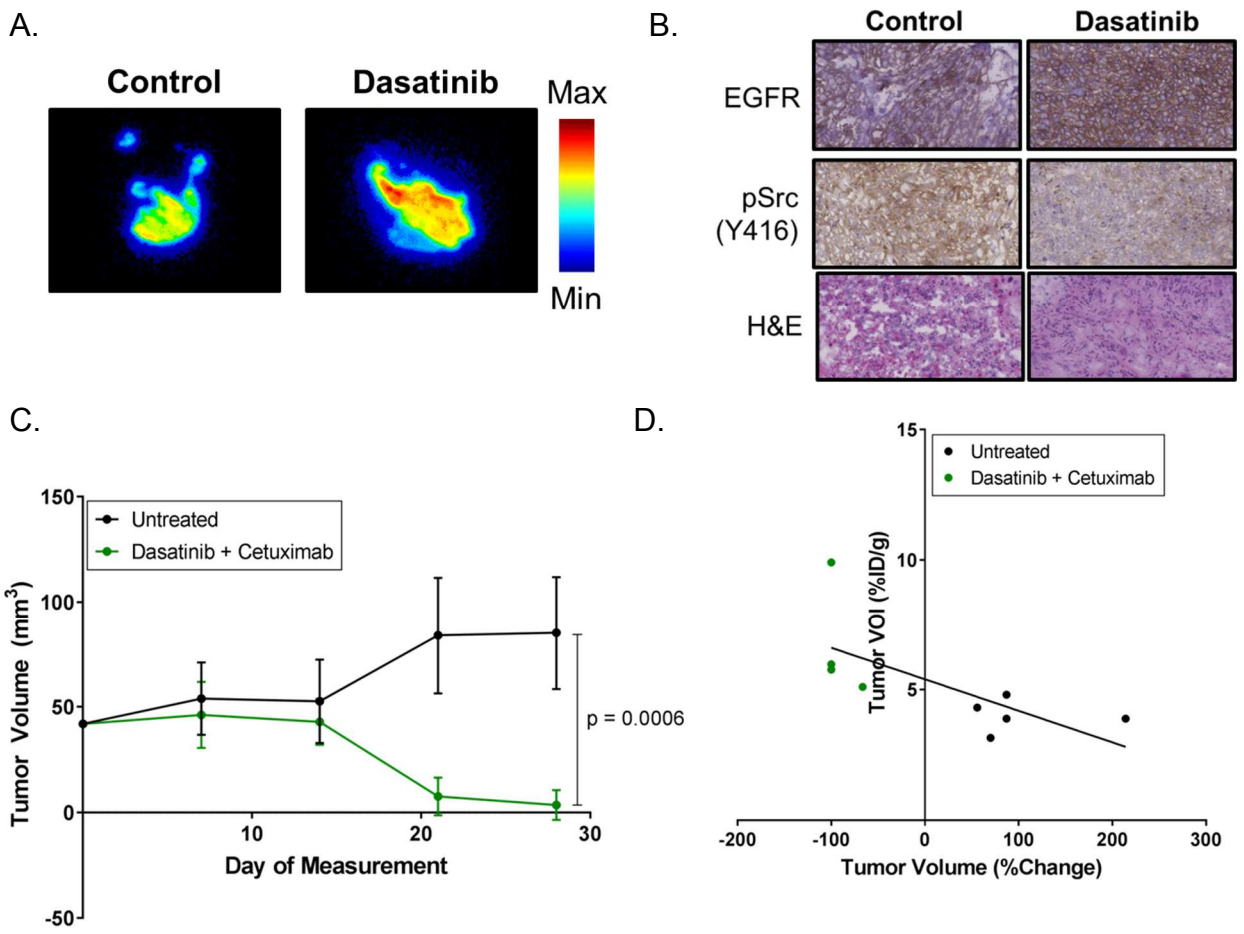

Figure 37. Ex vivo tumor TM00089 tumor analysis and extended combination treatment. *Ex vivo* autoradiography (A), H&E (B, bottom), and IHC of EGFR (B, top) and pSrc (Y416, B, middle) shows differences in tracer localization and expression after dasatinib treatment (right) compared to control (left). Correlation between ^{89}Zr-cetuximab tumor VOI (%ID/g) and percent change in tumor volume after treatment regimen in TM00089 (C). Tumor volume (mm^3) of TM00089 tumors undergoing treatment for 30 days (D).

3.3 DISCUSSION

Recently, ^{89}Zr-labelled antibodies nimotuzumab(245), imgatuzumab(246), and panitumumab(36,247), and affibody ZEGFR:2377(22) have been under investigation for use in imaging EGFR expression *in vivo* in addition to ^{89}Zr-cetuximab(248). Throughout these studies, EGFR has been established as a promising and robust target for

immunoPET imaging and targeted radiotherapeutics(249). Unfortunately, disparities between *in vivo* EGFR expression and ^{89}Zr-cetuximab PET uptake have been observed(248). This may be in part, due to the compartmentalization of EGFR between the nucleus and plasma membrane(168). The non-receptor tyrosine kinase Src has shown to be a key modulator of nEGFR translocation(239), and is an important downstream node of cetuximab response pathways(166,168,240,250). The literature and these studies have shown that targeting Src with dasatinib in TNBC cell lines expressing high levels of nEGFR *in vitro* resulted in a translocation of EGFR to the plasma membrane, suggesting this pathway a strategy to enhance EGFR available for further anti-EGFR treatments(251). Additionally, patients with high nEGFR expression have poor survival and prognosis in non-small cell lung cancer(237).

The Window of Opportunity Trial of dasatinib in operable triple negative BCs with nEGFR (NCT02720185) is currently underway to determine if dasatinib can prevent nuclear translocation of EGFR in stage I-III TNBC. Patients will be subjected to oral dasatinib (100 mg) treatment 7-10 days prior to planned surgery or research biopsy and plasma membrane EGFR expression will be measured. An increase of at least 25% membrane EGFR expression from baseline to post-dasatinib treatment will be considered significant. With this perspective, the initiative to validate ^{89}Zr-cetuximab as a tool to non-invasively monitor the translocation of nEGFR to the membrane is potentially useful for selection patients who’ve responded to dasatinib and could further benefit from EGFR targeted therapies.

Specifically, these results have shown that ^{89}Zr-cetuximab detects higher plasma membrane EGFR expression with concomitant nEGFR translocation after 48 h of

dasatinib treatment, as shown by binding and internalization assays. The lower internalization was coupled with an increase in total EGFR levels and a decrease in pSrc(Y416) levels, which confers Src response to dasatinib, as measured by western blots. *In vivo* studies demonstrated ^{89}Zr-cetuximab uptake increased after dasatinib treatment in TNBC xenografts MDA-MB-231 and MDA-MB-468. This was validated through *ex vivo* autoradiography, histology, and western blots. Immunohistochemistry looking at EGFR localization demonstrated an increase in membranous EGFR after dasatinib treatment in all xenografts, coupled with a decrease in pSrc(Y416) expression. Western blots of tumor lysates have shown an increase in total EGFR levels, with a concomitant decrease in pEGFR(Y845) and pSrc (Y416) levels, conferring response to dasatinib. Further analysis into utilizing this read out as a predictive biomarker of cetuximab response was evaluated in KRAS mutant cells MDA-MB-231, and KRAS wt cells MDA-MB-468. Tumor VOI significantly correlated with tumor response to treatment in MDA-MB-468 cells, and was coupled with a significant treatment benefit, whereas in MDA-MB-231 cells, there was no benefit to cetuximab observed. Taken collectively, ^{89}Zr-cetuximab PET imaging can potentially be utilized in clinical trials to measure EGFR translocation from the nucleus to the membrane in patients treated with dasatinib, and potentially other Src inhibitors.

CHAPTER 4. UTILIZING IMMUNOPET IMAGING TO MONITOR TUMOR RESPONSE TO IMMUNOTHERAPY

This chapter was adapted in full from “Interferon-gamma PET imaging as a predictive tool for monitoring response to tumor immunotherapy” by Heather Gibson, Brooke McKnight, Agnes Malysa, Greg Dyson, Wendy Wiesend, Claire McCarthy, Joyce Reyes, Wei-Zen Wei, and Nerissa T. Viola-Villegas originally published in Cancer Research and used with their full permission.

4.1 INTRODUCTION

During adaptive immunotherapy, activated T cells infiltrating a tumor are often the principal components of treatment providing a “search-and-destroy” mechanism through specific recognition of tumor-associated antigens (TAA)(252,253). Recent emerging tumor-targeted ITx strategies are met with positive and durable outcomes in a subset of patients, however many remain non-responsive, exposing a strong urgency for consistent methods to monitor therapeutic response in a timely manner(203). Peripheral immune monitoring assays are often restricted to one antigen, are non-standardized, and may not reflect the dynamic activity occurring within the tumor(254,255). Post-treatment biopsy can be used to evaluate tumor infiltrates(256) however tumor heterogeneity and general accessibility may impact the adequacy and/or feasibility of this approach(257). Image-guided focal analysis of intratumoral immune activity may eliminate these issues by providing non-invasive, real-time efficacy predictions *in situ*. To date, ITx positron emission tomography (PET) tracer development has focused on immune cell surface molecule detection, particularly against CD3(47), and CD8(258). Others have developed tracers targeting immune checkpoint molecules PD1/PD-L1(42,43,259–262) to help identify candidate patients for checkpoint blockade therapy. These probes are limited,

however, as they do not mark functional downstream effector tumoricidal activity.

The cytokine interferon-γ (IFN-γ) is predominantly produced by activated Type 1 T helper (Th1)-skewed CD4 T cells, cytotoxic CD8 T cells (CTL), and both NK and NKT cells(263). Both Th1 and CTL contribute to antigen-specific tumor cell recognition and destruction, which is particularly advantageous in the context of immunotherapeutic approaches including checkpoint blockade, adoptive cell therapies, and vaccination(264–266). IFN-γ signaling contributes to tumor cell killing by a variety of mechanisms including upregulation of Fas/FasL and MHC molecules (267,268), however tumor expression of PD-L1 is also positively regulated by IFN-γ signaling, which ultimately serves as a feedback mechanism to quell immune activation.

The focus of this study described in this chapter underscores the development of a monoclonal antibody PET tracer targeting IFN-γ. The results show that IFN-γ PET associates with response to immunotherapy. Tumors treated with TAA DNA vaccination show increased IFN-γ detection with an influx of T cells. The level of IFN-γ uptake inversely correlates to tumor growth rate. Alternatively, in a model of induced T cell exhaustion, T cells were found to infiltrate the tumor but failed to produce detectable IFN-γ as measured by PET imaging. Results further demonstrated that IFN-γ PET provides consistent sensitivity for the detection of immunotherapy response when compared to antigen-specific peripheral immune monitoring. Collectively, IFN-γ PET may serve as a non-invasive, comprehensive approach to the evaluation of tumor immunotherapy.

4.2 RESULTS

4.2.1 PET imaging to visualize Neu+ tumors and CD3+ T cell infiltration

First, tumors bearing Neu, which is the target of our vaccine in subsequent studies,

were visualized by imaging tumor bearing mice with an anti-neu probe, ^{64}Cu-Ab4. ^{64}Cu was selected as the tracer due to its short half-life ($t_{1/2}$ ~ 12.07 h) and its applicability towards serial imaging studies. NeuT mice (n = 4) with palpable tumors exhibited a tumor uptake of 5.43 ± 0.72 %ID/g at 4 h p.i., and increased to 7.15 ± 0.45 %ID/g at 24 h p.i. (p = 0.5163)(Fig. 38A). Time-course imaging displayed a significant decrease in liver (17.0 ± 2.2 %ID/g to 9.5 ± 2.38 %ID/g, p < 0.0001) and heart (15.5 ± 2.3 %ID/g to 6.7 ± 1.8 %ID/g, p < 0.0001) uptake from 4 h to 24 h, respectively (Fig. 38B). Tumor volumes as measured in mm^3 were significantly correlated to tumor uptake at 24 h p.i. (r =0.832, p = 0.002)(Fig. 38C).

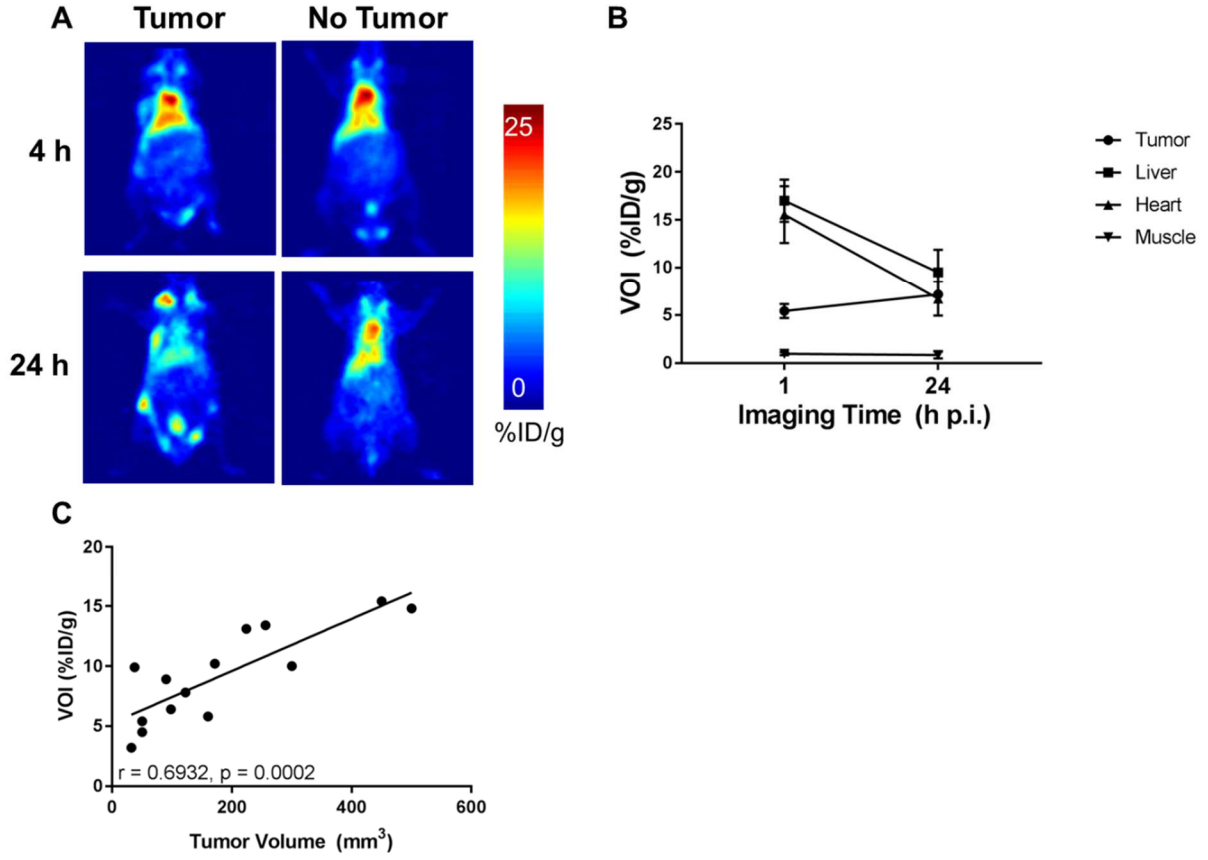

Figure 38. Visualizing presence of Neu+ tumors with ^{64}Cu-Ab4. NeuT mice bearing palpable tumors (left) or no tumor (right) were imaged with ^{64}Cu-Ab4 4 h or 24 h p.i. (A); time course imaging uptake of tumor, liver, heart, and muscle (B); NeuT tumor volumes were correlated to tumor uptake as measured in %ID/g at 24 h p.i. (C).

CD3+ T-cell infiltrates were next visualized within the tumor microenvironment with an anti-CD3 tracer, ^{89}Zr-anti-CD3. Tumor bearing NeuT mice were injected with ^{89}Zr-anti-CD3 and serially imaged from 4 h to 72 h p.i. (Fig. 39). Tumor uptake did not significantly change over time, with 3.4 ± 0.5 %ID/g at 4 h p.i., and decreasing to 3.1 ± 0.6 %ID/g at 72 h p.i. ($p = 0.960$). Heart uptake increased from 5.35 ± 2.8 %ID/g to 6.23 ± 3.83 %ID/g after 72 h p.i. ($p = 0.607$). Liver uptake significantly increased after 72 h, from 8.28 ± 2.02 %ID/g to 10.78 ± 1.36 %ID/g ($p = 0.005$). Spleen uptake significantly increased after just 48 h, from 10.08 ± 0.9 %ID/g to 16.58 ± 1.65 %ID/g ($p < 0.0001$), and continued to rise after 72 h to 18.53 ± 3.0 %ID/g ($p < 0.0001$).

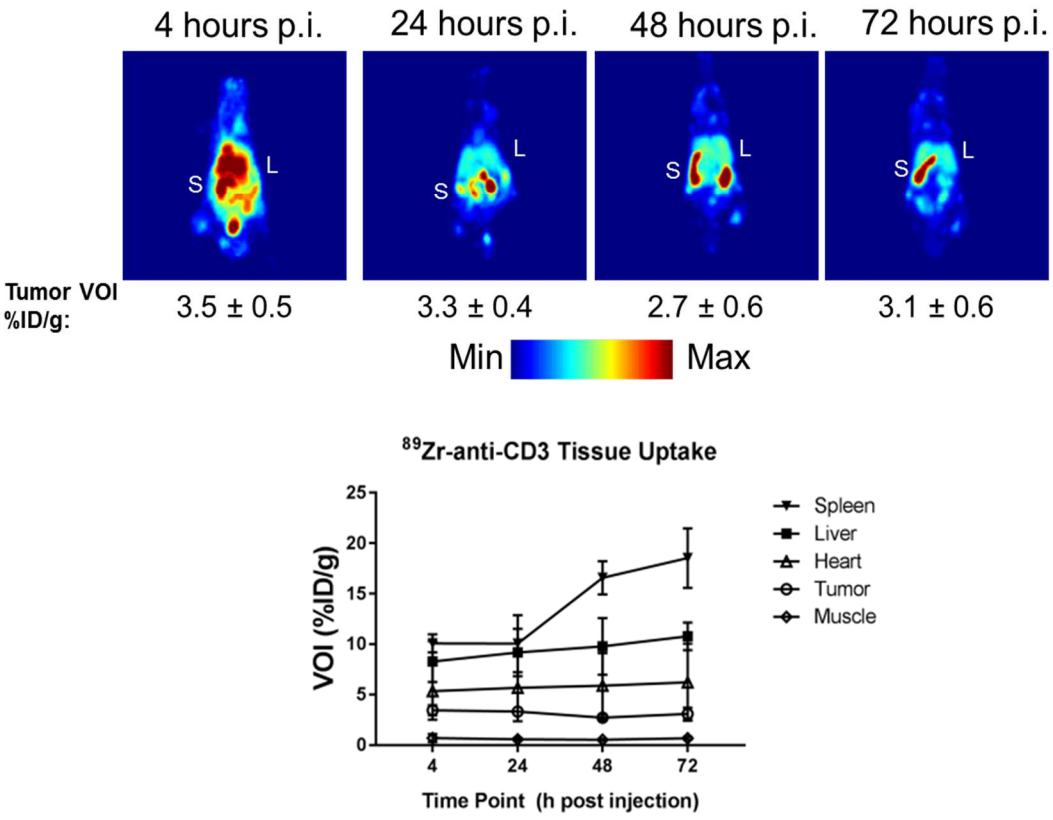

Figure 39. Time course imaging of ^{89}Zr-anti-CD3. Mice were injected with ^{89}Zr-anti-CD3 and images of MIP are shown for each time point (top). L = liver, S = spleen. A plot of the volumes-of-interest obtained from select tissues is shown over time from 4-72 h p.i.

4.2.2 ^{89}Zr-anti-IFN-γ PET tracer identifies localized IFN-γ production

The rat mAb AN-18 to murine IFN-γ was labeled with ^{89}Zr using desferrioxamine as the chelate (^{89}Zr-anti-IFN-γ) in good yields and purities according to previously reported methods(269). Timecourse imaging was performed on mice bearing tumors at 24, 72, and 120 h p.i. (Fig. 41). At 24 h, there was 12.0 ± 3.2% ID/g within the tumor. At 72 h p.i., there was 11.7 ± 3.1 %ID/g within the tumor, and plateaued at 12.7 ± 3.0 %ID/g after 120 h p.i. Time activity curves demonstrate a consistently low muscle uptake. At 72 h p.i., heart uptake decreases to below tumor uptake levels, and is the time where we determined subsequent imaging experiments would take place. Spleen uptake, a secondary lymphoid organ, was consistent throughout all timepoints.

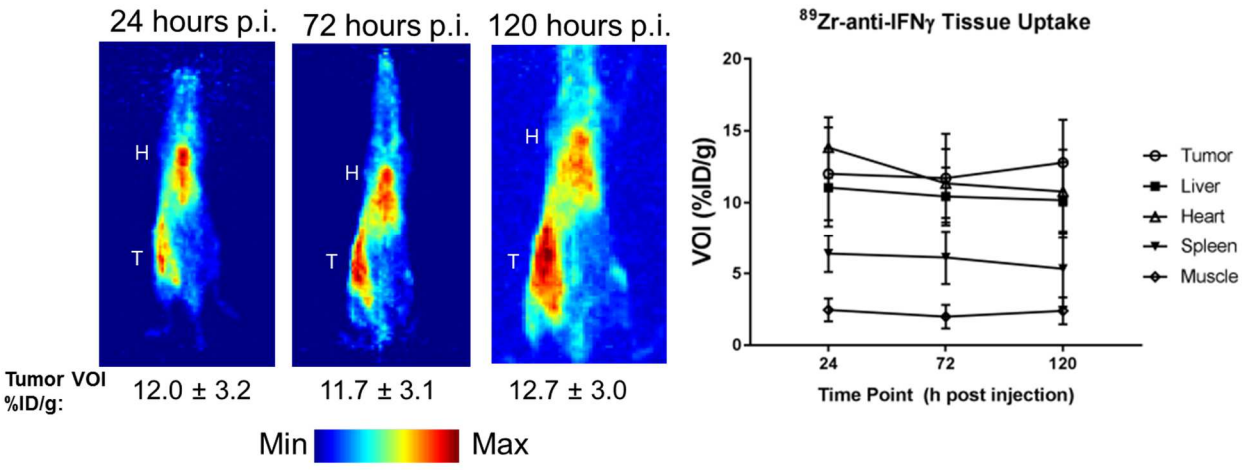

Figure 40. Time course imaging of ^{89}Zr-anti-IFNγ. Mice were injected with ^{89}Zr-anti-IFNγ and images of MIP are shown for each time point (top). H = heart, T = tumor. A plot of the volumes-of-interest obtained from select tissues is shown over time from 24-120 h p.i.

In mice treated with CpG-ODN to stimulate IFN-γ, whole-body PET images were acquired 72 h p.i., a time point identified to exhibit reliable tracer uptake in the tumor, with

low liver and blood pool background (Fig. 41A). VOIs drawn on splenic tissues demonstrated higher tracer accumulation (3.50 ± 0.61 %ID/g, n=3) in CpG-ODN-treated groups compared to untreated controls (Ctrl: 0.83 ± 0.12 %ID/g, n=3) (Fig. 38B).

Tissue distribution of ^{89}Zr-anti-IFN-γ at 72 h p.i. demonstrated 20.04 ± 12.2 %ID/g uptake in the spleen (Fig. 41B, Table 14). Uptake within the blood circulation (0.67 ± 0.69 %ID/g), as well as tissues responsible for excretion, liver (9.77 ± 9.12 %ID/g), and kidneys (3.93 ± 0.6 %ID/g) were low. There was also low uptake in the bone and muscle. Specificity was further confirmed through competitive binding experiment where a decrease in spleen uptake (20.04 ± 12.20 vs. 1.88 ± 2.74 %ID/g, n=4, p=0.0061) with 10X cold mAb blockade was observed, consequently increasing non-specific tissue accumulation in the blood (19.46 ± 12.69 %ID/g, p=0.0043), heart (10.57 ± 8.91, p=0.30), and liver (11.69 ± 9.82 %ID/g, p=0.99). Notable differences in splenic uptake in the imaging and tissue distribution (10-fold lower mass) are due to “mass effects”, wherein a greater mass of protein administered potentially saturated receptor binding sites and rendered slower pharmacokinetics(57).

Since IFN-γ is a soluble protein, the mechanism of localized IFN-γ imaging was investigated. Plated TUBO tumor cells were exposed to IFN-γ and/or ^{89}Zr-anti-IFN-γ tracer in quintuplicate followed by analysis of membrane binding and internalization (Fig. 41C). TUBO cells incubated with ^{89}Zr-anti-IFN-γ alone show limited tracer surface binding (1.13 ± 0.28%) and internalization (0.29 ± 0.13%). When TUBO is pre-incubated with IFN-γ, enhanced ^{89}Zr-anti-IFN-γ surface binding (13.62 ± 2.60%) and internalization (3.93 ± 1.07%) is observed (membrane: p=0.00039, internalized: p=0.0015). Detection of tracer binding to TUBO cells after IFN-γ exposure suggests localized imaging may be due to

sequestration of IFN-γ on its receptor *in vivo.*

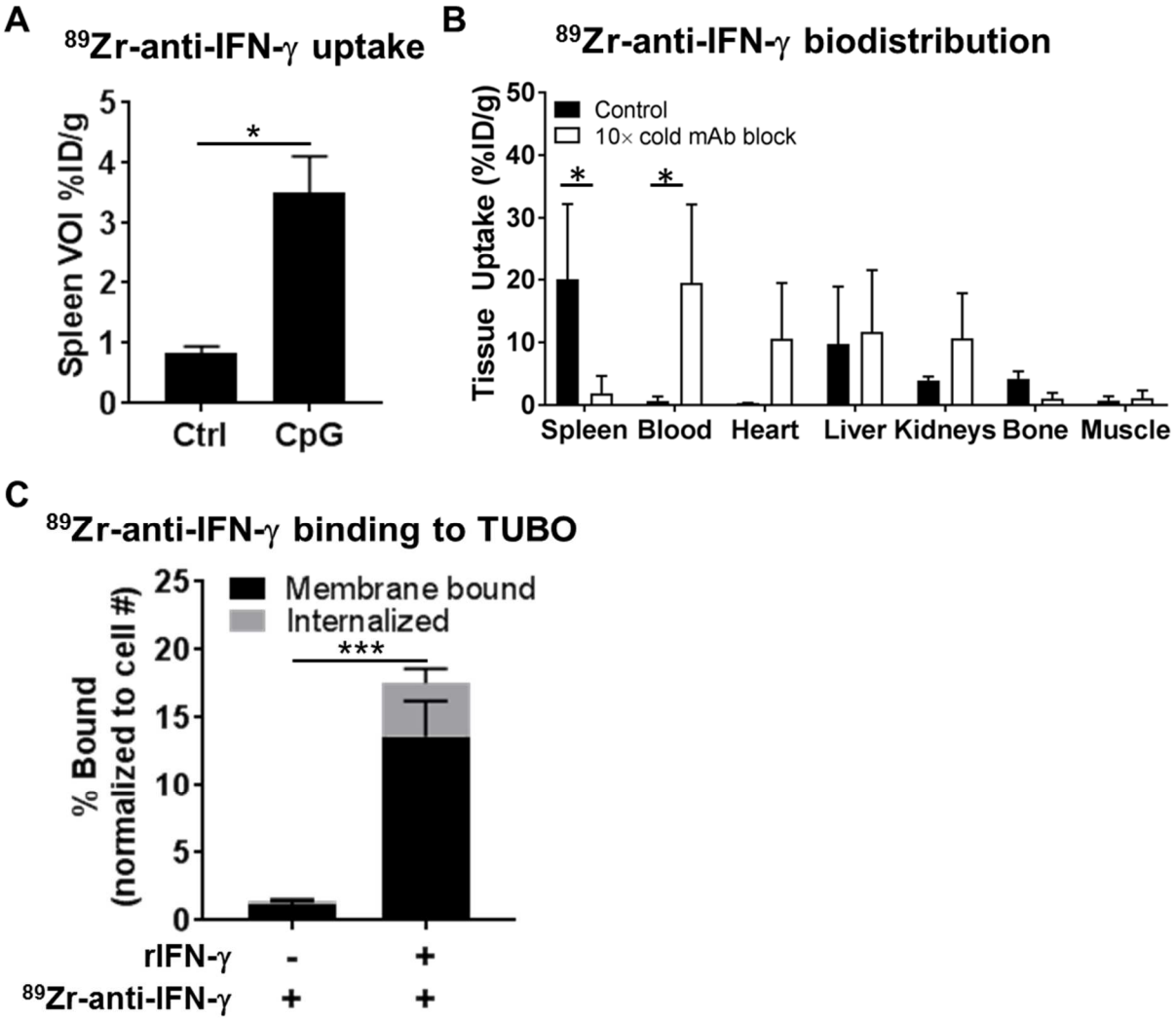

Figure 41. Validation of specificity of ^{89}Zr-anti-IFN-γ A) BALB/c mice treated with CpG-ODN and imaged with the tracer 72 h p.i. displayed higher uptake in the spleen compared to control (Ctrl) untreated cohorts (n=3 each). B) Tissue distribution of ^{89}Zr-anti-IFN-γ at 72 h p.i. demonstrated lower probe accumulation in the spleen upon competitive saturation with 10× cold AN-18 mAb (n=4 each). C) Binding of ^{89}Zr-anti-IFN-γ receptor-localized IFN-γ was tested *in vitro*. TUBO cells were incubated with ^{89}Zr-anti-IFN-γ alone (n=5), or with recombinant IFN-γ (rIFN-γ) and washed before addition of ^{89}Zr-anti-IFN-γ (n=5). Activity was measured by a gamma counter and adjusted for cell count. * denotes $p < 0.05$, *** denotes $p < 0.001$.

Tissue	Control		10× mAb block		
	Mean ± S.D.		Mean ± S.D.		p-value
Spleen	20.04	± 12.20	1.88	± 2.74	0.0061
Blood	0.67	± 0.69	19.46	± 12.69	0.0043
Heart	0.30	± 0.04	10.57	± 8.91	0.2956
Liver	9.77	± 9.12	11.69	± 9.82	0.9999
Kidneys	3.93	± 0.60	10.64	± 7.18	0.7755
Bone	4.19	± 1.18	1.01	± 0.94	0.9951
Muscle	0.73	± 0.65	1.08	± 1.23	>0.9999

Table 14. Biodistribution with ^{89}Zr-anti-IFNγ

4.2.3 IFN-γ PET detects active anti-tumor immunity *in situ* in a syngeneic tumor model

To test the capacity of ^{89}Zr-anti-IFN-γ as a non-invasive measure of anti-tumor immune response, neu+ TUBO tumor bearing BALB/c mice were imaged after receiving two rounds of HER2/neu DNA vaccination as detailed in Figure 42A. This vaccine induces HER2-specific humoral and T cell responses and ~10% equivalent of cross-reactive anti-neu T cells without cross-reactive neu-specific antibody(270). Tumor volumes began to stabilize or regress within 1 week after the second vaccination compared to untreated TUBO-bearing mice (Fig. 42A). Mice were injected with ^{89}Zr-anti-IFN-γ tracer for PET imaging (Fig. 42B and Fig. 43) at 72 h p.i. A nearly two-fold increase in tumor uptake was

observed in vaccinated (Vx: 10.07 ± 1.50 %ID/g, n=6) versus control mice (Ctrl: 5.97 ± 0.61 %ID/g, n=6, p=0.0001). An ^{89}Zr-labeled rat IgG isotype control tracer demonstrated similar tumor accumulation (72 h p.i.) in both untreated (5.27 ± 0.79 %ID/g) and vaccinated (5.93 ± 0.85 %ID/g) mice. This suggests baseline intratumoral IFN-γ levels are low without treatment. The notable low accumulation of the isotype control tracer after vaccination supports the specificity of the IFN-γ tracer and suggests increased ^{89}Zr-anti-IFN-γ uptake is not simply due vascular permeability and retention effects post-ITx.

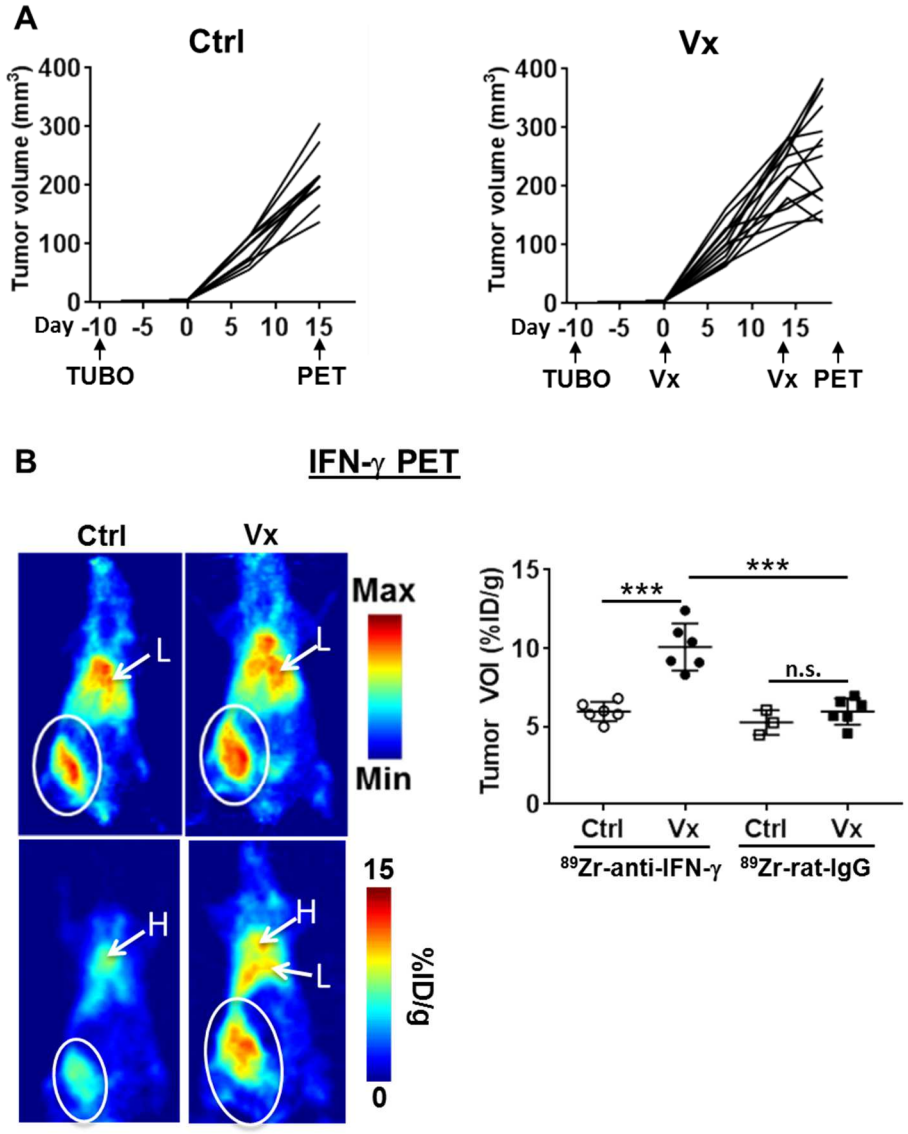

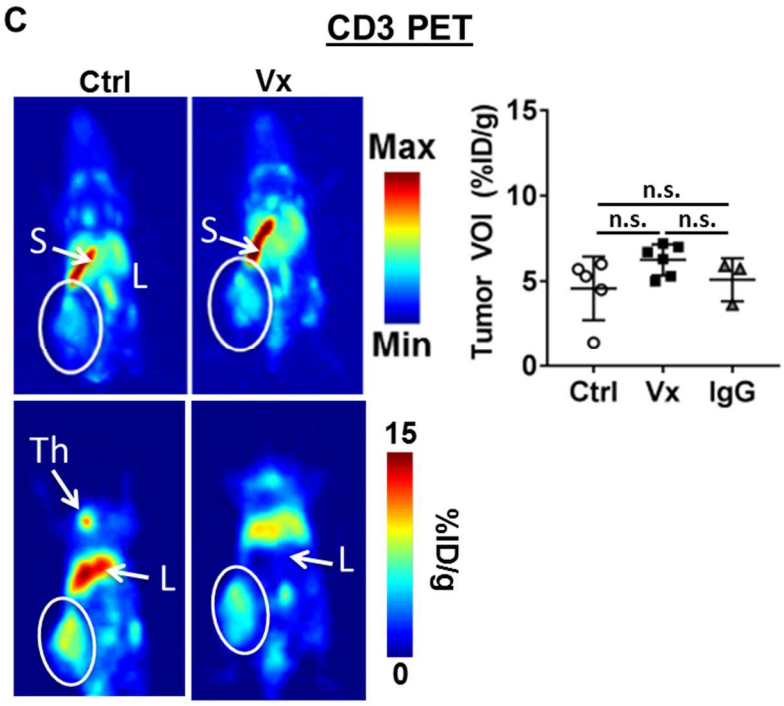

Figure 42. PET evaluation of immunotherapy response in orthotopic TUBO mammary tumors. Tumor volume was monitored in both untreated control (Ctrl, n=11, left) and vaccinated (Vx, n=12, right) tumors. TUBO cells were inoculated 10 days prior to the start of vaccinations, given on days 0 and 14. PET imaging was conducted on day 15 (Ctrl) and 21 (Vx) (A); Representative whole body maximum intensity projections (MIP, top row) and planar (bottom row) images of control (left panels, n=6) and vaccinated (right panels, n=6) mice with ^{89}Zr-anti-IFN-γ tracer (left). White circle = tumor, L = liver, H = heart, S = spleen, Th = Thymus. Tumor VOIs were measured for each mouse with an ^{89}Zr labeled rat IgG isotype control included for each treatment group (n=3, untreated control; n=6, vaccinated control) (B); MIP image (top panels) and planar sections (bottom panels) of ^{89}Zr-anti-CD3 images in control (left, n=5) and vaccinated mice (middle, n=6) (C). A non-specific ^{89}Zr labeled Armenian hamster IgG isotype control was used to measure tumor VOI in a separate group of untreated mice (right, n = 3).

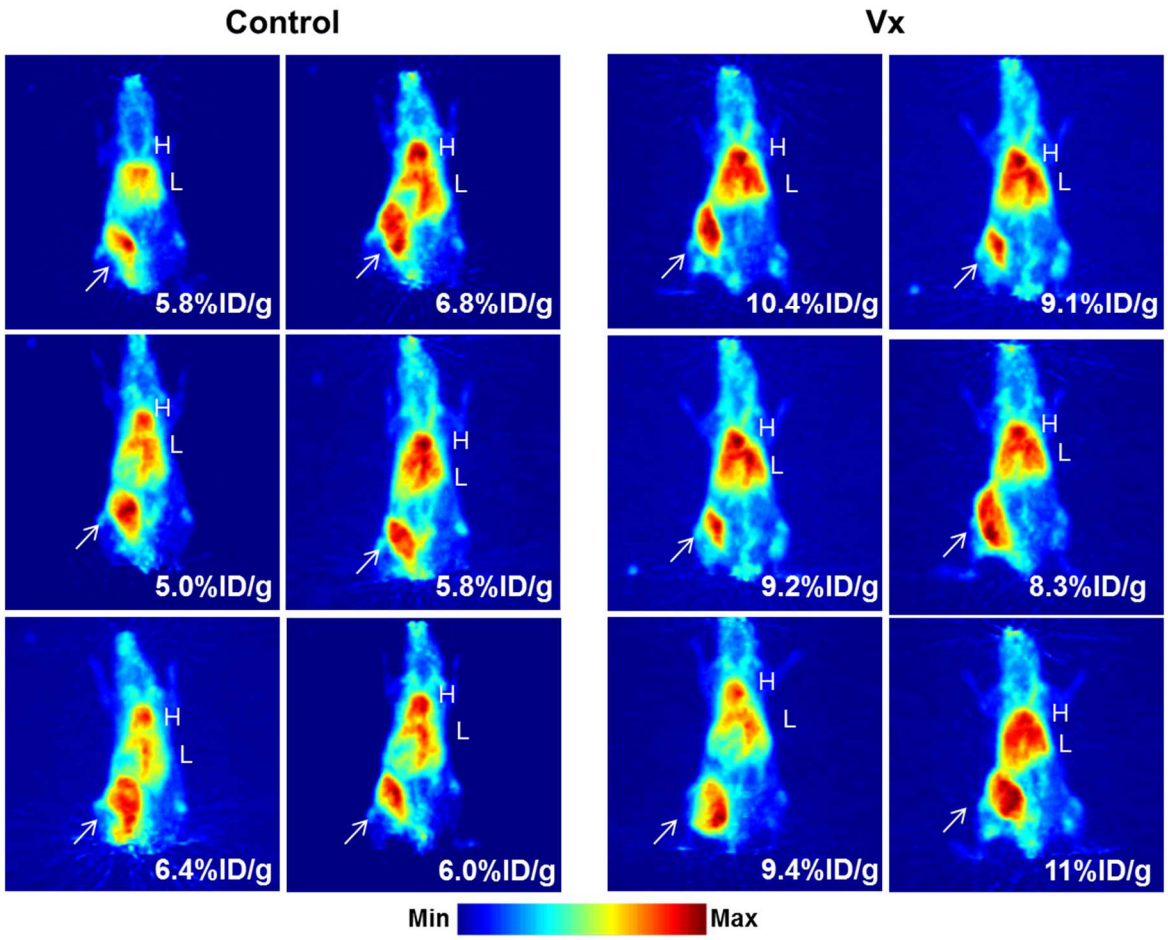

Figure 43. MIP images of ^{89}Zr-anti-IFNγ. Detection in all control (left) and vaccinated (right) TUBO bearing mice.

4.2.4 Detection of tumor infiltrating lymphocytes via CD3 immunoPET

Total T cell presence in the tumor microenvironment was assessed in separate groups of mice via immunoPET imaging of CD3+ tumor infiltrating lymphocytes using ^{89}Zr-anti-CD3 (Fig. 42C and Fig. 44). Vaccinated tumors exhibited a modest, insignificant increase of CD3 tracer binding compared to control (6.25 ± 0.37 %ID/g, n=6 vs. 4.58 ± 0.83 %ID/g, n=5, p=0.16). Both cohorts failed to demonstrate a significant change in uptake compared to Armenian hamster isotype control IgG (5.90 ± 1.26 %ID/g, n=3, p=0.87 (Ctrl), p=0.49 (Vx)). Untreated TUBO tumors have endogenous T cell infiltrates as detected by flow cytometry upon dissociation (Fig. 45A). However, CD3 immunoPET

suboptimally detected these TILs in both untreated and vaccinated mice with measured VOIs similar to the non-specific IgG tumor accumulation. This may be due to excessive uptake by the spleen, a T cell-homing secondary lymphoid tissue (Ctrl: 17.06 ± 3.56 %ID/g, Vx: 18.36 ± 1.49 %ID/g, Fig. 45B), which can act as a tracer "sink." In contrast, limited splenic accumulation was observed with the IFN-γ PET probe (Ctrl: 3.58 ± 0.81 %ID/g, $p<0.0001$, Vx: 4.97 ± 0.97 %ID/g, $p<0.0001$).

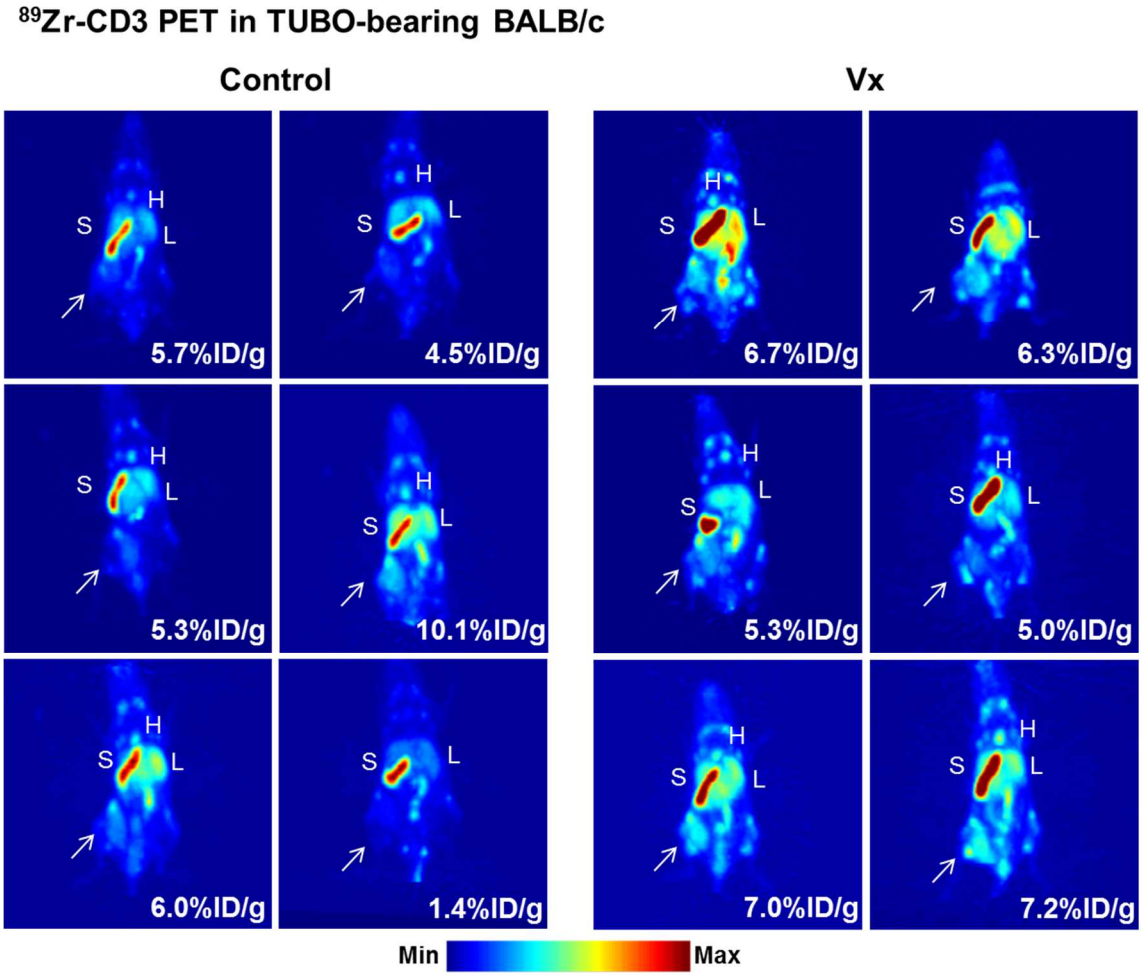

Figure 44. MIP images of ^{89}Zr-anti-CD3. Detection in all control (left) and vaccinated (right) TUBO bearing mice.

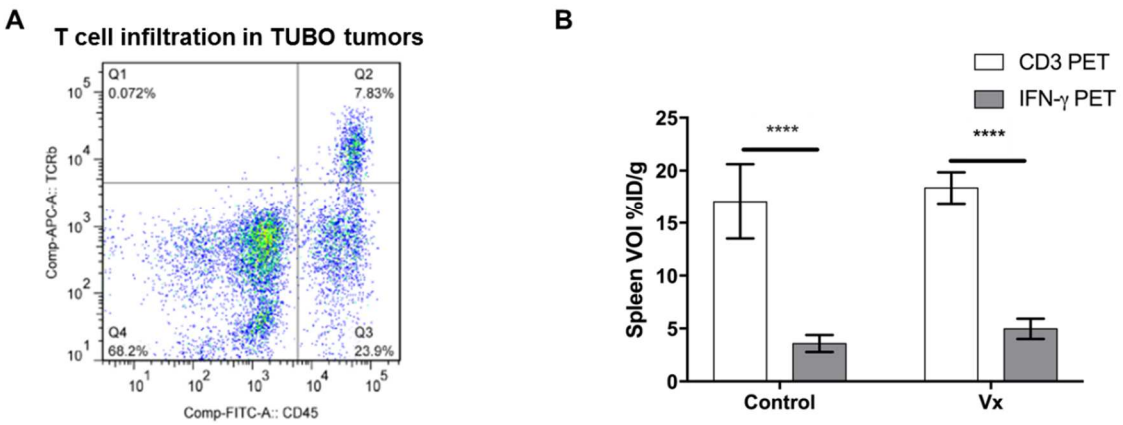

Figure 45. T cell detection in TUBO-bearing BALB/c. Tumors from untreated TUBO-bearing mice were dissociated and stained with CD45, to detect total leukocyte infiltrates, and the T cell receptor beta chain (TCRβ), to identify the T cell fraction, by flow cytometry (A); spleen VOIs were calculated for each TUBO-bearing mouse imaged with either ^{89}Zr-anti-IFNγ or ^{89}Zr-anti-CD3 (B).

4.2.5 *Ex vivo* validation via IHC, qPCR, and ELISA

Upon completion of imaging, tissues were collected for *ex vivo* validation. Tumor tissue was assessed to verify $CD3^+$ and $CD8^+$ T cell presence, as well as expression of IFN-γ. Transcripts levels of CD3, CD8 and IFN-γ were increased in tumor tissue after vaccination (Fig. 46A, Ctrl: n=11, Vx: n=13), in concordance with the PET imaging data. Cultured TUBO cell cDNA is included as a negative control. CD3 and CD8 proteins were increased after treatment (46B) and intratumoral IFN-γ protein was also confirmed and quantitated by ELISA (Fig. 46C). ELISA results showed higher total IFN-γ in Vx (n=11) versus Ctrl (n=10) TUBO tumors (85.37 ± 65.89 vs. 41.69 ± 20.12 pg/mg tissue, p=0.043).

Peripheral vaccine-induced immunity was measured by HER2/neu-specific serum IgG (Fig. 46D) and splenic T cell responses (Fig. 46E). HER2-specific IgG was only detected in vaccinated mice (18.68 ± 7.40 μg/mL, n=14, p<0.0001). TUBO tumors constitutively express the cell surface oncogene neu, which is foreign in wild-type BALB/c mice. Neu-specific IgG is detected in unvaccinated control TUBO-bearing mice (1.58 ±

1.60 μg/mL, n=13), which is further increased in vaccinated animals (6.18 ± 7.34 μg/mL, n=14, p=0.0019). While the HER2 DNA vaccine itself does not induce anti-neu IgG(270), tumor cell killing likely enhances immune activity to this foreign antigen. Detection of HER2-specific IFN-γ-producing T cells was restricted to vaccinated mice, similar to anti-HER2 IgG (119.40 ± 95.18/10^6 splenocytes (SC), n=7, vs. 0.83 ± 2.04/10^6 SC in untreated controls, n=6, p=0.0012). Peripheral anti-neu T cells were detected in all vaccinated animals (8.33 ± 7.75/10^6 SC) while only 1 of 4 untreated controls showed T cell responsiveness to neu (0.83 ± 2.04/10^6 SC, p=0.033). The absolute quantities of HER2 and neu-specific IgG and T cells were ~10-fold lower than similarly vaccinated non-tumor-bearing mice(270). This may be due to tumor-associated immune suppression by myeloid-derived suppressor cells or regulatory T cells (Tregs), which are reportedly increased in TUBO-bearing mice(270–272).

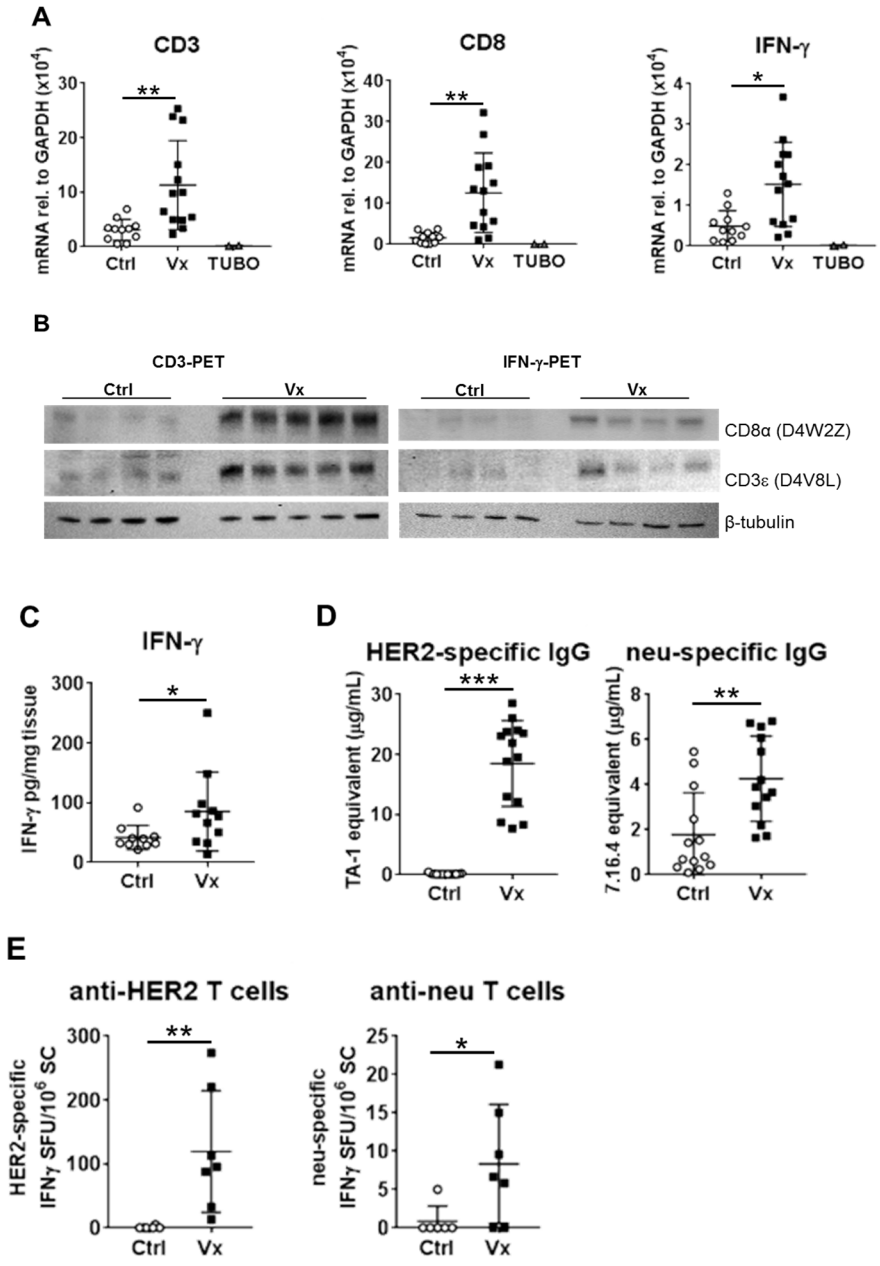

Figure 46. Ex Vivo validation of immunotherapy response in TUBO-bearing mice. Tumors were removed after imaging and validated. A) Total RNA obtained from Ctrl (n=11) and Vx (n=13) tumor tissue was analyzed by qPCR with primers specific to CD3 (left), CD8 (middle), and IFN-γ (right). Cultured TUBO cells serve as control (n=2). B) Western blots from lysed decayed tumor tissues post-CD3 or IFN-γ PET were conducted to analyze presence of CD3 and CD8 protein in the Vx vs Ctrl mice. C) IFN-γ ELISA was conducted with protein lysates of TUBO tumor segments of control Ctrl (n=10) and Vx (n=11) mice. D) HER2 and neu-specific IgG were measured in serum by flow cytometry (Ctrl: n=13, Vx: n=14). E) HER2 and neu-responsive T cells were measured by IFN-γ ELISPOT (Ctrl: n=6, Vx: n=7). * denotes $p < 0.05$, ** denotes $p < 0.01$, *** denotes $p < 0.001$.

4.2.6 Detection of ITx response in a spontaneous tumor model

The capacity of IFN-γ PET imaging to detect anti-tumor immune activity was tested in a spontaneous tumor setting. Neu transgenic (NeuT) mice are engineered to express a transforming rat neu under the mouse mammary tumor virus promoter(273), allowing immune system recognition of neu as a self-antigen(270). Studies were conducted in male NeuT mice, which develop 1-2 spontaneous neu+ salivary tumors between 30-40 weeks of age(273). Once tumors were palpable, Tregs were depleted using anti-CD25 mAb clone PC61 to enhance ITx response given NeuT mice are immune tolerant to rat neu(270,274), followed by two HER2/neu DNA vaccinations. Vaccination of NeuT mice (n=7) controlled tumor growth rate compared to untreated (n=6) tumor-bearing NeuT mice (Fig. 47A, p=0.032). IFN-γ PET of vaccinated tumors displayed a nearly two-fold higher uptake of ^{89}Zr-anti-IFN-γ (8.37 ± 0.35 %ID/g, n=4) vs. control (4.63 ± 0.47 %ID/g, n=3, p=0.001), indicating infiltration of functional anti-tumor T cells (Fig. 47B and Fig. 48B). An examination of tumor infiltrates via CD3 PET (Fig. 47C and Fig. 48B) revealed a similar trend (8.05 ± 1.47 %ID/g vs. 4.43 ± 0.72 %ID/g, n=3 per group, p=0.012).

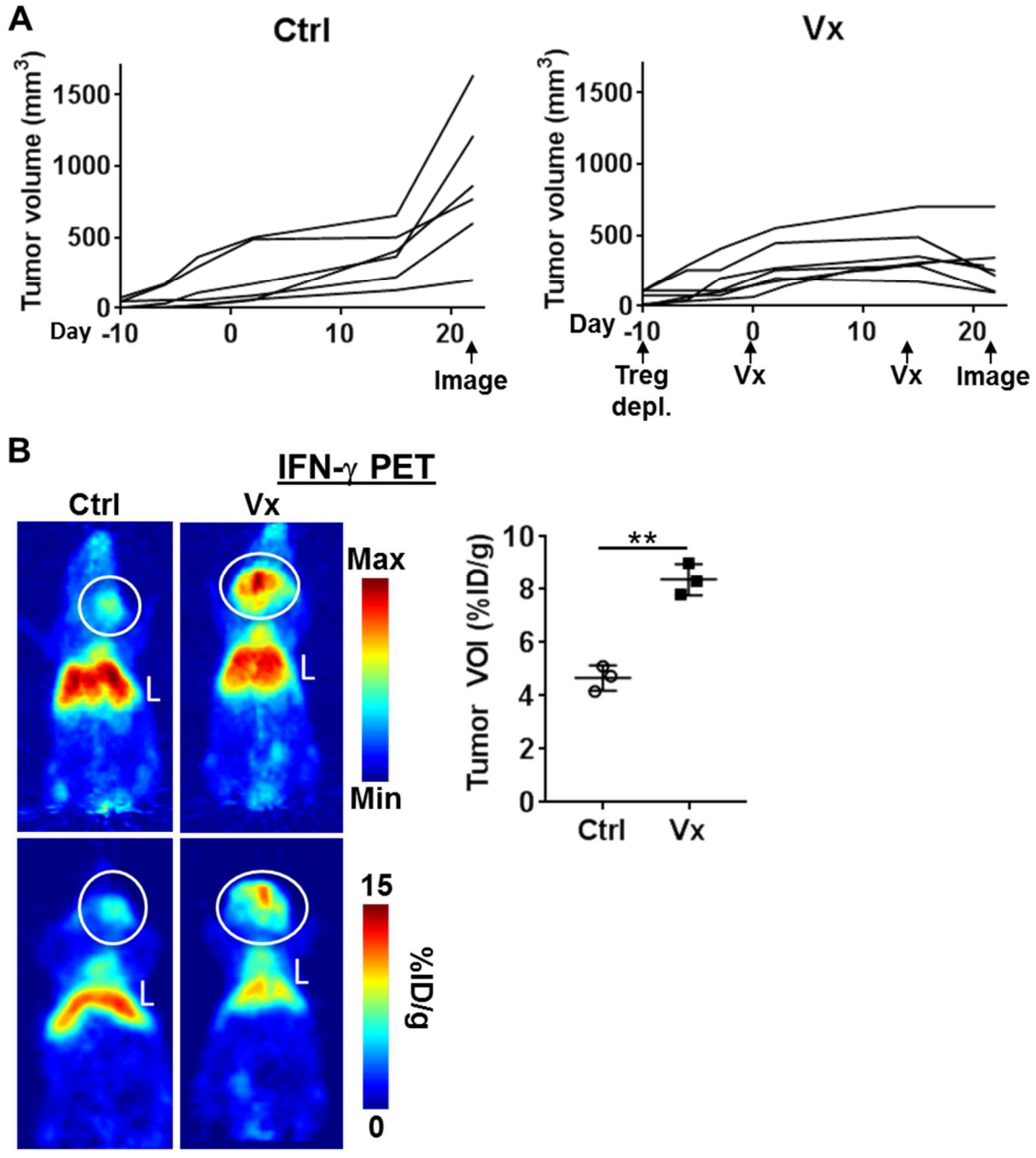
A
Ctrl
Vx
Tumor volume (mm3)
1500
1000
500
0
Day -10
0
10
20
Image
Treg depl.
Vx
Vx
Image
B
IFN-γ PET
Ctrl
Vx
Max
Min
L
15
0
%ID/g
Tumor VOI (%ID/g)
10
8
6
4
2
0
**
Ctrl
Vx

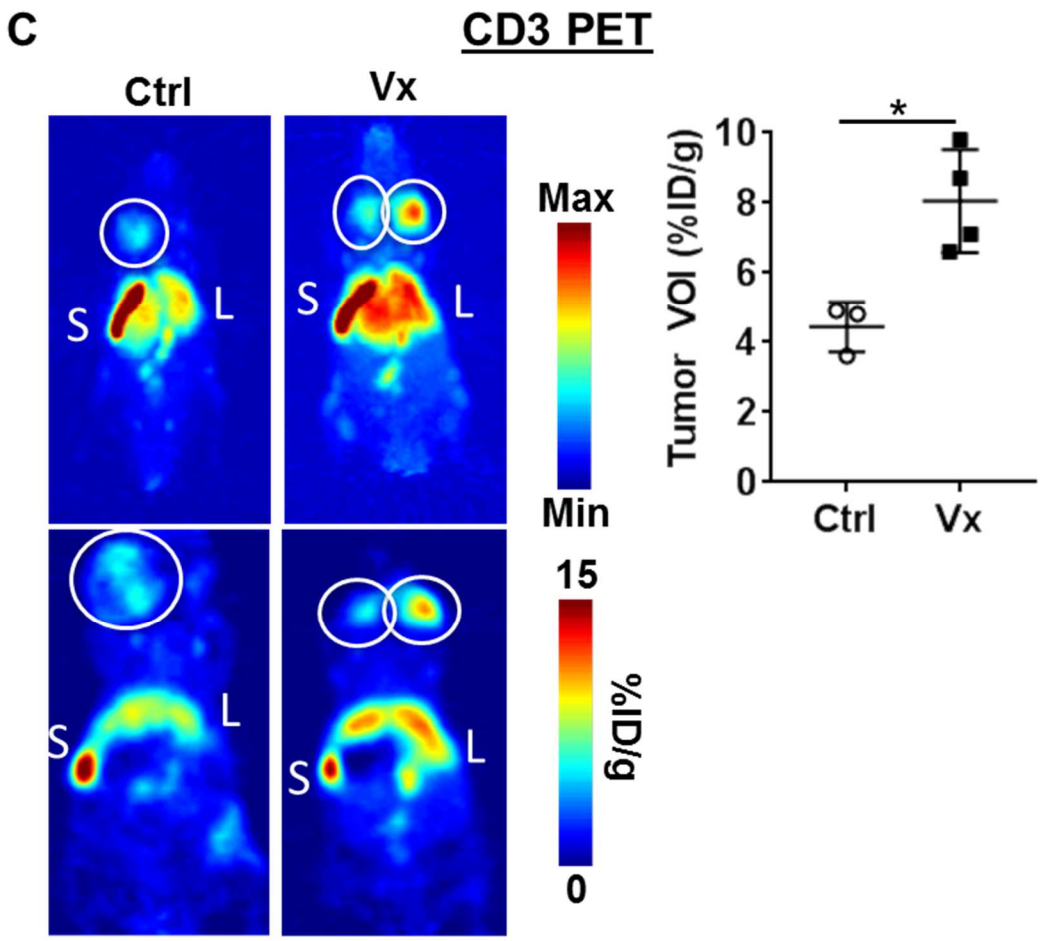

Figure 47. PET detection of anti-tumor immunity in spontaneous tumor-bearing NeuT mice. Control, untreated mice (Ctrl, n=6) were imaged by PET after palpable tumors were permitted to grow 31 days. For vaccinated mice (Vx, n=7), upon detection of palpable spontaneous salivary tumors, regulatory T cells (Treg) were depleted 10 d prior to the first vaccination. Mice received two HER2/neu DNA vaccinations 14 d apart. PET imaging was conducted 7 days after the final vaccination (A); representative whole body maximum intensity projections (MIP, top row) and planar (bottom row) images of control (left panels, n=3) and HER2/neu DNA-vaccinated (right panels, n=4) mice with ^{89}Zr-anti-IFN-γ tracer (left) (B). White circle = tumor, L = liver, S = spleen. Tumor VOIs were calculated for each mouse. C) Representative CD3 PET images of MIP (top) and planar sections (bottom) are shown for Ctrl (left) vs. Vx groups (right). * denotes $p < 0.05$.

A.

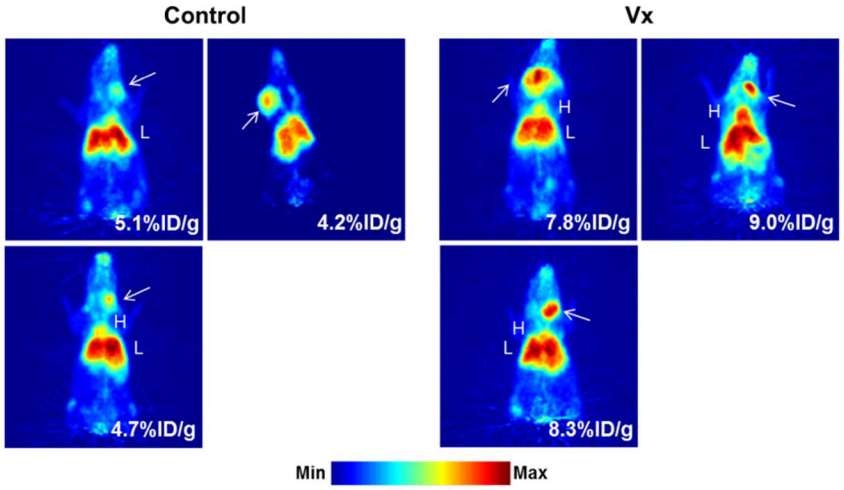

B.

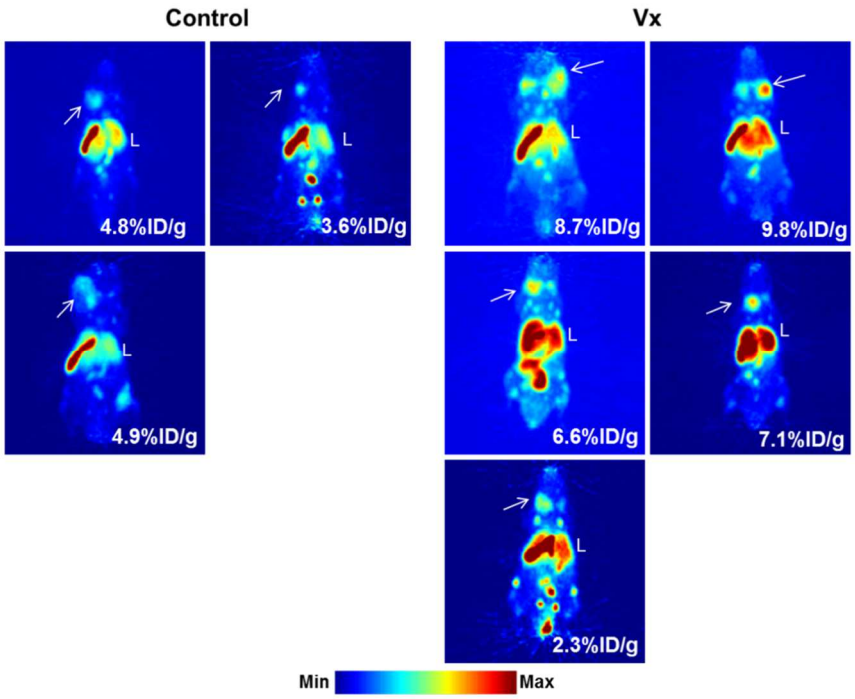

Figure 48. ^{89}Zr-anti-IFNγ and ^{89}Zr-anti-CD3 PET in all tumor-bearing NeuT mice. MIP images of (A) ^{89}Zr-anti-IFNγ and (B) ^{89}Zr-anti-CD3 detection in all control (left) and vaccinated (right) NeuT mice bearing spontaneous salivary tumors. Tumors are indicated by arrow; L = liver.

Validation of T cell infiltration and IFN-γ production was conducted by qPCR in tumor tissue samples (Fig. 49A). CD3 and CD8 detection showed a variable modest,

insignificant increase after vaccination, while IFN-γ mRNA increased (Ctrl: n=3, Vx: n=5, p=0.036). Peripheral immune response to the vaccine was evaluated by measuring serum anti-HER2 and anti-neu IgG as well as spleen-resident HER2- and neu-responsive IFN-γ-producing T cells. Tolerance to HER2/neu in NeuT mice was apparent with a comparatively lower ITx response vs. wild-type BALB/c mice bearing TUBO tumors in Figure 2. HER2-specific IgG was detected in vaccinated animals (Fig. 49B, 8.7 ± 4.9 μg/mL, n=8, p=0.0016 vs. Ctrl, n=5), while anti-neu IgG was negligible or absent in all samples tested. Despite increased intratumoral detection of IFN-γ in vaccinated NeuT mice by PET, peripheral T cell response to neu was low (Fig. 49C, 15.80 ± 8.84/10^6 SC, n=5) with HER2 vaccination, and was not significantly increased relative to untreated control (n=5, p=0.27). that detected in non-immune tolerant BALB/c mice bearing TUBO (10.0%, Fig. 49C). These results support the hypothesis that peripheral immune monitoring may be an inadequate measure of anti-tumor immunity with tumor-responsive T cells preferentially localizing within the tumor, supporting the use of *in situ* analysis methods such as PET imaging.

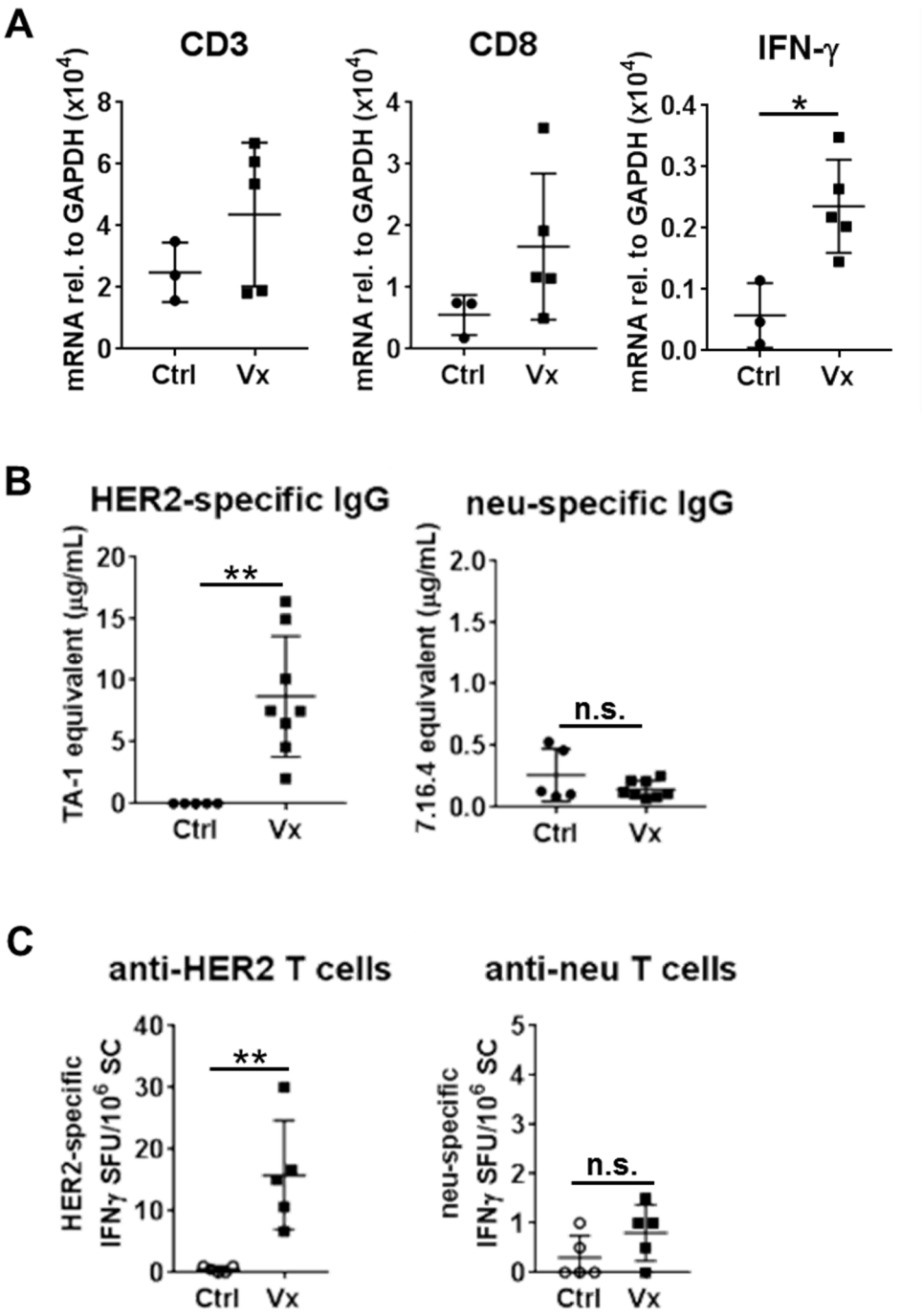

Figure 49. Ex vivo validation of anti-tumor immunity in spontaneous tumor-bearing NeuT mice. A) Total RNA was isolated from tumor tissue and qPCR analysis for CD3, CD8, and IFN-γ was conducted (n=3 each) B) Serum HER2 (Ctrl, n=5; Vx, n=8) and neu-specific IgG (Ctrl, n=5; Vx n=8) was measured by flow cytometry. C) HER2 and neu-responsive T cells were measured by IFN-γ ELISPOT (n=5 each). * denotes $p < 0.05$, ** denotes $p < 0.01$.

4.2.7 IFN-γ PET imaging is an indicator of immune activation status *in situ*

To test the capacity of ^{89}Zr-anti-IFN-γ to predict treatment outcomes, BALB/c mice (n=11) bearing variably-sized TUBO tumors were treated with our HER2 vaccine as described previously, resulting in a range of growth slopes (Fig. 50A, Fig. 51). ^{89}Zr-anti-IFN-γ PET imaging was conducted two weeks after the final vaccination and tumor volume was monitored for an additional ten days. Tumor-localized ^{89}Zr-anti-IFN-γ tracer uptake inversely correlated with tumor growth rate (Fig. 50B and Fig. 4.13, r=-0.64, 95% CI: (-0.90,-0.06); p=0.034), suggesting IFN-γ PET is an indicator of the effects of ITx on these tumors.

The outcome of IFN-γ PET in a setting where tumor-infiltrating T cells are present but have become exhausted was evaluated. TUBO-bearing mice were treated with passive ITx, mAb 7.16.4 to rat neu. This mAb has been shown to inhibit neu signaling in addition to initiating host anti-tumor immunity(275,276). Once tumors were established at ~50 mm^3, 1 mg doses of 7.16.4 were given i.p. at 3-4 day intervals for a total of 5 treatments, which reduced and stabilized tumor growth (Fig. 50C). ^{89}Zr-anti-IFN-γ (n=5) or control IgG (n=6) PET imaging was conducted on day 30 after treatment onset, at which time tumor growth had resumed. Tumor uptake of IFN-γ tracer was indistinguishable from IgG control, suggesting a lack of immune activity (Fig. 50D). CD8 T cell infiltration was evaluated by IHC (Fig. 50E). Blinded pathologist enumeration of the three regions with highest infiltration was calculated, showing a 12-fold increase in CD8 T cells after 7.16.4 treatment versus control (Ctrl: 3 ± 1, 7.16.4: 36 ± 19). Vaccinated TUBO tumor had the largest detected CD8 infiltration (74 ± 25). Overall, CD8$^+$ tumor infiltration was intermittent, with high-density regions scattered among areas with no

detectable $CD8^+$ TILs (Fig. 50E). We further validated CD8 T cell infiltration after 7.16.4 therapy by flow cytometry in a parallel cohort of treated and control mice (Fig. 50F, n=4 each). An overall increase in CD45+ infiltrates (Ctrl: 6.84 ± 1.85%, 7.16.4: 16.95 ± 5.88%, p=0.036) and CD8+ T cells (Ctrl: 0.41 ± 0.19%, 7.16.4: 4.96 ± 1.96%, p=0.018) was detected after mAb treatment. Interestingly, the majority of CD8+ TILs expressed the T cell exhaustion marker PD-1 (Fig. 50G, 79.7 ± 10.3%) compared to control tumors (20.5 ± 9.3%, p=0.0001). Collectively these results suggest this treatment model promotes an inactive and exhausted CD8 T cell status despite tumor infiltration, leading to reduced IFN-γ production which can be detected by ^{89}Zr-anti-IFN-γ PET imaging.

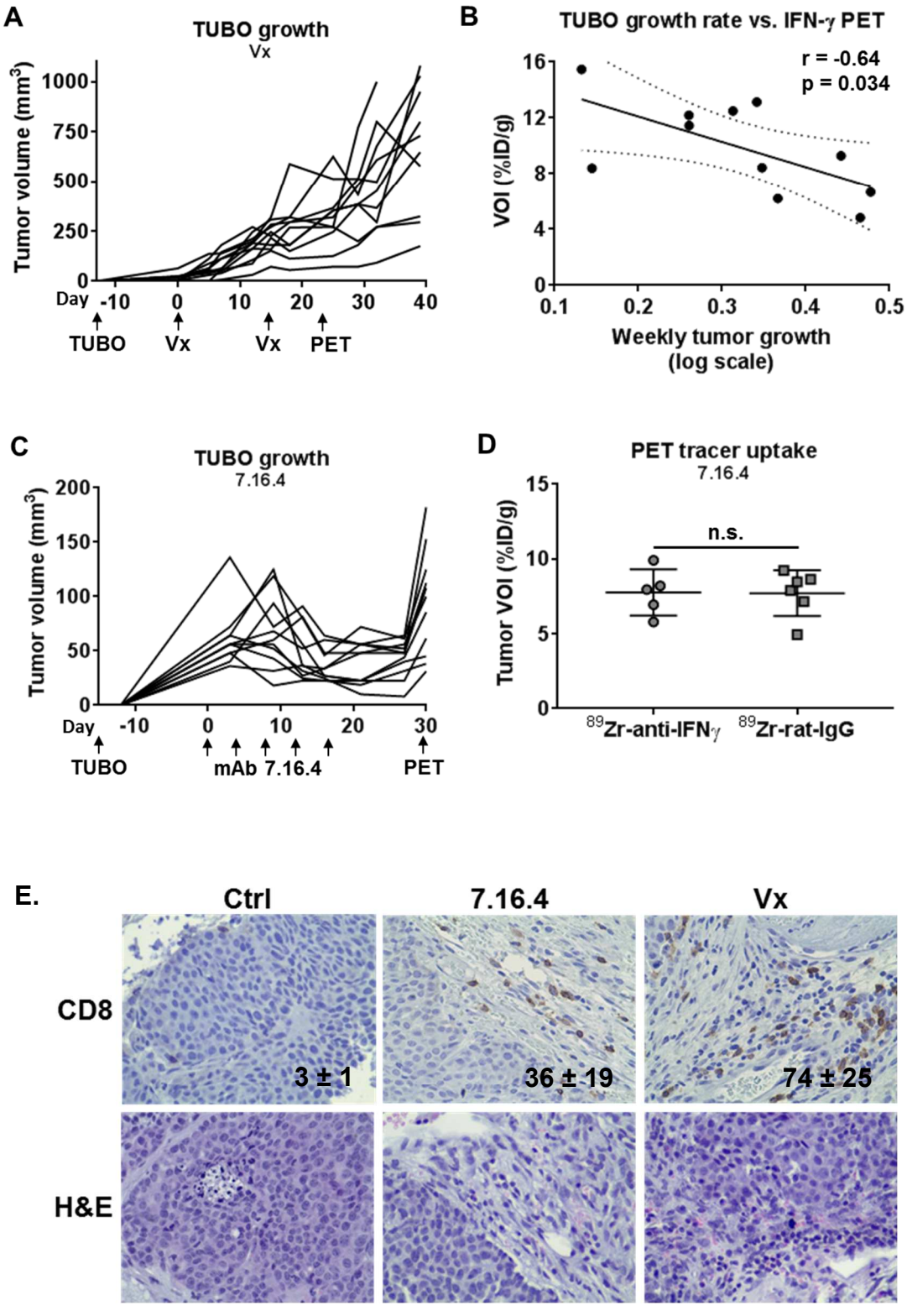
A
TUBO growth
Vx
Tumor volume (mm3)
1000
750
500
250
0
Day -10 0 10 20 30 40
TUBO
Vx
Vx
PET
B
TUBO growth rate vs. IFN-γ PET
r = -0.64
p = 0.034
VOI (%ID/g)
16
12
8
4
0
0.1 0.2 0.3 0.4 0.5
Weekly tumor growth
(log scale)
C
TUBO growth
7.16.4
Tumor volume (mm3)
200
150
100
50
0
Day -10 0 10 20 30
TUBO
mAb 7.16.4
PET
D
PET tracer uptake
7.16.4
Tumor VOI (%ID/g)
15
10
5
0
n.s.
89Zr-anti-IFNγ
89Zr-rat-IgG
E.
Ctrl
7.16.4
Vx
CD8
3 ± 1
36 ± 19
74 ± 25
H&E

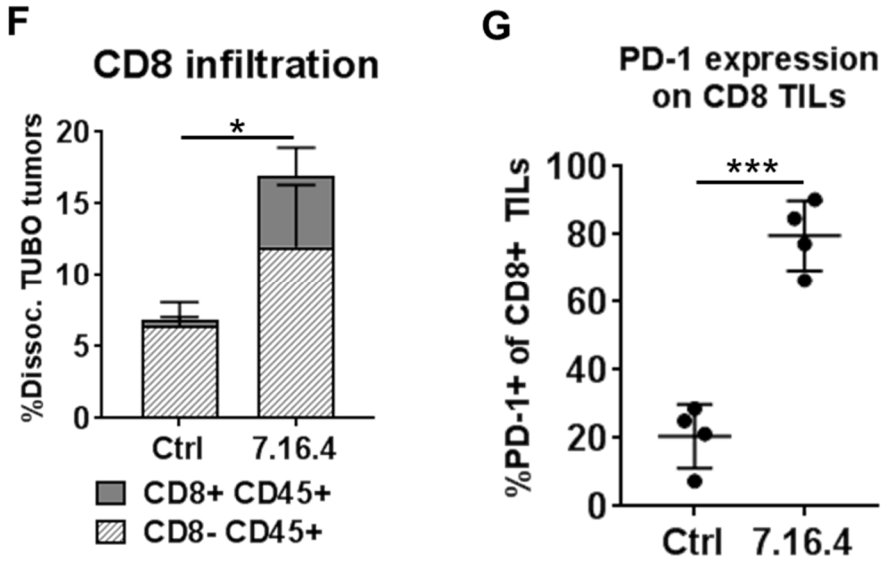

Figure 50. IFN-γ PET depicts response to ITx. Tumor volume was monitored in TUBO-bearing vaccinated BALB/c mice (n=11). TUBO cells were inoculated 13 days prior to the start of vaccinations, to allow for variability in tumor volumes at treatment onset. Vaccines were given on days 0 and 14. PET imaging was conducted on day 28 (A); weekly tumor growth rate, calculated by regression analysis of log tumor growth, versus ^{89}Zr-anti-IFN-γ tracer uptake is plotted for each mouse and evaluated by Pearson's correlation (B); tumor growth was monitored during passive immunotherapy with anti-neu mAb 7.16.4, given as 5 doses at 1.5 mg i.p. every 3-4 days as indicated beginning 15 days after tumor inoculation. ^{89}Zr-anti-IFN-γ (n=5) or ^{89}Zr-rat-IgG control (n=6) PET imaging was conducted 30 days after treatment onset (C); tumor VOIs were calculated for ^{89}Zr-anti-IFN-γ or ^{89}Zr-rat-IgG tracers in 7.16.4 treated TUBO-bearing mice (D); intratumoral localization of CD8 was analyzed by IHC on FFPE tissue (400×). H&E sections are included. CD8 enumeration is found in the lower right corner of each panel (E); control and 7.16.4-treated tumors (n=4 each) were dissociated and analyzed for T cell infiltration by flow cytometry by staining for CD45 and CD8 (F); PD-1 expression was analyzed by flow cytometry (G) on CD8+ tumor infiltrates from (F). * denotes $p < 0.05$, ***denotes $p < 0.001$.

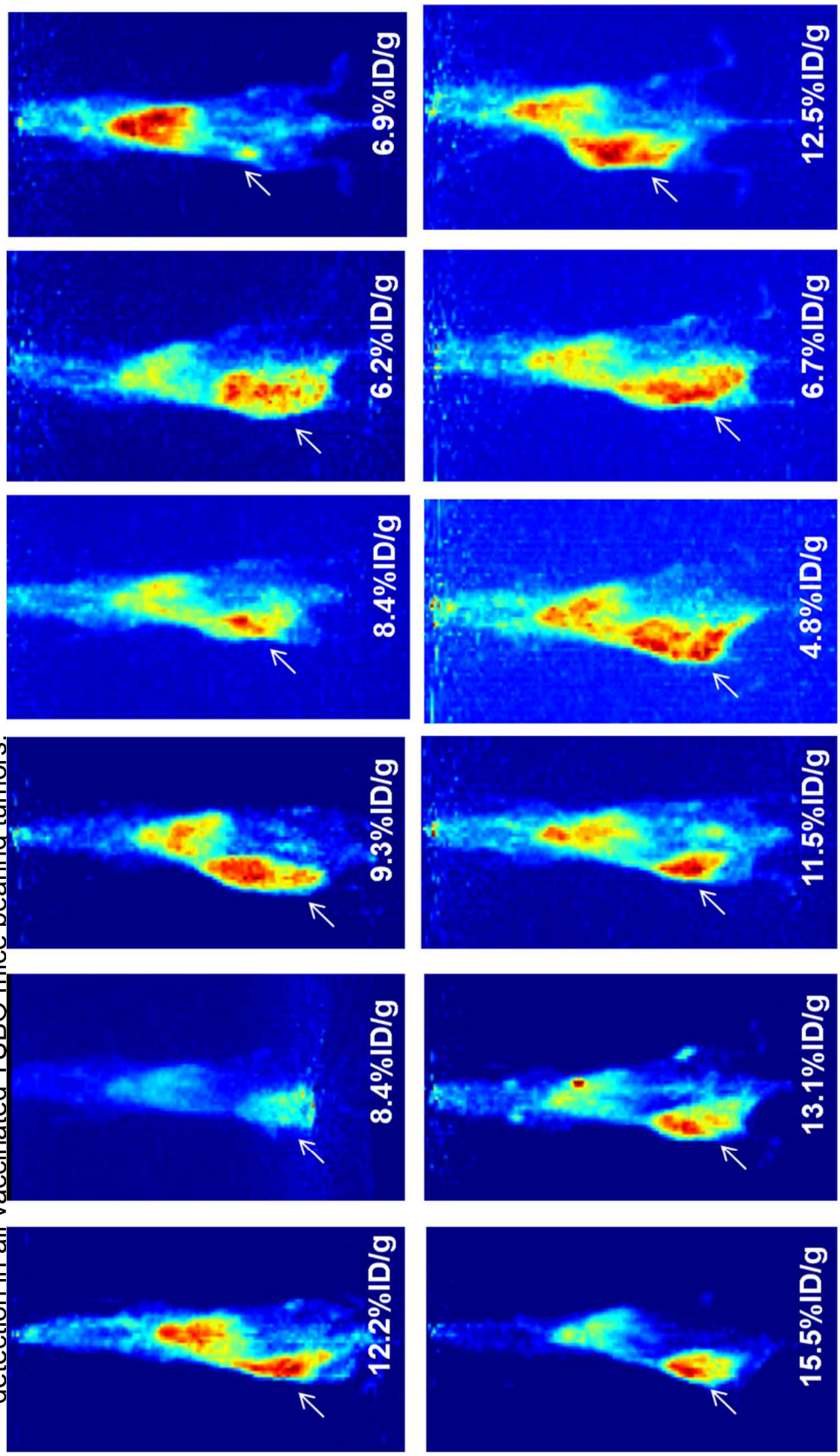

Figure 51. ^{89}Zr-IFN-γ PET of vaccinated mice for correlation to tumor growth. MIP images of ^{89}Zr-anti-IFNγ detection in all vaccinated TUBO mice bearing tumors.

4.3 DISCUSSION

Several major drawbacks to the use of general T cell surface markers and immune checkpoint ligands for PET imaging can complicate the assessment of immunotherapy response. T cells are densely present in normal secondary lymphoid tissues, such as the spleen, thymus and lymph nodes, which may hinder tumor-specific T cell imaging. Intratumoral detection of total $CD3^+$ T cells and $CD8^+$ cytotoxic lymphocytes has been shown to positively correlate with patient outcomes(277,278). However, the chronic inflammatory tumor microenvironment promotes checkpoint molecule expression, driving cytotoxic T cells into an exhausted state with diminished effector activity. Visualizing components of checkpoint signaling axes (e.g. PD1/PD-L1) can provide go-or-no-go treatment decisions by selecting patients with higher likelihood of responding to checkpoint blockade(279). In general, these methods do not measure downstream effector function of cytotoxic T cells. Larimer *et al.* reported on the utility of a peptide-based imaging tracer specific granzyme B, a cytotoxin released by activated CTL using a syngeneic colon cancer model(45). The tracer identified responders from non-responders after mono- or combinatorial anti-CTLA-4 and anti-PD1 targeted inhibition; however, it is unclear whether the peptide tracer (7.46 ± 2.24 μg per mouse) solicited inhibitory effects on the enzymatic activity of granzyme B. Nevertheless, the study substantiates the rationale that imaging effector molecules along the T cell signaling axis may provide a better readout of immune response to treatment.

In this study, the capabilities of IFN-γ PET were demonstrated to measure active anti-tumor immunity, providing a predictive tool for non-invasive *in situ* tumor evaluation. This approach is highly specific to the tumor compared to total T cell imaging due to the

fact that IFN-γ is secreted by CTLs within the tumor. Imaging CD3, on the other hand, targets the general T cell population that are not only localized in the tumor but also in other lymphoid tissues. Find antibody-based tracers to immune cell surface molecules were found to may create artifacts in the experimental system. Efforts to label CD8-specific full-length mAbs (clones 2.43 and non-depleting YTS-105.18) resulted in depletion of the target cell population and tracer accumulation in the kidneys with lack of secondary lymphoid tissue detection (data not shown) despite detection of CD8+ tumor infiltrates by flow cytometry and IHC (Fig. 6E-F). Anti-CD3 mAb clone 2C11 is routinely utilized for its pan-T cell receptor agonist activity, which may also potentially alter T cell function *in vivo*. Alternatively, it is conceivable that tracers to surface receptors may antagonize signaling, which could create off-target effects. Careful selection of antibody clones or construction of antibody fragment-based tracers like the CD8 diabody generated by Tavare et al.(213) or the VHH probe by Rashidian et al.(258) may alleviate some of these factors, but thorough quality control is necessary. Tracers targeting soluble cell products may also circumvent many of these problems.

A caveat to detection of cytokines by PET imaging is the soluble nature of these proteins. Localization of ^{89}Zr-anti-IFN-γ was observed in the spleen after CpG-ODN treatment and in the tumor after HER2/neu vaccination, suggesting the tracer is sequestered within the tissue.^{89}Zr-anti-IFN-γ complexes *in vitro* and find maximal binding when TUBO cells are pre-incubated with IFN-γ, supporting the working hypothesis that localized imaging is due to detection of IFN-γ associated with its receptor.

Ex vivo validation experiments showed a general trend in agreement with the PET imaging results, a direct correlation to tracer uptake is difficult to establish. These assays,

similar to a biopsy, are sampling a fragment of a heterogeneous tumor, yielding opportunity for equivocal results. Further, our IHC analyses on TUBO tumors (Fig. 6E) show the tissue is non-uniform, with regions of variable CD8 T cell infiltration after ITx ranging from moderate density to a virtual absence. For these reasons, imaging tools like immunoPET are advantageous, bridging a clinical need by providing a more comprehensive view of the entire tumor microenvironment.

These results showed ^{89}Zr-anti-IFN-γ tracer uptake can be indicative of response to therapy in both cancer vaccination and TAA-specific mAb models. IFN-γ PET further demonstrated it may be more sensitive for determining response to immunotherapy when compared to peripheral immune evaluation, a point which should be evaluated further. IFN-γ PET has the potential to serve as a universal non-invasive measurement of immune activity *in situ* for a variety of cancers with virtually any immunotherapy modality with no need for knowledge of specific antigens or cumbersome *ex vivo* antigen recall assays. Additionally, the utility of IFN-γ PET can potentially expand beyond cancer immune monitoring to include examination of localized inflammatory conditions such as injury, infection, or autoimmune disease. Taken together, these results support the development of IFN-γ PET tracers for clinical evaluation of tumor immunotherapy.

CHAPTER 5. MATERIALS AND METHODS

5.1 *In vitro* cell culture and *in vitro* tumor induction

5.1.1 Cell culture and propagation

All cells were adhered and grown at 37 °C with 5% CO_2 according to the following conditions listed in Table 15. All cells were split once they reached 80% confluence and were tested for mycoplasma with MycoAlert Mycoplasma Detection Kit (Lonza) and certified by the Biobanking and Correlative Services Core at Wayne State University.

Cell Line	Characteristic	Media	Passage	Obtained
BT-474	ER+, HER2+	1:1 DMEM:F12 (VWR) + 5% FBS + 1% Pen-Strep + 1% NEAA	1×/ week	Dr. Jason S. Lewis (MSKCC, NY, USA)
JIMT-1	HER2+, trastuzumab resistant	DMEM + 1% Pen-strep + 5% FBS	2×/week	Dr. Jason S. Lewis (MSKCC, NY, USA)
MDA-MB-468	TNBC, EGFR-high		3×/week	Dr. Julie Boerner (Wayne State, Detroit, USA)
MDA-MB-231	TNBC, EGFR-high		2×/week	Dr. Steven Patrick (Wayne State, Detroit, USA)
MDA-MB-453	TNBC-EGFR low		2×/week	ATCC
TUBO	Neu+	DMEM (High Glucose),10% NCTC, 10% FBS, 1% L-glutamine, 1% NEAA, 1% Pen-Strep, 0.1% 2-mercaptoethanol, 1% Sodium Bicarbonate, oxalacetic acid, sodium pyruvate, insulin	3×/week	Dr. Guido Forni (U. Torino, Torino, Italy)

Table 15. Cell lines and growth conditions.

5.1.2 Tumor induction

All animal handling and manipulations were conducted in accordance with the guidelines set by Wayne State University Institutional Animal Use and Care Committee. Female athymic nu/nu mice (6-8 week old) were purchased from Charles Rivers Laboratories (Wilmington, MA). All cells in 150 µL 1:1 media:Matrigel (BD Biosciences, Bedford, MA) were injected on the right shoulder at concentrations listed in Table 16. Monitoring of tumor growth was performed weekly with calipers. The tumor volume was calculated using the formula: length × width × height × pi/6. Mice with tumor volumes ranging from 150 – 250 mm^3 were utilized.

Cell Line	Characteristic	Xenograft Protocol (cells)
BT-474	ER+, HER2+	Estrogen pellet 3 days prior (0.72 mg slow-release) 10×10^6
JIMT-1	HER2+, trastuzumab resistant	5×10^6
MDA-MB-468	TNBC, EGFR-high	3×10^6
MDA-MB-231	TNBC, EGFR-high	5×10^6
MDA-MB-453	TNBC-EGFR low	5×10^6
TM00089	TNBC, PDX	-

Table 16. Tumor inoculation protocol.

5.1.3 NeuT mice and TUBO tumor induction

Heterozygous BALB/NeuT (NeuT) mice were in-house bred and provided to us by the lab of Professor Wei-Zen Wei. NeuT male mice, which express a transforming rat *neu*, develop atypical ductal hyperplasia in 1-2 parotid glands by 6 weeks of age which progresses to multifocal acinic cell adenocarcinoma *in situ* at ~19 weeks of age(273).

BALB/c mice (6-8 week old) were purchased from Charles River Laboratories (Wilmington, MA) and were inoculated with TUBO cells in the #4 mammary fat pad. Monitoring of tumor growth was performed weekly with calipers.

5.2 Antibody conjugation to chelates

p-Benzyl-isothiocyanate-desferrioxamine (DFO-Bz-SCN, Macrocylics, Inc.) or *p*-SCN-Bn-1,4,7-triazacyclononane-1,4-7-triacetic acid (NOTA, Macrocyclics, Inc.) was conjugated to the antibodies listed on Table 17 according to previously published protocols(269). The synthesis was performed using the mole equivalence of DFO or NOTA to the antibody listed in Table 17 in 0.9% saline, pH ~9 at 37 °C for 1 h. The monoclonal antibody (mAb) DFO- or NOTA-conjugates were obtained by passing through a spin column filter with a molecular weight cut-off of 30 kDa (GE Vivaspin 500) using sterile saline as eluting buffer.

Antibody	Company	DFO:mAb Mole Ratio	Specific Activity (mCi/mg)	Clone or Catalog No. (if applicable)
Trastuzumab (Herceptin ®)	Genentech	1:4	4	
Non-specific human IgG	Sigma-Aldrich	1:4	5	14506
Cetuximab (Erbitux®)	Genentech	1:5	5	
Anti-CD3	eBioscience	1:5	5	145-2C11
Anti-IFNγ	eBioscience	1:5	5	AN-18
Anti-rat IgG	Jackson ImmunoResearch	1:5	5	012-000-003
Anti-armenian hamster IgG	Jackson ImmunoResearch	1:5	5	eBio299Arm
Anti-neu	In House	1:4* (NOTA:mAb)	5	7.16.4

Table 17. Antibodies and labeling conditions.
Note: *the chelate used for conjugation was NOTA.

5.3 Radiochemistry

5.3.1 ^{89}Zr-radiochemistry

Approximately 1 mCi (37 MBq) of ^{89}Zr-oxalate (3D Imaging, LLC) was neutralized to pH 7.0 – 7.2 using 1 M Na_2CO_3. mAb-DFO (200 µg) was added to the ^{89}Zr solution and pH was adjusted back to 7.0 if needed. The reaction was quenched after 1-1.5 h incubation at room temperature upon addition of 5 µL of 50 mM ethylenediaminetetraacetic acid (EDTA) (pH ~7.0) to eliminate any non-specifically bound radiometal.

5.3.2 ^{64}Cu-radiochemistry

mAb-NOTA (200 µg) was added to 1 mCi (37 MBq) ^{64}Cu solution and the pH was adjusted to ~5 with 0.1 M ammonium acetate. The reaction was quenched after 1-1.5 h incubation at room temperature upon addition of 5 µL of 50 mM EDTA (pH ~7.0) to eliminate any non-specifically bound radiometal.

5.3.3 Radiolabeling efficiency

Radiolabeling efficiency was determined via radio-instant thin layer chromatography (iTLC) using silica gel-impregnated iTLC strip (Agilent Technologies, Santa Clara, CA) and 50 mM EDTA as the solid and mobile phase respectively. Pure ^{89}Zr-mAb or ^{64}Cu-mAb was obtained through spin column centrifugation (GE Vivaspin 500, MWCO: 30 kDa) with saline used for eluting unbound radiometal. mAbs were assessed for immunoreactivity as previously described(280).

5.4 Drugs and Treatments

Drug	Company	Treatment Dose	Treatment Length	Delivery Vehicle
Dasatinib (Sprycel™)	Sellechem	75 mg/kg (Aim 1) 50 mg/kg (Aim 2)	7 or 14 d 5 d	1:1 water:glycerol
Cetuximab	Genentech	0.3 mg	2×/week 3 weeks	Saline i.p. injection
CpG-ODN	Integrated DNA Technologies	100 μg	1 h prior to imaging	PBS Intramuscular injection
HER2/neu DNA Vaccine	In house	20 μg pGM-CSF + 50 μg pE2TM	See scheme in Chapter 4	PBS Intramuscular injection
7.16.4	In house	1 mg in filtered ascites	5× every 3-4 d	PBS i.p. injection

Table 18. Drugs used in the studies.

5.4.1 Molecular therapy

Dasatinib was administered to tumor-bearing mice via oral gavage (p.o.) for treatment length described in Table 18. Untreated control mice were given a 1:1 mix of water and glycerol (150 μL total volume via oral gavage) as placebo. Cetuximab (i.p.) was administered intraperitoneally (i.p.) to tumor bearing mice (Table 18). Food and water was given *ad libitum.* Tumor volumes were recorded 2-3 times per week. Percent change in tumor volume was analyzed using measurements obtained before the start of treatment to the time of imaging following formula: ((start tumor volume – end tumor volume)/start tumor volume)×100.

5.4.2 Immunotherapy

For NeuT vaccination, mice were depleted of Tregs by intraperitoneal (i.p.) injection of 500 μg anti-CD25 mAb PC61 10 days prior to the first vaccination. The HER2/neu DNA vaccine consists of an admixture of 20 μg of pGM-CSF (encoding murine GM-CSF) and 50 μg pE2TM (encoding the extracellular and transmembrane regions of

human HER2) in 50 µL PBS, which is injected intramuscularly (i.m.) into each gastrocnemius followed immediately by application of electrode gel and square wave electroporation using a BTX830 (BTX Harvard Apparatus, Holliston, MA).

Mice bearing TUBO tumors were injected i.p. 5 times every 3-4 days with sterile-filtered ascites containing 1 mg anti-neu mAb 7.16.4 diluted in PBS to a final volume of 300 µL.

5.5 IC_{50} Calculations

Wells (96-well clear bottom plate, Corning) were seeded with ~1×10^4 cells and incubated for 18 h. Dasatinib was dissolved in DMSO (Sigma-Aldrich) at a 50 mM concentration. Serial dilutions of dasatinib (1nM to 1 mM) were made and cells were treated in 100 µL complete media and incubated for 72 h. Media was removed and cells were washed 1× with phosphate buffered saline (PBS) before addition of alamar blue (Life Technologies) in fresh media (1:10 Alamar blue:media) to measure cell viability. After 4 h incubation, absorbance was read at 570 nm on an Infinite M200 plate reader (Tecan). IC_{50} was calculated as the log(concentration) vs. absorbance – control well absorbance in GraphPad Prism (v. 7.02).5.5

5.6 Internalization Assay

Internalization of radiolabeled antibodies was evaluated on appropriate cell lines. Wells were seeded with ~5×10^5 cells and incubated for 18 h. Cells were treated with the established IC_{50} for dasatinib (Sellechem, reconstituted in DMSO) in complete media. After incubation, media was removed, and cells were washed 1 × PBS. Radiolabeled protein [1 µCi/mL (37 kBq/mL), 150 ng] in 1 mL of media was then added to each well. The plates were incubated at 37 °C for 2 h. Following the incubation period, the media

was collected, and the cells were rinsed with 1 mL 1× PBS, twice. Surface-bound activity was removed by washing the cells in 1 mL 100 mM acetic acid + 100 mM glycine (1:1, pH 3.5) at 4 °C. The cells were then lysed with 1 mL 1 M NaOH. All washes (media plus PBS, acid and alkaline) were collected in separate tubes and measured for bound activity using a gamma counter (Perkin Elmer). The %-internalized activity was calculated as the ratio of the activity of the lysate and the total activity collected from the media, PBS, acid and base washes, normalized to 50,000 cells counted using a Countess II Automated Cell Counter (Thermo Fisher).

5.7 In vitro competitive binding assay

Binding of radiolabeled mAbs was evaluated in appropriate cell lines. Wells were seeded with ~10×10^4 cells and incubated for 18 h. After incubation, radiolabeled protein [1 μCi/mL (37 kBq/mL, 100 ng)] in 1 mL of media was added to each well with or without 10-fold excess unlabeled mAb (1 μg). The plates were incubated at 4 °C for 1 h. Following the incubation period, the media was collected and the cells were rinsed with 1 mL 1× phosphate buffered saline (PBS) twice. The cells were then lysed with 1 mL 1 M NaOH. All washes (media plus PBS and alkaline) were collected in separate tubes and measured for counts using a gamma counter (Perkin Elmer). The %-bound activity was calculated as the ratio of the activity of the lysate and the total activity collected from the media, PBS, acid and base washes, and was normalized to cell count using a Countess II Automated Cell Counter (Thermo Fisher).

5.8 Western Blotting

Cells were lysed on ice using 1× RIPA buffer (Pierce) supplemented with HALT protease and phosphatase inhibitor cocktail (Pierce.). Tumors were mechanically lysed

using a handheld homogenizer Polytron PE 1200E (VWR) in the same buffer. Total protein was calculated by the Pierce BCA Protein Assay Kit (Thermo Fisher) using the microplate procedure and read at A562 nm.

Lysates were prepared in NuPAGE lithium dodecyl sulfate (LDS) sample buffer (Life Technologies) supplemented with 2-mercaptoethanol (Sigma-Aldrich), and brought up to 15 μL with lysis buffer, and incubated at 95 °C for 5 min. Proteins (15 μg for cell lysates, and 10 μg for tumor lysates) and ladder (Precision Plus, BioRad) were separated on a 4-12% before transfer to Immobilon-P polyvinylidene difluoride (PVDF) membrane (Millipore Sigma. Membranes were blocked in 5% non-fat dry milk in tris-buffered saline (TBS) (KD Medical)-0.1% Tween20 (Amresco) for 1 h at room temperature. Primary antibodies were diluted 1:1000 in TBST with 0.02% sodium azide and incubated at 4 °C for 16 h with gentle rocking before blotting with horseradish peroxidase (HRP)-linked secondary antibodies in 5% milk-TBST for 2 h at room temperature (Table 19). Proteins were visualized using Amersham ECL (GE) and images collected using a ChemiDoc (BioRad) system. Images were analyzed using Image Lab (BioRad) software and densitometry was calculated using ImageJ software
(NIH) following previously described protocol (SYBIL).

Antibody	Clone	Company (Catalog Number)
HER2	D8F12	Cell Signaling (4290)
pHER2 (Y1221/1222	6B12	Cell Signaling (2243)
Src	36D10	Cell Signaling (2109)
pSrc (Y416)	D49G4	Cell Signaling (6943)
EGFR-XP	D38B1	Cell Signaling (8839)
pEGFR (Y845)	N/A	Cell Signaling (2231)
CD8α	D4W2Z	Cell Signaling (98941)
CD3ε	D4V8L	Cell Signaling (99940)
GAPDH	G-9	Santa Cruz (365062)
B-tubulin	9F3	Cell Signaling (2128)
Histone H3	1B1B2	Cell Signaling (14269)

Table 19. Antibody clones and catalog numbers used for western blotting.

Anti-rabbit and anti-mouse HRP-linked secondary antibodies were purchased from GE (NA934, NA931).

5.9 PET Imaging

Injections were administered intravenously (i.v.) in the lateral tail vein in 100-150 μL sterile saline (Table 20). Small-animal PET scans were acquired from 1-120 hours p.i. using a microPET R4 or Focus220 scanner (Siemens Concorde Microsystems). The mice were fully anesthetized with 1-2% isoflurane (Baxter, Deerfield, IL) during the scan. Images were reconstructed via filter back projection. ASIPro VM^{TM} software (Concorde Microsystems) was used to analyze volumes-of-interest (VOI) on various planar sections from the acquired image by manually drawing on the tumor site and on select organs. The average VOI was calculated and expressed as % injected dose per gram of tissue (%ID/g).

Tracer	Imaging Dose (μCi)	Antibody Dose (μg)	Imaging Time (h p.i.)
^{18}F-FDG	150-200	-	1 h
^{89}Zr-trastuzumab	200-240	66.7-80	48 h
^{89}Zr-IgG (human)	200-240	66.7-80	48 h
^{89}Zr-cetuximab	180-200	36-40	48 h
^{89}Zr-anti-IFNγ	180-240	42.8 – 57.1	72 h
^{89}Zr-anti-CD3			72 h
^{89}Zr-anti-rat IgG			72 h
^{89}Zr-anti-hamster IgG			72 h
^{64}Cu-Ab4	200-240	66.8 - 80	24 h

Table 20. Tracers and used imaging or antibody doses.

5.10 Biodistribution

^{89}Zr-trastuzumab biodistribution was performed 48 h p.i. in BT-474 or JIMT-1 tumor bearing Nude mice. To prove specificity, ^{89}Zr-IgG [20-30 μCi, 0.74-1.11 MBq, 336.02-504.0 nmol, 5-7.5 μg] was injected in mice with BT-474 or JIMT-1 tumors to assess non-specific accumulation of the tracer. ^{89}Zr-anti-IFNγ biodistribution was performed at 72 h p.i. in BALB/c mice, and for blocking studies, 80 μg of cold AN-18 was co-injected with the probe in a separate cohort of mice. Select organs were harvested post-sacrifice, weighed and measured for bound radioactivity with a gamma counter (Perkin Elmer 2480 Wizard 2).

20-30 μCi of the tracer [20-30 μCi, 0.74-1.11 MBq, 336.02-504.0 nmol, 5-7.5 μg] was injected into the lateral tail vein. Tissues of interest were removed at indicated timepoints and counts were performed using a gamma counter (Perkin Elmer Wizard2). The %ID/g was calculated as the % of activity bound to the tissue normalized against total administered activity per gram of tissue weight.

5.11 Autoradiography and immunohistochemistry (IHC)

5.11.1 Autoradiography

Autoradiography was performed following previously reported protocols(281). Briefly, after PET imaging tumors were excised and snap frozen in liquid nitrogen before being embedding in OCT medium and cut into 5 μm sections (Leica CM 1850) and mounted on positively charged slides (Fisher). Digital autoradiography was performed by placing slides in a film cassette against a phosphor imaging plate (Fujifilm BAS-MS2325, Fuji Photo Film) at -20 °C for 18 h. Phorphor imaging plates were read at a pixel resolution of 25 μm with a Typhoon 7000 IP plate reader (GE Healthcare).

5.11.2 Frozen immunohistochemistry and hematoxylin and eosin (H&E)

Sections were fixed in ice-cold acetone for 10 minutes and dried at room temperature for 20 minutes. Endogenous peroxidase activity was blocked with 3% H_2O_2 for 10 minutes before blocking with protein block solution from the mouse and rabbit specific HRP/3,3'-diaminobenzidine(DAB) detecting IHC kit (abcam, ab64264) for 1 h at room temperature. Slides were incubated with primary antibodies for 18 h at 4 °C (Table 21). Slides were developed using the same HRP/DAB detecting IHC kit and dehydrated with alcohols and xylenes before being covered with permount and coverslipped. Imaging was performed using a slide scanner (Leica SCN400) and visualized using Leica SCN400 image viewer software.

Antibody	Clone	Catalog Number	Dilution
HER2	D8F12	4290	1:200
Src	36D10	2109	1:50
EGFR-XP	D38B1	8839	1:50

Table 21. Antibody catalog numbers and dilutions for IHC.

5.11.3 FFPE Immunohistochemistry and H&E

After euthanasia, tumors were harvested and fixed in formalin before being embedded in paraffin. Blocks were sectioned into 4 μm sections using a Sakura Accu-Cut SRM microtome (Catalog#: SRM-200 CV) and adhered onto positively charged slides (Histomax Plus, VWR). Slides were then incubated for 12 minutes at 65 °C and deparrafinized in washes of xylene and graded alcohols. Antigen retrieval was performed in PT module buffer (TA-250-PM4X, Fisher) for CD8 (1:200). Primary antibody incubations were performed for 1 h at room temperature in a humidified chamber. Secondary antibody incubations and DAB were performed following manufacturers protocols. CD8 T cell enumeration was conducted by a blinded board-certified pathologist. Each tumor sample was screened for hotspots of CD8 lymphocytes using a Nikon Eclipse Ci microscope at 100× magnification. The number of $CD8^+$ T lymphocytes was counted in the three regions of highest infiltration at 400x magnification with a 0.55 mm field diameter, and an average was calculated. For H&E staining, tissue sections were dipped in xylenes, graduated alcohol and distilled water washes. They were then stained with hematoxylin (TA-125-MH, Fisher) for 5 minutes, rinsed with an acid wash for 1 minute and a bluing agent for 15 seconds. Eosin staining was applied to slides for 1

minute and slides were rinsed in 95% ethanol three times. Lastly, sections went through a series of graded alcohol and xylenes steps to dehydrate sections in preparation for mounting with Permount (UN1294, Fisher). Pictures were taken with a Spot Idea camera using Spot 5.2 software (Spot, Sterling Heights, MI).

5.12 Quantitative real-time PCR

Tumor tissue was snap frozen in liquid nitrogen. Total tumor RNA was collected by Trizol preparation (Thermo Fisher, Waltham, MA) after homogenization. cDNA was synthesized with ProtoScript II reverse transcriptase (New England Biolabs, MA). Real-time qPCR was conducted with iTaq Universal SYBR Green Supermix (Bio-Rad Laboratories, Hercules, CA) using 10 ng cDNA/well and 500 nM primers specific to the indicated gene (Life Tech, Carlsbad, CA) (Table 22). Relative mRNA quantities are calculated by $2^{-\Delta CT}$ compared to GAPDH.

Target	Forward primer	Reverse primer
CD3	CACTCTGGGCTTGCTGATGG	TCATAGTCTGGGTTGGAACAGG
CD8	GCTGGTAGTCTGCATCCTGCTTC	TTGCTAGCAGGCTATCAGTGTTGTG
IFNγ	GAGCTCATTGAATGCTTGGC	GCGTCATTGAATCACACCTG
PD-1	CGTCCCTCAGTCAAGAGGAG	GTCCCTAGAAGTGCCCAACA
GAPDH	AAGCTCACTGGCATGGCCTTC	TGCTTCACCACCTTCTTGATGTC

Table 22. qPCR primers.

5.13 ELISA

Tumor tissue was homogenized in standard RIPA buffer with protease inhibitor cocktail (Sigma-Aldrich). Protein concentration was measured by BCA assay (ThermoFisher). High protein binding plates (ThermoFisher) were coated with 3 µg/mL anti-mouse-IFN-γ mAb clone AN-18 (eBioscience) in coating buffer (0.1 M Na_2HPO_4, pH

to 9.0) and washed prior to addition of samples or standard curve using recombinant mouse IFN-γ (Peprotech, Rocky Hill, NJ) in duplicate. IFN-γ was detected with biotin-conjugated anti-mouse IFN-γ clone R4-6A2 (eBioscience), avidin-HRP (ThermoFisher), and TMB substrate (ThermoFisher).

5.14 Serum IgG measurement

Serum HER2- and neu-specific IgG were quantified by flow cytometry with a BD FACSCanto II flow cytometer (Becton Dickinson, Franklin Lakes, NJ), using HER2 over-expressing SKOV3 cells or neu transfected 3T3/NKB cells as previously described(282). Regression analysis was conducted using standard curves of anti-HER2 mAb TA-1 (Calbiochem, Burlington, MA) or anti-neu mAb 7.16.4 (Calbiochem, Burlington, MA).

5.15 IFN-γ ELISPOT

HER2- and neu-specific IFN-γ production was measured by ELISPOT assay as previously described(283). Recombinant HER2 or neu (10 μg/mL, Sino Biologicals, Beijing, China) were incubated with splenocytes for 48 h in round-bottom wells, followed by transfer to anti-IFN-γ coated (clone AN-18, eBioscience) ELISPOT plates (Millipore Sigma, Burlington, MA) for an additional 48 h. Spots were detected by biotinylated anti-IFN-γ (clone R4-6A2, eBioscience) and avidin-HRP (Becton Dickinson, Franklin Lakes, NJ), followed by enumeration with an ImmunoSpot analyzer (Cellular Technology Limited, Cleveland, OH). Results are expressed as spot forming units (SFU) per 10^6 cells.

5.16 Tumor dissociation and flow cytometry

TUBO tumors from untreated BALB/c mice were dissociated using the GentleMACs Dissociator and mouse tumor dissociation kit (Miltenyi, Germany) following the manufacturer protocol. Cells were stained with a combination of antibodies listed in

Table 23. All antibodies/dyes were purchased from eBIoscience (San Diego, CA). Samples were analyzed on a BD FACSCantoII flow cytometer (Becton Dickinson, Franklin Lakes, NJ) and samples were gated on the viable fraction.

Antibody	Fluorophore	Clone
CD45	FITC	30-F11
TCRβ	APC	H57-597
CD8	PE-Cy7	53-6.7
PD-1	APC	J43
Viability dye	eFluor780	

Table 23. Flow cytometry antibodies and reagents.

5.17 Statistical Analysis

Statistical analysis was performed using two-way ANOVA test in *in vitro* assays and tumor uptake comparison. An unpaired t-test was used for tumor VOI comparisons. A value of $P<0.05$ was considered statistically significant. Data were expressed as the mean ± S.D.

CHAPTER 6. CONCLUSIONS AND FUTURE DIRECTIONS

The studies described herein encompass three parts including i) examination of ^{89}Zr-trastuzumab to "monitor the status of Src status after dasatinib treatment in HER2+ BC; ii) "Using ^{89}Zr-cetuximab pet imaging to visualize membrane EGFR expression following dasatinib treatment in triple negative breast cancer", and iii) "Using immunoPET imaging to monitor tumor response to immunotherapy." The results are summarized below.

6.1 Conclusions

In chapter 2, the relationship between Src activation and HER2 was investigated. ^{89}Zr-trastuzumab was hypothesized to provide a surrogate read out of Src inhibition in HER2+ breast cancer. ^{89}Zr-trastuzumab is specific for HER2+ breast cancers. After dasatinib treatment in mice bearing BT-474 or JIMT-1 tumors, ^{89}Zr-trastuzumab uptake decreased compared to control, untreated tumors, and where standard-of-care FDG-PET imaging did not visualize differences in uptake between treated and untreated groups. ^{89}Zr-trastuzumab tumor uptake correlated with tumor regression and abrogation of pSrc (Y416) levels as measured by tumor western blot. ^{89}Zr-trastuzumab can potentially assess tumor response to dasatinib in HER2+ breast cancer and could be used as a surrogate tool to monitor early changes in Src signaling downstream of HER2.

In chapter 3, ^{89}Zr-cetuximab was utilized as a surrogate marker of EGFR membrane expression and availability. Upon dasatinib treatment *in vitro* EGFR localized to the plasma membrane, and pSrc (Y416) levels decreased, suggesting dasatinib efficacy. ^{89}Zr-cetuximab was specific for high-EGFR expressing TNBC cell lines through *in vitro* uptake and internalization assays, and through *in vitro* PET imaging studies with

a lowly EGFR expressing MDA-MB-453 cell line used as an uptake control. After dasatinib treatment, EGFR localized to the plasma membrane, where ^{89}Zr-cetuximab binding and internalization increased. In tumor models, ^{89}Zr-cetuximab tumor uptake was significantly higher in dasatinib treated mice compared to control mice. Interestingly, in KRAS+ MDA-MB-468 tumors, this translocation was associated with a cetuximab treatment benefit when combining dasatinib and cetuximab after imaging, whereas in KRAS-mutant MDA-MB-231 tumors, there was no cetuximab treatment benefit, which has been observed clinically. In conclusion, ^{89}Zr-cetuximab could be used as a marker of EGFR localization to predict response to cetuximab treatment, while still keeping KRAS status in mind.

In chapter 4, a new immunoPET probe targeting IFN-γ was developmed. Using ^{89}Zr-IFN-γ PET imaging, active immunotherapy response was visualized, and it was concluded that targeting soluble cytokine IFNγ with ^{89}Zr-anti-IFNγ as a read out of activated cytotoxic T cells is superior to monitoring TILs with ^{89}Zr-anti-CD3 after immunotherapy. In a syngeneic and spontaneous tumor model, ^{89}Zr-anti-IFNγ tumor uptake increased after dendritic cell vaccine compared to untreated control, and response, as measured by tumor VOI, was correlated with tumor regression. There was an increase in CD3, CD8, and IFNγ mRNA after vaccination, an increase in CD8 T cell infiltration via IHC after vaccination, and an increase in IFNγ protein as measured by western blot. ^{89}Zr-anti-IFNγ PET uptake did not increase above baseline levels in a model where T cells have become exhausted and display PD-1. Collectively, IFN-γ PET may serve as a non-invasive, comprehensive approach to evaluate tumor immunotherapy.

6.2 Future directions

A main challenge surrounding cancer therapeutics is designing a treatment

strategy that targets many heterogeneous cancer populations. Currently, breast tumors are characterized individually and thoroughly prior to treatment to identify a personalized approach to therapy, yet challenges remain in accurate breast tumor subtyping. Inaccuracies arise from mistakes in the collection and laboratory processing step, and when metastasis has occurred, from the inability to collect samples from every lesion. Utilizing immunoPET would meet this need by enabling non-invasive, full body profiling of all lesions in the body before, during, and after treatments to tailor each regimen to the patient's tumor load. The studies described in this dissertation have supported this hypothesis through imaging response to tyrosine kinase inhibitors and immunotherapies alike, and these results provided fundamental insights into the biology of the tumor microenvironment, allowing for further refinement of treatment strategies.

A promising area of research for BC is through combination therapy. The most widely used combination treatments include targeting the PI3K/AKT/mTOR pathways(284). For example, the BOLERO study had demonstrated efficacy of combining a m-TOR inhibitor and endocrine therapy to restore hormonal sensitivity(284). Palbocib (Ibrance®) has been combined with letrozole (Femara®) to treat ER+/HER2- patients in the metastatic realm. Trastuzumab has been combined with lapatinib (Tykeb®) or pertuzumab (Perjeta®) to treat HER2+ metastatic BCs(284). Many clinical trials have also been evaluating the use of combination checkpoint inhibitors, for example combining the blockade of CTLA-4 and the PD-1/PD-L1 pathways. Early results have shown an increase in efficacy of immunotherapy and slowing of primary tumor growth and metastasis(285).

To enhance response rates, a number of studies have suggested combining checkpoint inhibitors with targeted therapies, since there is evidence linking oncogene

de-addiction and immunomodulation. In EGFR overexpressing TNBC, responses to PD-1 and PD-L1 antibodies have been dismal, potentially due to the PD1/PD-L1 pathway as a mechanism of resistance for EGFR-TKIs. In preclinical studies, mutant EGFR lung cancer models treated with anti-PD-1 have demonstrated delayed tumor growth, suggesting a synergistic effect between anti-EGFR therapies and anti-PD-L1 in the clinic(286). Additionally, PD-1/PD-L1 antibodies have been combined with VEGF blocking agents in vivo and resulted in a synergistic anti-tumor effect(287). Currently, a phase II clinical trial is recruiting for TNBC (NCT02849496) patients to undergo combination atezolizumab (Opdivo®, anti-PD-L1) and veliparib (ABT-888, PARP inhibition) therapy. A similar study in small cell lung cancer showed that combining atezolizumab with chemotherapy as first line treatment resulted in significantly longer overall survival and progression free survival compared to chemotherapy alone.

These strategies would allow for disruption of tumor-induced immunosuppression, and therefore allow for the immune system to recognize the tumor presence and improve the anti-tumor response of checkpoint inhibitors and targeted therapies. In order to improve anti-cancer responses, inhibitory molecules would be blocked first to allow the immune system to directly attack the cancer. One consideration is the issue of toxicity in combining therapies. It would be important to appropriately dose and time treatment regimens to achieve high response and low off-target effects, especially since immunomodulation typically targets the entire immune system. Additionally, it is important that synergy is achieved with combination therapy, and not just two independent responses, or one therapy decreasing the targetable population of its partner treatment.

A main challenge for combination therapy is designing a strategy that targets many

heterogeneous subtypes of cancer. To achieve this, though, the phenotype of each individual BC case should be thoroughly investigated and subtyped before treatment allowing researchers and clinicians to gather a general overview of what can be targeted. A more precise and personalized characterization of each cancer case and potential pathways of resistant on a patient-to-patient basis would be useful in determining appropriate treatments. This could include pre-treatment characterization of targetable tumor associated antigens (TAAs) (such as PD-1, HER2, or EGFR, for example) through IHC, FISH, or immunoPET imaging. Additionally, blood samples for immune cell population expression could be used to determine which T-cells to target. Whole genome profiling is also of use for prognosis. It is also important during treatment to constantly monitor the tumor microenvironment and immune profile to make necessary adjustments to combinations, and immunoPET could meet this need. For example, tumors can be monitored for expression of targetable biomarkers before treatment in a non-invasive way. After treatment has begun, tumors could be re-tested for continuous expression of the targeted biomarker, as well as surveillance of expression of known resistance pathways. Finally, after a treatment regimen has concluded, tumors can be re-imaged for expression of targeted biomarker to see if treatment was successful. Furthermore, we have demonstrated that targeted biomarkers can be visualized with various PET tracers, allowing for personalized imaging strategies.

In the final imaging study, panitumumab (Vectibix®) was labeled with ^{89}Zr at a target specific activity of 5 mCi/mg. Mice bearing MDA-MB-468 tumors were imaged following the scheme outlined in Figure 52A. At 42 h p.i., untreated mice demonstrated a 14.8 ± 1.2 %ID/g tumor uptake, compared to dasatinib treated mice with 16.9 ± 0.5%ID/g

($p < 0.001$)(Fig. 52B). ^{89}Zr-panitumumab imaged tumors had significantly higher uptake as compared to tumors imaged with a human IgG isotype control ($p < 0.001$)(Fig. 52C).

A.

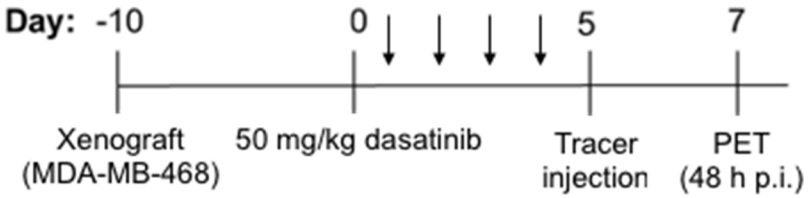

B.

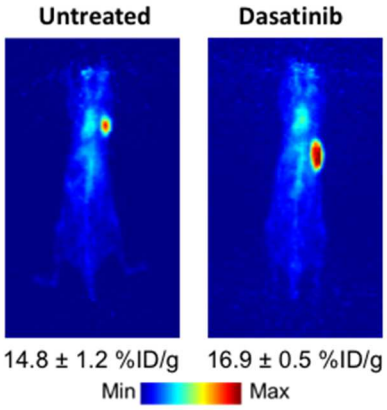

C.

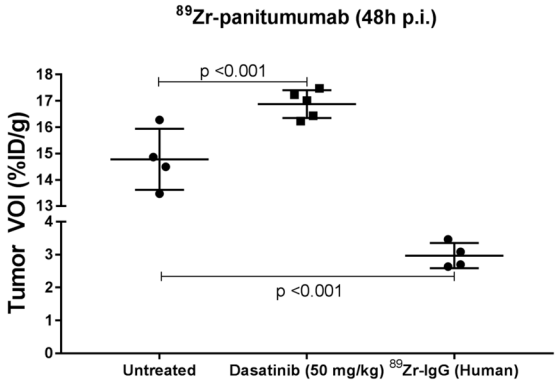

Figure 52. ^{89}Zr-panitumumab PET imaging in MDA-MB-468 tumors. Mice bearing MDA-MB-468 tumors were treated ith 50 mg/kg dasatinib for 5 d or left untreated before undergoing imaging with ^{89}Zr-panitumumab at 48 h p.i. (A); untreated mice (left) demonstrate lower tumor uptake compared to dasatinib treated mice (right) (B); ^{89}Zr-panitumumab imaged mice demonstrated significantly higher tumor uptake as compared to a non-specific isotype IgG (C).

When compared to ^{89}Zr-cetuximab PET imaging, ^{89}Zr-panitumumab imaged tumors demonstrated higher uptake (14.8 ± 1.2 %ID/g vs. 8.5 ± 1.7 %ID/g, $p < 0.001$)(Fig. 53). This body of work has demonstrated that cell-surface and soluble protein biomarkers can potentially be used to aid in diagnosis, treatment decisions, and treatment monitoring.

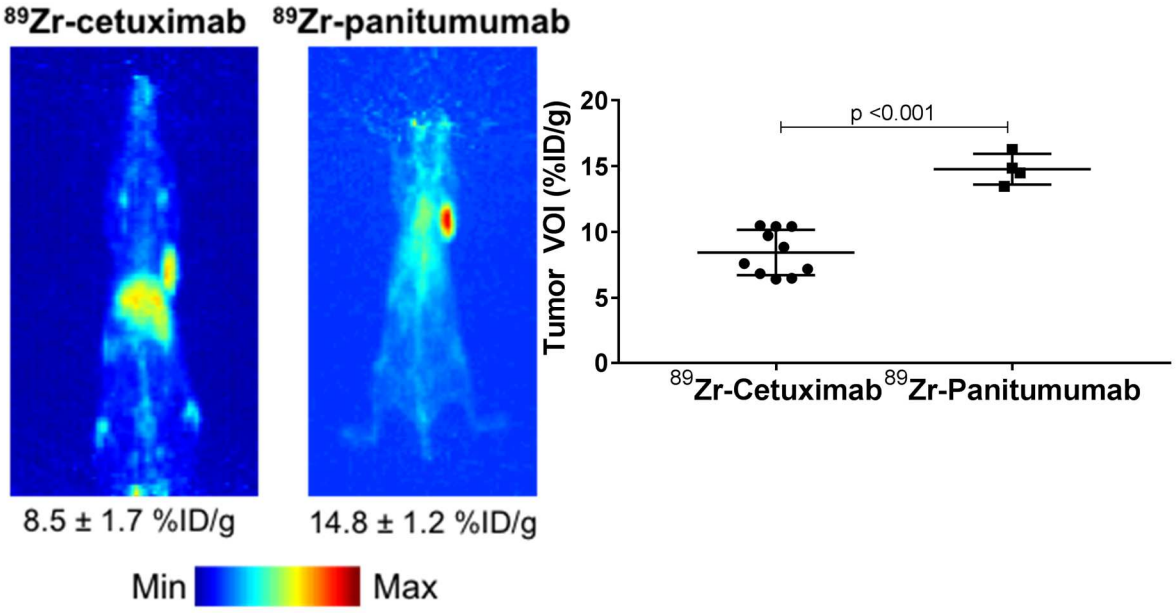

Figure 53. ^{89}Zr-panitumumab PET imaging compared to ^{89}Zr-cetuximab. Mice bearing MDA-MB-468 tumors were imaged with ^{89}Zr-cetuximab (left) or ^{89}Zr-panitumumab (right) at 48 h p.i.

APPENDIX – INTELLECTURAL PROPERTY

The information on the ^{89}Zr-α-IFNγPET tracer described in Chapter 4 comprises intellectual property of Wayne State University and is covered by a provisional patent filed by the university.

REFERENCES

1. Farwell MD, Pryma DA, Mankoff DA. PET/CT imaging in cancer: Current applications and future directions. Cancer. 2014. page 3433–45.
2. Gambhir SS. Molecular imaging of cancer with positron emission tomography. Nat. Rev. Cancer. 2002. page 683–93.
3. Peng H, S. Levin C. Recent Developments in PET Instrumentation. Curr Pharm Biotechnol. 2010;11:555–71.
4. Eubank WB, Mankoff DA, Schmiedl UP, Winter TC, Fisher ER, Olshen AB, et al. Imaging of oncologic patients: Benefit of combined CT and FDG PET in the diagnosis of malignancy. Am J Roentgenol. 1998;171:1103–10.
5. Van Wauwe JP, De Mey JR, Goossens JG. OKT3: a monoclonal anti-human T lymphocyte antibody with potent mitogenic properties. J Immunol. 1980;124:2708–13.
6. Grillo-López A, White C., Dallaire B, Varns C, Shen C, Wei A, et al. Rituximab: the first monoclonal antibody approved for the treatment of lymphoma. Curr Pharm Biotechnol [Internet]. 2000;1:278–87. Available from: http://dx.doi.org/10.1038/nrc3236%5Cnhttp://www.ncbi.nlm.nih.gov/pubmed/14576843%5Cnhttp://www.ncbi.nlm.nih.gov/pubmed/11467356%5Cnhttp://www.pubmedcentral.nih.gov/articlerender.fcgi?artid=2844047&tool=pmcentrez&rendertype=abstract
7. England TN. Use of Chemotherapy Plus a Monoclonal Antibody Against Her2. English J [Internet]. 2001;344:783–92. Available from:

http://www.nejm.org/doi/full/10.1056/NEJM200103153441101

8. Perez HL, Cardarelli PM, Deshpande S, Gangwar S, Schroeder GM, Vite GD, et al. Antibody-drug conjugates: Current status and future directions. Drug Discov. Today. 2014. page 869–81.
9. Shah DK, Haddish-Berhane N, Betts A. Bench to bedside translation of antibody drug conjugates using a multiscale mechanistic PK/PD model: A case study with brentuximab-vedotin. J Pharmacokinet Pharmacodyn. 2012;39:643–59.
10. Vasalou C, Helmlinger G, Gomes B. A Mechanistic Tumor Penetration Model to Guide Antibody Drug Conjugate Design. PLoS One. 2015;10.
11. Kovtun Y V, Goldmacher VS. Cell killing by antibody-drug conjugates. Cancer Lett [Internet]. 2007;255:232–40. Available from: http://www.ncbi.nlm.nih.gov/pubmed/17553616
12. Loganzo F, Sung M, Gerber H-P. Mechanisms of Resistance to Antibody–Drug Conjugates. Mol Cancer Ther [Internet]. 2016;15:2825–34. Available from: http://mct.aacrjournals.org/lookup/doi/10.1158/1535-7163.MCT-16-0408
13. Winter G, Harris WJ. Humanized antibodies. Immunol Today. 1993;14:243–6.
14. Tjandra JJ, Ramadi L, McKenzie IFC. Development of human anti-murine antibody (HAMA) response in patients. Immunol Cell Biol. 1990;68:367–76.
15. Nayak TK, Brechbiel MW. Radioimmunoimaging with longer-lived positron-emitting radionuclides: Potentials and challenges. Bioconjug. Chem. 2009. page 825–41.
16. Kaur S, Venktaraman G, Jain M, Senapati S, Garg PK, Batra SK. Recent trends in antibody-based oncologic imaging. Cancer Lett. 2012. page 97–111.
17. Holland JP, Sheh Y, Lewis JS. Standardized methods for the production of high

specific-activity zirconium-89. Nucl Med Biol. 2009;36:729–39.

18. Lindenberg M, Turkbey I, Adler S, Do K, Kummar S, Kurdziel K, et al. Dosimetry and first human experience with 89Zr Panitumumab. J Nucl Med [Internet]. 2015;56:1029-. Available from: http://jnm.snmjournals.org.libezproxy.open.ac.uk/content/56/supplement_3/1029.short

19. Tolmachev V, Velikyan I, Sandström M, Orlova A. A HER2-binding Affibody molecule labelled with 68Ga for PET imaging: direct in vivo comparison with the 111In-labelled analogue. Eur J Nucl Med Mol Imaging [Internet]. 2010;37:1356–67. Available from: http://www.scopus.com/inward/record.url?eid=2-s2.0-77954955636&partnerID=tZOtx3y1%5Cnhttp://dx.doi.org/10.1007/s00259-009-1367-7

20. Xavier C, Blykers A, Vaneycken I, D'Huyvetter M, Heemskerk J, Lahoutte T, et al. 18F-nanobody for PET imaging of HER2 overexpressing tumors. Nucl Med Biol. 2016;43:247–52.

21. Su X, Cheng K, Liu Y, Hu X, Meng S, Cheng Z. PET imaging of insulin-like growth factor type 1 receptor expression with a 64Cu-labeled Affibody molecule. Amino Acids [Internet]. 2015;47:1409–19. Available from: http://link.springer.com/10.1007/s00726-015-1975-4

22. Garousi J, Andersson KG, Mitran B, Pichl ML, Stahl S, Orlova A, et al. PET imaging of epidermal growth factor receptor expression in tumours using 89Zr-labelled ZEGFR:2377 affibody molecules. Int J Oncol. 2016;48:1325–32.

23. Eder M, Knackmuss S, Le Gall F, Reusch U, Rybin V, Little M, et al. 68Ga-labelled

recombinant antibody variants for immuno-PET imaging of solid tumours. Eur J Nucl Med Mol Imaging. 2010;37:1397–407.

24. Lütje S, Franssen GM, Sharkey RM, Laverman P, Rossi EA, Goldenberg DM, et al. Anti-CEA antibody fragments labeled with [18F]AlF for PET imaging of CEA-expressing tumors. Bioconjug Chem. 2014;

25. Wong P, Li L, Chea J, Delgado MK, Poku E, Szpikowska B, et al. Synthesis, Positron Emission Tomography Imaging, and Therapy of Diabody Targeted Drug Lipid Nanoparticles in a Prostate Cancer Murine Model. Cancer Biother Radiopharm [Internet]. 2017 [cited 2018 Jun 18];32:247–57. Available from: http://www.ncbi.nlm.nih.gov/pubmed/28910151

26. Zettlitz KA, Tavaré R, Knowles SM, Steward KK, Timmerman JM, Wu AM. ImmunoPET of malignant and normal B cells with89Zr- and124I-labeled obinutuzumab antibody fragments reveals differential CD20 internalization in vivo. Clin Cancer Res. 2017;23:7242–52.

27. Viola-Villegas NT, Sevak KK, Carlin SD, Doran MG, Evans HW, Bartlett DW, et al. Noninvasive imaging of PSMA in prostate tumors with 89Zr-Labeled huJ591 engineered antibody fragments: The faster alternatives. Mol Pharm. 2014;11:3965–73.

28. Knowles SM, Tavaré R, Zettlitz KA, Rochefort MM, Salazar FB, Jiang ZK, et al. Applications of immunopet: Using124I-anti-PSCA A11 minibody for imaging disease progression and response to therapy in mouse xenograft models of prostate cancer. Clin Cancer Res. 2014;20:6367–78.

29. Boyle AJ, Cao PJ, Hedley DW, Sidhu SS, Winnik MA, Reilly RM. MicroPET/CT

imaging of patient-derived pancreatic cancer xenografts implanted subcutaneously or orthotopically in NOD-scid mice using64Cu-NOTA-panitumumab F(ab')2fragments. Nucl Med Biol. 2015;

30. Deri MA, Zeglis BM, Francesconi LC, Lewis JS. PET imaging with 89Zr: From radiochemistry to the clinic. Nucl Med Biol. 2013;40:3–14.
31. Deri MA, Ponnala S, Zeglis BM, Pohl G, Dannenberg JJ, Lewis JS, et al. Alternative chelator for 89Zr radiopharmaceuticals: Radiolabeling and evaluation of 3,4,3-(LI-1,2-HOPO). J Med Chem. 2014;57:4849–60.
32. Verel I, Visser GWM, Boellaard R, Stigter-van Walsum M, Snow GB, van Dongen G a MS. 89Zr immuno-PET: comprehensive procedures for the production of 89Zr-labeled monoclonal antibodies. J Nucl Med. 2003;44:1271–81.
33. Perk LR, Vosjan MJWD, Visser GWM, Budde M, Jurek P, Kiefer GE, et al. P-Isothiocyanatobenzyl-desferrioxamine: A new bifunctional chelate for facile radiolabeling of monoclonal antibodies with zirconium-89 for immuno-PET imaging. Eur J Nucl Med Mol Imaging. 2010;37:250–9.
34. Holland JP, Williamson MJ LJ. Unconventional nuclides for radiopharmaceuticals. Mol Imaging Biol. 2010;36:729–39.
35. Zeglis BM, Davis CB, Aggeler R, Kang HC, Chen A, Agnew BJ, et al. Enzyme-mediated methodology for the site-specific radiolabeling of antibodies based on catalyst-free click chemistry. Bioconjug Chem. 2013;24:1057–67.
36. Bhattacharyya S, Kurdziel K, Wei L, Riffle L, Kaur G, Hill GC, et al. Zirconium-89 labeled panitumumab: A potential immuno-PET probe for HER1-expressing

carcinomas. Nucl Med Biol. 2013;40:451–7.

37. Holland JP, Caldas-Lopes E, Divilov V, Longo V a, Taldone T, Zatorska D, et al. Measuring the pharmacodynamic effects of a novel Hsp90 inhibitor on HER2/neu expression in mice using Zr-DFO-trastuzumab. PLoS One [Internet]. 2010;5:e8859. Available from: http://www.pubmedcentral.nih.gov/articlerender.fcgi?artid=2810330&tool=pmcentrez&rendertype=abstract

38. Bensch F, Lamberts LE, Smeenk MM, Jorritsma-Smit A, Lub-de Hooge MN, Terwisscha van Scheltinga AGT, de Jong JR, Gietema JA, Schröder CP, Thomas M, Jacob W, Abiraj K, Adessi C, Meneses-Lorente G, James I, Weisser M, Brouwers AH de V. 89Zr-Lumretuzumab PET Imaging before and during HER3 Antibody Lumretuzumab Treatment in Patients with Solid Tumors. Clin Cancer Res. 2017;23:6128–37.

39. Holland JP, Divilov V, Bander NH, Smith-Jones PM, Larson SM, Lewis JS. ^{89}Zr-DFO-J591 for immunoPET of prostate-specific membrane antigen expression in vivo. J Nucl Med. 2010;51:1293–300.

40. Perk LR, Visser OJ, Stigter-Van Walsum M, Vosjan MJWD, Visser GWM, Zijlstra JM, et al. Preparation and evaluation of 89Zr-Zevalin for monitoring of 90Y-Zevalin biodistribution with positron emission tomography. Eur J Nucl Med Mol Imaging. 2006;33:1337–45.

41. Vugts DJ, Heuveling DA, Stigter-van Walsum M, Weigand S, Bergstrom M, van Dongen GAMS, et al. Preclinical evaluation of 89Zr-labeled anti-CD44 monoclonal antibody RG7356 in mice and cynomolgus monkeys: Prelude to Phase 1 clinical

studies. MAbs [Internet]. 2014;6:567–75. Available from: http://www.ncbi.nlm.nih.gov/pubmed/24492295%5Cnhttp://www.pubmedcentral.nih.gov/articlerender.fcgi?artid=PMC3984344

42. England CG, Ehlerding EB, Hernandez R, Rekoske BT, Graves SA, Sun H, et al. Preclinical Pharmacokinetics and Biodistribution Studies of 89Zr-Labeled Pembrolizumab. J Nucl Med [Internet]. 2017;58:162–8. Available from: http://www.ncbi.nlm.nih.gov/pubmed/27493273%5Cnhttp://www.pubmedcentral.nih.gov/articlerender.fcgi?artid=PMC5209640

43. Cole EL, Kim J, Donnelly DJ, Smith RA, Cohen D, Lafont V, et al. Radiosynthesis and preclinical PET evaluation of89Zr-nivolumab (BMS-936558) in healthy non-human primates. Bioorganic Med Chem. 2017;25:5407–14.

44. Nagengast WB, de Vries EG, Hospers GA, Mulder NH, de Jong JR, Hollema H, et al. In Vivo VEGF Imaging with Radiolabeled Bevacizumab in a Human Ovarian Tumor Xenograft. J Nucl Med [Internet]. 2007;48:1313–9. Available from: http://jnm.snmjournals.org/cgi/doi/10.2967/jnumed.107.041301

45. Larimer BM, Wehrenberg-Klee E, Dubois F, Mehta A, Kalomeris T, Flaherty K, et al. Granzyme B PET imaging as a predictive biomarker of immunotherapy response. Cancer Res. 2017;77:2318–27.

46. Gibson HM, McKnight BN, Malysa A, Dyson G, Wiesend WN, McCarthy CE, et al. IFNγ PET Imaging as a Predictive Tool for Monitoring Response to Tumor Immunotherapy. Cancer Res. 2018;

47. Larimer BM, Wehrenberg-Klee E, Caraballo A, Mahmood U. Quantitative CD3 PET Imaging Predicts Tumor Growth Response to Anti-CTLA-4 Therapy. J Nucl Med

[Internet]. 2016;57:1607–11. Available from: http://jnm.snmjournals.org/cgi/doi/10.2967/jnumed.116.173930

48. Tavare R, McCracken MN, Zettlitz KA, Salazar FB, Olafsen T, Witte ON, et al. Immuno-PET of Murine T Cell Reconstitution Postadoptive Stem Cell Transplantation Using Anti-CD4 and Anti-CD8 Cys-Diabodies. J Nucl Med [Internet]. 2015;56:1258–64. Available from: http://jnm.snmjournals.org/cgi/doi/10.2967/jnumed.114.153338

49. Girgis MD, Federman N, Rochefort MM, McCabe KE, Wu AM, Nagy JO, et al. An engineered anti-CA19-9 cys-diabody for positron emission tomography imaging of pancreatic cancer and targeting of polymerized liposomal nanoparticles. J Surg Res. 2013;185:45–55.

50. Lohrmann C, O'Reilly E, ODonoghue J, Yu K, Pandit-Taskar N, Lyashchenko S, Ruan S, Wu J, DeNoble P, Carrasquillo J, Schmidtlein C, Teng R, Lowery M, Varghese A, Estrella H, Scholz W, Maffuid P, Lewis J and WW. First-in-Human Study of 89Zr-DFO-HuMab-5B1 (MVT-2163) PET/CT imaging with and without HuMab-5B1 (MVT-5873) in patients with pancreatic cancer and other CA 19-9 positive malignancies. J Nucl Med. 2017;58:385.

51. Börjesson PKE, Jauw YWS, Boellaard R, de Bree R, Comans EFI, Roos JC, et al. Performance of immuno-positron emission tomography with zirconium-89-labeled chimeric monoclonal antibody U36 in the detection of lymph node metastases in head and neck cancer patients. Clin Cancer Res [Internet]. 2006;12:2133–40. Available from: http://www.ncbi.nlm.nih.gov/pubmed/16609026

52. Siravegna G, Marsoni S, Siena S, Bardelli A. Integrating liquid biopsies into the

management of cancer. Nat. Rev. Clin. Oncol. 2017. page 531–48.

53. Lorenz JM. Updates in Percutaneous Lung Biopsy: New Indications, Techniques and Controversies. Semin Intervent Radiol. 2012;319–24.

54. Ulaner GA, Hyman DM, Ross DS, Corben A, Chandarlapaty S, Goldfarb S, et al. Detection of HER2-Positive Metastases in Patients with HER2-Negative Primary Breast Cancer Using 89Zr-Trastuzumab PET/CT. J Nucl Med [Internet]. 2016;57:1523–8. Available from: http://jnm.snmjournals.org/cgi/doi/10.2967/jnumed.115.172031

55. El-Osta H, Hong DS, Wheler JJ, Fu S, Naing A, Falchook GS, et al. Outcomes of research biopsies in phase I clinical trials: the MD anderson cancer center experience. Oncologist [Internet]. 2011;16:1292–8. Available from: http://www.pubmedcentral.nih.gov/articlerender.fcgi?artid=3228176&tool=pmcentrez&rendertype=abstract

56. Ben-Haim S, Ell P. 18F-FDG PET and PET/CT in the Evaluation of Cancer Treatment Response. J Nucl Med. 2009;

57. Pandit-Taskar N, O'Donoghue JA, Durack JC, Lyashchenko SK, Cheal SM, Beylergil V, et al. A Phase I/II Study for Analytic Validation of 89Zr-J591 ImmunoPET as a Molecular Imaging Agent for Metastatic Prostate Cancer. Clin Cancer Res [Internet]. 2015;21:5277–85. Available from: http://clincancerres.aacrjournals.org/cgi/doi/10.1158/1078-0432.CCR-15-0552

58. Pandit-Taskar N, ODonoghue JA, Ruan S, Lyashchenko SK, Carrasquillo JA, Heller G, et al. First-in-Human Imaging with 89Zr-Df-IAB2M Anti-PSMA Minibody in Patients with Metastatic Prostate Cancer: Pharmacokinetics, Biodistribution,

Dosimetry, and Lesion Uptake. J Nucl Med [Internet]. 2016;57:1858–64. Available from: http://jnm.snmjournals.org/cgi/doi/10.2967/jnumed.116.176206

59. Dijkers EC, Oude Munnink TH, Kosterink JG, Brouwers a H, Jager PL, de Jong JR, et al. Biodistribution of 89Zr-trastuzumab and PET imaging of HER2-positive lesions in patients with metastatic breast cancer. Clin Pharmacol Ther [Internet]. 2010;87:586–92. Available from: http://dx.doi.org/10.1038/clpt.2010.12

60. Oude Munnink TH, Dijkers EC, Netters SJ, Lub-de Hooge MN, Brouwers AH, Haasjes JG, et al. Trastuzumab pharmacokinetics influenced by extent human epidermal growth factor receptor 2-positive tumor load. J. Clin. Oncol. 2010.

61. Bruno R, Washington CB, Lu JF, Lieberman G, Banken L, Klein P. Population pharmacokinetics of trastuzumab in patients with HER2+ metastatic breast cancer. Cancer Chemother Pharmacol. 2005;56:361–9.

62. Li C, Agarwal P, Gibiansky E, Jin JY, Dent S, Gonçalves A, et al. A Phase I Pharmacokinetic Study of Trastuzumab Emtansine (T-DM1) in Patients with Human Epidermal Growth Factor Receptor 2-Positive Metastatic Breast Cancer and Normal or Reduced Hepatic Function. Clin Pharmacokinet [Internet]. 2017 [cited 2018 Jun 4];56:1069–80. Available from: http://www.ncbi.nlm.nih.gov/pubmed/27995530

63. Agus DB, Gordon MS, Taylor C, Natale RB, Karlan B, Mendelson DS, et al. Phase I clinical study of pertuzumab, a novel HER dimerization inhibitor, in patients with advanced cancer. J Clin Oncol [Internet]. 2005;23:2534–43. Available from: http://www.ncbi.nlm.nih.gov/pubmed/15699478

64. Tran L, Baars JW, Aarden L, Beijnen JH, Huitema ADR. Pharmacokinetics of

rituximab in patients with CD20 positive B-cell malignancies. Hum Antibodies. 2010;19:7–13.

65. Jauw YWS, Zijlstra JM, de Jong D, Vugts DJ, Zweegman S, Hoekstra OS, et al. Performance of 89Zr-Labeled-Rituximab-PET as an Imaging Biomarker to Assess CD20 Targeting: A Pilot Study in Patients with Relapsed/Refractory Diffuse Large B Cell Lymphoma. Glod JW, editor. PLoS One [Internet]. 2017 [cited 2018 Jun 4];12:e0169828. Available from: http://www.ncbi.nlm.nih.gov/pubmed/28060891

66. Lamberts LE, Menke-Van Der Houven Van Oordt CW, Ter Weele EJ, Bensch F, Smeenk MM, Voortman J, et al. ImmunoPET with anti-mesothelin antibody in patients with pancreatic and ovarian cancer before anti-mesothelin antibody-drug conjugate treatment. Clin Cancer Res. 2016;22:1642–52.

67. Gebhart G, Lamberts LE, Wimana Z, Garcia C, Emonts P, Ameye L, et al. Molecular imaging as a tool to investigate heterogeneity of advanced HER2-positive breast cancer and to predict patient outcome under trastuzumab emtansine (T-DM1): The ZEPHIR trial. Ann Oncol. 2016;27:619–24.

68. Dijkers ECF, Kosterink JGW, Rademaker AP, Perk LR, van Dongen GAMS, Bart J, et al. Development and Characterization of Clinical-Grade 89Zr-Trastuzumab for HER2/neu ImmunoPET Imaging. J Nucl Med [Internet]. 2009;50:974–81. Available from: http://jnm.snmjournals.org/cgi/doi/10.2967/jnumed.108.060392

69. Carrasquillo J a, White JD, Paik CH, Raubitschek a, Le N, Rotman M, et al. Similarities and differences in 111In- and 90Y-labeled 1B4M-DTPA antiTac monoclonal antibody distribution. J Nucl Med. 1999;40:268–76.

70. Rizvi SNF, Visser OJ, Vosjan MJWD, van Lingen A, Hoekstra OS, Zijlstra JM, et al.

Biodistribution, radiation dosimetry and scouting of 90Y-ibritumomab tiuxetan therapy in patients with relapsed B-cell non-Hodgkin's lymphoma using 89Zr-ibritumomab tiuxetan and PET. Eur J Nucl Med Mol Imaging [Internet]. 2012;39:512–20. Available from: http://www.pubmedcentral.nih.gov/articlerender.fcgi?artid=3276758&tool=pmcentrez&rendertype=abstract

71. Laforest R, Lapi SE, Oyama R, Bose R, Tabchy A, Marquez-Nostra B V., et al. [89Zr]Trastuzumab: Evaluation of Radiation Dosimetry, Safety, and Optimal Imaging Parameters in Women with HER2-Positive Breast Cancer. Mol Imaging Biol. 2016;18:952–9.
72. Quinn B, Dauer Z, Pandit-Taskar N, Schoder H, Dauer LT. Radiation dosimetry of 18F-FDG PET/CT: Incorporating exam-specific parameters in dose estimates. BMC Med Imaging. 2016;
73. Breast Cancer Facts - National Breast Cancer Foundation [Internet]. [cited 2018 Jul 9]. Available from: http://www.nationalbreastcancer.org/breast-cancer-facts
74. Yarden Y, Pines G. The ERBB network: at last, cancer therapy meets systems biology. Nat Rev Cancer [Internet]. 2012 [cited 2018 Aug 3];12:553–63. Available from: http://www.ncbi.nlm.nih.gov/pubmed/22785351
75. Moasser MM. The oncogene HER2: Its signaling and transforming functions and its role in human cancer pathogenesis. Oncogene. 2007. page 6469–87.
76. Tzahar E, Waterman H, Chen X, Levkowitz G, Karunagaran D, Lavi S, et al. A hierarchical network of interreceptor interactions determines signal transduction by Neu differentiation factor/neuregulin and epidermal growth factor. Mol Cell Biol.

1996;

77. Brand TM, Iida M, Wheeler DL. Molecular mechanisms of resistance to the EGFR monoclonal antibody cetuximab. Cancer Biol. Ther. 2011. page 777–92.

78. Cao H, Lei ZM, Bian L, Rao C V. Functional nuclear epidermal growth factor receptors in human choriocarcinoma JEG-3 cells and normal human placenta. Endocrinology. 1995;136:3163–-3172.

79. Marti U, Burwen SJ, Wells A, Barker ME, Huling S, Feren AM, et al. Localization of epidermal growth factor receptor in hepatocyte nuclei. Hepatology. 1991;13:15–20.

80. Lin SY, Makino K, Xia W, Matin a, Wen Y, Kwong KY, et al. Nuclear localization of EGF receptor and its potential new role as a transcription factor. Nat Cell Biol. 2001;3:802–8.

81. Lo HW, Hung MC. Nuclear EGFR signalling network in cancers: Linking EGFR pathway to cell cycle progression, nitric oxide pathway and patient survival. Br. J. Cancer. 2006. page 184–8.

82. Lo H-W, Xia W, Wei Y, Ali-Seyed M, Huang S-F, Hung M-C. Novel prognostic value of nuclear epidermal growth factor receptor in breast cancer. Cancer Res. 2005;65:338–48.

83. Psyrri A, Yu Z, Weinberger PM, Sasaki C, Haffty B, Camp R, et al. Quantitative determination of nuclear and cytoplasmic epidermal growth factor receptor expression in oropharyngeal squamous cell cancer by using automated quantitative analysis. Clin Cancer Res [Internet]. 2005;11:5856–62. Available from: http://www.ncbi.nlm.nih.gov/pubmed/16115926

84. Diaz LK, Cryns VL, Symmans WF, Sneige N. Triple negative breast carcinoma and

the basal phenotype: From expression profiling to clinical practice. Adv. Anat. Pathol. 2007. page 419–30.

85. Cortazar P, Zhang L, Untch M, Mehta K, Costantino JP, Wolmark N, et al. Pathological complete response and long-term clinical benefit in breast cancer: The CTNeoBC pooled analysis. Lancet. 2014;384:164–72.

86. Conlin AK, Seidman AD. Taxanes in breast cancer: An update. Curr. Oncol. Rep. 2007. page 22–30.

87. Koboldt DC, Fulton RS, McLellan MD, Schmidt H, Kalicki-Veizer J, McMichael JF, et al. Comprehensive molecular portraits of human breast tumours. Nature. 2012;

88. Bianchini G, Balko JM, Mayer IA, Sanders ME, Gianni L. Triple-negative breast cancer: Challenges and opportunities of a heterogeneous disease. Nat. Rev. Clin. Oncol. 2016. page 674–90.

89. Lehmann BD, Bauer JA, Chen X, Sanders ME, Shyr Y, Pietenpol JA. Transcriptome Analysis of Triple Negative Breast Cancers Identifies Six Distinct Biological Subgroups and Reveals Therapeutic Strategies. Present 33rd Annu San Antonio Breast Cancer Symp [Internet]. 2010;Abstract PD01-07. Available from: http://www.abstracts2view.com/sabcs10/view.php?nu=SABCS10L_842%5Cnhttp://ascopost.com/articles/february-15-2011/triple-negative-breast-cancer-proving-to-be-genetically-diverse

90. Lee A, Djamgoz MBA. Triple negative breast cancer: Emerging therapeutic modalities and novel combination therapies. Cancer Treat. Rev. 2018. page 110–22.

91. Changavi A, Shashikala A, Ramji A. Epidermal growth factor receptor expression

in triple negative and nontriple negative breast carcinomas. J Lab Physicians. 2015;

92. Park HS, Jang MH, Kim EJ, Kim HJ, Lee HJ, Kim YJ, et al. High EGFR gene copy number predicts poor outcome in triple-negative breast cancer. Mod Pathol. 2014;

93. Jeong W, Doroshow JH, Kummar S. United States Food and Drug Administration approved oral kinase inhibitors for the treatment of malignancies. Curr Probl Cancer [Internet]. NIH Public Access; 2013 [cited 2018 Jul 9];37:110–44. Available from: http://www.ncbi.nlm.nih.gov/pubmed/23972982

94. Moradi-Kalbolandi S, Hosseinzade A, Salehi M, Merikhian P, Farahmand L. Monoclonal antibody-based therapeutics, targeting theepidermal growth factor receptor family: from herceptin toPan HER. J Pharm Pharmacol. 2018;

95. Sacco AG, Worden FP. Molecularly targeted therapy for the treatment of head and neck cancer: a review of the ErbB family inhibitors. Onco Targets Ther [Internet]. 2016;9:1927–43. Available from: http://www.ncbi.nlm.nih.gov/pubmed/27110122%5Cnhttps://www.ncbi.nlm.nih.gov/pmc/articles/PMC4831599/pdf/ott-9-1927.pdf

96. Monteverde M, Milano G, Strola G, Maffi M, Lattanzio L, Vivenza D, et al. The relevance of ADCC for EGFR targeting: A review of the literature and a clinically-applicable method of assessment in patients. Crit. Rev. Oncol. Hematol. 2015. page 179–90.

97. Sunada H, Magun BE, Mendelsohn J, MacLeod CL. Monoclonal antibody against epidermal growth factor receptor is internalized without stimulating receptor phosphorylation. Proc Natl Acad Sci U S A [Internet]. 1986;83:3825–9. Available from:

http://www.pubmedcentral.nih.gov/articlerender.fcgi?artid=323616&tool=pmcentrez&rendertype=abstract

98. Gridelli C, Maione P, Ferrara ML, Rossi A. Cetuximab and other anti-epidermal growth factor receptor monoclonal antibodies in the treatment of non-small cell lung cancer. Oncologist. 2009;14:601–11.

99. Alanazi IO, Khan Z. Understanding EGFR Signaling in Breast Cancer and Breast Cancer Stem Cells: Overexpression and Therapeutic Implications. Asian Pacific J Cancer Prev [Internet]. 2016;17:445–53. Available from: http://koreascience.or.kr/journal/view.jsp?kj=POCPA9&py=2016&vnc=v17n2&sp=445

100. Martinelli E, De Palma R, Orditura M, De Vita F, Ciardiello F. Anti-epidermal growth factor receptor monoclonal antibodies in cancer therapy. Clin. Exp. Immunol. 2009. page 1–9.

101. Bonomo P, Loi M, Desideri I, Olmetto E, Delli Paoli C, Terziani F, et al. Incidence of skin toxicity in squamous cell carcinoma of the head and neck treated with radiotherapy and cetuximab: A systematic review. Crit Rev Oncol Hematol [Internet]. 2017;120:98–110. Available from: http://dx.doi.org/10.1016/j.critrevonc.2017.10.011

102. Baselga J, Gómez P, Greil R, Braga S, Climent MA, Wardley AM, et al. Randomized phase II study of the anti-epidermal growth factor receptor monoclonal antibody cetuximab with cisplatin versus cisplatin alone in patients with metastatic triple-negative breast cancer. J Clin Oncol. 2013;31:2586–92.

103. Carey LA, Rugo HS, Marcom PK, Mayer EL, Esteva FJ, Ma CX, et al. TBCRC 001:

Randomized phase II study of cetuximab in combination with carboplatin in stage IV triple-negative breast cancer. J Clin Oncol. 2012;

104. Chung KY, Shia J, Kemeny NE, Shah M, Schwartz GK, Tse A, et al. Cetuximab shows activity in colorectal cancer patients with tumors that do not express the epidermal growth factor receptor by immunohistochemistry. J Clin Oncol. 2005;23:1803–10.

105. De Roock W, Piessevaux H, De Schutter J, Janssens M, De Hertogh G, Personeni N, et al. KRAS wild-type state predicts survival and is associated to early radiological response in metastatic colorectal cancer treated with cetuximab. Ann Oncol. 2008;19:508–15.

106. Di Nicolantonio F, Martini M, Molinari F, Sartore-Bianchi A, Arena S, Saletti P, et al. Wild-type BRAF is required for response to panitumumab or cetuximab in metastatic colorectal cancer. J Clin Oncol. 2008;26:5705–12.

107. Huang F, Xu LA, Khambata-Ford S. Correlation between gene expression of IGF-1r pathway markers and cetuximab benefit in metastatic colorectal cancer. Clin Cancer Res. 2012;18:1156–66.

108. Nevo J, Mattila E, Pellinen T, Yamamoto DL, Sara H, Iljin K, et al. Mammary-derived growth inhibitor alters traffic of EGFR and induces a novel form of cetuximab resistance. Clin Cancer Res. 2009;15:6570–81.

109. Ross JS, Slodkowska EA, Symmans WF, Pusztai L, Ravdin PM, Hortobagyi GN. The HER-2 Receptor and Breast Cancer: Ten Years of Targeted Anti-HER-2 Therapy and Personalized Medicine. Oncologist [Internet]. 2009;14:320–68. Available from:

http://theoncologist.alphamedpress.org/cgi/doi/10.1634/theoncologist.2008-0230

110. Wolff AC, Hammond MEH, Hicks DG, Dowsett M, McShane LM, Allison KH, et al. Recommendations for Human Epidermal Growth Factor Receptor 2 Testing in Breast Cancer: American Society of Clinical Oncology/College of American Pathologists Clinical Practice Guideline Update. Arch Pathol Lab Med [Internet]. 2014;138:241–56. Available from: http://www.archivesofpathology.org/doi/abs/10.5858/arpa.2013-0953-SA

111. Myers MB. Targeted therapies with companion diagnostics in the management of breast cancer: Current perspectives. Pharmgenomics. Pers. Med. 2016. page 7–16.

112. Carlson RW, Moench SJ, Hammond MEH, Perez E a, Burstein HJ, Allred DC, et al. HER2 testing in breast cancer: NCCN Task Force report and recommendations. J Natl Compr Canc Netw. 2006;4 Suppl 3:S1-22; quiz S23-4.

113. Krishnamurti U, Silverman JF. HER2 in Breast Cancer: A Review and Update. Adv Anat Pathol. 2014;21:100–7.

114. Vincent-Salomon A, Jouve M, Genin P, Fréneaux P, Sigal-Zafrani B, Caly M, et al. HER2 status in patients with breast carcinoma is not modified selectively by preoperative chemotherapy and is stable during the metastatic process. Cancer. 2002;94:2169–73.

115. Tapia C, Savic S, Wagner U, Schönegg R, Novotny H, Grilli B, et al. HER2 gene status in primary breast cancers and matched distant metastases. Breast Cancer Res [Internet]. 2007;9:R31. Available from: http://www.ncbi.nlm.nih.gov/pubmed/17511881%5Cnhttp://www.pubmedcentral.ni

h.gov/articlerender.fcgi?artid=PMC1929093

116. Dehdashti farrokh, wu ningying, Naughton michael j., Ma CX, Marquez-Nostra B V., Diebolder P, et al. Evaluation of [89Zr]trastuzumab-PET/CT in differentiating HER2-positive from HER2-negative breast cancer. Breast Cancer Res Treat. 2018;1–8.

117. Cho HS, Mason K, Ramyar KX, Stanley AM, Gabelli SB, Denney DW, et al. Structure of the extracellular region of HER2 alone and in complex with the Herceptin Fab. Nature. 2003;421:756–60.

118. Franklin MC, Carey KD, Vajdos FF, Leahy DJ, De Vos AM, Sliwkowski MX. Insights into ErbB signaling from the structure of the ErbB2-pertuzumab complex. Cancer Cell. 2004;5:317–28.

119. Martínez MT, Pérez-Fidalgo JA, Martín-Martorell P, Cejalvo JM, Pons V, Bermejo B, et al. Treatment of HER2 positive advanced breast cancer with T-DM1: A review of the literature. Crit. Rev. Oncol. Hematol. 2016. page 96–106.

120. Wood ER, Truesdale AT, McDonald OB, Yuan D, Hassell A, Dickerson SH, et al. A unique structure for epidermal growth factor receptor bound to GW572016 (Lapatinib): Relationships among protein conformation, inhibitor off-rate, and receptor activity in tumor cells. Cancer Res. 2004;64:6652–9.

121. Rabindran SK, Discafani CM, Rosfjord EC, Baxter M, Floyd MB, Golas J, et al. Antitumor activity of HKI-272, an orally active, irreversible inhibitor of the HER-2 tyrosine kinase. Cancer Res. 2004;64:3958–65.

122. Martin M, Holmes FA, Ejlertsen B, Delaloge S, Moy B, Iwata H, et al. Neratinib after trastuzumab-based adjuvant therapy in HER2-positive breast cancer (ExteNET): 5-

year analysis of a randomised, double-blind, placebo-controlled, phase 3 trial. Lancet Oncol. 2017;

123. Perez EA, Romond EH, Suman VJ, Jeong J-H, Sledge G, Geyer CE, et al. Trastuzumab Plus Adjuvant Chemotherapy for Human Epidermal Growth Factor Receptor 2–Positive Breast Cancer: Planned Joint Analysis of Overall Survival From NSABP B-31 and NCCTG N9831. J Clin Oncol [Internet]. 2014 [cited 2019 Mar 14];32:3744–52. Available from: http://www.ncbi.nlm.nih.gov/pubmed/25332249
124. Murphy CG, Modi S. HER2 breast cancer therapies: a review. Biologics [Internet]. 2009;3:289–301. Available from: http://www.pubmedcentral.nih.gov/articlerender.fcgi?artid=2726059&tool=pmcentrez&rendertype=abstract
125. Geyer CE, Forster J, Lindquist D, Chan S, Romieu CG, Pienkowski T, et al. Lapatinib plus Capecitabine for HER2-Positive Advanced Breast Cancer. N Engl J Med. 2006;
126. Swain SM, Baselga J, Kim S-B, Ro J, Semiglazov V, Campone M, et al. Pertuzumab, Trastuzumab, and Docetaxel in HER2-Positive Metastatic Breast Cancer. N Engl J Med. 2015;
127. Verma S, Miles D, Gianni L, Krop IE, Welslau M, Baselga J, et al. Trastuzumab emtansine for HER2-positive advanced breast cancer. N Engl J Med. 2012;
128. Chan A, Delaloge S, Holmes FA, Moy B, Iwata H, Harvey VJ, et al. Neratinib after trastuzumab-based adjuvant therapy in patients with HER2-positive breast cancer (ExteNET): a multicentre, randomised, double-blind, placebo-controlled, phase 3

trial. Lancet Oncol [Internet]. 2016 [cited 2018 Oct 23];17:367–77. Available from: http://www.ncbi.nlm.nih.gov/pubmed/26874901

129. Yu S, Liu Q, Han X, Qin S, Zhao W, Li A, et al. Development and clinical application of anti-HER2 monoclonal and bispecific antibodies for cancer treatment. Exp. Hematol. Oncol. 2017.

130. Connell CM, Doherty GJ. Activating HER2 mutations as emerging targets in multiple solid cancers. ESMO Open [Internet]. 2017;2:e000279. Available from: http://esmoopen.bmj.com/lookup/doi/10.1136/esmoopen-2017-000279

131. Abe O, Abe R, Enomoto K, Kikuchi K, Koyama H, Masuda H, et al. Effects of radiotherapy and of differences in the extent of surgery for early breast cancer on local recurrence and 15-year survival: An overview of the randomised trials. Lancet. 2005.

132. Clarke R, Tyson JJ, Dixon JM. Endocrine resistance in breast cancer - An overview and update. Mol Cell Endocrinol. 2015;

133. Perez EA. Impact, mechanisms, and novel chemotherapy strategies for overcoming resistance to anthracyclines and taxanes in metastatic breast cancer. Breast Cancer Res. Treat. 2009.

134. Hudis CA. Trastuzumab--mechanism of action and use in clinical practice. N Engl J Med [Internet]. 2007;357:39–51. Available from: http://www.ncbi.nlm.nih.gov/pubmed/17611206

135. Miller TW, Pérez-Torres M, Narasanna A, Guix M, Stål O, Pérez-Tenorio G, et al. Loss of Phosphatase and tensin homologue deleted on chromosome 10 engages ErbB3 and insulin-like growth factor-I receptor signaling to promote antiestrogen

resistance in breast cancer. Cancer Res. 2009;

136. Li J, Yen C, Liaw D, Podsypanina K, Bose S, Wang SI, et al. PTEN, a putative protein tyrosine phosphatase gene mutated in human brain, breast, and prostate cancer. Science (80-). 1997;

137. Saal LH, Holm K, Maurer M, Memeo L, Su T, Wang X, et al. PIK3CA mutations correlate with hormone receptors, node metastasis, and ERBB2, and are mutually exclusive with PTEN loss in human breast carcinoma. Cancer Res. 2005;

138. Yeatman TJ. A renaissance for SRC. Nat Rev Cancer. 2004;

139. Zhang S, Yu D. Targeting Src family kinases in anti-cancer therapies: Turning promise into triumph. Trends Pharmacol. Sci. 2012. page 122–8.

140. Playford MP, Schaller MD. The interplay between Src and integrins in normal and tumor biology. Oncogene. 2004. page 7928–46.

141. Pene-Dumitrescu T, Smithgall TE. Expression of a Src family kinase in chronic myelogenous leukemia cells induces resistance to imatinib in a kinase-dependent manner. J Biol Chem [Internet]. American Society for Biochemistry and Molecular Biology; 2010 [cited 2018 Jul 9];285:21446–57. Available from: http://www.ncbi.nlm.nih.gov/pubmed/20452982

142. Guest SK, Ribas R, Pancholi S, Nikitorowicz-Buniak J, Simigdala N, Dowsett M, et al. Src Is a Potential Therapeutic Target in Endocrine-Resistant Breast Cancer Exhibiting Low Estrogen Receptor-Mediated Transactivation. PLoS One [Internet]. Public Library of Science; 2016 [cited 2018 Jul 9];11:e0157397. Available from: http://www.ncbi.nlm.nih.gov/pubmed/27308830

143. Chen Y, Alvarez EA, Azzam D, Wander SA, Guggisberg N, Jordà M, et al.

Combined Src and ER blockade impairs human breast cancer proliferation in vitro and in vivo. Breast Cancer Res Treat [Internet]. 2011 [cited 2018 Jul 9];128:69–78. Available from: http://www.ncbi.nlm.nih.gov/pubmed/20669046

144. Biscardi JS, Ishizawar RC, Silva CM, Parsons SJ. Tyrosine kinase signalling in breast cancer: epidermal growth factor receptor and c-Src interactions in breast cancer. Breast Cancer Res. 2000;

145. Riggins RB, Thomas KS, Ta HQ, Wen J, Davis RJ, Schuh NR, et al. Physical and functional interactions between Cas and c-Src induce tamoxifen resistance of breast cancer cells through pathways involving epidermal growth factor receptor and signal transducer and activator of transcription 5b. Cancer Res. 2006;66:7007–15.

146. Irby RB, Yeatman TJ. Role of Src expression and activation in human cancer. Oncogene. 2000;19:5636–42.

147. Sharma MR, Wroblewski K, Polite BN, Knost JA, Wallace JA, Modi S, et al. Dasatinib in previously treated metastatic colorectal cancer: A phase II trial of the University of Chicago Phase II Consortium. Invest New Drugs. 2012;30:1211–5.

148. Creedon H, Brunton VG. Src kinase inhibitors: promising cancer therapeutics? Crit Rev Oncog [Internet]. 2012 [cited 2018 Jul 9];17:145–59. Available from: http://www.ncbi.nlm.nih.gov/pubmed/22471705

149. Mayer EL, Krop IE. Advances in targeting Src in the treatment of breast cancer and other solid malignancies. Clin. Cancer Res. 2010. page 3526–32.

150. Miller AA, Pang H, Hodgson L, Ramnath N, Otterson GA, Kelley MJ, et al. A phase II study of dasatinib in patients with chemosensitive relapsed small cell lung cancer

(Cancer and Leukemia Group B 30602). J Thorac Oncol Off Publ Int Assoc Study Lung Cancer [Internet]. 2010;5:380–4. Available from: http://ovidsp.ovid.com/ovidweb.cgi?T=JS&CSC=Y&NEWS=N&PAGE=fulltext&D=med6&AN=20087228%5Cnhttp://nt2yt7px7u.search.serialssolutions.com/?sid=OVID:Ovid+MEDLINE%28R%29+%3C2008+to+2010%3E&genre=article&id=pmid:20087228&id=doi:10.1097%2FJTO.0b013e3181cee36e&is

151. Lara PN, Longmate J, Evans CP, Quinn DI, Twardowski P, Chatta G, et al. A phase II trial of the Src-kinase inhibitor AZD0530 in patients with advanced castration-resistant prostate cancer: A California Cancer Consortium study. Anticancer Drugs. 2009;20:179–84.

152. MacKay HJ, Au HJ, McWhirter E, Alcindor T, Jarvi A, MacAlpine K, et al. A phase II trial of the Src kinase inhibitor saracatinib (AZD0530) in patients with metastatic or locally advanced gastric or gastro esophageal junction (GEJ) adenocarcinoma: A trial of the PMH phase II consortium. Invest New Drugs. 2012;30:1158–63.

153. Gucalp A, Sparano JA, Caravelli J, Santamauro J, Patil S, Abbruzzi A, et al. Phase II trial of saracatinib (AZD0530), an oral SRC-inhibitor for the treatment of patients with hormone receptor-negative metastatic breast cancer. Clin Breast Cancer. 2011;11:306–11.

154. Arcaroli JJ, Touban BM, Tan AC, Varella-Garcia M, Powell RW, Eckhardt SG, et al. Gene array and fluorescence in situ hybridization biomarkers of activity of saracatinib (AZD0530), a Src inhibitor, in a preclinical model of colorectal cancer. Clin Cancer Res. 2010;16:4165–77.

155. Nagaraj NS, Smith JJ, Revetta F, Washington MK, Merchant NB. Targeted

Inhibition of Src Kinase Signaling Attenuates Pancreatic Tumorigenesis. Mol Cancer Ther [Internet]. 2010;9:2322–32. Available from: http://mct.aacrjournals.org/cgi/doi/10.1158/1535-7163.MCT-09-1212

156. Scaltriti M, Rojo F, Ocaña A, Anido J, Guzman M, Cortes J, et al. Expression of p95HER2, a truncated form of the HER2 receptor, and response to Anti-HER2 therapies in breast cancer. J Natl Cancer Inst. 2007;99:628–38.

157. Tan M, Li P, Klos KS, Lu J, Lan KH, Nagata Y, et al. ErbB2 promotes Src synthesis and stability: Novel mechanisms of Src activation that confer breast cancer metastasis. Cancer Res. 2005;65:1858–67.

158. Zhang S, Huang WC, Li P, Guo H, Poh SB, Brady SW, et al. Combating trastuzumab resistance by targeting SRC, a common node downstream of multiple resistance pathways. Nat Med [Internet]. 2011 [cited 2018 Feb 12];17:461–9. Available from: http://www.ncbi.nlm.nih.gov/pubmed/21399647

159. Mitra D, Brumlik MJ, Okamgba SU, Zhu Y, Duplessis TT, Parvani JG, et al. An oncogenic isoform of HER2 associated with locally disseminated breast cancer and trastuzumab resistance. Mol Cancer Ther [Internet]. 2009;8:2152–62. Available from: http://mct.aacrjournals.org/cgi/doi/10.1158/1535-7163.MCT-09-0295

160. Wang L, Yu X, Dong J, Meng Y, Yang Y, Wang H, et al. Combined SRC inhibitor saracatinib and anti-ErbB2 antibody H2-18 produces a synergistic antitumor effect on trastuzumab-resistant breast cancer. Biochem Biophys Res Commun. 2016;479:563–70.

161. Biscardi JS, Maa MC, Tice DA, Cox ME, Leu TH, Parsons SJ. C-Src-mediated phosphorylation of the epidermal growth factor receptor on Tyr845 and Tyr1101 is

associated with modulation of receptor function. J Biol Chem. 1999;

162. Maa MC, Leu TH, McCarley DJ, Schatzman RC, Parsons SJ. Potentiation of epidermal growth factor receptor-mediated oncogenesis by c-Src: implications for the etiology of multiple human cancers. Proc Natl Acad Sci U S A. 1995;

163. Osherov N, Levitzki A. Epidermal-Growth-Factor-Dependent Activation of the Src-Family Kinases. Eur J Biochem. 1994;

164. Sato K-I. Cellular functions regulated by phosphorylation of EGFR on Tyr845. Int J Mol Sci [Internet]. Multidisciplinary Digital Publishing Institute (MDPI); 2013 [cited 2018 Jul 17];14:10761–90. Available from: http://www.ncbi.nlm.nih.gov/pubmed/23702846

165. Nagaraj NS, Washington MK, Merchant NB. Combined blockade of Src kinase and epidermal growth factor receptor with gemcitabine overcomes STAT3-mediated resistance of inhibition of pancreatic tumor growth. Clin Cancer Res. 2011;17:483–93.

166. Wheeler DL, Iida M, Kruser TJ, Nechrebecki MM, Dunn EF, Armstrong E a, et al. Epidermal growth factor receptor cooperates with Src family kinases in acquired resistance to cetuximab. Cancer Biol Ther. 2009;8:696–703.

167. Nautiyal J, Majumder P, Patel BB, Lee FY, Majumdar APN. Src inhibitor dasatinib inhibits growth of breast cancer cells by modulating EGFR signaling. Cancer Lett. 2009;

168. Li C, Iida M, Dunn EF, Ghia AJ, Wheeler DL. Nuclear EGFR contributes to acquired resistance to cetuximab. Oncogene. 2009;

169. Dunn EF, Iida M, Myers RA, Campbell DA, Hintz KA, Armstrong EA, et al. Dasatinib

sensitizes KRAS mutant colorectal tumors to cetuximab. Oncogene. 2011;30:561–74.

170. Xie YM, Hung MC. Nuclear localization of P185neuTyrosine kinase and its association with transcriptional transactivation. Biochem Biophys Res Commun. 1994;

171. Wang D, DuBois RN. Immunosuppression associated with chronic inflammation in the tumor microenvironment. Carcinogenesis [Internet]. Oxford University Press; 2015 [cited 2018 Jul 9];36:1085–93. Available from: http://www.ncbi.nlm.nih.gov/pubmed/26354776

172. Ascierto ML, Kmieciak M, Idowu MO, Manjili R, Zhao Y, Grimes M, et al. A signature of immune function genes associated with recurrence-free survival in breast cancer patients. Breast Cancer Res Treat [Internet]. 2012 [cited 2018 Jun 4];131:871–80. Available from: http://www.ncbi.nlm.nih.gov/pubmed/21479927

173. Alexe G, Dalgin GS, Scanfeld D, Tamayo P, Mesirov JP, DeLisi C, et al. High Expression of Lymphocyte-Associated Genes in Node-Negative HER2+ Breast Cancers Correlates with Lower Recurrence Rates. Cancer Res [Internet]. 2007 [cited 2018 Jun 4];67:10669–76. Available from: http://www.ncbi.nlm.nih.gov/pubmed/18006808

174. Denkert C, Loibl S, Noske A, Roller M, Müller BM, Komor M, et al. Tumor-Associated Lymphocytes As an Independent Predictor of Response to Neoadjuvant Chemotherapy in Breast Cancer. J Clin Oncol [Internet]. 2010 [cited 2018 Jun 4];28:105–13. Available from: http://www.ncbi.nlm.nih.gov/pubmed/19917869

175. Ernst B, Anderson KS. Immunotherapy for the Treatment of Breast Cancer. Curr

Oncol Rep [Internet]. Springer US; 2015 [cited 2018 Jun 4];17:5. Available from: http://link.springer.com/10.1007/s11912-014-0426-9

176. Schreiber RD, Old LJ, Smyth MJ. Cancer Immunoediting: Integrating Immunity's Roles in Cancer Suppression and Promotion. Science (80-) [Internet]. 2011 [cited 2018 Jul 2];331:1565–70. Available from: http://www.ncbi.nlm.nih.gov/pubmed/21436444

177. Vesely MD, Kershaw MH, Schreiber RD, Smyth MJ. Natural Innate and Adaptive Immunity to Cancer. Annu Rev Immunol [Internet]. 2011 [cited 2018 Jul 2];29:235–71. Available from: http://www.ncbi.nlm.nih.gov/pubmed/21219185

178. Mahmoud SMA, Paish EC, Powe DG, Macmillan RD, Grainge MJ, Lee AHS, et al. Tumor-Infiltrating CD8 $^{+}$ Lymphocytes Predict Clinical Outcome in Breast Cancer. J Clin Oncol [Internet]. 2011 [cited 2018 Jul 2];29:1949–55. Available from: http://www.ncbi.nlm.nih.gov/pubmed/21483002

179. Ramakrishnan R, Assudani D, Nagaraj S, Hunter T, Cho H-I, Antonia S, et al. Chemotherapy enhances tumor cell susceptibility to CTL-mediated killing during cancer immunotherapy in mice. J Clin Invest [Internet]. 2010 [cited 2018 Jul 2];120:1111–24. Available from: http://www.ncbi.nlm.nih.gov/pubmed/20234093

180. Rech AJ, Mick R, Martin S, Recio A, Aqui NA, Powell DJ, et al. CD25 Blockade Depletes and Selectively Reprograms Regulatory T Cells in Concert with Immunotherapy in Cancer Patients. Sci Transl Med [Internet]. 2012 [cited 2018 Jul 2];4:134ra62-134ra62. Available from: http://www.ncbi.nlm.nih.gov/pubmed/22593175

181. Jiang X, Shapiro DJ. The immune system and inflammation in breast cancer. Mol

Cell Endocrinol. 2014;

182. DeNardo DG, Coussens LM. Inflammation and breast cancer. Balancing immune response: crosstalk between adaptive and innate immune cells during breast cancer progression. Breast Cancer Res [Internet]. 2007 [cited 2018 Jul 2];9:212. Available from: http://www.ncbi.nlm.nih.gov/pubmed/17705880

183. Bohling SD, Allison KH. Immunosuppressive regulatory T cells are associated with aggressive breast cancer phenotypes: a potential therapeutic target. Mod Pathol 2008 2112 [Internet]. Nature Publishing Group; 2008 [cited 2018 Jul 3];21:1527. Available from: https://www.nature.com/articles/modpathol2008160

184. Ladoire S, Mignot G, Dabakuyo S, Arnould L, Apetoh L, Rébé C, et al. In situ immune response after neoadjuvant chemotherapy for breast cancer predicts survival. J Pathol. 2011;

185. Rosenberg SA, Yang JC, Sherry RM, Kammula US, Hughes MS, Phan GQ, et al. Durable complete responses in heavily pretreated patients with metastatic melanoma using T-cell transfer immunotherapy. Clin Cancer Res. 2011;

186. Larkin J, Chiarion-Sileni V, Gonzalez R, Grob JJ, Cowey CL, Lao CD, et al. Combined Nivolumab and Ipilimumab or Monotherapy in Untreated Melanoma. N Engl J Med. 2015;

187. Tumeh PC, Harview CL, Yearley JH, Shintaku IP, Taylor EJM, Robert L, et al. PD-1 blockade induces responses by inhibiting adaptive immune resistance. Nature. 2014;

188. Oncolytic Virus Therapy Shows Benefit in Patients with Melanoma - National Cancer Institute [Internet]. [cited 2018 Nov 5]. Available from:

https://www.cancer.gov/news-events/cancer-currents-blog/2015/oncolyticvirus-melanoma

189. Neves H, Kwok HF. Recent advances in the field of anti-cancer immunotherapy. BBA Clin. 2015. page 280–8.

190. Emens LA. Breast cancer immunobiology driving immunotherapy: vaccines and immune checkpoint blockade. Expert Rev Anticancer Ther [Internet]. 2012 [cited 2018 Jun 4];12:1597–611. Available from: http://www.ncbi.nlm.nih.gov/pubmed/23253225

191. Corraliza-Gorjón I, Somovilla-Crespo B, Santamaria S, Garcia-Sanz JA, Kremer L. New Strategies Using Antibody Combinations to Increase Cancer Treatment Effectiveness. Front Immunol [Internet]. Frontiers; 2017 [cited 2018 Jul 5];8:1804. Available from: http://journal.frontiersin.org/article/10.3389/fimmu.2017.01804/full

192. Dine J, Gordon R, Shames Y, Kasler MK, Barton-Burke M. Immune Checkpoitn Inhibitors: An Innovation in Immunotherpay for the Treatment and Managment of Paatients With Cancer. Asia Pac J Oncol Nurs. 2017;

193. Commissioner O of the. Press Announcements - FDA approves first cancer treatment for any solid tumor with a specific genetic feature. Office of the Commissioner; [cited 2018 Nov 8]; Available from: https://www.fda.gov/newsevents/newsroom/pressannouncements/ucm560167.htm

194. Melero I, Gaudernack G, Gerritsen W, Huber C, Parmiani G, Scholl S, et al. Therapeutic vaccines for cancer: an overview of clinical trials. Nat Rev Clin Oncol [Internet]. 2014 [cited 2018 Jun 4];11:509–24. Available from:

http://www.ncbi.nlm.nih.gov/pubmed/25001465

195. Mittendorf EA, Clifton GT, Holmes JP, Schneble E, van Echo D, Ponniah S, et al. Final report of the phase I/II clinical trial of the E75 (nelipepimut-S) vaccine with booster inoculations to prevent disease recurrence in high-risk breast cancer patients. Ann Oncol Off J Eur Soc Med Oncol [Internet]. Oxford University Press; 2014 [cited 2018 Jul 6];25:1735–42. Available from: http://www.ncbi.nlm.nih.gov/pubmed/24907636

196. Kantoff PW, Higano CS, Shore ND, Berger ER, Small EJ, Penson DF, et al. Sipuleucel-T Immunotherapy for Castration-Resistant Prostate Cancer. N Engl J Med [Internet]. 2010 [cited 2018 Jun 4];363:411–22. Available from: http://www.ncbi.nlm.nih.gov/pubmed/20818862

197. Hammerstrom AE, Cauley DH, Atkinson BJ, Sharma P. Cancer Immunotherapy: Sipuleucel-T and Beyond. Pharmacotherapy [Internet]. 2011 [cited 2018 Jul 6];31:813–28. Available from: http://www.ncbi.nlm.nih.gov/pubmed/21923608

198. Park JW, Melisko ME, Esserman LJ, Jones LA, Wollan JB, Sims R. Treatment with autologous antigen-presenting cells activated with the HER-2 -based antigen lapuleucel-T: Results of a phase I study in immunologic and clinical activity in HER-2-overexpressing breast cancer. J Clin Oncol. 2007;

199. Lacroix M, Toillon R-A, Leclercq G. p53 and breast cancer, an update. Endocr Relat Cancer [Internet]. 2006 [cited 2018 Jul 2];13:293–325. Available from: http://www.ncbi.nlm.nih.gov/pubmed/16728565

200. Hamidullah, Changkija B, Konwar R. Role of interleukin-10 in breast cancer. Breast Cancer Res Treat [Internet]. 2012 [cited 2018 Jun 4];133:11–21. Available from:

http://www.ncbi.nlm.nih.gov/pubmed/22057973

201. Yao S, Zhu Y, Chen L. Advances in targeting cell surface signalling molecules for immune modulation. Nat Rev Drug Discov [Internet]. 2013 [cited 2018 Jun 4];12:130–46. Available from: http://www.ncbi.nlm.nih.gov/pubmed/23370250

202. Hodi FS, Ballinger M, Lyons B, Soria J-C, Nishino M, Tabernero J, et al. Immune-Modified Response Evaluation Criteria In Solid Tumors (imRECIST): Refining Guidelines to Assess the Clinical Benefit of Cancer Immunotherapy. J Clin Oncol [Internet]. 2018 [cited 2018 Nov 6];36:850–8. Available from: http://ascopubs.org/doi/10.1200/JCO.2017.75.1644

203. Kohrt HE, Tumeh PC, Benson D, Bhardwaj N, Brody J, Formenti S, et al. Immunodynamics: A cancer immunotherapy trials network review of immune monitoring in immuno-oncology clinical trials. J. Immunother. Cancer. 2016.

204. Riley JL. Combination Checkpoint Blockade — Taking Melanoma Immunotherapy to the Next Level. N Engl J Med. 2013;

205. Moodie Z, Price L, Janetzki S, Britten CM. Response determination criteria for ELISPOT: Toward a standard that can be applied across laboratories. Methods Mol Biol. 2012;

206. Mori A, Deola S, Xumerle L, Mijatovic V, Malerba G, Monsurrò V. Next generation sequencing: New tools in immunology and hematology. Blood Res. 2013.

207. Marciscano AE, Thorek DLJ. Role of noninvasive molecular imaging in determining response. Adv Radiat Oncol [Internet]. Elsevier; 2018 [cited 2018 Nov 6];3:534–47. Available from: http://www.ncbi.nlm.nih.gov/pubmed/30370353

208. Ponomarev V. Advancing Immune and Cell-Based Therapies Through Imaging.

Mol Imaging Biol. 2017;

209. Chatterjee S, Lesniak WG, Miller MS, Lisok A, Sikorska E, Wharram B, et al. Rapid PD-L1 detection in tumors with PET using a highly specific peptide. Biochem Biophys Res Commun. 2017;

210. Bensch F, Veen E van der, Jorritsma A, Hooge ML, Boellaard R, Oosting S, et al. Abstract CT017: First-in-human PET imaging with the PD-L1 antibody ^{89} Zr-atezolizumab. Cancer Res. 2017;

211. Schwarzenberg J, Radu CG, Benz M, Fueger B, Tran AQ, Phelps ME, et al. Human biodistribution and radiation dosimetry of novel PET probes targeting the deoxyribonucleoside salvage pathway. Eur J Nucl Med Mol Imaging. 2011;

212. Namavari M, Chang YF, Kusler B, Yaghoubi S, Mitchell BS, Gambhir SS. Synthesis of 2'-Deoxy-2'-[18F]fluoro-9-β- DArabinofuranosylguanine: A novel agent for imaging T-cell activation with PET. Mol Imaging Biol. 2011;

213. Tavaré R, Escuin-Ordinas H, Mok S, McCracken MN, Zettlitz KA, Salazar FB, et al. An effective immuno-PET imaging method to monitor CD8-dependent responses to immunotherapy. Cancer Res. 2016;76:73–82.

214. Tavare R, McCracken MN, Zettlitz KA, Knowles SM, Salazar FB, Olafsen T, et al. Engineered antibody fragments for immuno-PET imaging of endogenous CD8+ T cells in vivo. Proc Natl Acad Sci. 2014;

215. Ryan Q, Ibrahim A, Cohen MH, Johnson J, Ko C -w., Sridhara R, et al. FDA Drug Approval Summary: Lapatinib in Combination with Capecitabine for Previously Treated Metastatic Breast Cancer That Overexpresses HER-2. Oncologist [Internet]. 2008;13:1114–9. Available from:

http://theoncologist.alphamedpress.org/cgi/doi/10.1634/theoncologist.2008-0816

216. Hortobagyi GN. Trastuzumab in the Treatment of Breast Cancer. N Engl J Med [Internet]. 2005;353:1734–6. Available from: http://www.nejm.org/doi/abs/10.1056/NEJMe058196

217. Gonzalez-Angulo AM, Morales-Vasquez F, Hortobagyi GN. Overview of resistance to systemic therapy in patients with breast cancer. Adv. Exp. Med. Biol. 2007. page 1–22.

218. Muthuswamy SK. Trastuzumab resistance: All roads lead to SRC. Nat Med. 2011;17:416–8.

219. Talpaz M, Shah NP, Kantarjian H, Donato N, Nicoll J, Paquette R, et al. Dasatinib in Imatinib-Resistant Philadelphia Chromosome–Positive Leukemias. N Engl J Med [Internet]. 2006;354:2531–41. Available from: http://www.nejm.org/doi/abs/10.1056/NEJMoa055229

220. Seoane S, Montero JC, Ocaña A, Pandiella A. Effect of multikinase inhibitors on caspase-independent cell death and DNA damage in HER2-overexpressing breast cancer cells. J Natl Cancer Inst. 2010;102:1432–46.

221. Ocana A, Gil-Martin M, Martín M, Rojo F, Antolín S, Guerrero Á, et al. A phase I study of the SRC kinase inhibitor dasatinib with trastuzumab and paclitaxel as first line therapy for patients with HER2-overexpressing advanced breast cancer. GEICAM/2010-04 study. Oncotarget [Internet]. 2017; Available from: http://www.oncotarget.com/fulltext/17113

222. Boerner RJ, Kassel DB, Barker SC, Ellis B, DeLacy P, Knight WB. Correlation of the phosphorylation states of pp60(c-Src) with tyrosine kinase activity: The

intramolecular pY530-SH2 complex retains significant activity if Y419 is phosphorylated. Biochemistry. 1996;35:9519–25.

223. Lan KH, Lu CH, Yu D. Mechanisms of trastuzumab resistance and their clinical implications. Ann N Y Acad Sci. 2005. page 70–5.

224. Belsches-Jablonski AP, Biscardi JS, Peavy DR, Tice D a, Romney D a, Parsons SJ. Src family kinases and HER2 interactions in human breast cancer cell growth and survival. Oncogene [Internet]. 2001;20:1465–75. Available from: http://www.ncbi.nlm.nih.gov/pubmed/11313890

225. Peiró G, Ortiz-Martínez F, Gallardo A, Pérez-Balaguer A, Sánchez-Payá J, Ponce JJ, et al. Src, a potential target for overcoming trastuzumab resistance in HER2-positive breast carcinoma. Br J Cancer. 2014;111:689–95.

226. Veach DR, Namavari M, Pillarsetty N, Santos EB, Beresten-Kochetkov T, Lambek C, et al. Synthesis and biological evaluation of a fluorine-18 derivative of dasatinib. J Med Chem. 2007;50:5853–7.

227. Fan P, McDaniel RE, Kim HR, Clagett D, Haddad B, Craig Jordan V. Modulating therapeutic effects of the c-Src inhibitor via oestrogen receptor and human epidermal growth factor receptor 2 in breast cancer cell lines. Eur J Cancer [Internet]. Pergamon; 2012 [cited 2018 Jul 16];48:3488–98. Available from: https://www.sciencedirect.com/science/article/pii/S0959804912003711

228. Massicano AVF, Marquez-Nostra B V., Lapi SE. Targeting HER2 in Nuclear Medicine for Imaging and Therapy. Mol Imaging. 2018;17.

229. Schneider BP, Winer EP, Foulkes WD, Garber J, Perou CM, Richardson A, et al. Triple-Negative Breast Cancer: Risk Factors to Potential Targets. Clin Cancer Res

[Internet]. 2008 [cited 2018 Aug 3];14:8010–8. Available from: http://www.ncbi.nlm.nih.gov/pubmed/19088017

230. Corkery B, Crown J, Clynes M, O'Donovan N. Epidermal growth factor receptor as a potential therapeutic target in triple-negative breast cancer. Ann Oncol [Internet]. 2009 [cited 2018 Aug 3];20:862–7. Available from: http://www.ncbi.nlm.nih.gov/pubmed/19150933

231. Lehmann BD, Bauer JA, Chen X, Sanders ME, Chakravarthy AB, Shyr Y, et al. Identification of human triple-negative breast cancer subtypes and preclinical models for selection of targeted therapies. J Clin Invest [Internet]. 2011 [cited 2018 Aug 3];121:2750–67. Available from: http://www.ncbi.nlm.nih.gov/pubmed/21633166

232. Nakai K, Hung M-C, Yamaguchi H. A perspective on anti-EGFR therapies targeting triple-negative breast cancer. Am J Cancer Res [Internet]. e-Century Publishing Corporation; 2016 [cited 2018 Aug 3];6:1609–23. Available from: http://www.ncbi.nlm.nih.gov/pubmed/27648353

233. Masuda H, Zhang D, Bartholomeusz C, Doihara H, Hortobagyi GN, Ueno NT. Role of epidermal growth factor receptor in breast cancer. Breast Cancer Res Treat [Internet]. 2012 [cited 2018 Aug 3];136:331–45. Available from: http://www.ncbi.nlm.nih.gov/pubmed/23073759

234. Gelmon K, Dent R, Mackey JR, Laing K, McLeod D, Verma S. Targeting triple-negative breast cancer: optimising therapeutic outcomes. Ann Oncol [Internet]. 2012 [cited 2018 Aug 3];23:2223–34. Available from:

http://www.ncbi.nlm.nih.gov/pubmed/22517820

235. Brand TM, Iida M, Li C, Wheeler DL. The nuclear epidermal growth factor receptor signaling network and its role in cancer. Discov Med [Internet]. 2011 [cited 2018 Aug 3];12:419–32. Available from: http://www.ncbi.nlm.nih.gov/pubmed/22127113

236. Han W, Lo H-W. Landscape of EGFR signaling network in human cancers: Biology and therapeutic response in relation to receptor subcellular locations. Cancer Lett [Internet]. 2012 [cited 2018 Aug 3];318:124–34. Available from: http://www.ncbi.nlm.nih.gov/pubmed/22261334

237. Traynor AM, Weigel TL, Oettel KR, Yang DT, Zhang C, Kim K, et al. Nuclear EGFR protein expression predicts poor survival in early stage non-small cell lung cancer. Lung Cancer [Internet]. NIH Public Access; 2013 [cited 2018 Aug 3];81:138–41. Available from: http://www.ncbi.nlm.nih.gov/pubmed/23628526

238. Lo HW, Hsu SC, Hung MC. EGFR signaling pathway in breast cancers: From traditional signal transduction to direct nuclear translocalization. Breast Cancer Res. Treat. 2006. page 211–8.

239. Brand TM, Iida M, Dunn EF, Luthar N, Kostopoulos KT, Corrigan KL, et al. Nuclear epidermal growth factor receptor is a functional molecular target in triple-negative breast cancer. Mol Cancer Ther [Internet]. NIH Public Access; 2014 [cited 2018 Aug 3];13:1356–68. Available from: http://www.ncbi.nlm.nih.gov/pubmed/24634415

240. Li C, Iida M, Dunn EF, Wheeler DL. Dasatinib blocks cetuximab- and radiation-induced nuclear translocation of the epidermal growth factor receptor in head and neck squamous cell carcinoma. Radiother Oncol [Internet]. NIH Public Access;

2010 [cited 2018 Aug 3];97:330–7. Available from: http://www.ncbi.nlm.nih.gov/pubmed/20667610

241. van Loon J, Even AJG, Aerts HJWL, Öllers M, Hoebers F, van Elmpt W, et al. PET imaging of zirconium-89 labelled cetuximab: A phase I trial in patients with head and neck and lung cancer. Radiother Oncol [Internet]. 2017 [cited 2018 Aug 3];122:267–73. Available from: http://www.ncbi.nlm.nih.gov/pubmed/28012793

242. Even AJG, Hamming-Vrieze O, van Elmpt W, Winnepenninckx VJL, Heukelom J, Tesselaar MET, et al. Quantitative assessment of Zirconium-89 labeled cetuximab using PET/CT imaging in patients with advanced head and neck cancer: a theragnostic approach. Oncotarget [Internet]. 2017 [cited 2018 Aug 3];8:3870–80. Available from: http://www.ncbi.nlm.nih.gov/pubmed/27965472

243. Menke-van der Houven van Oordt CW, Gootjes EC, Huisman MC, Vugts DJ, Roth C, Luik AM, et al. 89Zr-cetuximab PET imaging in patients with advanced colorectal cancer. Oncotarget [Internet]. 2015;6:30384–93. Available from: http://www.ncbi.nlm.nih.gov/pubmed/26309164%0Ahttp://www.pubmedcentral.nih.gov/articlerender.fcgi?artid=PMC4745807

244. van Dijk LK, Boerman OC, Kaanders JHAM, Bussink J. PET Imaging in Head and Neck Cancer Patients to Monitor Treatment Response: A Future Role for EGFR-Targeted Imaging. Clin Cancer Res [Internet]. 2015 [cited 2018 Aug 3];21:3602–9. Available from: http://clincancerres.aacrjournals.org/cgi/doi/10.1158/1078-0432.CCR-15-0348

245. Chekol R, Solomon VR, Alizadeh E, Bernhard W, Fisher D, Hill W, et al. 89Zr-nimotuzumab for immunoPET imaging of epidermal growth factor receptor I.

Oncotarget [Internet]. Impact Journals, LLC; 2018 [cited 2018 Aug 3];9:17117–32. Available from: http://www.ncbi.nlm.nih.gov/pubmed/29682209

246. Pool M, Kol A, Lub-de Hooge MN, Gerdes CA, de Jong S, de Vries EGE, et al. Extracellular domain shedding influences specific tumor uptake and organ distribution of the EGFR PET tracer 89Zr-imgatuzumab. Oncotarget [Internet]. Impact Journals, LLC; 2016 [cited 2018 Aug 3];7:68111–21. Available from: http://www.ncbi.nlm.nih.gov/pubmed/27602494
247. Wei L, Shi J, Afari G, Bhattacharyya S. Preparation of clinical-grade 89Zr-panitumumab as a positron emission tomography biomarker for evaluating epidermal growth factor receptor-targeted therapy. J Label Compd Radiopharm. 2014;57:25–35.
248. Aerts HJWL, Dubois L, Perk L, Vermaelen P, van Dongen GAMS, Wouters BG, et al. Disparity Between In Vivo EGFR Expression and 89Zr-Labeled Cetuximab Uptake Assessed with PET. J Nucl Med [Internet]. 2008 [cited 2018 Aug 7];50:123–31. Available from: http://www.ncbi.nlm.nih.gov/pubmed/19091906
249. Sihver W, Pietzsch J, Krause M, Baumann M, Steinbach J, Pietzsch H-J. Radiolabeled Cetuximab Conjugates for EGFR Targeted Cancer Diagnostics and Therapy. Pharmaceuticals (Basel) [Internet]. Multidisciplinary Digital Publishing Institute (MDPI); 2014 [cited 2018 Aug 7];7:311–38. Available from: http://www.ncbi.nlm.nih.gov/pubmed/24603603
250. Brand TM, Iida M, Dunn EF, Luthar N, Kostopoulos KT, Corrigan KL, et al. Nuclear Epidermal Growth Factor Receptor Is a Functional Molecular Target in Triple-Negative Breast Cancer. Mol Cancer Ther [Internet]. 2014 [cited 2018 Aug

3];13:1356–68. Available from: http://www.ncbi.nlm.nih.gov/pubmed/24634415

251. Brand TM, Iida M, Dunn EF, Luthar N, Kostopoulos KT, Corrigan KL, et al. Nuclear Epidermal Growth Factor Receptor Is a Functional Molecular Target in Triple-Negative Breast Cancer. Mol Cancer Ther [Internet]. 2014 [cited 2018 Aug 3];13:1356–68. Available from: http://mct.aacrjournals.org/cgi/doi/10.1158/1535-7163.MCT-13-1021

252. Restifo NP, Dudley ME, Rosenberg SA. Adoptive immunotherapy for cancer: Harnessing the T cell response. Nat. Rev. Immunol. 2012. page 269–81.

253. Kroemer G, Senovilla L, Galluzzi L, André F, Zitvogel L. Natural and therapy-induced immunosurveillance in breast cancer. Nat. Med. 2015. page 1128–38.

254. Hoos A, Janetzki S, Britten CM. Advancing the field of cancer immunotherapy: MIATA consensus guidelines become available to improve data reporting and interpretation for T-cell immune monitoring. Oncoimmunology. 2012;1:1457–9.

255. Yuan J, Hegde PS, Clynes R, Foukas PG, Harari A, Kleen TO, et al. Novel technologies and emerging biomarkers for personalized cancer immunotherapy. J. Immunother. Cancer. 2016.

256. Chen PL, Roh W, Reuben A, Cooper ZA, Spencer CN, Prieto PA, et al. Analysis of immune signatures in longitudinal tumor samples yields insight into biomarkers of response and mechanisms of resistance to immune checkpoint blockade. Cancer Discov. 2016;6:827–37.

257. Gerlinger M, Rowan AJ, Horswell S, Larkin J, Endesfelder D, Gronroos E, et al. Intratumor Heterogeneity and Branched Evolution Revealed by Multiregion Sequencing. N Engl J Med [Internet]. 2012;366:883–92. Available from:

http://www.nejm.org/doi/abs/10.1056/NEJMoa1113205

258. Rashidian M, Ingram JR, Dougan M, Dongre A, Whang KA, LeGall C, et al. Predicting the response to CTLA-4 blockade by longitudinal noninvasive monitoring of CD8 T cells. J Exp Med [Internet]. 2017;214:2243–55. Available from: http://www.jem.org/lookup/doi/10.1084/jem.20161950

259. Natarajan A, Mayer AT, Xu L, Reeves RE, Gano J, Gambhir SS. Novel Radiotracer for ImmunoPET Imaging of PD-1 Checkpoint Expression on Tumor Infiltrating Lymphocytes. Bioconjug Chem. 2015;

260. Truillet C, Oh HLJ, Yeo SP, Lee CY, Huynh LT, Wei J, et al. Imaging PD-L1 Expression with ImmunoPET. Bioconjug Chem. 2018;29:96–103.

261. Kikuchi M, Clump DA, Srivastava RM, Sun L, Zeng D, Diaz-Perez JA, et al. Preclinical immunoPET/CT imaging using Zr-89-labeled anti-PD-L1 monoclonal antibody for assessing radiation-induced PD-L1 upregulation in head and neck cancer and melanoma. Oncoimmunology [Internet]. 2017 [cited 2018 Jun 12];6:e1329071. Available from: http://www.ncbi.nlm.nih.gov/pubmed/28811971

262. Hettich M, Braun F, Bartholomä MD, Schirmbeck R, Niedermann G. High-resolution PET imaging with therapeutic antibody-based PD-1/PD-L1 checkpoint tracers. Theranostics. 2016;

263. Schoenborn JR, Wilson CB. Regulation of interferon-gamma during innate and adaptive immune responses. Adv. Immunol. 2007.

264. Coussens LM, Zitvogel L, Palucka AK. Neutralizing tumor-promoting chronic inflammation: A magic bullet? Science (80-.). 2013.

265. Li K, Baird M, Yang J, Jackson C, Ronchese F, Young S. Conditions for the

generation of cytotoxic CD4+ Th cells that enhance CD8+ CTL-mediated tumor regression. Clin Transl Immunol. 2016;

266. Knutson KL, Disis ML. Tumor antigen-specific T helper cells in cancer immunity and immunotherapy. Cancer Immunol. Immunother. 2005.

267. Xu X, Fu X, Plate J, Chong AS. IFN-y Induces Cell Growth Inhibition by Fas-mediated Apoptosis : Requirement of STATI Protein for Up-Regulation of Fas and FasL Expression1 Fas FasL ^. Cell. 1998;

268. Zaidi MR, Merlino G. The two faces of interferon-?? in cancer. Clin. Cancer Res. 2011.

269. Viola-Villegas NT, Sevak KK, Carlin SD, Doran MG, Evans HW, Bartlett DW, et al. Noninvasive imaging of PSMA in prostate tumors with89Zr-Labeled huJ591 engineered antibody fragments: The faster alternatives. Mol Pharm. 2014;11:3965–73.

270. Jacob J, Radkevich O, Forni G, Zielinski J, Shim D, Jones RF, et al. Activity of DNA vaccines encoding self or heterologous Her-2/neu in Her-2 or neu transgenic mice. Cell Immunol. 2006;

271. Deng L, Liang H, Burnette B, Beckett M, Darga T, Weichselbaum RR, et al. Irradiation and anti-PD-L1 treatment synergistically promote antitumor immunity in mice. J Clin Invest. 2014;124:687–95.

272. Linch SN, Kasiewicz MJ, McNamara MJ, Hilgart-Martiszus IF, Farhad M, Redmond WL. Combination OX40 agonism/CTLA-4 blockade with HER2 vaccination reverses T-cell anergy and promotes survival in tumor-bearing mice. Proc Natl

Acad Sci. 2016;

273. Diodoro MG, Carlo E Di, Zappacosta R, Iezzi M, Coletti A, Modesti A, et al. Salivary carcinoma in HER-2/neu transgenic male mice: An angiogenic switch is not required for tumor onset and progression. Int J Cancer. 2000;
274. Ambrosino E, Spadaro M, Iezzi M, Curcio C, Forni G, Musiani P, et al. Immunosurveillance of Erbb2 carcinogenesis in transgenic mice is concealed by a dominant regulatory T-cell self-tolerance. Cancer Res. 2006;66:7734–40.
275. Whittington PJ, Piechocki MP, Heng HH, Jacob JB, Jones RF, Back JB, et al. DNA vaccination controls Her-2+ tumors that are refractory to targeted therapies. Cancer Res [Internet]. 2008 [cited 2018 Jun 12];68:7502–11. Available from: http://cancerres.aacrjournals.org/cgi/doi/10.1158/0008-5472.CAN-08-1489
276. Park S, Jiang Z, Mortenson ED, Deng L, Radkevich-Brown O, Yang X, et al. The therapeutic effect of anti-HER2/neu antibody depends on both innate and adaptive immunity. Cancer Cell [Internet]. 2010 [cited 2018 Jun 12];18:160–70. Available from: http://linkinghub.elsevier.com/retrieve/pii/S1535610810002485
277. Stanton SE, Disis ML. Clinical significance of tumor-infiltrating lymphocytes in breast cancer. J Immunother cancer [Internet]. 2016 [cited 2018 Jun 13];4:59. Available from: http://jitc.biomedcentral.com/articles/10.1186/s40425-016-0165-6
278. Gooden MJM, de Bock GH, Leffers N, Daemen T, Nijman HW. The prognostic influence of tumour-infiltrating lymphocytes in cancer: a systematic review with meta-analysis. Br J Cancer [Internet]. 2011 [cited 2018 Jun 13];105:93–103. Available from: http://www.nature.com/articles/bjc2011189
279. Gnjatic S, Bronte V, Brunet LR, Butler MO, Disis ML, Galon J, et al. Identifying

baseline immune-related biomarkers to predict clinical outcome of immunotherapy. J. Immunother. Cancer. 2017.

280. Lindmo T, Boven E, Cuttitta F, Fedorko J, Bunn PA. Determination of the immunoreactive function of radiolabeled monoclonal antibodies by linear extrapolation to binding at infinite antigen excess. J Immunol Methods. 1984;72:77–89.

281. McKnight BN, Kuda-Wedagedara ANW, Sevak KK, Abdel-Atti D, Wiesend WN, Ku A, et al. Imaging EGFR and HER3 through 89Zr-labeled MEHD7945A (Duligotuzumab). Sci Rep [Internet]. Nature Publishing Group; 2018 [cited 2018 Jul 11];8:9043. Available from: http://www.nature.com/articles/s41598-018-27454-6

282. Gibson HM, Veenstra JJ, Jones R, Vaishampayan U, Sauerbrey M, Bepler G, et al. Induction of HER2 Immunity in Outbred Domestic Cats by DNA Electrovaccination. Cancer Immunol Res [Internet]. 2015 [cited 2018 Jun 12];3:777–86. Available from: http://www.ncbi.nlm.nih.gov/pubmed/25711535

283. Gibson HM, Veenstra JJ, Jones R, Vaishampayan U, Sauerbrey M, Bepler G, et al. Induction of HER2 Immunity in Outbred Domestic Cats by DNA Electrovaccination. Cancer Immunol Res. 2015;3:777–86.

284. Zanardi E, Bregni G, de Braud F, Di Cosimo S. Better Together: Targeted Combination Therapies in Breast Cancer. Semin Oncol [Internet]. 2015 [cited 2018 Jul 5];42:887–95. Available from: http://www.ncbi.nlm.nih.gov/pubmed/26615133

285. Li Z, Qiu Y, Lu W, Jiang Y, Wang J. Immunotherapeutic interventions of Triple Negative Breast Cancer. J Transl Med [Internet]. BioMed Central; 2018 [cited 2018 Jul 5];16:147. Available from: https://translational-

medicine.biomedcentral.com/articles/10.1186/s12967-018-1514-7

286. Santabarbara G, Maione P, Rossi A, Palazzolo G, Gridelli C. Novel immunotherapy in the treatment of advanced non-small cell lung cancer. Expert Rev Clin Pharmacol [Internet]. 2016 [cited 2018 Jul 5];9:1571–81. Available from: http://www.ncbi.nlm.nih.gov/pubmed/27623999

287. Yasuda S, Sho M, Yamato I, Yoshiji H, Wakatsuki K, Nishiwada S, et al. Simultaneous blockade of programmed death 1 and vascular endothelial growth factor receptor 2 (VEGFR2) induces synergistic anti-tumour effect *in vivo*. Clin Exp Immunol [Internet]. 2013 [cited 2018 Jul 5];172:500–6. Available from: http://www.ncbi.nlm.nih.gov/pubmed/23600839

ABSTRACT

UTILIZING IMMUNOPET TO MONITOR TUMOR RESPONSE TO TREATMENT IN BREAST CANCER

by

BROOKE N. MCKNIGHT

May 2019

Advisor: Dr. Nerissa Viola

Major: Cancer Biology

Degree: Doctor of Philosophy

With a broad spectrum of therapies available for treating breast cancer, the need for personalized medicine tailoring the cure according to phenotype is evident. Such an approach may be fully realized with the development of quantitative imaging technologies for disease detection, staging and diagnosis, without increasing patient burden. Immuno-positron emission tomography (PET) combines the targeted specificity of antibodies with the sensitivity of PET for whole body imaging by targeting molecular features amplified in lesions. ImmunoPET probes targeting different antigens and their utility to measure response to treatment were explored. ^{89}Zr-trastuzumab was employed as a surrogate readout of Src inhibition after dasatinib treatment in HER2+ breast cancer. ^{89}Zr-cetuximab was also employed to measure cell-surface EGFR expression following dasatinib treatment in triple negative breast cancer. Tumor infiltrating T-cells were measured using ^{89}Zr-anti-CD3 and ^{89}Zr-anti-IFNγ after vaccination in a murine model of breast cancer. All studies utilized *in vitro* uptake assays, autoradiography, IHC, and western blots to validate tracer specificity. PET scans were analyzed after treatment to determine changes in tracer retention. In each study PET was able to detect tumor uptake changes which

occurred early (within 1 week) of treatment. Through these projects I provide clinically relevant imaging strategies to better predict treatment outcomes and aid clinicians in cancer management.

AUTOBIOGRAPHICAL STATEMENT

EDUCATION

Wayne State University **2014-2018**
Doctor of Philosophy: Cancer Biology

University of Michigan, Ann Arbor **2010-2014**
Bachelor of Science: Cell and Molecular Biology

GRANTS

DeRoy Fellowship **2018**
Rumble Fellowship **2018**
T-32 Training Grant – National Institutes of Health (NIH) **2016-2018**
Wayne State University IBS Fellowship **2014-2016**

AWARDS

AAI Young Investigator Award, TRCCC Annual Meeting **2018**
2nd place Oral Presentation, TRCCC Annual Meeting **2018**
Immunology Program travel award, TRCCC Annual Meeting **2018**
Scholar-in-training award, WMIC Annual Meeting **2017**
Cancer Biology student scholar award, WMIC Travel Award **2017**
2nd place Oral Presentation, Cancer Biology Symposium **2017**
Immunology Program travel award, AAI Introductory Immunology Course
Cancer Biology directors award **2016**
2014

SELECTED PUBLICATIONS

Brooke N. McKnight and Nerissa Viola-Villegas. Monitoring Src status after dasatinib treatment in HER2+ breast cancer with ^{89}Zr-trastuzumab PET imaging. Breast Cancer Research 2018; 20:130.

Heather M. Gibson*, **Brooke N. McKnight*,** Joyce Reyes, Wei-Zen Wei, Nerissa T. Viola-Villegas. Interferon-g PET Imaging as a Predictive Tool for Monitoring Response to Tumor Immunotherapy. Cancer Research 2018; 79(19):5706-17.

Brooke N. McKnight, Akhila N. W. Kuda-Wedagedara, Kuntal K. Sevak, Dalya Abdel-Atti, Wendy N. Wiesend, Anson Ku, Dakshnamurthy Selvakumar, Sean D. Carlin, Jason S. Lewis, Nerissa T. Viola-Villegas. Imaging EGFR and HER3 through ^{89}Zr-labeled MEHD7945A (Duligotuzumab). Scientific Reports 2018;8:9043.

McKnight B, and Viola-Villegas N. Zr-ImmunoPET Companion Diagnostics and the Impact in Clinical Drug Development. Journal of Labelled Compounds and Radiopharmaceuticals. 2018;69:727-38.

McFall T, **McKnight B**, Rosati R, Huang L, Viola-Villegas N, and Ratnam M. Progesterone receptor A promotes invasiveness and metastasis of luminal breast cancer by suppressing regulation of critical micro RNAs by estrogen. Journal of Biological Chemistry. 2018;293:1163-77.

Khoriaty R, Vogel N, Hoenerhoff M, Zhu G, Everett L, Nelson B, Durairaj H, **McKnight B**, Zhang B, Ernst S, Ginsburg D, Williams J.A. SEC23B is essential for pancreatic acinar cell function in adult mice. Mol Biol Cell 2017;28:2146-54.

Khoriaty R, Everett L, Chase J, Zhu G, Hoenerhoff M, **McKnight B**, Vasievich MP, Zhang B, Williams J, Maillard I, Ginsburg D. Pancreatic SEC23B Deficiency is Sufficient to Explain the Perinatal Lethality of SEC23B Deficient Mice. Scientific Reports 2016;6:27802.